

City Research Online

City St George's, University of London

Citation: Abdallah, Riyadh A (2007). Finite Element Based Beam Propagation Analysis of Optical Semiconductor Devices. (Unpublished Doctoral thesis, City, University of London)

This is the accepted version of the paper.

This version of the publication may differ from the final published version. To cite this item please consult the publisher's version.

Permanent repository link: https://openaccess.city.ac.uk/id/eprint/20121/

Copyright and Reuse: Copyright and Moral Rights remain with the author(s) and/or copyright holders. Copies of full items can be used for personal research or study, educational, or not-for-profit purposes without prior permission or charge, unless otherwise indicated, provided that the authors, title and full bibliographic details are credited, a hyperlink and/or URL is given for the original metadata page and the content is not changed in any way. For full details of reuse please refer to City Research Online policy.

City Research Online: http://openaccess.city.ac.uk/ publications@citystgeorges.ac.uk

Finite Element Based Beam Propagation Analysis of Optical Semiconductor Devices

By

Riyadh A. Abdallah

A thesis submitted to the City University for the Degree of Doctor in Philosophy

City University

Photonics Research Group
School of Engineering and Mathematical Sciences
Northampton Square, London EC1V 0HB, UK.

August 2007

Table of Contents

Table of Contents ii

List of Tables vi

List of Figures vii

Acknowledgement xviii

Declaration xix

Symbols and Abbreviations xx

Abstract xxi

1.0 Introduction 1
- 1.1 Lightwave Technology 1
  - *1.1.1 Integrated Photonics* 3
  - *1.1.2 Optical Technology Evolution* 4
  - *1.1.3 Optical Communication Research and Technology* 7
  - *1.1.4 Market Overview* 9
- 1.2 Optical Waveguide Structures 10
- 1.3 Analysis of Optical Waveguide Structures 16
- 1.4 Analytical Approximation Solution Techniques 18
  - *1.4.1 Marcatili's Method* 18
  - *1.4.2 The Effective Index Method* 20
- 1.5 Numerical Solution Techniques 21
  - *1.5.1 The Method of Lines* 22
  - *1.5.2 The Boundary Element Method* 23
  - *1.5.3 The Point Matching Method* 24
  - *1.5.4 The Mode Matching Method* 24
  - *1.5.5 The Spectral Index Method* 25
  - *1.5.6 The Finite Difference Method* 26
  - *1.5.7 The Finite Element Method* 28
  - *1.5.8 The Beam Propagation Method* 29
- 1.6 Aims and Objectives of the Thesis 30
- 1.7 Structure and Format of the Thesis 32

2.0 Optical Amplifiers 35
- 2.1 Introduction 35
- 2.2 Overview of Optical Amplifiers 35
- 2.3 Optical Amplifier Classification 36

2.4 Fibre Amplifiers 37
2.4.1 Erbium doped Fibre Amplifiers 38
2.4.2 Raman Amplifiers 39
2.5 Semiconductor Optical Amplifiers 41
2.6 Semiconductor Optical Amplifiers Classification 42
2.6.1 Fabry-Perot Amplifiers 43
2.6.2 Travelling Wave Amplifiers 44
2.7 SOA - Basic Description 45
2.8 Fundamental Device Characteristics 46
2.9 High Saturation Output Power Structures 50
2.9.1 Basic Model for Amplifier Saturation Characteristics 50
2.9.2 Improving Saturation Output Power 52
2.10 Applications of Optical Amplifiers 52
2.11 Theory of Far field Pattern 54
2.12 The Diffraction Formula 56
2.13 Directionality of Laser Beams 60
2.14 Summary 62

3.0 The Finite Element Method 63
3.1 Introduction 63
3.2 Brief Historical Background of FEM 64
3.3 Steps involved in FEM Analysis 65
3.4 Applications of the FEM 66
3.5 Basic Equations 67
3.5.1 Maxwell's Equations 67
3.5.2 Boundary Conditions 69
3.6 Variational Formulations 72
3.6.1 Scalar Field Formulation 73
3.6.2 Vector Field Formulations 74
3.6.3 Natural Boundary Conditions 77
3.7 Optical Waveguides Application 78
3.8 Spurious Solutions 80
3.9 Mathematical Formulation of FEM 81
3.9.1 Shape Function 81
3.9.2 Element and Global Matrices 85
3.10 The Infinite Elements 88
3.11 Summary 91

4.0 The Beam Propagation Method 93
4.1 Introduction 93
4.2 Brief history of the Beam Propagation Method 94
4.3 Overview of Propagation Algorithms 95
4.3.1 Fast Fourier Transform Beam Propagation Method 95
4.3.2 Finite Difference Beam Propagation Method 96
4.3.3 Modal Propagation Method 98
4.3.4 Finite Element Beam Propagation Method 100
4.4 Perfectly Matched Layer Boundary Condition 101
4.5 The Wave Equations 107
4.6 Formulation of the Finite Elements 109

4.7 The Imaginary Axis Propagation 120
4.8 Power Calculation 122
4.9 Summary 123

5.0 The Beam Propagation Method Analysis of SOA Waveguides 124
5.1 Introduction 124
5.2 Modal Solution by Beam Propagation Method 126
5.3 Tapered Semiconductor Optical Amplifier Waveguides 134
5.3.1 Design of the SOA Tapered Waveguides 135
5.3.2 Propagation Analysis of the Modal Field 136
5.4 Study of the Evolution Beam along Tapered waveguides 140
5.4.1 Variation of Waveguide Width along the axial direction 140
5.4.2 Variation of Normalised Power along the axial direction 142
5.4.3 Variations of Spot Size along the axial direction 142
5.5 Mode Beating in Tapered SOA Structures 144
5.5.1 Effect of the re-meshing steps,m 149
5.5.2 Effect of the Tapered Angle 151
5.5.3 The Output Field Profile 154
5.6 Comparison between the TE- and TM-polarized modes 157
5.7 Elimination of Mode Beating in SOA Structures 157
5.8 Summary 176

6.0 The Carrier Rate Equation, Gain Analysis and Gain Saturation in SOA Structures 178
6.1 Introduction 178
6.2 The Carrier Rate Equation Analysis 179
6.3 Gain Analysis of SOA Structures 192
6.4 Gain Saturation in SOA Structures 194
6.5 Simulation Results 195
6.6 Summary 214

7.0 Far field Patterns and Birefringence in SOA structures 216
7.1 Introduction 216
7.2 Mode Expansion Method for Planar Waveguides 217
7.3 Simulation Results 219
7.4 Birefringence in Layered Waveguides 224
7.5 Summary 228

8.0 Conclusions and Future Works 229
8.1 Overview of the Work 229
8.2 Future Works 233

Appendix 1	**Calculation of the Element Matrices**	**236**
Appendix 2	**Power Calculation**	**238**
Appendix 3	**List of Publications by the Author**	**240**
References		**242**

List of Tables

Table 1.1: Classification of optical waveguides according to the number of dimensions of light confinement.

Table 2.1: Main features of OFAs and OSAs.

Table 2.2: Comparison of typical values of the main parameters for fibre amplifiers.

Table 2.3: Typical values of the main parameters on both types of Semiconductor Optical Amplifiers.

Table 2.4: Desirable properties of a practical SOA.

Table 6.1: Device parameters for the tapered model.

List of Figures

Figure 1.1: Technology evolution for optical components.

Figure 1.2: Basic structure and refractive index profile of optical waveguide.

Figure 1.3: Reflection and refraction of light ray in a slab waveguide.

Figure 1.4: Geometry of a rectangular buried waveguide, which can be modelled by Marcatili's method.

Figure 1.5: A waveguide geometry used for modal analysis employing Marcatili's method (the shaded regions are not considered in this analysis).

Figure 2.1: Semiconductor Optical Amplifiers.

Figure 2.2: Schematic diagram of an SOA.

Figure 2.3: Typical SOA gain versus output signal power.

Figure 2.4: A plane wave in incident normally on a long narrow slit of width w. According to geometrical optics, only the region LM will be illuminated.

Figure 2.5: A plane wave propagating along the z-axis is incident normally on a diffracting aperture ϕ.

Figure 2.6: Diffraction of a Gaussian beam.

Figure 3.1: The Interface between two different media.

Figure 3.2: (a) Planar waveguide (one-dimensional).

Figure 3.2: (b) Arbitrarily-shaped waveguide (two-dimensional).

Figure 3.3: Optical waveguide with arbitrary subdomains with different materials.

Figure 3.4: The First-order triangular element showing the coordinates and node numbers.

Figure 3.5: Rectangular dielectric waveguide discretised into orthodox and infinite elements.

Figure 3.6: Infinite Element of width b in the y direction and extending to infinity in the x direction.

Figure 4.1: Different PML regions along an optical waveguide cross-section.

Figure 4.2: Shape functions and different cases of weighting functions for discretisation along the longitudinal z-axis.

Figure 5.1: (a) Transverse field profile of the Gaussian input plane.

Figure 5.1: (b) Variation of the normalised power along the axial direction from a Gaussian input field.

Figure 5.1: (c) Variation of the power loss along the axial direction from a Gaussian input field.

Figure 5.1: (d) Transverse output field profile due to Gaussian input field.

Figure 5.1: (e) Transverse field profile of the mode output plane.

Figure 5.1: (f) Variation of the spot-size along the axial direction from a Gaussian input field.

Figure 5.1: (g) Variation of the spot-size along the axial direction from a mode input field.

Figure 5.1: (h) Variation of the confinement factor along the axial direction from a Gaussian input field.

Figure 5.1: (i) Variation of the confinement factor along the axial direction from a Gaussian input field.

Figure 5.2: (a) Variations of the power loss along the axial direction from a Gaussian input field.

Figure 5.2: (b) Transverse field profile of the Gaussian output plane.

Figure 5.2: (c) Variation of the spot-size along the axial direction from a Gaussian input field.

Figure 5.2: (d) Variation of the confinement factor along the axial direction from a Gaussian input field.

Figure 5.3: (a) Variation of the power loss along the axial direction from a Gaussian input feild.

Figure 5.3: (b) Variation of the spot-size along the axial direction from a Gaussian input field.

Figure 5.3: (c) Variation of the confinement factor (Γ) along the axial direction from a Gaussian input field.

Figure 5.4: Variation of the power loss with different W_o (μm) values.

Figure 5.5: Variation of the spot size for different widths (W).

Figure 5.6: Variation of the modal birefringence for different widths (W).

Figure 5.7: Schematic diagram of a rectangular waveguide.

Figure 5.8: (a) Transverse field profile of the evolved beam at $z = 50$ μm.

Figure 5.8: (b) The 3D view of the evolved beam at $z = 50$ μm.

Figure 5.9: Transverse field profile of the evolved beam at $z = 100$ μm.

Figure 5.10: Transverse field profile of the evolved beam at $z = 200$ μm.

Figure 5.11: Transverse field profile of the evolved beam at $z = 400$ μm.

Figure 5.12: Transverse field profile of the evolved beam at $z = 557$ μm.

Figure 5.13: The 3D view of the evolved beam at $z = 557$ μm.

Figure 5.14: Schematic diagram of the tapered semiconductor amplifier, including a short uniform section at the beginning.

Figure 5.15: Variations of the normalized power and local width along the axial direction.

Figure 5.16: Variations of the spot size and local width along the axial direction.

Figure 5.17: Input and output beam profiles.

Figure 5.18: Variations of the spot-sizes for two different tapered angles.

Figure 5.19: (a) 3-D plot of the evolving beam at axial position, $z = 218$ μm.

Figure 5.19: (b) 3-D plot of the evolving beam at axial position, $z = 225$ μm.

Figure 5.19: (c) 3-D plot of the evolving beam at axial position, $z = 234$ μm.

Figure 5.19: (d) 3-D plot of the evolving beam at axial position, $z = 243$ μm.

Figure 5.20: Variations of the H_y field profiles in the vertical direction at two axial positions.

Figure 5.21: Lateral variations of the evolved beam, normalized to their amplitudes, at four different axial positions.

Figure 5.22: Variations of the H_y field profile for the TE polarized optical beam at axial positions, $z = 275$ μm and 287 μm and their difference.

Figure 5.23: Lateral variations of the evolved beam, at axial positions $z = 234$ μm and 243 μm and their difference.

Figure 5.24: Variations of the spot-size, local width and normalized power for two different remeshing schemes.

Figure 5.25: Effect of width change for two m values.

Figure 5.26: Variations of the normalized power for three different tapered angles.

Figure 5.27: Variations of the spot-size along the axial direction for three different tapered angles for a wider semiconductor amplifier.

Figure 5.28: Spot-size expansion limited by the diffraction angle.

Figure 5.29: Transverse field profile of the evolved beam at the output plane.

Figure 5.30: Lateral variation of the evolved beam at two different axial positions and their difference.

Figure 5.31: Variations of the phase angle of the evolved beam along the lateral direction (x) at two different axial positions.

Figure 5.32: Variations of the spot-size and the normalized power along the axial direction for the TE- and TM-polarized waves.

Figure 5.33: Schematic diagram of a deep-etched tapered SOA Structure.

Figure 5.34: Variations of the spot-size along the axial direction with different m values

Figure 5.35: Lateral variation of the evolved beam at two different axial positions z = 530 μm and 538 μm and their difference.

Figure 5.36: Lateral variation of the evolved beam at two different axial positions z = 538 μm and 546 μm and their difference.

Figure 5.37: Variations of the spot-size along the axial direction.

Figure 5.38: Variations of the effective indices with the waveguide width (W).

Figure 5.39: Variations of the local $\Delta\beta$ as the width (W) increases.

Figure 5.40: Variation of beat length ($\mathbf{L_B}$) to the width (W).

Figure 5.41: Variations of the beat length as the width increases along the axial direction for different values of m.

Figure 5.42: Variations of the beat length along the axial direction for different values of m.

Figure 5.43: Variations of the beat length when the width increases from FEM calculation and BPM propagation.

Figure 5.44: Variations of the spot-size along the axial direction with different step size (m) values.

Figure 5.45: Variations of the spot-size along the axial direction.

Figure 5.46: Lateral variation of the evolved beam at two different axial positions z = 206 μm and 207 μm and their difference.

Figure 5.47: Schematic diagram of the tapered waveguide.

Figure 5.48: Variations of the spot size along the axial direction for re-meshing step, $m = 10$.

Figure 5.49: Variations of the spot size along the axial direction for re-meshing step, $m = 5$.

Figure 5.50: Variations of the spot size along the axial direction for re-meshing step, $m = 10$, with higher mesh distribution.

Figure 5.51: Variations of the spot size along the axial direction for re-meshing step, $m = 7$.

Figure 5.52: Variations of the spot size along the axial direction for re-meshing step, $m = 5$, where $\Delta x = \Delta w$.

Figure 5.53: Variations of the spot size along the axial direction for re-meshing steps, $m = 5$ and 10, with different mesh distribution.

Figure 5.54: Variations of the gain (dB) along the axial direction for re-meshing steps, $m = 5$ and 10, with different mesh distribution.

Figure 6.1: Schematic diagram of the deep-etched tapered semiconductor amplifier.

Figure 6.2: Schematic diagram of the active region of a linear TW SOA.

Figure 6.3: Transverse gain profile ($g(x)$) along the horizontal direction.

Figure 6.4: Variations of the Gain (dB) along the axial direction with different b values and the effect of n_i.

Figure 6.5: Variations of the confinement factor, Γ, along the axial direction.

Figure 6.6: Variations of the confinement factor, Γ, along the axial direction for different tapered angles, θ.

Figure 6.7: Normalised field profiles along the transverse direction for $b = 0$ and $b = 1.0$.

Figure 6.8: Variation of the total optical gain (dB) along the axial direction with different n_i values for a uniform guide (Gain).

Figure 6.9: Variation of the normalised power along the axial direction with different n_i values for a uniform guide (Gain).

Figure 6.10: Variation of the total optical gain (dB) along the axial direction with different negative n_i values for a uniform guide (Loss).

Figure 6.11: Variation of the normalised power along the axial direction with different negative n_i values for a uniform guide (Loss).

Figure 6.12: The variation of the spot-size along the axial direction for different values of b.

Figure 6.13: Variation of the field amplitude with the width for different values of b.

Figure 6.14: Variation of the phase angle with the width at different values of b.

Figure 6.15: The transverse variation of the gain coefficient, $g(x,y,z)$, at different axial position.

Figure 6.16: The transverse variation of the power density ($S(x,y,z)$) at different axial position.

Figure 6.17: Variations of gain with different gain coefficients (g_{mo}) and the effect of gain saturation.

Figure 6.18: Variations of the gain (dB) along the axial direction for different S_s values.

Figure 6.19: Variations of the power density along the axial direction with different S_s values.

Figure 6.20: Variations of the power density at different axial positions (z) along the transverse (x) direction.

Figure 6.21: Transverse variation of the n_i (x) at different axial positions (centre of the active area).

Figure 6.22: Variation of the power density along the axial direction (z) when different n_i values are used.

Figure 6.23: Variation of the power density along the axial direction (z) when different tapered angles, θ, with low input power.

Figure 6.24: Variation of the power density along the axial direction (z) when different tapered angles, θ, with high input power.

Figure 6.25: Variations of the power density along the axial direction with different input power, for both tapered and untapered SOA.

Figure 6.26: Variations of the total power along the axial direction with different input powers.

Figure 6.27: Variations of the gain along the axial direction with different tapered angles for a wider semiconductor amplifier.

Figure 6.28: Variations of gain (dB) and current (A) against tapered angle with different S_s values.

Figure 6.29: Effect of the tapered angles (degrees) on the overall gain with different input power.

Figure 6.30: Variations of the gain (dB) along the axial direction for different input powers.

Figure 6.31: Variations of gain (dB) along the axial direction for the TE and TM polarized modes at different input widths.

Figure 6.32: Variations of the gain and total output power for different tapered angles with different input powers.

Figure 6.33: Variations of power density along the axial direction for different m values with high input power.

Figure 6.34: Variations of power density along the axial direction for different m values with low input power.

Figure 6.35: Variation of the total power along the axial direction when different *m* values (re-meshing steps) was used.

Figure 7.1: Variation of the farfield with different angles, for both absolute and real and imaginary inputs.

Figure 7.2: Variation of the farfield at different width locations.

Figure 7.3: Variation of the farfield at different angles.

Figure 7.4: Variation of the farfield on the vertical direction with different angles.

Figure 7.5: Variation of the spot-size area and farfield angles at different widths.

Figure 7.6: Schematic cross section of the layered waveguide.

Figure 7.7: Variations of the effective indexes against Ratio (h_g: h_s).

Figure 7.8: Variation of the birefringence with the ratio (h_g: h_s).

Acknowledgements

It is a pleasure to thank the many people who made this thesis possible.

Firstly, and most importantly, I would like to gratefully thank my supervisors Prof. B. M. A. Rahman and Dr. M. Rajarajan for their continual support, inspiration and encouragement over the study period. Special thanks to Prof. K. T. V. Grattan for his valuable advice and assistance all through the research work.

I would also like to thank all members of the Photonics Modelling Group for all the good times we spent together. I am also grateful to my wife who always supported me all through my research work.

Finally, sincere thanks to the EPRSC who financially supported me all through my research with out their support this work would not have been possible.

Declaration

The City University Librarian is hereby granted powers of discretion to allow this thesis to be copied in whole or in part without further reference to the author. This permission is only for single copies made for the purposes of study and subjects to the normal conditions of acknowledgement.

Symbols and Abbreviations

BEM	Boundary Element Method
BPM	Beam Propagation Method
EDFA	Erbium-doped Fiber Amplifier
EIM	Effective Index Method
FDBPM	Finite Difference Beam Propagation Method
FDM	Finite Difference Method
FEBPM	Finite Element Beam Propagation Method
FEM	Finite Element Method
FFTBPM	Fast Fourier Transform Beam Propagation Method
LSBR	Least Squares Boundary Residuals
MMM	Mode Matching Method
MoL	Method of Lines
MPA	Modal Propagation Algorithms
NA	Numerical Aperture
OA	Optical Amplifier
OFA	Optical Fiber Amplifier
PML	Perfectly Matched Layer
PMM	Point Matching Method
RAM	Ray Approximation Method
SBS	Stimulated Brillouin Scattering
SIM	Spectral Index Method
SLA	Semiconductor Laser Amplifier
SOA	Semiconductor Optical Amplifier
SRS	Stimulated Raman Scattering
TBC	Transparent Boundary Condition
TE	Transverse Electric
TM	Transverse Magnetic
TWA	Travelling Wave Amplifier
VM	Variational Method
WDM	Wavelength Division Multiplexing
WKB	Wantzel, Kramers and Brillouin Method
λ	Operating Wavelength
θ	Tapered Angle
β	Propagation Constant
ε	Permittivity
μ	Permeability
c	Velocity of Light
k	Wavenumber
ω	Angular Frequency
α	Loss Factor
Γ	Confinement Factor

Abstract

Compact and low-cost semiconductor laser sources have significant potential for use in applications that are currently dominated by expensive solid-state lasers. The direct application of high-power semiconductor lasers for free-space and satellite communications, visual displays, biomedical applications and remote sensing, optical recording, spectroscopy, optical data storage, laser printers, laser radar and also for materials processing is becoming increasingly attractive due to the remarkable improvement in performance of high-power laser diodes. In addition, high-power spatially and spectrally coherent sources are required for the efficient pumping of solid-state and fiber lasers and efficient nonlinear frequency conversion to the short-wavelength part of the visible spectrum, which is not readily available with semiconductor sources directly.

The early development of the semiconductor amplifier had initially been assisted by the use of the semi-analytical and numerical approaches, which has been extended to include segmented sections to allow for lateral variations of the optical and electronic parameters. In this work, a vectorial finite element beam propagation method (FEBPM), which is numerically efficient and has incorporated a wide-angle approach to tackle rapid axial variations and the perfectly matched boundary condition, to avoid reflections from the orthodox computational window, has been employed to study and design the guided-wave photonic devices. The evolution of the optical beam profile along a high power tapered semiconductor amplifier has been demonstrated by employing this method. Numerically simulated results indicate the generation of many higher order modes, and their interference with the fundamental mode causes a variation of the optical beam, both along the transverse and the axial directions, which could significantly modify the output beam quality, which also leads to beam filamentation.

In this thesis, the FEBPM approach has also been utilized to study rigorously the complex refractive index profiles, which provide modal gain in the semiconductor structures. The power gain in an active photonic device, such as a laser or an amplifier is due to the presence of the imaginary part of the complex refractive index in the core. The injected current generates carrier density and when the density is above the transparent carrier density then the optical field can be amplified. In case of a high-power tapered semiconductor optical amplifier (SOA), the width of the SOA changes continuously, which reduces the power density to improve the total gain. The modal gain properties and field expansion have therefore been examined in this work. The effect of gain reduction along the transverse directions due to non-uniform transverse field profile is also demonstrated. Furthermore, the effect of gain saturation on the total optical gain of the amplifier is studied by considering both the transverse and axial variation of the local gain coefficient.

Finally, the study of the far field profiles and birefringence for various tapered waveguide structures, with particular interest to the very wide width SOA structures is carried out.

1.0 Introduction

1.1 Lightwave Technology

The use of light as communication methods can date back to antiquity if we define optical communications in a broad way. The modern fibre-optic communications started around 1970s when the GaAs semiconductor laser was invented and the optical fibre loss could be reduced to 20 dB/km in the wavelength region near 1μm. Since then, fibre-optic communications have rapidly developed and the enormous progress of lightwave systems can be grouped into several generations, as discussed below [1].

The first generation of lightwave systems was made commercially available in 1980. It operated near the wavelength 800 nm and used GaAs semiconductor lasers. The data rate of these lightwave systems could reach 45 Mb/s with repeater spacing up to 10 km.

The second generation of lightwave systems became commercially available in late 1980s. It operated in the wavelength region near 1.3μm, where fibre loss is below 1 dB/km and optical fibre has exhibited minimum dispersion in this region. From the early 1980s, the developments of InGaAsP semiconductor lasers and detectors operating near 1.3μm and the use of single-mode fibres have contributed to the availability of the second generation of lightwave systems. By 1987, the second-generation lightwave systems with data rate of 1.7 Gb/s and a repeater spacing of 50 km were available.

The third-generation lightwave systems with data rates of 2.5 Gb/s became commercially available in 1990. It was known that silica fibres had the minimum loss (0.2-dB/km) near the wavelength of 1.55μm. Unfortunately, there is large fibre dispersion near 1.55μm. To overcome this problem, dispersion-shifted fibre and single-longitudinal-mode lasers were developed. The drawback of the third-generation

lightwave system was that the signal has to be electronically regenerated periodically, with the repeater spacing of typically from 60 to 70 km.

The use of erbium-doped fibre amplifiers (EDFA) and wavelength-division multiplexing (WDM) is the distinct character of fourth-generation lightwave systems. EDFA was developed in 1985 and commercially available in 1990. EDFA made it possible to transmit optical signals up to tens of thousands of kilometers without using an electronic regenerator. The advent of the WDM technique started a revolution and increased the capacity of lightwave system enormously. By 1996, commercial transatlantic and transpacific cable systems became available and a demonstration of optical transmission over 11,300 km using actual submarine cables at a data-rate of 5Gb/s was realized in the same year. Since then, many submarine lightwave systems have been developed worldwide.

The next generation of lightwave systems, has been under development for some time. The emphasis of research can be commonly categorized into two groups. One emphasis is to extend the wavelength range to L-band (1570nm – 1610nm) and S-band (1485nm – 1520nm) to increase the number of channels in WDM. The lightwave systems are operating in the conventional wavelength window, known as C-band, which is from 1530 nm to 1565 nm. Another emphasis is to increase the data-rate of each channel. Many experiments have been done operating at data rate of 10 Gb/s or 40 Gb/s since year 2000. In such higher data rate lightwave systems, dispersion compensation management and combating of nonlinearity degrading effects like SPM (Self-phase modulation), XPM (Cross-phase modulation) and FWM (Four-wave mixing) are becoming urgent. In this issue, modulation formats have been a key factor. As the data-rate of lightwave systems is increasing to 10Gb/s or 40Gb/s, the optical signals are becoming more sensitive to the linear and nonlinear degrading effects. Polarisation mode dispersion (PMD) has become one of the major obstacles to upgrade the current per-channel bit rates to 40 Gb/s and beyond in dense wavelength division- multiplexing systems.

Consequently, NRZ (non-return-to-zero) that has been used for a long time in lightwave system is no longer an optimal modulation format in the next generation of

lightwave systems. A modulation format that is more tolerant to linear and nonlinear impairments is needed. The capacity of lightwave system, bit rate-distance product, will be improved dramatically using optimal modulation formats compared to NRZ format. In addition, spectral efficiency would be improved using optimal modulation format thus more information could be conveyed per wavelength or more wavelengths can be co-propagated over fibres. From an economical point of view, optimal modulation formats will permit service providers to develop their existing lightwave network without an overall upgrade and to utilize most of the existing systems, thereby saving costs.

1.1.1 Integrated Photonics

As a result of new developments, associated also with other technologies, such as electronics, new disciplines have appeared connected with optics: electro–optics, opto–electronics, quantum electronics, waveguide technology, etc. Thus, classical optics, initially dealing with lenses, mirrors, filters, etc., has been extended to describe a new family of much complex devices such as lasers, semiconductor detectors, light modulators, etc. The quantum nature of light is important and the operation of these devices must be described in terms of photons as well as of electronics, giving birth to a mixed discipline called *photonics*.

This new discipline emphasises the increasing role that electronics play in optical devices, and also necessity of treating light in terms of photons rather than waves, in particular in terms of matter–light interaction (optical amplifiers, lasers, semiconductor devices, etc.).

For 30 years after the invention of the transistor, the processing and transmission of information were based on electronics that used semiconductor devices for controlling the electron flux. But at the beginning of the 1980s, electronics was slowly supplemented by and even in some cases replaced by optics, where photons substituted for electrons as information carriers.

Nowadays, photonic and opto-electronic devices based on integrated photonic circuits have grown in such a way that they not only clearly dominate long-distance communications through optical fibres, but have also opened up new fields for applications, such as sensor devices, and are also beginning to penetrate into the field of the information processing technology.

The first optical waveguides, fabricated at the ends of the 1960s, were two-dimensional devices on planar substrates. In the mid 1970s the successful operation of three-dimensional devices waveguides was demonstrated in a wide variety of materials, from glasses to crystals and semiconductors.

The technology and fabrication methods associated with integrated optical circuits and components vary widely. In addition, they depend on the substrate material on which the optical device is fabricated. Optical integration can expand in two directions: serial integration and parallel integration. In serial integration for optical devices the different elements of the optical chip are consecutively interconnected: laser and driver, modulator and driver electronics, and detector and receiver electronics. In parallel integration, the chip is built by bars of amplifiers, bars of detectors and wavelength (de) multiplexors. The highest level of integration (whether serial or parallel) is achieved in monolithic integration, where all the optical elements including light sources, light control, electronics and detectors are incorporated in a single substrate. The most promising materials to achieve full monolithic integration are semiconductor materials, in particular GaAs and InP.

1.1.2 Optical Technology Evolution

From the technological aspect of the industry, optical components may need to go through the same kind of generations that the electronics industry went through, from discrete components to printed circuit board, and to solid-state devices. Today, the optical components industry is still in the discrete, bulky optics phase. It is possible that the industry will go through low-level, medium-level, and then high-level integration. Technology enables two evolution paths to create value

(a) consistent performance and lower cost

(b) consistent price and higher performance

In Fig. 1.1, a proposed possible evolution path for optical technology evolution is reported. Because the nature of the photon is very different from the electron, optical technology will have some major differences compared with the electronic technology evolution. It may go through more steps before large-scale integration possible. The technology evolution path will depend on how technology breakthrough will develop in the future. Below is shown a brief analysis of each stage for the proposed evolution of optical technology:

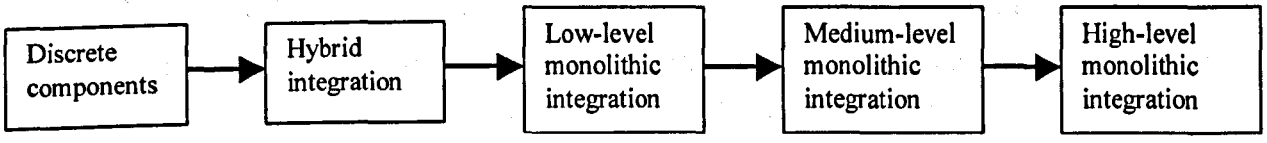

Fig. 1.1 Technology evolution for optical components.

(a) *Discrete components*: Except for a few components, like array waveguide gratings (AWGs) made from planar technology, most of the components used are made of bulky, discrete manner such as thin-film filters and FP tunable filters. Considerable labour is involved to put them together and each component performs a specific function. Customer design integration is required to make them fit into modules or subsystems, such as fibre amplifier modules, OC-192 transmitter/receiver modules and optical switching modules. The performance of these modules are determined by the performance of key components. For the same function, there are several technology options available, such as WDM filters using three technologies: thin-film filter, fibre Bragg grating, or array waveguide grating. There is no clear "winning" technology transition from one generation to another generation. At the very base technology level the optical component industry is still relatively immature as is probable that optical integration is 15-20 years behind the semiconductor industry. There are numerous opportunities for inventions and innovations in both the components and subsystems levels.

(b) Hybrid integration: At this stage, several functional components made with different materials can be integrated on a common platform such as silicon "optical bench" and ceramic substrates to hold active and passive components in place and using silica or polymer waveguides to guide light from one component to another. This process can potentially reduce packaging size, cost and increase module functional density and scalability, while maintaining a high level of performance. This is a transitional step for monolithic component integration. The main objective is to reduce overall cost to enable low-cost optical modules for metro or access applications. On the other hand, the small packaging may enable high-speed ($\geq$ 40 Gb/s) applications.

(c) *Low-Level Monolithic Integration*: While hybrid integration provides several functions on a common platform, monolithic integration combines several functions on the same material or chip. Because of the great challenge we are facing with material, processing, and the very basic physics of optical devices, only a few functions can be integrated in one chip. Due to its high potential, there are a lot companies targetting on this solution right now using different technologies. These firms include JDS Uniphase, Corning, K2 Optronics and IBM

(d) *Medium-Level and High-Level Monolithic Integrations*: As the material and processing technologies advance, more and more functions can be integrated on one chip. We divide these into medium- and high-level integration because we believe that the technology that will be able to achieve high-level integration may be very different from those in the low- and medium-level integrations. Furthermore, optical integration may never reach the level of integration and number of functions you can put on a semiconductor electronic chip. The wavelengths of light of interest to telecommunications are of order 10,000 times bigger than the size of an electron. Therefore, levels of optical integration will be limited to 100s of elements, as opposed to the millions encountered in electronic ICs. Nonetheless, there is much to be gained over current discrete optics, and integrated optical circuits represent the next level of efficiency and performance in fibre optic components.

1.1.3 Optical Communication Research and Technology

During the past several years, optical communications have evolved from a speculative research activity plagued with many practical problems to a point where systems implementation is a reality. This success was assured when, in 1970, the first 20 dB/km optical fibre was demonstrated. Before this event, typical fibre attenuations ranged in the thousands of dB/km range, a loss level, which precluded consideration of optical light guides for data transfer. With optical fibre losses now below 1 dB/km, and with the development of suitable solid-state diode light sources and detectors, there are no insurmountable technological barriers remaining, which will prevent fibre optical transmission systems from finding widespread commercial and military applications in the near future. The technological advantages offered by fibre implementation on data transfer systems guarantee the use of optical fibres at the very least specialized applications, regardless of economic issues.

The military possesses the greatest variety of specialized applications, and it is the military, which will most likely capitalize most rapidly on this technology. The telecommunications and computer industries on the other hand can take advantage of this technology after economic viability has been demonstrated. In view of their prior, high capital investment in conventional "transmission" technology, fibres are being used initially in replacement and expansion situations.

This optimistic future for optical communication was achieved only after many different and various approaches to utilize light as an information carrier were attempted. With the invention of the laser in the early 1960s, the exploitation of the immense information-carrying capacities promised by optical frequency radiation was widely envisioned. However, progress was limited by two factors: components and the transmission media. Component progress during the sixties was continuous with several types of optical transmitters (lasers and LEDs), modulators, and photo-detectors being developed. Suitable sources with the adequate power existed at the end of the sixties for transmission in low-loss media. However, a transmission medium with acceptable transmission characteristics did not then exist.

Transmission in the open atmosphere was long recognized to be unacceptable and unreliable for light transmission. Transmission outages caused by adverse weather conditions significantly degraded system performance. A controlled atmosphere using evacuated pipes was postulated as a means of circumvent the transmission outage problems. In order to maintain beam quality, periodic refocusing was required. The most promising approach employed a conduit filled with a gas, which had a radial temperature gradient to refocus the optical beam. The radial temperature profile was obtained using suitably placed interactive servo-controlled heater elements, which gave rise to a radial gas-density gradient and thus a radial index of refraction gradient. Radially graded refractive indices provided continuous beam refocusing and in a sense formed a waveguide. Technical feasibility was established for this approach: however, practical considerations of index profile control and size precluded system utilization of this approach. The realization of 20 dB/km fibre by Corning radically changed the outlook for optical communications by providing for a stable, flexible, low-loss transmission media. Cylindrical fibres step or graded index was quickly perfected, with transmission losses now being reduced to below 1 dB/km and tensile strengths in 1 km lengths. Detector technology for communications application was already available and only had to be optimized. When the 20 dB/km fibre appeared (*1970*) sources compatible with optical fibre use only existed in laboratory models. Diode lasers and LEDs were still in the exploratory stage of development. Five years of research quickly led to the development of long-life ($>10^5$ hr), high brightness sources with performance characteristics compatible with fibre optic usage.

Early source deficiencies such as low brightness and fibre strength issues resulted in the first fibre system demonstrations using fibre bundles containing hundreds of fibres per channel. These bundles captured a large fraction of the emitted light and because of their size proved to be easy to terminate and interconnect. As fibre and source performance improved, single fibre per channel technology developed and has now replaced bundle technology. Connectors and splices for single fibre per bundle cables have been developed and outperform analogous bundle connectors in terms of connection loss. Single-fibre per channel technology, however, is utilized in longer length applications such as encountered in the telecommunications industry and larger intraplatform (ships) applications. Performance and fibre economy strongly favour single fibre approaches.

1.1.4 Market Overview

The optical component market can be divided into two different segments: components and modules/subsystems. Components are the basic building blocks for modules, subsystems, as well as the final systems. Optical components can be classified as active components, which are devices that generate or manipulate light, such as lasers, modulators, and receivers, and passive components, which handle light, such as wavelength division multiplexing (WDM) filters, couplers, isolators and circulators. Modules and subsystems are multiple components packaged together to perform one or a few functions, such as transmitters/receivers, erbium-doped fibre amplifiers (EDFAs), Raman amplifiers, optical add/drop multiplexers (OADMs), and optical switches.

The interaction between systems and components development has been particularly strong and efficient for the fibre optical communications industry as compared to many other technological industries because of the complexity involved in optical systems. For many years, optical technology remained in the academic realm and always viewed as a "future technology". Today's advanced optical systems are made possible with a large number of technological breakthroughs such as low-loss fibres, high-speed semiconductor lasers, WDM filters, erbium doped fibre amplifiers, etc. The demand for new components depends on the demand for advanced optical systems from telecommunications carriers and other network operators. After 5 years in the late 1990s significant demand with double or triple digit growth, there has been a slowdown in both components and systems over the last few years.

On the other hand, optical component technology is still in the early development stage. No dominant design has been established for most components. Almost every component has several technology options. For example, optical filters are important components in optical systems for combining and separating optical signals. Overall, because fibre optic communications provide the best performance/price ratio to deliver bandwidth over the net, the industry will enjoy a solid growth in the long term. Optical technology is also penetrating into metro and access markets and each generation of the network will need new components and more and more optical contents are embedded in the network.

Overall, there are still requirement for advanced technological innovation to produce advanced optical components for optical systems to bring enhanced value to the end users.

1.2 Optical Waveguide Structures

Integrated photonics devices are based on the processing of light confined in optical structures called *optical waveguides*. These optical structures allow the confinement of light within its boundaries by total internal reflection. They consist of a core (where the light is confined) and a cladding, or substrate surrounding the core as shown in Fig. 1.2. The refractive index of the core, n_g is higher than that of the cladding n_s. Therefore the light beam that is coupled to the end face of the waveguide is confined in the core by the total internal reflection.

The condition for total internal reflection at the core-cladding interface is given as

$$n_g \sin(\pi/2 - \phi) \geq n_s \tag{1.1}$$

Since the angle, ϕ (given in radians) is related with the incident angle, θ by

$$\sin\theta = n_g \sin\phi \leq \sqrt{n_g^2 - n_s^2} \tag{1.2}$$

we obtain the critical condition for the total internal reflection as

$$\theta \leq \sin^{-1}\sqrt{n_g^2 - n_s^2} \equiv \theta_{\max} \tag{1.3}$$

The refractive index difference between core and cladding is of the order of $n_g - n_s$, then $\theta_{\max}$ in equation 1.3 can be approximated as

$$\theta_{\max} \cong \sqrt{n_g^2 - n_s^2} \tag{1.4}$$

θ_{max} denotes the maximum light acceptance angle of the waveguide and is known as the *Numerical Aperture* (*NA*).

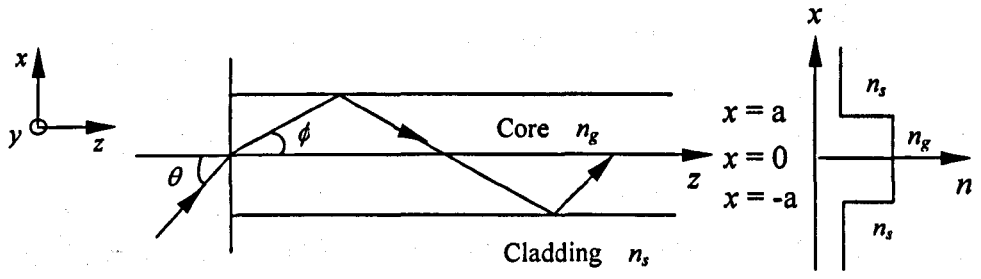

Fig. 1.2 Basic structure and refractive index profile of optical waveguide.

An optical waveguide classification can be produced by considering the number of dimensions in which the light is confined as shown in Table 1.1. Planar optical waveguides confine the optical radiation in a single transverse direction. They are the key to construct integrated optical circuits and semiconductor lasers. Considering the refractive index distribution in the planar structure, planar waveguides can be classified as *step-index waveguides* or *graded index waveguides.*

The step-index planar waveguide is the simplest structure of light confinement, and is formed by a uniform planar film with a constant refractive index, surrounded by two dielectric media of lower refractive indices. The homogenous upper medium, or *upper cladding* has a refractive index of n_c, and the lower medium with refractive index n_s, is often called *substrate*. Usually it is assumed that the refractive index of the upper cladding is less than or equal to the refractive index of the substrate, $n_c \leq n_s$, and in this way we have $n_g > n_s \geq n_c$. In fact, in many cases the upper cladding is air, and therefore $n_c = 1$. If the upper and lower media are the same, $n_s = n_c$ (equal optical constants), the structure forms a symmetrical planar waveguide. On the other hand, if the upper and lower media are different, it is an asymmetrical planar waveguide.

If the high index film is not homogenous, but its refractive index is depth dependent (along the x-axis) the structure is called a *graded index planar waveguide*. Usually the refractive index is maximum at the top of the surface, and its value decreases with depth until it reaches the value corresponding to the refractive index of the substrate. This kind of structure is present in waveguide fabrication methods based on the

surface modification of a substrate, whether by physical processes (ion implantation, metal diffusion, etc.), or by chemical modification of the substrate (ionic exchange methods).

In planar waveguides, the light confinement is restricted to a single dimension (along the x-direction) and if the light propagates along a given direction (z-axis), the light can spread out in a perpendicular direction (y-axis) due to diffraction. To avoid this effect and keep the light beam well confined, it is necessary for total internal reflection to take place not only at the upper and lower interfaces, but also at the lateral boundaries. This confinement is attained in *channel waveguides*, or 2D waveguides, in which the core region (where the optical energy is concentrated) has a refractive index greater than any of the surrounding media.

Dimensions of light confinement	Classification of optical waveguides
1D	Planar waveguides
2D	Channel waveguides
	Optical fibres
3D	Photonic crystals

Table 1.1 Classification of optical waveguides according to the number of dimensions of light confinement.

Although many types of channel waveguides have been proposed, three are the most common basic structures used. The easiest way to build a channel waveguide is to deposit a stripe made of a high refractive index material on top of a lower refractive index substrate. This kind of channel waveguide is called *stripe waveguide*, and can be made by either depositing the stripe directly onto the substrate, or simply by conveniently etching a previously deposited film. If the etch process is not complete and does not reach the substrate, a channel waveguide is also produced, providing that the thickness and height of the structure are conveniently tailored; this waveguide geometry is called *rib waveguide*. Another common type of channel waveguide is the *buried channel waveguide*. In this case the waveguide is fabricated by including a

local increase of the substrate refractive index, which is usually performed experimentally, by diffusion methods.

Optical fibres are special type of channel waveguides, from the point of view of their geometry and manufacturing methods as well as their applications. They have cylindrical geometry, and are constituted by a cylindrical core of radius a and refractive index n_g, surrounded by a cladding of slightly lower refractive index n_s. Optical fibres are a best choice when low loss and high transmission bandwidth is required in long-distance optical communications.

Structures also exist that confine light in the three dimensions. These constitute a very special case of optical waveguides: since the radiation is confined in all directions, it cannot propagate. Therefore, these structures in fact form light traps, and are often called *photonic crystals*. The light confinement in this case obviously cannot be based on total internal reflection; instead, photonic crystals are fabricated by means of tri-dimensional periodical structures, in which the light confinement is based on Bragg reflection. Photonic crystals have very interesting properties, and their use in several devices and applications have been proposed, such as miniaturised lasers with virtually no threshold power, waveguide bends with very small curvature radii and dimensions, or narrow-band filters [2].

The slab waveguide is the simplest and most basic type of optical waveguide. It can support a finite number of guided modes, which are associated with an infinite number of unguided radiation modes. The boundary value problem can be formulated using Maxwell's equations taking into account the boundary condition at interfaces to solve for such modes. The guided modes of the slab waveguide can be extracted using the approximation that is valid for short wavelength of light known as "*geometrical or ray optics*".

Let's consider the cladding guide interface and a light ray, **A**, as shown in Fig. 1.3 incident at an angle θ_1, between the light field normal and the normal to the interface. By using Snell's law, the refraction can be expressed as

$$\frac{n_g}{n_s} = \frac{\sin\theta_1}{\sin\theta} \tag{1.5}$$

where θ is the exit angle of the refracted wave **AB**.

From using Snell's law the guide cladding interface can also be expressed as

$$\frac{n_c}{n_g} = \frac{\sin\theta}{\sin\theta_2} \tag{1.6}$$

where θ_2 is the angle of the refracted ray **BC,** with the normal to the guide cladding interface.

Since $n_g > n_c$, an incident ray is reflected into the guided region, following the path **AB** and when $\theta < \theta_c$, the total reflection conditions are not met at the guide-cladding interface, therefore the ray is reflected to the cladding region. Similarly when the incident angle $\theta > \theta_c$, the total reflection occurs and the light ray will be following the path **BD**.

When the incident angle $\theta < \theta_s$, at the guide substrate interface, then the light ray may refract back in to the substrate through which the light escapes from the structure (substrate radiation modes).

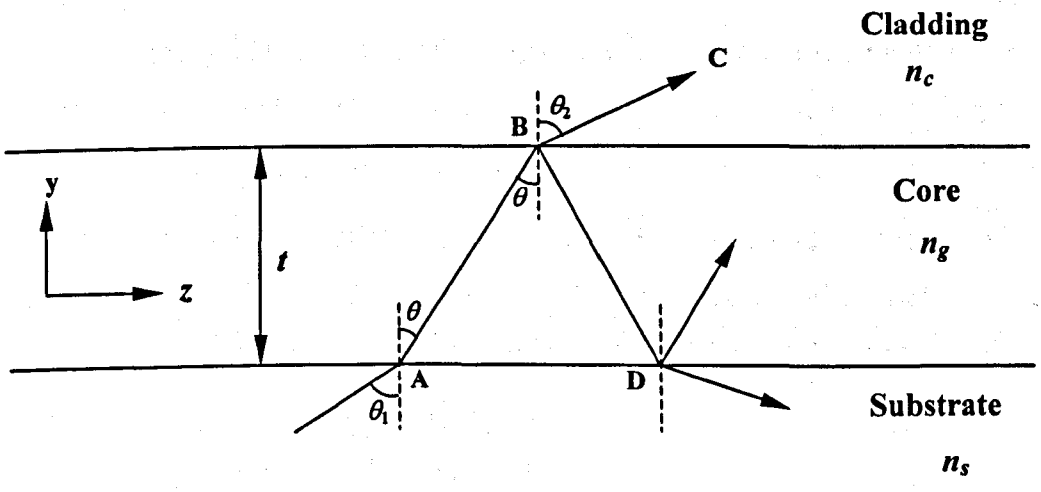

Fig. 1.3 Reflection and refraction of light ray in a slab waveguide.

When θ is large enough total internal reflection occurs in both interfaces. This leads to the light in the guide to be trapped and confined and propagates in a zigzag pattern along the z direction. These are hence referred to as the *guided modes*.

These guided modes can be described as Transverse Electric (TE) or Transverse Magnetic (TM) modes. For the TE mode, the electric fields are perpendicular to the direction of the propagation. On the other hand, for TM mode the magnetic fields are perpendicular to the direction of the propagation.
The waves travel with a wave vector kn_g usually in the direction of the wave where the absolute value k is,

$$k = \frac{2\pi}{\lambda} = \frac{\omega}{c} \tag{1.7}$$

k is termed as the wavenumber, λ, ω and c are the free-space wavelength, angular frequency and velocity of light in the vacuum, respectively. The mode propagation constant, β, and the phase velocity, v_p, of the light wave can be expressed as [3]

$$\beta = \frac{\omega}{v_p} = \mathrm{k}n_g \sin\theta \tag{1.8}$$

The condition for all the multiple reflected waves to add in phase is that the total phase change experienced by the plane wave for it to travel one round trip, up and down across the guide should equal $2m\pi$, where integer, m, is the mode order. The phase change for the plane wave to cross the thickness, t, of the guide twice, up and down, is $2\mathrm{k}n_g \cos\theta$. Furthermore, the wave suffers a phase shift of $-2\phi_s$, on the total reflection at the guide-substrate boundary and phase shifts $-2\phi_c$, due to the total reflection at the guide-cladding interface. The above relationship yields the self-consistency condition for the guided mode in a planar slab optical waveguide as

$$2\mathrm{k}n_g t\cos\theta - 2\phi_s - 2\phi_c = 2m\pi \tag{1.9}$$

The above equation is also termed as the eigenvalue or transcendental equation. By employing the Fresnel formulae for each polarisation [3], the phase shifts ϕ_s and ϕ_c, for the TE waves can be expressed as

$$\tan\phi_s = \frac{\sqrt{n_g^2 \sin^2\theta - n_s^2}}{n_g \cos\theta} \tag{1.10a}$$

$$\tan\phi_c = \frac{\sqrt{n_g^2 \sin^2\theta - n_c^2}}{n_g \cos\theta} \tag{1.10b}$$

and in case of the TM waves,

$$\tan\phi_s = \frac{n_g^2\sqrt{n_g^2 \sin^2\theta - n_s^2}}{n_s^2 n_g \cos\theta} \tag{1.11a}$$

$$\tan\phi_c = \frac{n_g^2\sqrt{n_g^2 \sin^2\theta - n_c^2}}{n_c^2 n_g \cos\theta} \tag{1.11b}$$

Similarly, expressions can also be calculated for the guide-substrate interface, by substituting the refractive index of the cladding n_c, with the refractive index of the substrate, n_s.

1.3 Analysis of Optical Waveguide Structures

The ray optic approach can be used in the qualitative description of light behaviour in an optical waveguide, to establish the types of mode that can be found in such structures, to calculate the number of guided modes that support a waveguide, and to determine its propagation constants. Nevertheless, for many applications it is essential to know the electric field distribution of the radiation within the waveguide structure, and this method does not provide such information. If one wants to determine the optical fields or the intensity distribution associated with the light propagation in

waveguide structures, it becomes necessary to invoke a more rigorous formalism, based on the electromagnetic theory of the light. Therefore, implementing the Maxwell's equations to the electromagnetic fields in a given structure, which defines the waveguide, can solve the problem; the solutions for the fields will correspond to the propagation modes.

There have been various analysis methods suggested for solving the optical waveguide problems. These methods can be classified into two broad categories as

(a) Analytical approximation solution techniques

(b) Numerical solution techniques

An exact treatment of the modal characterisation in 2D waveguide is not possible, even in the simplest case of a symmetrical rectangular waveguide. Therefore, in order to solve this problem, some analytical approximation should be made. These analytical approximation solutions are mostly based upon the ray approximation method (RAM) [4] and the Wentzel, Kramers and Brillouin (WKB) method [5]. However, these analytical solution methods do not satisfy the boundary conditions, hence not being suitable for solving and analysing more practically used three-dimensional optical waveguides whose field are of hybrid nature.

Numerical solution techniques can be classified into two groups, the domain techniques and the boundary techniques. For the domain solution technique (differential technique) the whole domain of the optical waveguide structure is considered, while with the boundary technique (integral technique) only the boundary or discontinuity regions are considered. The domain solution technique includes the finite element method (FEM), finite difference method (FDM), beam propagation method (BPM), and variational method (VM). The boundary solution technique includes boundary element method (BEM), mode-matching method (MMM) and point-matching method (PMM).

1.4 Analytical Approximation Solution Techniques

Analytical approximation techniques had been widely used in the modelling of opto-electronic waveguides such as rib waveguides, tapers, buried waveguides and directional couplers. In the next sub-sections two widely used analytic methods will be explained: Marcatili's method and the effective index method. While the first one allows us to calculate the electromagnetic field in a rectangular waveguide (with a homogenous central core), with the latter we can obtain the optical modes supported by a waveguide with arbitrary geometry (in principle, but not easy), even with graded index regions (whether the core or the surroundings).

1.4.1 Marcatili's Method

This approximation method can be used to calculate the propagation constants and modal fields supported by a rectangular waveguide, whether stripe or buried, as the one shown in Fig. 1.4. This method was developed for guiding structures, with large dimensions, in which the refractive index difference between guiding and cladding materials is small, less than 5%. Under these assumptions, the field is assumed to exist only in the core waveguide region and in four neighbouring cladding regions, which are obtained by extending in turn the width and height of the waveguide to infinity.

Marcatili's method [6] allows the ability to model a waveguide geometry as shown in Fig. 1.5, which consists of a central homogenous high index core surrounded by four homogenous low index regions. The waveguide core, referred to as region I in the figure, has a rectangular cross-section with dimensions, a and b in the x and y directions respectively, and a refractive index n_1. The central core is surrounded by homogenous regions II, III, IV and V as indicated in Fig. 1.5, which have refractive indices n_2, n_3, n_4 and n_5, respectively.

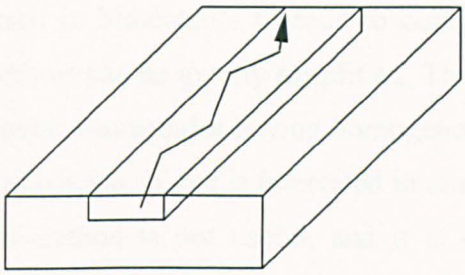

Fig. 1.4 Geometry of a rectangular buried waveguide, which can be modelled by Marcatili's method.

If the propagation constant β of the mode is far from the cut-off ($\beta \approx k_0 n_1$), the electromagnetic field is confined mainly in the core (region I), and only a small fraction of the energy carried by the optical mode spreads out to the surrounding regions (regions II, III, IV and V).

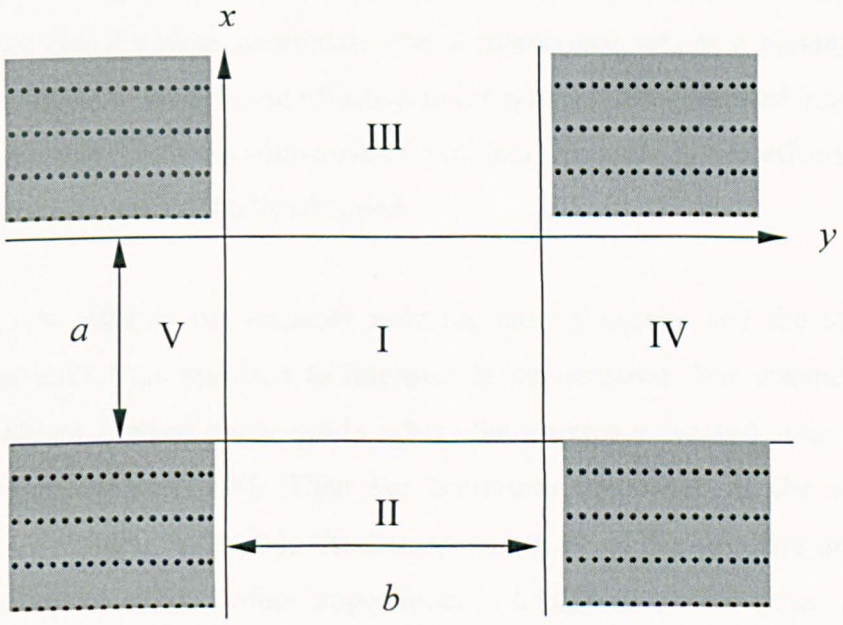

Fig. 1.5 A waveguide geometry used for modal analysis employing Marcatili's method (the shaded regions are not considered in this analysis).

Moreover, the fields penetrate even less in the four corners (dotted regions in the Fig. 1.5), and therefore in these regions there is little energy of the mode. However, poor results are obtained using this method if the mode is near the cut-off [7].

This is the argument used in Marcatali's method to completely ignore these corner regions, and thus the analysis can be greatly simplified. Therefore, Marcatili's method is only *valid* for rectangular waveguides having homogenous regions, and for guided modes far from cut-off condition. If one is interested in analysing a waveguide with a different geometry, this method is not useful, and it is necessary to turn to other approximate methods, such as the effective index method.

1.4.2 The Effective Index Method

The effective index method (EIM) is an approximate analysis for calculating the propagation modes of waveguides. This method was first proposed by Knox and Toulois in 1970 [8] with a view of extending the Marcatili's method. It is one of the simplest approximate methods for obtaining the modal fields and the propagation constant in channel waveguides having the arbitrary geometry and index profiles. It consists of solving the problem in one dimension, described as the x coordinate, in such a way that the other coordinate (the y coordinate) acts as a parameter. In this way, one obtains a y-dependent effective index profile; this generated index profile is treated once again as a one-dimensional problem from which the effective index of the propagating mode is finally obtained.

However, the EIM is not accurate near the cut-off region, and the several other techniques have been reported to improve its performance. For instance, EIM has been used for a trapped image guide, where the original waveguide was replaced by an equivalent structure [9]. Then the transverse resonance at the air-dielectric interface is imposed, to include the free-space region of the structure and solve the problem in terms of the surface impedances in an approximate manner, and achieve an improved accuracy at low frequencies.

The drawback of this method is that it does not yield good results when the structure operates near the cut-off region. However, this method can be applied to a wide variety of structures, including channel waveguides, strip waveguides and arrays of such waveguides [10]. Due to the simplicity and speed of this method many engineers have been encouraged to search for different approaches that will improve the

accuracy. As a result, many different variants of the EIM have been developed such as the EIM based on linear combinations of solutions [11], or the EIM with perturbation correction [10].

1.5 Numerical Solution Techniques

Numerical techniques generally require more computation than analytical techniques or expert systems, but they are very powerful analysis tools. Without making *a priori* assumptions about which field interactions are most significant, numerical techniques analyze the entire geometry provided as input. They calculate the solution to a problem based on a *full-wave* analysis.

The complex nature of modern optical devices has restricted the use of analytical methods to only simple structures such as those involving single layered slab waveguides. As a result, increasing attention has been focused upon improving existing numerical techniques and in other cases developing novel semi-analytical methods [12,13].

The selection of appropriate numerical analysis method for analyzing the optical waveguiding structures is based upon several factors, which should be taken into consideration, and based on published reviews [14-16] these factors are:

(a) the shape of the cross-section area, whether it is convex or concave or whether it is uniform or non-uniform.
(b) whether the dominant mode or other higher order modes are required.
(c) whether the numerical method can deal with more than two homogenous dielectric layers.
(d) whether the field distribution or cut-off frequency is required or both.
(e) the accuracy of the technique in specific frequency ranges, especially near cutoff frequencies.
(f) the accuracy of the technique with regard to dielectric boundaries and regions.

(g) whether the technique generates spurious solutions and if so whether the technique can identify and/or eliminate them.
(h) the computational efficiency and storage capabilities.
(i) whether the technique should be programmable, being able to solve a wide range of structures, or it has to be programmed specifically for each region of the structure separately.
(j) the degree and understanding required from the user.
(k) the assumptions and limitations of the numerical approach, for particular cases.

The commonly used numerical solution techniques will be briefly discussed in the following subsections.

1.5.1 The Method of Lines

The method of lines (MoL) is a semi-analytical technique, which is mostly suitable for the analysis of hybrid modes in optical waveguiding structures. Schulz and Pregla [17] first suggested this method for the analysis of dispersion characteristics of planar isotropic waveguides and microstrips. Most optical waveguide structures have a geometry with multiplayer cross section. The channel waveguide, the rib waveguide, and the strip-loaded waveguide can be seen as types of this class of optical waveguide structures.

However, for a cross section with straight interface the method of lines [18,19] was proven as an analysis procedure with the higher accuracy. Structures with curved interfaces have also been modelled by the MoL previously using high number of inhomogeneous layers with straight interfaces [19]. This technique has also been applied to model optical waveguides with lossy inhomogeneous anisotropic media. In this approach, the optical waveguide is enclosed inside a rectangular box with electric or magnetic walls at the sides to satisfy the boundary conditions for the required polarisation.

The cross section is then divided into a number of equidistant lines along the transverse direction leading to the discretisation of the fields, which are solved analytically along the longitudinal direction. A system of coupled ordinary differential equations, for each dielectric layer is obtained, by substituting different operators for the second derivatives of the electromagnetic wave equations. The above system is uncoupled and the equations can be solved analytically, through suitable matrix transformation. However, this technique is disadvantageous when applied to curved boundaries and the accuracy near the cut-off regions is limited.

1.5.2 The Boundary Element Method

The boundary element method (BEM) is a technique in which the basic equations are boundary integral ones which are numerically solved on the numerically divided integration domain. This technique utilizes information only upon the boundaries of interest, and thus reduces the dimension of any field problem by one. For differential operators, the response at any given point to sources and boundary conditions depends only on the response at neighbouring points.

In BEM, the governing differential equations are transformed into integral variables, which are applicable over the boundary surface of the region. The integrals are numerically integrated over the boundary, which is divided into boundary elements. If the boundary conditions are satisfied, a system of linear algebraic equations may be established for which a unique solution can be found.

Unlike the FEM, the BEM can easily incorporate boundary conditions at infinity, and hence, no infinite elements are required. Another advantage of the BEM is that it can deal with odd-shaped boundaries, as the FEM, but with far less number of unknowns as the unknowns are set only at the boundary points while for FEM, the unknowns at nodes covering the whole cross section are solved for. However, the BEM is applicable only to homogenous structures, and also some nonphysical solutions, known as resonant solutions, may be difficult to avoid. The method also requires some analytical treatments and in some cases, the Green's function has some singularities with respect to the integral equations. The FEM is as numerically

efficient as the BEM formulation leads to dense matrices, while in the FEM the matrices remain sparse [20].

1.5.3 The Point Matching Method

One of the oldest and simplest "boundary solution" method for the analysis of isotropic homogeneous dielectric waveguides is the point matching method (PMM). Goell [21] initially used this method for solving rectangular waveguide problems, where the radial variations of the electromagnetic fields are represented by a series of circular harmonics. The idea was to express the electromagnetic fields inside the core by a sum of Bessel functions and their derivatives, with the fields outside represented by a sum of modified Bessel functions and their derivatives, then both multiplied by trigonometric functions.

By imposing the boundary conditions of the above field at a finite number of points at the interface, known as "*matching points*", a system of linear equations is obtained. By matching the tangential field elements at the interface yields to continuity equations, whose solution gives the eigenvalues and eigenvectors when arranged into a matrix equation.

The PMM is more computationally efficient than other numerical techniques, as the matching points are needed only at the boundaries rather than the whole computational domain. This method is capable of use for analyzing dielectric waveguides having arbitrary cross sections, coupled waveguides and composite dielectric waveguides. However, the PMM is difficult when applied to three-dimensional waveguide structures with inhomogeneous index distribution, such as the graded index fibres.

1.5.4 The Mode Matching Method

The mode matching method (MMM) is an approximate solution method for open dielectric waveguides. It is also known as the equivalent network method. In this

method the waveguide is artificially bounded, and the open waveguide cross section is presented in terms of building blocks or constituent parts, which are portions of uniform dielectric layered structures interfaced by dielectric step discontinuities. These step discontinuities are represented by transformers, where equivalent network admittance take into consideration the effect of the outer region. The uniform transmission lines with their characteristic impedance represent the uniform dielectric regions.

The whole spectrum of the open waveguide structure can be modeled as a cascade of uniform regions and step discontinuities. When the boundary condition to the different modes and transverse resonance condition are applied, for a particular mode, the total admittance to all the ports are zero, this allows the dispersion for the propagation constant to be obtained.

The TE-TM coupling and the continuous modal spectrum at the sides of the waveguide are neglected, since the open waveguide structure is artificially bounded. Dagli and Fonstand [22] presented a more accurate technique by discretising the continuous modal spectrum using suitable basis function expansions rather than artificially bounding the open waveguide structure.

However, a full-vectorial analysis of the optical rectangular waveguides by MMM, where the TE-TM coupling and the discretisation of the continuous modal spectrum have been taken into consideration have been reported [23].

1.5.5 The Spectral Index Method

The spectral index method (SIM) has traditionally been applied to the analysis of rectangular semiconductor rib waveguides, [24,25], and was subsequently used to analyse multiple rib waveguide structures [26,27]. Further developments led to its successful application to the analysis of rib waveguide based spot-size transformers [28]. The method accurately predicts longitudinal propagation constants and field profiles for this class of waveguide. This, together with the relative simplicity of the method means it is ideally suited as a CAD tool for the analysis of the polarised

modes of optical waveguides and to its extension to a wider range of optical components and circuits.

The SIM approach begins by modifying the physical semiconductor-air boundary in the transverse plane of the waveguide by replacing that boundary with a polarization dependant evanescent boundary, upon which the field is set to zero. Exact solutions to the scalar wave equation are then formulated in the upper guiding or rib region and the underlying substrate region of the waveguide. These solutions are then matched along the boundary of the two regions using a variational principle to give a simple transcendental eigenvalue equation for the longitudinal propagation constant.

The SIM is an accurate and fast technique, as it requires far less computational time than other numerical methods. Like the FEM, in the presence of dielectric corners, where the electric field exhibits singularities produced by its transverse components, it leads to more complicated field distribution [29].

1.5.6 The Finite Difference Method

The finite-difference method (FDM) is probably the most popular technique for modelling dielectric waveguides. When applied to step-index waveguides, however, the accuracy is heavily dependent on the difference equations that are used at points near to interfaces between regions of different refractive index. If the interface changes direction sharply, such as at a rectangular dielectric corner, further complications occur because of the singular nature of the field.

The FDM application to the modelling of optical waveguides dates from the early 1980s, originally evolving from previous FD models for metal waveguides [30]. The FD method discretisizes the cross-section of the device being analysed and is therefore suitable for modelling arbitrarily shaped dielectric guides which could be made out of isotropic homogeneous, inhomogeneous, anisotropic or lossy material.

The essence of the FD method is to map the structure onto a rectangular mesh, allowing for the material discontinuities only along mesh lines. There are two possible

ways of placing nodes on the mesh: at the center of each mesh cell so that node is associated with a constant refractive index, [31], and on mesh points so that each node can be associated to maximum of four different refractive indices [32].

The differential vector, semi-vectorial or scalar wave equation is then approximated, usually with a five points finite difference form, in terms of the fields at the nodes of the mesh. For improved convergence more accurate difference forms can be used. Taking into account the continuity conditions of the electric and magnetic field components at the grid interfaces, the eigenvalue problem becomes of the form

$$[A]\Phi = \beta^2\Phi \tag{1.12}$$

where $[A]$ is a band matrix which is symmetric for scalar modes or non-symmetric for semi-vectorial and vector modes. Here β, is the modal propagation constant, β^2 is the eigenvalue and Φ is the eigenvector representing the modal field profile.
Equation (1.12) can be solved using direct method such as Gaussian elimination (suitable when the matrix is small) or more efficiently, using iterative methods such as the shifted inverse power iteration method [33].

Whilst the FDM is in principle straightforward to implement, numerical modelling of the open boundaries, typical of dielectric waveguides, needs care. The problem is overcome either by

(a) enclosing a structure in a sufficiently large rectangular "box" which does not disturb the penetration of the field and on which the zero field condition is imposed, or,

(b) imposing an open or matched boundary condition on the "box" sides, for example, by assuming exponential decay of the field in the outward normal direction, in which case the size of the box can be somewhat relaxed.

(c) Radiation is allowed to freely escape the problem without appreciable reflection, whereas radiation flux back into the

problem region is prevented by employing transparent boundary condition (TBC).

However, when the device operates near cut-off, the size of the box for both cases has to be sufficiently large to allow for substantial penetration of the field into the substrate. If a uniform mesh is used it can result in a very large number of nodes and large matrices. To make the FDM more flexible for modelling of large and complex geometries, non-uniform meshes have been proposed such that a finer mesh is applied on regions where the field changes rapidly, and a coarser mesh for regions where field is stationary [34]. Although, the method increases the error in the differences from second to first order and makes the matrix [*A*] more complicated, on the whole it produces more accurate results, especially in cases where field singularities are present.

The accuracy of the method therefore depends on the mesh size, the assumed nature of the electromagnetic field, (scalar, polarised or vector) and the order of the finite difference scheme used. The symmetry (or asymmetry) of the structure can also be exploited to advantage of the mesh size, taking care that the appropriate boundary conditions are applied along the symmetry (asymmetry) lines.

The popularity of the FDM in modeling dielectric waveguides is due to its ease of use and generality. Disadvantages become apparent when a device has large dimensions and/or operates near cut-off, in which cases an adequate mesh has to be employed and extra care has to be taken in modeling the open boundaries, both of which require long run times and high memory requirements.

1.5.7 The Finite Element Method

The finite element method (FEM) is a well-established and powerful numerical technique for solving optical waveguide problems. This method is based upon dividing the problem region into non-overlapping polygons, usually triangular elements. The field over each element is then expressed in terms of low-degree

interpolating polynomials weighted by the field values at the nodes of each element. The total field is found as a linear summation of the fields over each element.

The accuracy of the FEM can be increased by using a finer mesh or by employing higher order polynomials. The appearance of spurious solutions is a serious downside of the method and is caused by not satisfying the divergence condition $(\nabla \cdot H = 0)$. Formulating the variational expression in terms of various field components has been tried to avoid spurious solutions. A number of formulations have been proposed, out of which the full **H**-field formulation is the most commonly used in modeling optical waveguides due to a much easier treatment of boundary conditions.

The suppression of spurious solutions can be alternatively achieved by introducing a penalty term into the variational expression with a penalty parameter defined heuristically, [35], or by checking the zero divergence condition for each obtained mode and discarding ones that do not satisfy it [36]. Another approach is to use edge elements that force spurious solutions exactly at zero frequency [37]. In this approach, the interpolating functions are defined as vectors and the continuity of tangential components across elements is satisfied. The continuity of normal field components is not satisfied which gives rise to a non-zero divergence. However, all spurious solutions are forced to zero frequency and hence easily identifiable.

In modeling of complex geometries, the FEM is considered more flexible than the FDM, due to the greater flexibility of triangular elements and the ability to use irregular mesh. The Finite element method will be discussed in greater depth in the next chapter.

1.5.8 The Beam Propagation Method

The Beam Propagation method (BPM) describes the evolution of the total field propagating along waveguides such as tapers, Y-Junctions, gratings and bends.

The method was first formulated based upon the Fast Fourier transform (FFT) by Feit and Fleck [38]. The FFT-BPM was developed for the case of weakly guiding structures, neglecting the vectorial properties of the field. The use of the paraxial

approximation limited the method to structures where the beam propagates in directions that make small angle with respect to the axis of propagation. This made the method unsuitable for commonly used nowadays semiconductor optical waveguides with high step index difference.

Since then, many BPM approaches have been reported which include scalar, semi-vectorial and full vectorial based upon the finite difference method [39,40]. Comparisons between the FFT- and the FD-BPM show that for comparable accuracy the FD-BPM employs larger propagation step size. Also the computational time per propagation step in the FD-BPM is much lower which makes it a more efficient tool for the analysis of complex structures. With the FD implementation, the BPM was soon extended to include vectorial properties for two-dimensional and three-dimensional propagation.

Recently, FD-BPM schemes based on structures-related coordinate schemes that naturally follow the geometry of a structure have been described and shown to be particularly useful when the angle between the waveguide and propagation direction increases [41,42]. The FEM has also been utilized to develop BPM approaches for both the TE and TM wave propagating in strongly guiding longitudinally varying optical waveguides.

Recently, a full vectorial BPM algorithm based on the finite element method has been reported [43]. In this approach only the two transverse components of the magnetic field are considered and incorporates, the perfectly matched layer (PML) boundary condition to offer a reflectionless boundary to the unwanted radiation waves to leave the computational domain. In Chapter four, the full vectorial BPM will be presented and the mathematical details associated with it discussed.

1.6 Aims and Objectives of the Thesis

The goal of integrated optics is to develop miniaturized optical circuits of high functionality on a common substrate. As optics becomes more and more attractive, especially for a wide range of communication systems and for instrumentation techniques, there exists a growing interest in the development of more and more

complex integrated optical devices. The information presented in the introduction to this thesis forms as the backbone to the work reported. The aims and objectives of this research work can be briefly outlined as:

(a) To develop further and investigate the rigorous finite element technique based on the **H**-field variational formulation for the analysis of optical waveguide problems.

(b) To implement further and investigate more fully the full-vectorial Finite Element based Beam Propagation Method (FEBPM) for guided-wave photonic devices, which are important for a wide range of systems. This numerically efficient approach was used to develop and investigate semiconductor optical amplifiers.

(c) To use the FEBPM to obtain the transformation of the optical beam profile in truly 3-D tapered region in a guided-wave device.

(d) To generate a carrier profile and investigate the effects it has on the optical gain of opto-electronic devices.

(e) To study and investigate the evolution of the beam along the waveguide structures more importantly tapered waveguide structures, which includes the variations of the waveguide width, the total guided power, the spot size etc., along the axial distance.

(f) To investigate the polarisation issues e.g. the variations between the transverse electric (TE) and transverse magnetic (TM) modes and their influence on the polarization dependent performance.

(g) To investigate the mode beating in tapered semiconductor optical amplifiers (the existence of higher order modes along with the fundamental mode), which deteriorates the beam quality significantly, contributing towards beam filamentation problem.

(h) To investigate and determine the modal gain and the effects of gain saturation in deeply-etched tapered semiconductor amplifier, with its effects on the total optical gain of the device.

(i) To study the farfield pattern for various tapered waveguide structures, with particular interest to the very wide width structures.

(j) To investigate and examine birefrigence in the tapered waveguide structures.

1.7 Structure and Format of the Thesis

The work presented in this thesis is based on research carried out by the author in the use of the finite element based beam propagation method (FEBPM), which is a well-established numerical technique for the solution of wide range of guided wave problems. The FEBPM was developed to study the evolution of the optical beam profile along semiconductor optical amplifiers. Various types of semiconductor waveguide structures were considered. The discussion in this section outlines the structure of this thesis, which commences with the introduction, presented in this first chapter. The first chapter embraces a general overview of lightwave technology, the establishment of integrated photonics, followed by the contribution of optical communications research and technology in the modern world. The study and analysis of optical waveguide structures is also discussed and several analysis techniques are described which include both analytical approximation solution techniques and numerical solution techniques. The following chapters will explain the numerical methods used in this research work followed by various semiconductor optical amplifier designs achieved, with finally the presentation of the numerical results.

The general overview of Optical Amplifiers (OAs) and their applications is reported in Chapter 2. This Chapter begins with the history of the generation of the OA and a classification of the OA is reported which includes the Optical Fibre Amplifiers (OFAs) and the Optical Semiconductor Amplifiers (OSAs). The features of both of these amplifiers have been examined. The Semiconductor Optical Amplifier (SOA) has been reported in the literature; available to provide high gain with low power consumption and its single-mode waveguide structure makes it particularly suitable for use with monomode fibre. In the remaining part of this chapter the SOA is examined in more detail, including: the features, characteristics and applications of the device. The general applications of the OAs are reported. Finally, the theory of the farfield pattern creation is presented.

The theoretical basis of the finite element method as a powerful and well-established numerical technique for analyzing optical waveguides is reported in Chapter 3. The essence of the finite element method is reported followed by a brief historical background of the method. This is followed by a general overview of the FEM analysis and its applications. The fundamental mathematical relations derived from

Maxwell's equations, for the application of the technique in the solution of optical waveguide problems with several variational formulations is considered, with a more detailed **H**-field finite element formulation reported. The triangular elements, coordinates, shapes and infinite elements are studied, to determine the propagation constants and the field profiles of different modes propagating through an optical waveguide. The presence of "*spurious modes*" with the fundamental mode in this vector formulation is examined, as a result the "penalty function" method is studied which avoids the appearance of these modes.

The development of the vector BPM approach based on the versatile FEM is reported in Chapter 4. This starts with a brief history of the BPM followed by an overview of the various propagation algorithms. The features of these propagation algorithms includes the Fast Fourier transform (FFT), the Finite Difference Method (FDM), the Modal Propagation Algorithms (MPA) and the Finite Element Method (FEM) and these are all reviewed. The mathematical derivation of the FEBPM is also reported. The concept of the perfectly matched layer (PML) boundary condition in absorbing the unwanted radiation waves and its inclusion into the finite element formulation is also reported. The approach presented is truly fully vectorial as it accounts for both the polarization effect and coupling, as it is based on only the transverse magnetic field components.

In Chapter 5, the evolution of the optical beam along tapered semiconductor laser structures, by using the rigorous vectorial numerical approaches based on the finite-element method, is reported. The approach is numerically efficient and has incorporated a wide-angle approach to tackle rapid axial variations and the perfectly matched boundary condition to avoid reflections from the orthodox computational window. The technique is used to obtain the transformation of the optical beam profile in a truly 3-D tapered region of the guided-wave device. In this chapter, buried semiconductor tapered structures are considered, and the expansion of the beam shape is also observed, but together with the presence of significant modal interference between the fundamental mode with higher order modes. This likely contributes towards the beam filamentation, and ultimately the degradation of the beam quality. Thus in general, a numerical analysis of mode beating in tapered semiconductor amplifiers is undertaken.

A study of the evolution of the optical beam along deeply-etched semiconductor laser structures, through the use of the vectorial numerical approaches based on the finite element method, is presented in Chapter 6. In this Chapter, the FEBPM approach has been utilized to study rigorously the complex refractive index profiles to provide modal gain in such structures. The modal gain properties and field expansion has also been examined. The effect of gain reduction along the transverse directions due to transverse field profile is demonstrated. Furthermore, the effect of gain saturation on the total optical gain of the amplifier, by considering both the transverse and axial variation of the local gain coefficient, is presented.

In Chapter 7, the farfield pattern of the near field input profile and output field profile of the optical beam are examined, as is also the effect of the tapered angle contribution to the shape of the farfield pattern is considered. Furthermore, in this chapter the principles of birefringence in tapered waveguide structures are examined and the effective indexes for the TE and TM equations presented, followed by some relevant simulation results.

The general conclusions arrived at from this research work are summarized and explored in Chapter 8. Possible future research on the basis of this work has also been suggested. Finally a list of references is cited in the thesis with a list of relevant publications by the author.

2.0 Optical Amplifiers

2.1 Introduction

Optical amplifiers have expanded the design possibilities and the performance of fibre optic systems. They can be used to increase the transmitter optical output, as in-line amplifiers or as optical preamplifiers of detectors, increasing in all applications the power budget of the fibre optic network into which they are incorporated. When the history of scientific progress throughout the 20th century is analysed it will become apparent that the discovery of light amplification phenomena has associated with it considerable depth of scientific and technological development.

Optical amplification has had a very particular impact on fibre optic applications due to the development of semiconductor amplifiers and fibre optic amplifiers [44-46], which can be easily integrated in fibre optic devices and networks. The traditional way of compensating for optical loss in light-wave communication systems has been the rather cumbersome procedure of regeneration. In many applications, direct optical amplification of the light signal is advantageous.

2.2 Overview of Optical Amplifiers

The physical phenomenon responsible for amplification is stimulated emission introduced by Albert Einstein [47] in 1917. Unlike spontaneous emission, which spreads evenly in every direction, stimulated emission only takes place in the same direction as the stimulating beam.

The implementation of these ideas came in 1960, when the first laser was achieved by Maiman [48] who used a ruby rod pumped by a pulsed lamp. In 1961 the first gas laser was achieved, the *He-Ne* laser [49], which showed a lower emitted power but worked on continuous operation. Throughout the 1960s researchers found a wide

variety of methods to obtain laser action and managed to develop most of today's known laser types; although these first lasers still needed further improvement. For example, in 1962 the first semiconductor laser was achieved [50], a *GaAs* pulsed laser with a required working temperature of 77K. The interest in these devices brought great attention to their further development, which led to devices working using continuous operation at room temperatures [51]. In 1964 the first results on amplification in a multi-mode *Nd* doped optical fibre [52] was obtained, and in 1965 amplification was accomplished in an *Er* doped fibre [53] (although pumping was achieved with a lamp surrounding the fibre which was very inefficient). But the great leap of optical amplification took place during the second half of the 1980's when amplification was achieved in single-mode optical fibres, doped with either *Nd* [54] or *Er* [55,56].

The great expansion of optical communications in the 1990's led to serious consideration being given to the idea of substituting opto-electronic regenerators for optical amplifiers, which allowed a superior bandwidth and were transparent to encoding methods (therefore it was not necessary to the amplifier when changing the encoding method). This led to a huge development of semiconductor and fibre amplifiers. Nowadays, these amplifiers are not only useful in optical communications, but are also employed in processes involving optical signals whose power must be increased, as in the case of optical sensors or exploiting nonlinear optics.

2.3 Optical Amplifier Classification

The transmission distance of any fibre-optic communication system is eventually limited by fibre losses. For long-haul systems, the limitation has traditionally been overcome using optoelectronic repeaters in which the optical signal is first converted into an electric current and then regenerated using a transmitter. Such generators become quite complex and expensive for wavelength-division multiplexed (WDM) lightwave systems.

An alternative approach to loss management makes use of optical amplifiers, which amplify the optical signal directly without requiring its conversion to the electric

domain. Several kinds of optical amplifiers were developed during the 1980s, and the use of optical amplifiers for long-haul lightwave systems became widespread during the 1990s. Within the currently accepted optical amplifiers categories, only two of the aforementioned types namely,

a) Optical Fibre Amplifiers (OFAs)
b) Optical Semiconductor Amplifiers (OSAs)

are useful for optical fibre technology, given their low size, low electrical power consumption and their facility for easy and stable coupling to optical fibres.

Feature	OFA	OSA
Typical max. internal gain (dB)	30 – 50	30
Typical insertion loss (dB)	0.1 – 2	6 - 10
Polarisation sensitivity	No	Weak (< 2dB)
Pump source	Optical	Electrical
3dB gain bandwidth (nm)	30	30 – 50
Nonlinear effects	Negligible	Yes
Saturation output power (dBm)	10 –15	5 - 20
Typical intrinsic noise figure (dB)	3 – 5	7 – 12 dBm
Photonic integrated circuit compatible	No	Yes
Functional device possibility	No	Yes

Table 2.1 Main features of OFAs and OSAs [57].

2.4 Fibre Amplifiers

There are three basic types of optical fibre amplifiers; rare earth doped fibre amplifiers, Stimulated Brillouin Scattering (SBS) amplifiers and Stimulated Raman Scattering (SRS) based amplifiers. In the rare–earth doped fibre amplifier the optical fibre core is doped with a lanthanide (*Er* or *Pr* principally) and stimulated emission takes place between two energy levels of the dopant ions, which set the amplification wavelengths. Pumping is carried out through radiative transitions (optical pumping) that excite the ions from the ground level to levels with higher energy then the upper level of the laser transition, from where they "fall" to this last level and populate it.

In the case of fibre amplifiers based on SBS or SRS, the pumping is carried out by laser light, with a transition to a virtual state that acts as an upper laser level. Therefore, the amplification wavelength can be modified as desired, as it is determined by the position of the virtual level, which depends on the wavelength of the pump laser.

SBS amplifiers have a major drawback that makes them of little practical use in communications systems (and hence are not discussed in the later sub-sections); their bandwidth is limited to less than 0.1nm, while for the rest of the amplifiers considered this value is in the order of a few tens of nm.

Semiconductor amplifiers show some disadvantages over optical fibre amplifiers, such as higher insertion losses, higher polarisation gain dependence and more severe channel distortion and crosstalk. Nevertheless, semiconductor amplifiers have a smaller size and a large amplification bandwidth than those based on doped fibre or SRS. Furthermore, they are readily integrable with other functional devices, and this thesis focuses on the design issues of high power semiconductor optical amplifiers.

2.4.1 Erbium doped Fibre Amplifiers

Erbium doped fibre amplifiers (EDFAs) are those with the best features among the rare earth doped fibre amplifiers. First, they achieve gains over 40dB in weak signal operation (using few tens of mW for pumping) and output powers of a few watts in saturation regime (higher powers are limited by the appearance of non-linear effects created by the signal and the pump) [58,59].

Also their amplification spectrum is typically located in the 1.53 to 1.55 μm wavelength range, which corresponds to the so-called "third window" and this has a special interest for optical communications due to the low loss exhibited by silica fibres in these wavelengths.

One of the problems of EDFAs is that interaction effects between the erbium ions can lead to up conversion effects and thus, decreasing the population inversion. Since

these effects only occur for high enough erbium concentrations, they can be avoided using low erbium concentration fibres. In recent years semiconductor lasers have been developed which provide powers over 500 mW. The first such lasers were usually made from GaAs/AlGaAsP structures with the second usually employing InGaAsP/InGaAsP structures.

In recent years optical communication systems have evolved towards wavelength division multiplexing as a method for increasing data transmission capacity, simultaneously propagating in a single fibre signals of different wavelengths, each carrying different data [3,60]. The lack of flatness of the gain spectrum of erbium in silica, for instance, makes the different wavelengths multiplexed comes across different gain values and therefore very high power differences might result, which is highly undesirable. To avoid this problem some gain flattening methods have been developed [61] e.g. using ZBLAN fibres doped with erbium or high aluminium concentrations in the core of silica-based erbium-doped fibres, using spectral filters, Bragg gratings or active filters (for example acusto-optic filters) to control dynamically the output power of each wavelength, etc. With these methods some good results have been achieved.

2.4.2 Raman Amplifiers

Raman effect amplifiers, widely considered some years ago, especially in the high speed telecommunications systems and soliton transmission context, are receiving renewed consideration [62]. In fact, commercialisation of Raman amplifiers, lasers and pump units for them was carried throughout year 2000 [63]. Gains of 40 dB and output powers of +26 dBm had been previously demonstrated at 1310nm [64].

The basis of Raman amplifiers is the Raman scattering. Such scattering, which takes significant values when high power light interacts with optical fibres, generates new optical frequencies higher and lower than the original incoming light. The proximity of these new lateral bands to the original light frequency is strongly dependent on the material used. The Raman scattering is caused by optical vibrational modes of the material. In a Raman effect amplifier, signal amplification takes place when its optical

frequency matches the scattering spectrum of the pump laser. In this case the signal generates stimulated emission at its optical frequency and thus *gain* is obtained.

In the optical spectrum region where no absorption peak exists, optimum Raman gain is determined by pump light wavelength. Optimum gain is achieved for the wavelength with maximum scattering. For example silica fibres pumped at 1500nm, Raman scattering yields optimum amplification at wavelengths around 80 nm higher and lower than this pump wavelength. Usually gain obtained for every pump mW in a Raman amplifier is approximately two orders magnitude lower than in erbium- doped silica amplifiers. However, the new available semiconductor laser with output powers higher than 1W make the Raman amplifier a commercial reality. The main reason is that Raman amplification can be achieved at every desired wavelength. Gain spectrum for Raman amplifiers is determined by fibre composition, pump wavelength and fibre length. In general, if the fibre length is optimised to obtain highest gain, the amplification bandwidth will be reduced. Table 2.2 highlights typical values of the main parameters of erbium doped fibre and Raman amplifiers.

	ERBIUM DOPED FIBRE AMPLIFIER	RAMAN AMPLIFIER
Typical Gain	25 – 40 dB	10 – 40 dB
Typical Bandwidth	35 nm	25 nm
Saturation Power	10 – 20 dBm	10 – 25 dBm
Pump Power	20 – 100 mW	0.35 – 5 W
Noise Figure	3.5 – 6 dB	> 3dB

Table 2.2 Comparison of typical values of the main parameters for fibre amplifiers [57].

However, rather than the lumped version of this kind of amplifier, it is the distributed one which resurrected Raman amplification as a viable commercial technology. The distributed Raman-assisted transmission usually acts on a low-noise preamplifier to maintain signal integrity. When a distributed Raman amplifier is concatenated with an EDFA post amplifier, the equivalent noise factor of the system is lower than that of two cascaded EDFAs.

Increasing the Raman gain, the overall noise figure decreases up to a certain value of Raman gain [62]. This hybrid amplification system has been employed to transmit 40Gbit/s signals over 400km [65].

2.5 Semiconductor Optical Amplifiers

The first studies on Semiconductor Optical Amplifiers (SOAs) were carried out around the time of invention of the semiconductor laser in the 1960s. The early devices were based on GaAs homojunctions operating at low temperatures. The arrival of double heterostructure devices spurred further investigation into the use of SOAs in optical communication systems. In the 1970s Zeidler and Personick carried out early work on SOAs [66,67].
In the 1980s there were further important advances on SOA device design and modelling. Early studies concentrated on AlGaAs SOAs operating in the 830 nm range [68]. In the late 1980s studies on InP/InGaAsP SOAs designed to operate in the 1.3 μm and 1.55 μm regions began to appear [69].

In 1989 SOAs began to be designed as devices in their own right, with the use of more symmetrical waveguide structures giving much reduced polarisation sensitivities [70]. Since then SOA design and development has progressed in tandem with advances in semiconductor materials, device fabrication, antireflection coating technology, packaging and photonic integrated circuits, to the point where reliable cost competitive devices are now available for use in commercial optical communication systems.

The advent of SOAs preceded that of fibre optic amplifiers. Their major advantage is their small size. Also interesting is their ability to be integrated in a substrate along with light sources, detectors and any other optical waveguide type devices, giving the ability to generate small size structures for routing and signal processing in optical domain. Additional advantages include a higher bandwidth than that of fibre amplifiers and lower power consumption. However, their major drawbacks are their difficult connection to optical fibres and higher noise levels than other types of amplifiers. They are also more dependent on the polarisation state of input signals, i.e., SOAs are polarisation sensitive. This is due to a number of factors including the waveguide structure and the gain material. Polarisation sensitivity can be improved by the use of square-cross section waveguides and strained quantum-well material. The gain of SOA is influenced by the input signal power and internal noise generated by the amplification process. By integrating spot-size converters, coupling to optical fibres can also be improved.

2.6 Semiconductor Optical Amplifiers Classification

SOAs will play an important role in future optical systems, both for optical fibre transmission and for optical data processing. Semiconductor optical amplifiers provide high gain, with low power consumption and their single-mode waveguide structure makes them particularly suitable for use with monomode fibre. There have been many studies, but it was not until recent years that high performance SOAs (with for example, low threshold current, narrow far field radiation patterns, and good antireflection coatings) became available.

The most common semiconductor optical amplifiers are divided into two groups

a) Fabry-Perot Amplifiers
b) Travelling Wave Amplifiers (TWAs)

2.6.1 Fabry-Perot Amplifiers

In essence, semiconductor amplifiers are laser diodes operated beneath the laser oscillation threshold. For Fabry-Perot amplifiers, both ends of the semiconductor optical waveguide where stimulated emission is achieved act as reflectors (as shown in Fig. 2.1 (a)) creating a cavity, just as in semiconductor lasers. Typical reflectivities for the semiconductor – air transition take values around 32% but this can be modified using reflective layers. In short, the light to be amplified enters the cavity from one end and gets amplified through successive reflections in mirrors, obtaining an output signal with higher optical power than that of the input one.

In this way, the gain curve of Fabry-Perot amplifier depends on the reflective characteristics of the cavity and the gain provided by the waveguide. Moreover, this curve is strongly dependent on light wavelength and cavity modes. Its dependency on optical frequency is given by [71]

$$G(\nu)=\frac{G_s(1-R_1)(1-R_2)}{(1-\sqrt{R_1R_2}G_s)^2+4\sqrt{R_1R_2}G_s\sin^2\left[\frac{2\pi(\nu-\nu_0)L}{c}\right]} \qquad (2.1)$$

where $G(\nu)$ is the gain as a function of optical frequency ν, R_1 and R_2 are the reflectivities of each of the two faces of the cavity, G_s is the single path peak signal gain and ν_0 is the central optical frequency at which the gain is maximum, c is the light speed in a vacuum and L is the length of the cavity.

From the above equation (2.1) it is easy to obtain the amplification bandwidth, (considering $R_1 = R_2$)

$$\Delta V_{3dB}=\frac{c}{\pi L}\sin^{-1}\left[\frac{1-RG_s}{2\sqrt{RG_s}}\right] \qquad (2.2)$$

Then the relation between available bandwidth and maximum gain G_{max} ($G(\nu = \nu_0)$) can be expressed as

$$\sqrt{G_{\max}}\cdot\Delta V_{3dB} = \frac{c}{2L\pi}\frac{1-RG_s}{2\sqrt{RG_s}} \qquad (2.3)$$

The above equation (2.3) states that a compromise solution must be taken between amplification bandwidth and gain for this type of amplifier. Also notice that a Fabry-Perot amplifier is useful only if $G_{max} > G_s$. If this condition does not hold, a single path configuration (travelling wave amplifier) is preferable.

2.6.2 Travelling Wave Amplifiers (TWAs)

An ideal travelling wave amplifier (TWA) can be defined as a Fabry-Perot amplifier in which the ends of the active waveguide have been matched to achieve *null* reflectivity. Fig. 2.1 (b) shows the shape and direction of the amplifying medium, and without going through the filtering effect of the Fabry-Perot resonator. Generally, apart from higher power consumption and larger size, TWAs have better performance than Fabry-Perot amplifiers. This is shown on Table 2.3, which summarises some typical values of the main parameters on both types of semiconductor optical amplifiers.

TWAs have been widely studied as a possible way to achieve all optical switching [72-74], or wavelength conversion [75]. Despite their poor performance compared to fibre amplifiers, TWAs are also believed to regain importance as in-line amplifiers in spectral windows where there are no other obvious candidates or in optical local area networks (LANs) where the smaller dimensions are possibly lower cost, compared to fibre amplifiers, will be important factors for choice of amplifiers.

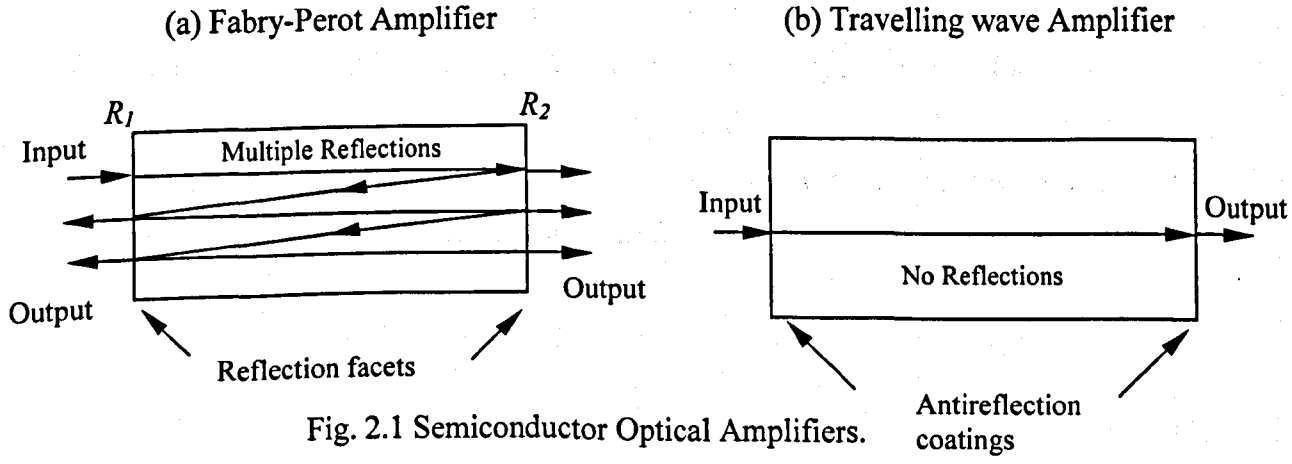

Fig. 2.1 Semiconductor Optical Amplifiers.

	TRAVELLING WAVE AMPLIFIER	FABRY-PEROT AMPLIFIER
Typical Gain	30 dB	20 – 30 dB
Typical Bandwidth (at 20 dB gain)	10 000 GHz	1 – 10 GHz
Saturation Power	10 – 20 dBm	-10 – -5 dBm
Injection Current	100 – 200 mA	20 mA
Noise Figure	7 dB	10 dB

Table 2.3 Typical values of the main parameters on both types of Semiconductor Optical Amplifiers [57].

2.7 SOA - Basic Description

An SOA is an optoelectronic device that under suitable operating conditions can amplify an input signal. A schematic diagram of a basic SOA is shown in Fig. 2.2. The active region in the device imparts *gain* to an input signal. An external electric current provides the energy source that enables gain to take place. An embedded waveguide is used to confine the propagating signal wave to the active region. However, the optical confinement is weak so some of the signal will leak into the surrounding lossy cladding regions. The input signal is accompanied by noise. This additive noise is usually produced by the amplification process itself and so cannot be entirely avoided. The amplifier facets are reflective causing ripples in the gain spectrum. Anti-reflection coatings can be used to create SOAs with facet reflectivities $< 10^{-5}$.

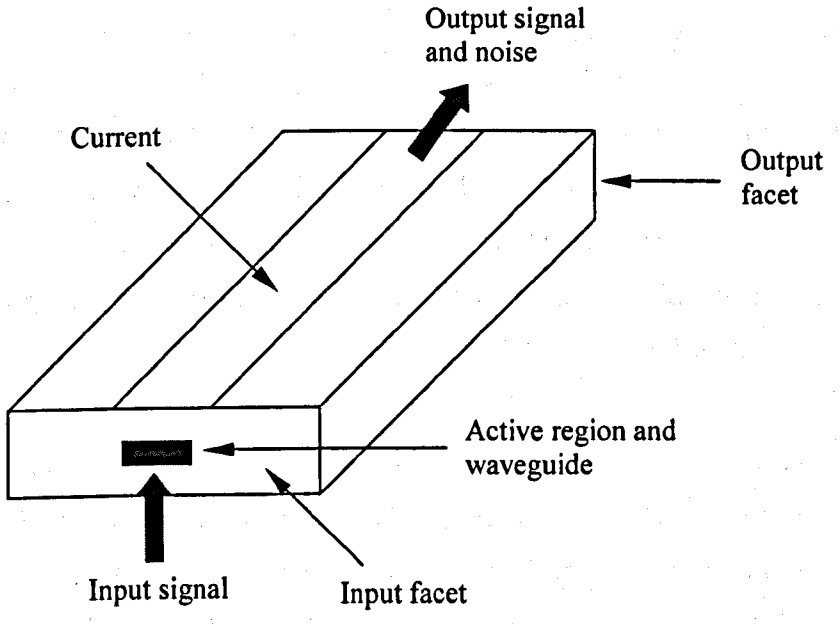

Fig. 2.2 Schematic diagram of an SOA.

2.8 Fundamental Device Characteristics

The most common application of SOAs is as a basic optical gain block. For such an application, a list of desirable properties are anticipated which are given in Table 2.4. The goal of most SOA research and development is to realise these properties in practical devices.

Property
High gain and gain bandwidth
Negligible facet reflectivities
Low Polarisation sensitivity
High Saturation output power
Additive noise near the theoretical limit
Insensitive to the input signal modulation characteristics
Multichannel amplification with no crosstalk
No nonlinearities

Table 2.4 Desirable properties of a practical SOA.

a) High gain and gain bandwidth

In general there are two basic gain definitions for SOAs. The first is the intrinsic gain G of SOA, which is simply the ratio of the input signal power at the input facet to the signal power at the output facet. The second definition is the fibre-to-fibre gain, which includes the input and output coupling losses. These gains are usually expressed in dB. The gain spectrum of a particular SOA depends on its structure, materials and operational parameters. For most applications high gain and wide gain bandwidth are desired.

The gain bandwidth of the amplifier is defined as the wavelength range over which the signal gain is not less than half of its peak value. Wide gain bandwidth SOAs are especially useful in systems where multichannel amplification is required such as in WDM networks. A wide gain bandwidth can be achieved in an SOA with an active region fabricated from quantum well or multiple quantum wells (MQW) material. Typical maximum internal gains achievable in practical devices are in the range of 30 to 35 dB. Typically small-signal gain bandwidths are in the range of 30 to 60 nm.

b) Polarisation sensitivity

In general the gain of an SOA depends on the polarisation state of the input signal. This dependency is due to a number of factors including waveguide structure, the polarisation dependent nature of anti-reflection coatings and the gain material. Cascaded SOAs accentuate this polarisation dependence.

The amplifier waveguide is characterised by two mutually orthogonal polarisation modes termed the Transverse Electric (TE) and Transverse Magnetic (TM) modes. The input signal polarisation state usually lies somewhere between these two extremes. The polarisation sensitivity of an SOA is defined as the magnitude of the difference between the TE mode gain G_{TE} and TM mode gain G_{TM} expressed as

$$G_{TE/TM} = \left| G_{TE} - G_{TM} \right| \text{ (dB)} \qquad (2.4)$$

c) Signal gain saturation

The gain of an SOA is influenced both by the input signal power and internal noise generated by the amplification process. As the signal power increases the carriers in the active region become depleted leading to a decrease in the amplifier gain as shown in Fig. 2.3. This gain saturation can cause significant signal distortion. It can also limit the gain achievable when SOAs are used as multi-channel amplifiers in wavelength division (WDM) multiplexed systems.

A useful parameter for quantifying gain saturation is the saturation output power, $P_{o,Sat}$, which is defined as the amplifier output signal power at which the amplifier gain is half the small-signal gain. Values in the range of 5 to 20 dBm for $P_{o,Sat}$ are typical of practical devices. Techniques for realising SOAs with high $P_{o,Sat}$ are discussed later in this research work.

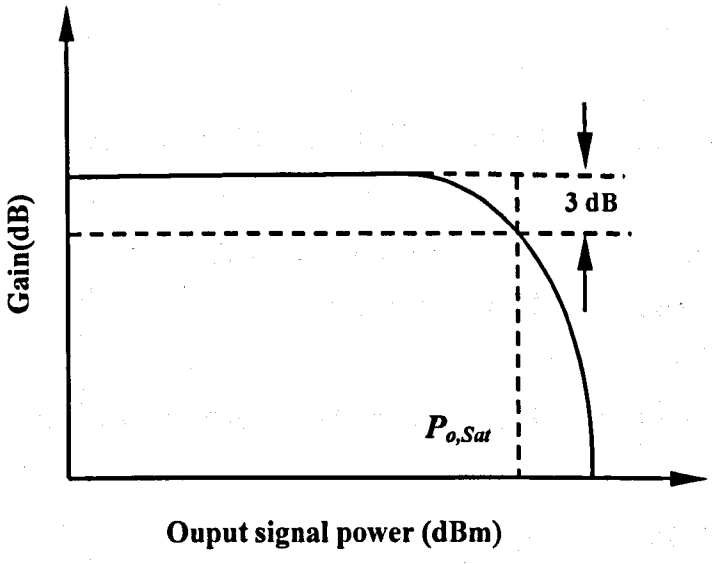

Fig. 2.3 Typical SOA gain versus output signal power.

d) Noise figure

A useful parameter for quantifying optical amplifier noise is the noise figure. *F*, defined as the ratio of the input and output signal to noise ratios, i.e.

$$F = \frac{(S/N)_i}{(S/N)_o} \tag{2.5}$$

The signal to noise ratio in equation (2.5) are those obtained when the input and output powers of the amplifiers are detected by an ideal photo-detector. In the limiting case where the amplifier gain is much larger than unity and the amplifier output is passed through a narrowband optical filter the noise figure is given by

$$F = 2n_{sp} \tag{2.6}$$

where n_{sp} is the spontaneous emission factor and the lowest value possible for n_{sp} is unity, which occurs where there is complete inversion of the atomic medium, i.e., $N_1 = 0$, giving $F = 2$ (i.e. 3dB). Typical intrinsic (not including coupling losses) noise figures of practical SOAs are in the range of 7 to 12 dB. The noise figure is degraded by the amplifier input coupling loss. Coupling losses are usually of the order of 3dB, so the noise figure of typical packaged SOAs is between 10 and 15 dB.

e) Dynamic effects

SOAs are normally used to amplify modulated light signals. If the signal power is high then gain saturation will most likely to occur. This would not be a serious problem if the amplifier gain dynamics were a slow process. However in SOAs the gain dynamics are determined by the carrier recombination lifetime. This means that the amplifier gain will react relatively quickly to change in the input signal power. This dynamic gain can cause signal distortion, which becomes more severe as the modulated signal bandwidth increases. These effects are even more important in multi-channel systems where the dynamic gain leads to interchannel crosstalk. This is in contrast to optical fibre amplifiers, which have recombination lifetimes of the order of milliseconds leading to negligible signal distortion.

f) Nonlinearities

SOAs exhibit nonlinear behaviour. These nonlinearities can cause problems such as frequency chirping and generation of intermodulation products. However, nonlinearities can also be of use in using SOAs as functional devices such as wavelength converters.

2.9 High Saturation Output Power Structures

High saturation output power is a desirable SOA characteristic, particularly for power booster and multi-channel application. High saturation output power is inevitable for linear SOAs because its linear output power is always limited to a value 5 or 6 dB lower than the saturation output power in order to avoid the waveform distortion due to the pattern effect when amplifying optical signals.

By reducing the active layer thickness in the waveguide structure, saturation output power can be increased significantly while maintaining low polarization sensitivity. Reducing the active layer thickness causes the optical field to expand widely out of the active layer so that the optical confinement factor decreases much. Therefore, a thin active layer can have a large d/Γ value, where d is the thickness of the active layer. Additionally, because the saturation output power strongly depends on the carrier density in the active layer, it is important to obtain a realistic current injection to the model. However, a reduced modal confinement, Γ, will also reduce the modal gain of the SOA.

2.9.1 Basic Model of Amplifier Saturation Characteristics

To determine the factors that influence SOA gain at high input powers, a simple rate equation model can be used. In this case, the amplifier is assumed to have zero facet reflectivities. The material gain coefficient g_m at the signal wavelength is assumed to be a linear function of carrier density, n_1,

$$g_m = a_1(n_1 - n_o) \tag{2.7}$$

where a_1 is the differential of g_m with respect to n_1 and is assumed here to be a constant and n_o is the transparency carrier density. The carrier density obeys the rate equation expressed as

$$\frac{dn}{dt} = \frac{J}{ed} - \frac{n_1}{\tau} - a_1(n_1 - n_o)\frac{I_s}{\hbar v} \tag{2.8}$$

The propagation of the signal intensity I_s through the SOA is described by the travelling-wave equation expressed as

$$\frac{dI_s}{dz} = \left[\Gamma a_1 (n_1 - n_o) - \alpha\right] I_s \tag{2.9}$$

In equations (2.8) and (2.9), t is the time, z is the propagation direction (along the amplifier axis), J is the active region current density, e the electron charge, d is the active region thickness, τ is the spontaneous carrier lifetime, $\hbar$ the Planck's constant, ν is the signal optical frequency and α the waveguide loss coefficient. Under steady state conditions the differential in equation (2.8) is zero.

The saturation intensity, I_{sat}, and saturation power, P_{sat}, are given by

$$I_{sat} = \frac{\hbar \nu}{a_1 \tau} \tag{2.10}$$

$$P_{sat} = \frac{A I_{sat}}{\Gamma} \tag{2.11}$$

where A is the active region cross-section area. A/Γ is the amplifier mode cross-section area. Hence,

$$\frac{dI_s}{dz} = \left[\frac{\Gamma g_o}{1 + I_s / I_{sat}} - \alpha\right] I_s \tag{2.12}$$

where the unsaturated material gain coefficient g_o is given by

$$g_o = a_1 \left[\frac{\tau J}{ed} - n_o\right] \tag{2.13}$$

2.9.2 Improving Saturation Output Power

The saturation output power of an SOA can be improved by increasing I_{sat}. This can be achieved by reducing τ and a_1. In practice τ is inversely proportional to carrier density, so operating at high bias currents leads to increase $P_{o,Sat.}$. However, as the carrier density increases the amplifier gain will also increase making resonance effects more significant. The single-pass gain can be maintained by reducing Γ or the amplifier length.

The choice of gain material can also influence the saturation behaviour of the amplifier via a_1. In bulk materials a_1 is relatively sensitive to changes in carrier density.

It is also possible to increase $P_{o,Sat}$ by increasing A/Γ. An approach based on this concept, is to unfold the amplifier waveguide width towards the output facet [76,77]. This increases the modal field area at the amplifier output.

2.10 Applications of Optical Amplifiers

In this section a brief review of the multiple applications of optical amplifier will be given. The most common applications include

a) Optical amplifiers as repeaters

Line optical amplifiers are one of the most common applications in telecommunication links. The concatenation of a number of them is used in point-to-point links in order to cover hundreds of *km* avoiding the utilization of classical repeaters and enabling wavelength division multiplexing.

b) Power amplifiers

The fibre amplifier should either be operators in the small-signal regime or as a power booster amplifier. The most fundamental system application of optical amplifiers is as preamplifier or line amplifiers. However, there has been an increased interest in

power amplifiers, not only as signal booster in long-haul transmission links but also as power amplifiers for optical distribution systems. The preferred choice of high-power amplifiers is LD-pumped erbium doped fibres.

c) Remote pumping

One of the important advantages of fibre amplifiers is that the amplification can be achieved remotely, launching the pump power at the extreme of the fibre. This offers the possibility that a repeater station can be built that requires no local electrical power supply. This possibility is very appealing for undersea links. An alternative is distributed amplification, which is based on the same concept.

d) Wavelength converters

One application of optical amplification that could be extremely important in the wavelength multiplexed transmission networks is optical frequency conversion. Wavelength converters allow the re-utilization and relocation of the channels on the different optical carriers so that the flexibility of the network increases and the maximum number of optical carriers does not limit the system.
Different schemes for 'transparent' wavelength converters have been presented based on semiconductor optical amplifiers or optical fibre amplifiers. The semiconductor amplifiers are the most favoured candidates to succeed since their bandwidth is slightly higher than the fibre amplifier one. Besides SOAs consume less power, have a smaller size and can be integrated along with other semiconductor devices, such as those that will be present on future optical routing nodes.

e) Soliton transmission

Soliton transmission could mark the next generation of fibre optic systems. Solitons are narrow optical pulses with high peak powers and special shapes. When a soliton propagates along an optical fibre, it does not change shape. Soliton pulse takes advantage of nonlinear effects in silica to overcome the pulse broadening effect of group velocity dispersion. By using solitons it is possible for narrow pulses to be propagated at very high speeds over thousands of kilometres without waveform

distortion. These pulses required constant signal power along the fibre and only Raman amplification could offer this performance. But the introduction of erbium-doped amplifiers overcame almost all problems involved in demonstrating practical soliton communication.

f) Amplifiers for wavelength division multiplexed networks

Optical amplifiers, particularly EDFAs, started their applications in single-channel systems. As the demand for bandwidth continues to grow, optical amplified WDM system are becoming a very interesting alternative to higher-speed time-division-multiplexing systems. Thus optical amplifiers have started to deal with simultaneous independent wavelength signals. Classical erbium doped silica fibre amplifiers have been strongly claimed as optimal devices for WDM because of their large amplification bandwidth and transparency to the modulation format. However, two problems arise when several wavelengths are simultaneously introduced which are gain competition and gain diversity for different wavelengths.

2.11 Theory of Far field Pattern

In diffraction theory we refer to the field emitted from the laser waveguide as the *near field* and the diffracted field some distance away as the *far field*. The transition occurs roughly at w^2/λ, where w is some characteristic full-width of near-field pattern. In a real index-guided waveguide, the wavefronts are planar as they approach the emitting facet. They remain approximately planar in the near field, but begin to show noticeable curvature in the transition to the far field. After some distance to the far field, the wavefronts approach a spherical shape with a radius of curvature measured from the centre of the emitted mode at the facet where the wavefronts are planar. The most narrow, planar wavefront location is termed the *beam waist* in Gaussian mode theory.

Consider a plane wave incident normally on along narrow slit of width w as shown in Fig. 2.4. If we have a screen beyond the slit then according to geometrical optics, only the region ***LM*** will be illuminated and the remaining portion (which is known as the

geometrical shadow) will be absolutely dark. However, experiments tell us that there is some light in the geometrical shadow; this spreading of light is due to the phenomenon of *diffraction*. In most applications it is desirable to capture this output light into some other waveguide or detector. The amount of light actually captured depends on the size and shape of the beam at the cross section of the capturing object amongst other things. Thus, it is useful to predict the field profile as it extends beyond the output facet.

In the experimental arrangement shown in Fig. 2.4, diffraction will occur along the x-direction and the amount of (diffraction) spreading increases with

a) increase in wavelength and
b) decrease in the width of the slit

Thus the smaller the slit width, the greater will be the spread due to diffraction.

The phenomenon of diffraction is usually divided into two categories

i) Fresnel diffraction
ii) Fraunhofer diffraction

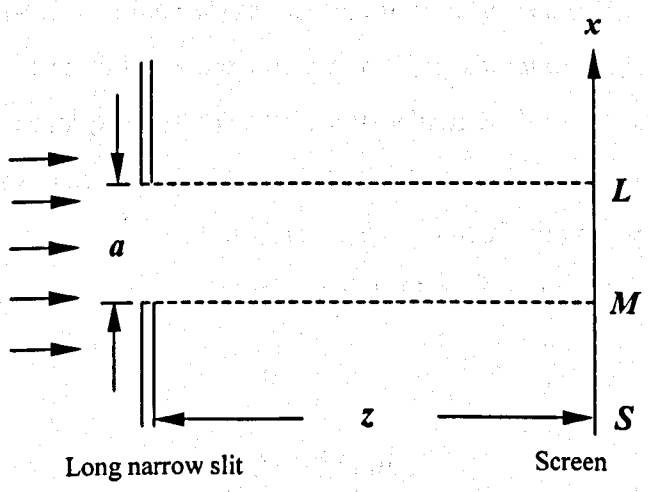

Fig. 2.4 A plane wave in incident normally on a long narrow slit of width w. According to geometrical optics, only the region LM will be illuminated.

In Fresnel diffraction, the source of light or the screen (or both) are at a finite distance from the diffracting aperture. For example, in both the arrangement in Fig. 2.4, since the screen is at a finite distance from the diffracting aperture, it corresponds to the

Fresnel diffraction. In Fraunhofer diffraction, the source and the screen are at infinite distances from the aperture; this is easily achieved by placing the source on the focal plane of a convex lens and placing the screen on the focal plane of another convex lens. The two lenses effectively move the light beam parallel and the second lens makes a point on the screen receive a parallel beam of light. Indeed in the arrangement shown in Fig. 2.4, if the distance z between the aperture and the screen satisfies

$$Z >> a^2/\lambda \tag{2.14}$$

where a is the dimension of the aperture, then the diffraction pattern observed on the screen will be essentially of the Fraunhofer type. It turns out that it is much easier to calculate the intensity distribution corresponding to Fraunhofer diffraction and fortuitously, it is the Fraunhofer diffraction pattern which is of greater importance in optics. Furthermore, the Fraunhofer diffraction pattern is not difficult to observe.

2.12 The Diffraction Formula

We first consider a plane wave incident normally on a diffracting aperture ϕ as shown in Fig. 2.5. The field at the point P can be calculated approximately by using the Huygens-Fresnel principle according to which each point on a wavefront is a source of secondary disturbance and the secondary wavelets emanating from different points mutually interfere. Now, the field at the point P due to spherical waves emanating from the area $d\xi d\eta$ around the point Q whose coordinates are (ξ,η,O) will be proportional to

$$A(e^{-jkr}/r)d\xi d\eta \tag{2.15}$$

where, A represents the amplitude of the plane wave in the plane of the aperture and

$$r = \left[(x-\xi)^2 + (y-\eta)^2 + z^2\right]^{1/2} \tag{2.16}$$

represents the distance ***QP***. In order to calculate the field at the point ***P*** due to the entire aperture we will have to sum over all the infinitesimal areas and if we replace the summation by an integral we will obtain

$$u(P) = C \iint_{\phi} A(e^{-jkr}/r)d\xi d\eta \tag{2.17}$$

where C is the proportionality constant which can be determined by noting that in the absence of the aperture $u(P)$ must be equal to Ae^{-jkz}. Thus

$$C \int\int_{-\infty}^{+\infty} A(e^{-ikr}/r)d\xi d\eta = Ae^{-ijkz} \tag{2.18}$$

If we carry out the above integration under the approximation that most of the contribution to the integral comes from the domain $|x-\xi|$, $|y-\eta| << z$, we will obtain

$$C = j/\lambda \tag{2.19}$$

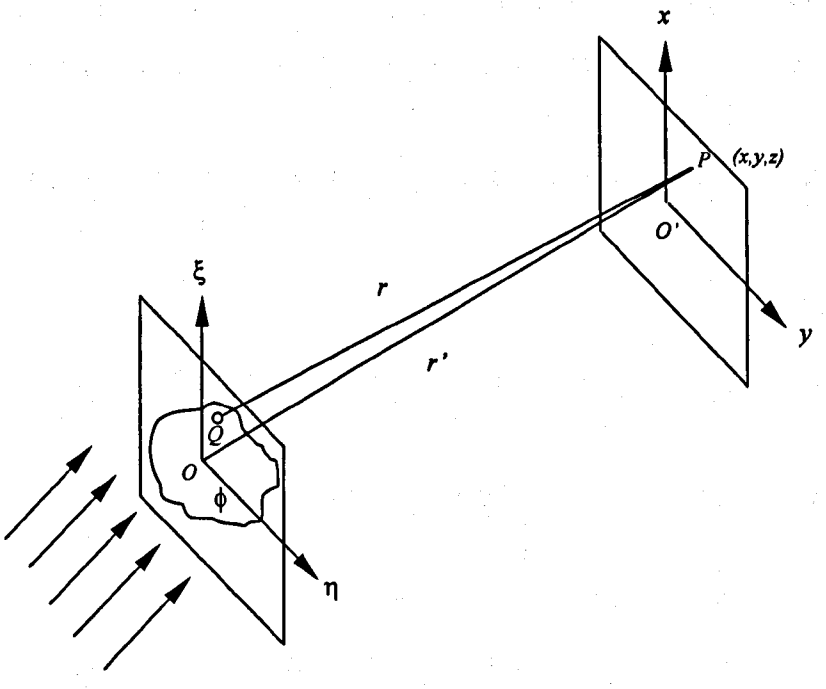

Fig. 2.5 A plane wave propagating along the z-axis is incident normally on a diffracting aperture ϕ.

Thus,

$$u(P) = \frac{jA}{\lambda}\int\int \frac{e^{-jkr}}{r} d\xi d\eta \qquad (2.20)$$

It should be mentioned here that a more rigorous analysis based on the solution of the scalar wave equation gives the same result as equation (2.20) provided we neglect the obliquity factor [78].

In most problems of practical interest, the dimension of the aperture is small so that the quantity, r, does not vary appreciably over the area of the aperture and very little error will be involved if r in the denominator is replaced by r' and taken out of the integral i.e.,

$$u(P) \approx (jA/\lambda r')\int\int_{\phi} e^{-jkr}\, d\xi d\eta \qquad (2.21)$$

where r' represents the distance of the point P from a conveniently chosen origin in the aperture. Even when we have an infinitely extended aperture (such as a long narrow slit) we will see that the major contribution to the integral in equation (2.21) comes from a small domain of the aperture where r can be assumed to be a constant. We choose a convenient point O (on the plane of the aperture) as the origin to the coordinate system. Let (ξ, η, O) and (x, y, z) represent the coordinates of arbitrary points Q and P on the planes of the aperture and of the screen respectively. Thus, the distance QP is given by

$$r = QP = \left[(x-\xi)^2 + (y-\eta)^2 + z^2\right]^{1/2}$$

$$r' = \left[1 - \frac{2(x\xi + y\eta)}{r'^2} + \frac{\xi^2 + \eta^2}{r'^2}\right]^{1/2} \qquad (2.22)$$

where $r' = (x^2 + y^2 + z^2)^{1/2}$ represents the distance of the point P from the original O. Since the dimensions of the aperture are, in general, very small compared to the distance r', we make a binomial expansion to obtain

$$r = r' - \frac{x\xi + y\eta}{r'} + \left[-\frac{(x\xi + y\eta)^2}{2r'^3} + \frac{\xi^2 + \eta^2}{2r'} \right] + \ldots\ldots \qquad (2.23)$$

Now, if r' is so large that the quadratic (and higher order terms) in ξ and η can be neglected, then we have what is known as *Fraunhofer diffraction.* If it is necessary to retain terms that are quadratic in ξ and η then we have what is known as *Fresnel diffraction.*

In general, for an aperture of dimension a, the pattern will be Fraunhofer if

$$a^2/\lambda z << 1 \qquad (2.24)$$

The quantity $a^2/\lambda z$ is known as the Fresnel *number* of the aperture, thus while discussing Fraunhofer we may write

$$r = r' - (l\xi + m\eta) \qquad (2.25)$$

where

$$l = x/r' = \cos\alpha \text{ and } m = y/r' = \cos\beta \qquad (2.26)$$

represent the direction cosines ***OP*** along the x and y-directions; α and β represent the angles that ***OP*** makes with the x and y axes. Substituting in equation (2.21) we obtain

$$u(P) = C \iint_{\phi} e^{jk(l\xi + m\eta)} d\xi d\eta \qquad (2.27)$$

where

$$C = \frac{jA}{\lambda} \frac{e^{-jkr'}}{r'} \qquad (2.28)$$

The factor $e^{-jkr'}$ is a constant which will give a factor of unity when we take the *squared modulus* of $u(P)$ to get the light intensity, therefore it is dropped.

Hence we can write the final expression for the complex amplitude at ***P***,

$$u(P) = \frac{jA}{\lambda r} \iint_{\phi} e^{jk(l\xi+m\eta)} d\xi d\eta \qquad (2.29)$$

C is a constant. If we define an aperture function ***P*** (ξ,η) by

$$\left.\begin{aligned} P(\xi,\eta) &= 1 \text{ for } (\xi,\eta) \text{ inside the aperture} \\ &= 0 \text{ otherwise} \end{aligned}\right\} \qquad (2.30)$$

then equation (2.27) can be written as

$$u(P) = C\int\int_{-\alpha}^{+\alpha} P(\xi,\eta) e^{jk(l\xi+m\eta)} d\xi d\eta \qquad (2.31)$$

Equation (2.31) is nothing other than the Fourier transform of the aperture function *P(x,y)*. If instead of an aperture we have an amplitude distribution *A(x,y)* across the wavefront, then the above equation would be modified to

$$u(P) = C\int\int_{-\alpha}^{+\alpha} A(\xi,\eta) e^{jk(l\xi+m\eta)} d\xi d\eta \qquad (2.32)$$

Sine the Fourier transform of a Gaussian function is another Gaussian function, if we consider a beam whose transverse intensity distribution is Gaussian, then the transverse intensity distribution associated with the Fraunhofer diffraction pattern will also be Gaussain. Indeed, even the Fresnel diffraction pattern is also Gaussian.

2.13 Directionality of Laser Beams

An ordinary source of light radiates in all directions. On the other hand, the output from a laser is usually such its divergence is primarily due to diffraction effects. The output from a laser has usually a transverse intensity distribution and can be expressed as

$$u = u_o e^{-r/w_o{}^2}, \quad r^2 = x^2 + y^2 \tag{2.33}$$

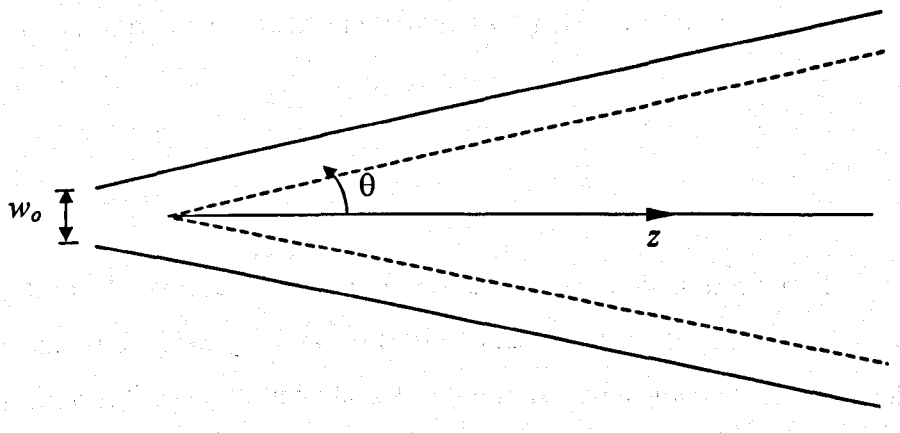

Fig. 2.6 Diffraction of a Gaussian beam.

the propagation is along the z-axis and the quantity w_o is usually referred to as the *spot-size of the beam.* When the beam propagates (along the z-direction) the spot-size increases as shown in Fig. 2.6.

$$w(z) = w_o(1 + \lambda^2 z^2 / \pi^2 w_o{}^4)^{1/2} \tag{2.34}$$

thus from equation (2.14)

$$Z >> \pi w_o{}^2 / \lambda \tag{2.35}$$

The beam width increases as

$$w(z) \approx \lambda z / \pi w_o \tag{2.36}$$

hence the diffraction divergence is given by

$$\theta \approx w(z)/z \approx \lambda / \pi w_o \tag{2.37}$$

It can be observed that the greater the radius of the beam the smaller will be the size of the focused spot and hence the greater will be the intensity at the focused spot. Indeed one may use the beam expander to produce a beam of greater size and hence a smaller focused spot-size. However, the beam would then have a greater divergence and therefore it would expand within a very short distance.

2.14 Summary

In this chapter, the general overview of optical amplifiers has been presented, including the history of its generation, classification, their properties and applications. Moreover, the comparison between the fibre and semiconductor optical amplifiers has been outlined.

In this research work the semiconductor optical amplifiers has been given more attention more specifically the travelling wave amplifiers. Therefore, the basic description and fundamental characteristics of these devices has been detailed in this chapter. The final section of this chapter discusses the mathematical theory of the far field pattern for different waveguide structures.

3.0 The Finite Element Method

3.1 Introduction

The finite element method (FEM) is now firmly accepted as one of the most powerful general technique for the numerical solution of a variety of problems encountered in engineering. Applications range from stress analysis of solids to the solution of acoustical, neutron physics and fluid dynamics problems.

A finite element model of a problem gives a *piecewise* approximation to the governing equations. The basic premise of the finite element method is that a solution region can be analytically modelled or approximated by replacing it with an assemblage of discrete elements. Since these elements can be put together in a variety of ways, they can be used to represent exceedingly complex shapes. The method solves the governing equations through a discretisation process. The finite element discretisation procedures reduce the problem to one of a finite number of unknowns by dividing the solution region into elements and by expressing the unknown field variable in terms of assumed approximating functions within each element. The approximating functions (sometimes called *interpolation functions*) are defined in terms of the values of the field variables at specified points called *nodes* or *nodal points*. The nodal values of the field variable and the interpolation functions for the elements completely define the behaviour of the field variable within the elements.

For the finite element representation of a problem the nodal values of the field variable become the unknowns. Once these unknowns are found, the interpolation functions define the field variable throughout the assemblage of elements.

Clearly, the nature of the solution and the degree of approximation depend not only on the size and number of the elements used but also on the interpolation function selected.

The finite element method has developed its superiority over other methods due to two well-known features. Initially, a geometrically simple complex domain of the problem is represented as a collection of geometrically simple sub-domains, called *elements*, avoiding the difficulties governed with the "whole domain" techniques.

Secondly, over each element the approximation functions are derived using the basic idea that any continuous function can be represented by a linear combination of algebraic polynomials.

3.2 Brief Historical Background of FEM

Although, the label *finite element method* first appeared in 1960, when it was used by Clough [79] in a paper on plane elasticity problems, the ideas of finite element analysis date back much further. The first effort to use piecewise continuous functions defined over triangular domains appears in the applied mathematics literature with the work of Courant in 1943 [80]. Courant used an assemblage of triangular elements and the principle of minimum potential energy to study the St. Venant torsion problem.
The actual solution of plane stress problems by means of triangular elements whose properties were determined from the equations of elasticity theory was first given in the now classical 1956 paper of Turner, Clough, Martin, and Topp at the Boeing Aircraft Company [81]. They used the finite element method to calculate the stress-strain relations for complicated aircraft structures for which no known solutions were existed. With this paper together with many others, an explosive development of the finite element method in engineering applications began. In 1959 Greenstadt [82], outlined a discretisation approach involving "*cells*" instead of points; that is, he imagined the solution domain to be divided into a set of contiguous sub-domains. In his theory he describes a procedure for representing the unknown function by a series of functions, each associated with one cell, he then uses continuity requirements to tie together the equations for all the cells. This means he reduces the continuous problem to a discrete one. Greenstadt's theory allows for irregularly shaped cell meshes and contains many of essential and fundamental ideas that serve as the mathematical basis for the finite element method as we know it today.
Clough first introduced the name *finite element* in 1960 [79], in the early sixties, the method was viewed as sound and versatile, and it became a respectable area of study in the academic circle. A wide variety of elements were developed including bending elements, curved shell elements and the isometric concept was also introduced.
The method was soon recognised as a general method of solution for partial differential equations; its applicability to non linear and dynamic solid mechanics,

fluid mechanics, thermodynamics, electromagnetism, etc., produced solution to engineering problems.

3.3 Steps involved in FEM Analysis

Regardless of the approach used to find the element properties, the solution of a continuum problem by the finite element method always follow an orderly step-by-step process. The following summarise how the finite element method works in general terms.

a) *Discretise the Continuum.* The first step is to divide the continuum or the solution region into elements. A variety of element shapes may be used, and different element shapes may be employed in the same solution region.

b) *Select Interpolation Functions.* The next step is to assign nodes to each element and then choose the interpolation function to represent the variation of the field variable over the element. The field variable may be a scalar or vector. Often, polynomials are used as interpolation functions for the field variable because they are easy to integrate and differentiate. The degree of the polynomial chosen depends on the number of nodes assigned to the element, the nature and the number of unknowns at each node, and certain continuity requirements imposed at the nodes and along the element boundaries.

c) *Find the Element Properties.* Once the finite element model has been established (that is, once the elements and their interpolation functions have been selected), you determine matrix equations expressing the properties of the individual elements.

d) *Assemble the Element Properties to Obtain the System Equations.* To find the properties of the overall system modelled by the network of elements we must "assemble" all the element properties. In other words, we combine the matrix equations expressing the behaviour of the elements and form the matrix equations expressing the behaviour of the entire system. The matrix equations for the system have the same form as the equations for an individual element except that they contain many more terms because they include all nodes. This is an attractive feature of the finite element method.

e) *Impose the Boundary Conditions.* Before the system equations are ready for solution they must be modified to account for the boundary conditions of the problem. At this stage we impose known nodal values of the dependent variables or nodal loads.

f) *Solve the System Equations.* The assembly process gives a set of simultaneous equations that we solve to obtain the unknown nodal values of the problem. If the problem describes steady or equilibrium behaviour, then we must solve a set of linear or nonlinear algebraic equations. While if the problem is unsteady, the nodal unknowns are a function of time, and we must solve a set of linear or nonlinear ordinary differential equations.

In classic analytic procedures, without subdivision processes, the system is modelled over the whole region using analytic functions, hence these approaches are only suitable for planar or one-dimensional structures.

3.4 Applications of the FEM

Applications of the FEM divide into three categories, depending on the nature of the problem to be solved.

a) *Equilibrium problems or time-independent problems.* The solution of equilibrium problems in solid mechanics area, we need to find the displacement distribution and the stress distribution for a given mechanical or thermal loading. Similarly, for the solution of equilibrium problems in fluid mechanics, we need to find pressure, velocity, temperature, and density distribution under steady state conditions.

b) *Eigenvalue problems* of solid and fluid mechanics. These are the steady-state problems whose solutions often require the determination of natural frequencies and modes of vibration of solids and fluids.

c) *Propagation problems or the multitude of time-dependent.* This category is composed of the problems that result when the time dimension is added to the problems of the first two categories.

The discussion in this chapter will mainly focus on the eigenvalue problem and is indeed of steady state nature. In terms of its nature, where the problem region is the waveguide cross-section, the waveguide problem can be regarded as a one- or two-dimensional problem.

3.5 Basic Equations

In this section we shall discuss the fundamental electromagnetic field equations, such as the Maxwell's equations and boundary conditions. These two equations are essential in order to employ the finite element method in the optical waveguide analysis problems hence considered.

3.5.1 Maxwell's Equations

Propagation of light through a waveguide is an electromagnetic phenomenon, and is described by Maxwell's equations. These equations form a basic set of equations of electromagnetic field theory, governing all electromagnetic phenomena. The equations can be addressed in both differential and integral forms, but in this work they are presented only in differential form, as it is the most convenient form to be implemented in the finite element method.

The differential form of Maxwell's equations in time-varying electromagnetic fields can be written as

$$\nabla \times \mathbf{E} = \frac{-\partial \mathbf{B}}{\partial t} \qquad \text{(Faraday's law)} \qquad (3.1)$$

$$\nabla \times \mathbf{H} = \frac{\partial \mathbf{D}}{\partial t} + \mathbf{J} \qquad \text{(Ampere's law)} \qquad (3.2)$$

$$\nabla . \mathbf{D} = \rho \qquad \text{(Gauss's law)} \qquad (3.3)$$

$$\nabla . \mathbf{B} = 0 \qquad \text{(Gauss's law of magnetics)} \qquad (3.4)$$

where

E = electric field intensity (Volts / meter)

H = magnetic field intensity (Amperes / meter)

D = electric flux density (Coulombs / meter^2)

B = magnetic flux density (Webers / meter^2)

J = electric current density (Amperes / meter^2)

ρ = electric charge density (Coulombs / meter^3)

The fundamental current continuity equation, which describes the conservation of charge can be expressed as

$$\nabla . \mathbf{J} = \frac{-\partial \rho}{\partial t} \qquad (3.5)$$

Associated with the Maxwell's equations are the constitutive relations which relate the field and the medium as follows

$$\mathbf{D} = \varepsilon \mathbf{E} \qquad (3.6)$$

$$\mathbf{B} = \mu \mathbf{H} \qquad (3.7)$$

where ε is the permittivity and μ is the permeability of the medium.

Lets assume the time dependence to be $\exp(j\omega t)$, where j is the imaginary part, ω is the angular frequency (radian), and t is the time, for convenience purposes. Thus the differential form of Maxwell's equations can be written as

$$\nabla \times \mathbf{E} = -j\omega\mathbf{B} \tag{3.8}$$

$$\nabla \times \mathbf{H} = j\omega\mathbf{D} + \mathbf{J} \tag{3.9}$$

$$\nabla . \mathbf{D} = \rho \tag{3.10}$$

$$\nabla . \mathbf{B} = 0 \tag{3.11}$$

the continuity equation hence can be written as

$$\nabla . \mathbf{J} = -j\omega\rho \tag{3.12}$$

3.5.2 Boundary Conditions

Certain conditions have to be accomplished at the interface between two media with different parameters; these conditions are called the "*boundary conditions*". Maxwell's equations, as presented above, are subjected to boundary conditions at surfaces where the refractive indices change abruptly. A key strength of the FEM is the ease and elegance with which it handles arbitrary boundary and interface conditions. Fig. 3.1 shows such a boundary between two different media with the unit normal vector $\boldsymbol{n}$ directed from medium 1 to medium 2.

When there is neither a surface charge ($\rho = 0$) nor a surface current ($J = 0$) the following boundary conditions remain valid

a) The tangential components of the electric field must be continuous.

$$\boldsymbol{n} \times (\mathbf{E}_1 - \mathbf{E}_2) = 0 \tag{3.13}$$

$$\mathbf{E}_{t_1} = \mathbf{E}_{t_2}$$

where $\mathbf{E}_{t_1}$ and $\mathbf{E}_{t_2}$ are the tangential electric field in medium 1 and medium 2, respectively.

b) The tangential components of the magnetic field must be continuous.

$$\boldsymbol{n} \times (\mathbf{H}_1 - \mathbf{H}_2) = 0 \qquad (3.14)$$

$$\mathbf{H}_{t_1} = \mathbf{H}_{t_2}$$

where $\mathbf{H}_{t_1}$ and $\mathbf{H}_{t_2}$ are the tangential magnetic field in medium 1 and medium 2, respectively.

c) The normal components of the electric flux density must be continuous.

$$\boldsymbol{n} \cdot (\mathbf{D}_1 - \mathbf{D}_2) = 0 \qquad (3.15a)$$

$$\mathbf{D}_{n_1} = \mathbf{D}_{n_2}$$

where $\mathbf{D}_{n_1}$ and $\mathbf{D}_{n_2}$ are the normal electric flux density in medium 1 and medium 2, respectively.

$$\varepsilon_1 \mathbf{E}_{n_1} = \varepsilon_2 \mathbf{E}_{n_2} \quad \text{where} \quad \mathbf{E}_{n_1} \neq \mathbf{E}_{n_2} \qquad (3.15b)$$

d) The normal components of the magnetic flux density must be continuous.

$$\boldsymbol{n} \cdot (\mathbf{B}_1 - \mathbf{B}_2) = 0 \qquad (3.16a)$$

$$\mathbf{B}_{n_1} = \mathbf{B}_{n_2}$$

where $\mathbf{B}_{n_1}$ and $\mathbf{B}_{n_2}$ are the normal magnetic flux density in medium 1 and medium 2, respectively.

$$\mu_1 \mathbf{H}_{n_1} = \mu_2 \mathbf{H}_{n_2} \tag{3.16b}$$

If the relative permeabilities in medium 1 and 2 are μ_{r_1} and μ_{r_2} respectively, then, for most of the optical waveguides, $\mu_{r_1} = \mu_{r_2} = 1$. Therefore, the magnetic field vectors at the boundary are equal.

$$\mathbf{H}_{n_1} = \mathbf{H}_{n_2} \tag{3.16c}$$

In an ideal case of a perfect electric conductor, another boundary condition is often used, this boundary condition can be termed as the "electric wall" which can be contributed when

$$\boldsymbol{n} \times \mathbf{E} = 0 \qquad \text{or} \qquad \boldsymbol{n} \,.\, \mathbf{H} = 0 \tag{3.17}$$

This boundary condition requires that the magnetic field vector, **H**, must vanish, and ensures the continuity of the electric field vector, **E**, at the boundary. A "magnetic wall" condition is normally imposed when one of the two media becomes a perfect magnetic conductor and

$$\boldsymbol{n} \times \mathbf{H} = 0 \qquad \text{or} \qquad \boldsymbol{n} \,.\, \mathbf{E} = 0 \tag{3.18}$$

The magnetic wall condition vanishes the electric field vector, **E**, and ensures the continuity of the magnetic field vector, **H**, at the boundary.

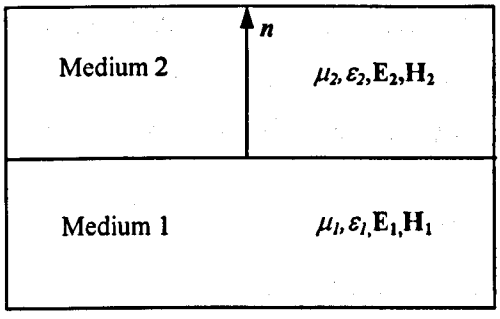

Fig. 3.1 The Interface between two different media.

3.6 Variational Formulations

The two major alternatives for formulating the finite element method are the variational [83] or weighted residual approach. It has been reported in literature that most of the solutions for wide variety of electromagnetic field problems have been based on the variational approach. The variational approach is more advantageous, regardless of the weighted residual being more straightforward; this is because only one global parameter, such as the propagation constant is needed. This approach has been extensively applied to a wide variety of electromagnetic field problems, in particular to the problem of wave propagation along the arbitrary shaped waveguides, with anisotropic material. In this work, only the variational approach will be considered.

When a variational expression is considered, it can be converted into a standard eigenvalue problem through the application of finite element method in the form

$$[\mathbf{A}]\{x\} = \lambda[\mathbf{B}]\{x\} \tag{3.19a}$$

$$[\mathbf{A}]\{x\} - \lambda[\mathbf{B}]\{x\} = 0 \tag{3.19b}$$

where $[\mathbf{A}]$ and $[\mathbf{B}]$ are real symmetric matrices, and $[\mathbf{B}]$ is also positive definite matrix. The eigenvalue λ may be k_o^2 (k_o is the free space wavenumber) or β^2

depending on the variational formulation and $\{x\}$ is the eigenvectors representing the unknown nodal fields. The resulting matrix equation is mostly desirable to be of the canonical form, to allow for robust and efficient solution. The equation (3.19*b*) can be solved by one of the various standard subroutines to obtain different eigenvectors and eigenvalues.

The two most commonly used variational formulations, which can be utilised in finite element method, are the scalar [84] and the vector formulations [36][85,86].

3.6.1 Scalar Field Formulation

This method has been applied to problems of electromagnetic wave propagation in homogenous, isotropic media, where a single potential or only one field component has been applied. It is the simplest form of the differential variational formulations. In this method its validity becomes apparent only in situations where the modes can be described predominantly as TE and TM modes. The following scalar variational expression has been proposed in the work of Mabaya [87];

$$J(\phi) = \iint_{\Omega} m\left[\left(\frac{\partial\phi}{\partial x}\right)^2 + \left(\frac{\partial\phi}{\partial y}\right)^2 + \left(\beta^2 - k_o{}^2 n^2\right)\phi^2\right] dxdy \qquad (3.20)$$

where

β is the propagation constant

n is the refractive index profile

k_o is the free-space wavenumber

In this case, Ω denotes the cross section domain where the integration is carried out. The eigenvector, $\phi(x,y)$ is the transverse field distribution, when $m = 1$, $\phi = E_x$ for the TE modes. A finite element program based on the above mentioned functional yields β^2 as the eigenvalue of the matrix equation for a given k_o.

On the other hand for the TM modes the scalar approximation can be expressed as

$$J(\psi) = \iint_{\Omega} m\left[\left(\frac{\partial \psi}{\partial x}\right)^2 + \left(\frac{\partial \psi}{\partial y}\right)^2 + \left(\beta^2 - k_o^2 n^2\right)\psi^2\right] dxdy \quad (3.21)$$

In this case, ψ denotes the cross section domain where the integration is carried out. The eigenvector, $\psi(x,y)$ is the transverse field distribution, when $m = 1/n^2$, $\psi = H_x$ for the TM modes.

The two scalar finite element formulations form an excellent approximation for the TE and TM modes of the optical waveguide. The main advantages of the scalar approximation are

a) The two scalar functionals are positive definite (or can immediately be made positive definite). All the eigenvalues are, therefore, positive and each one corresponds to a physical mode of the guide. This results in an ease to compute the higher order modes of the guide. This is of great significance in open dielectric waveguides where to compute higher order modes, it becomes very hard to differentiate between the spurious and non-physical modes.
b) In this method the dimensions of the matrices are reduced compared to the vector finite element method causing a reduction in the computer time.
c) It is easier to calculate modes close to the cut-off since it is possible to use more triangles to model the substrate for a given maximum matrix size.

3.6.2 Vector Field Formulations

The scalar formulation is inappropriate to solve and handle hybrid modes of anisotropic or inhomogeneous optical waveguide problems, vector wave analysis is important for an accurate evaluation of the propagation characteristics. Another advantage is that it offers a better solution convergence for some modal types as compared to corresponding scalar formulations.

One disadvantage of any vector finite-element method is the appearance of the spurious solutions or non-physical solutions, which appear mixed with the correct solutions. Later, on this chapter we shall discuss the generation and how these spurious solutions can be avoided.

For such vector wave analysis, there are a number of finite element methods depending on which electromagnetic field component is used for formulation, which are

a) Finite element method using the three electric field components, **(E)**.
b) Finite element method using the three magnetic field components, **(H)**.
c) Finite element method using the six electromagnetic field components, **(E + H)**.
d) Finite element method using the transverse electric field components, **(E_t)**.
e) Finite element method using the transverse magnetic field components, **(H_t)**.
f) Finite element method using the transverse electromagnetic field components, **($E_t + H_t$)**.
g) Finite element method using the longitudinal (axial) electromagnetic field components **($E_z + H_z$)**.

Berk [88] derived some vector variational expression in the form of Rayleigh quotients for loss-free resonators and microwave waveguides in terms of **H**-field, **E**-field or combination of both. Later, Morishita and Kumagai [85] established procedures to derive variational expression for both self-adjoint and self-adjoint operators.

The formulation of finite element using axial component of the fields (E_z and H_z) was one of the first vector formulation used in finite element to solve many different types of guiding structures problems [89]. However, this E_z-H_z formulation cannot without destroying the canonical form of the eigenvalue matrix treat general anisotropic problems. The satisfying of the boundary conditions in this method can be quite difficult, for a waveguide with arbitrary dielectric distribution. The other disadvantage of this method for optical dielectric waveguide problem is that it considers axial

components of the fields, which are the least important components of the six-vector field.

The vector **E**-field was first applied by English and Young [90], this method can solve general anisotropic problems. They considered a vector **E** formulation as it involved more Dirichlet (rather than Neumann) boundary conditions associated with the fields. Unfortunately, the boundary condition is that of a magnetic wall, which cannot be left free for an electric wall boundary. Since it is essential for boundary condition $n \times \mathbf{E} = 0$ be imposed on any conducting boundaries, it is an added difficulty to implement that boundary condition on arbitrarily shaped guided walls. Another drawback of this method is that the dielectric interface needs special consideration to ensure continuity of the tangential components of the fields.

Angkaew [91] formulated a variational expression suited for the finite element method in terms of the transverse electric (**E**) and magnetic (**H**) field components. This transverse formulation in this method is computationally costly as it involves additional differentiation [92], although a complete discrimination of the spurious mode solutions from guided mode solutions are confirmed.

Under all the criterias, a vector **H**-field formulation [93] has the advantage over all the others. For general optical waveguide problems, where the modes are hybrid, the transverse field components are dominant, and the materials may be generally anistropic, the vector **H**-field formulation appears to be the most accurate, versatile, and suitable method. For this formulation, we can consider general antisotropic problems, which are important for many active and passive integrated optics structures. In this method, the natural boundary condition is that of an electric wall, so that for arbitrary conducting guide walls it can be left free. The chosen field is continuous at the dielectric interfaces in this formulation making it very efficient for the finite element solution of dielectric waveguide problems.
The vector **H**-field formulation can be written as [35], [88]

$$\omega^2 = \frac{\int (\nabla \times \mathbf{H})^* . \varepsilon^{-1} . (\nabla \times \mathbf{H}) \, d\Omega}{\int \mathbf{H}^* . \mu . \mathbf{H} \, d\Omega} \tag{3.22}$$

where ε and μ are the general anisotropic permittivity and permeability of the loss-free medium, respectively. ω is the radian frequency while domain Ω is where the integration is carried over on the waveguide cross section.

Since the natural boundary conditions is that of an electric wall, we need not force any boundary condition on conducting guide walls. But for regularly shaped waveguides, and at the symmetric walls (if applicable), we can enforce the boundary condition to reduce the problem size. To obtain a stationary solution of the functional equation (3.22) this can be minimised with respect to each of the variables, which are unknown modal field components $\mathbf{H}_x$, $\mathbf{H}_y$ and $\mathbf{H}_z$, defined by a set of algebraic polynomials. The minimisation leads to a matrix eigenvalue equation as stated in equation (3.19*b*) where **[A]** is a complex Hermitian matrix and **[B]** is a real symmetric and positive definite matrix. The eigenvalue problem can be solved by one of the various standard subroutines to get different eigenvectors and eigenvalues. The eigenvectors $\{x\}$ represent the unknown field components at the nodal points for different modes with λ as their corresponding eigenvalues and also λ is proportional to ω^2. In order to obtain a mode of a given wavelength, the β value has to be changed iteratively until the output eigenvalue corresponds to that wavelength. Generation of spurious solution appear mixed up with correct solutions, which tends to be a drawback, later in this chapter we shall discuss how the spurious solutions can be avoided.

3.6.3 Natural Boundary Conditions

Natural boundary condition is the boundary condition which is satisfied automatically in the variational formulation. One significant feature of the variational formulation is that the natural boundary condition can be automatically be satisfied if left free.

The functional defined in equation (3.20) has the continuity of $m\left[\frac{\partial \phi}{\partial n}\right]$ where $m = 1$, as the natural boundary condition and the functional expressed in equation (3.21) has the continuity of $m\left[\frac{\partial \phi}{\partial n}\right]$ where $m = 1/n^2$ as the natural boundary condition, $\bar{n}$ is the outward normal unit vector. The vector **H**-field variation formulation given in equation (3.22) in contrast has the electric wall as the natural boundary condition

expressed as $n.\mathbf{H} = 0$. In some occasions it is essential to change the unsuitable natural boundary condition by introducing additional surface integral around the desired boundary, however, in case of symmetry of a waveguide exists, the natural boundary condition may be enforced, which reduces the matrix problem size, but it is of great significance to analyse the structure with complementary symmetry condition to obtain all the modes, although the exploitation of the symmetry greatly reduces the computational cost.

3.7 Optical Waveguides Application

The analysis of electromagnetic waveguide problems can be categorised as

i) One-dimensional
ii) Two-dimensional

The analysis method to consider depends on the eigenmode property of the waveguide which can be either a scalar or vector analysis. The vector analysis is more accurate and versatile when considering a two-dimensional problem, whilst the scalar analysis can be employed in both one and two-dimensional problems.

Since hybrid modes are generated by the arbitrarily-shaped waveguide, vector wave analysis is significant for precise evaluation of their propagation characteristics and polarisation issues, therefore considered. However, vector solution has the disadvantage of appearance of spurious solutions. These can be eliminated by either using the $\mathbf{H}_t$ (Hernandez-Figueroa *et al.*, 1994) formulation or by employing the penalty function [35] in the variational formulation.

When the optical waveguide with arbitrary cross-sectional shape, is build up of different materials, they can be described by the arbitrary permittivity (ε) and permeability (μ) tensors. These could be linear, nonlinear, isotropic, anisotropic or loss less.

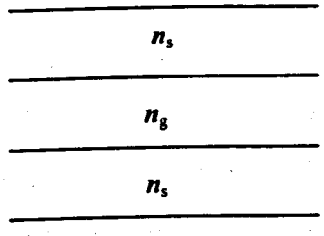

Fig. 3.2 (a) Planar waveguide (one-dimensional).

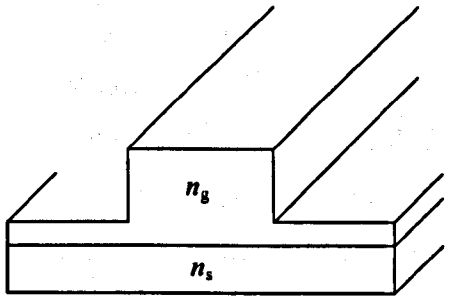

Fig. 3.2 (b) Arbitrarily-shaped waveguide (two-dimensional).

The waveguide is assumed to be uniform along the axis of propagation z-axis. Assuming the time (t) and z dependencies are given as $\exp(j\omega t)$ and $\exp(-j\beta z)$ respectively, where ω is the angular frequency and β is the propagation constant, the electric field $\mathbf{E}(x,y,z,t)$ and the magnetic field $\mathbf{H}(x,y,z,t)$ can be expressed as

$$\mathbf{E}(x,y,z,t) = \mathbf{E}(x,y)\exp[j(\omega t-\beta z)] \tag{3.23}$$

$$\mathbf{H}(x,y,z,t) = \mathbf{H}(x,y)\exp[j(\omega t-\beta z)] \tag{3.24}$$

The spatial variations of the electric and magnetic fields are $\mathbf{E}(x,y)$ and $\mathbf{H}(x,y)$ respectively.

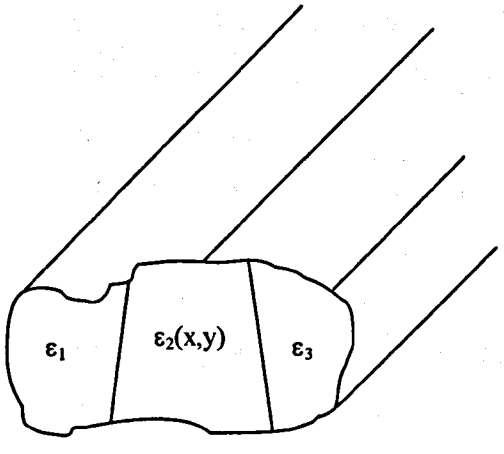

Fig. 3.3 Optical waveguide with arbitrary subdomains with different materials.

3.8 Spurious Solutions

The vector variational formulations suffer from the appearance of spurious or non-physical modes, which appear mixed up with the physical (true) solutions during computations. There are various methods employed to detect these spurious solutions from the true modes, such as for example examining the field. The characteristic of spurious solutions is the inconsistency and the random fashion of the field varied. The explanation to the cause of these spurious solutions could be due to the enforcement of the boundary conditions or the nonzero divergence of the trial fields [36], [93]. In electromagnetic waveguide problems the spurious modes do not arise if the trial field precisely satisfies the condition $\nabla.\mathbf{B} = 0$. Spurious modes occur in a full vector formulation where the divergence-free condition is neither implied nor forced and are distinctive in giving particularly high values of $\nabla.\mathbf{B}$.

To eliminate these spurious modes, it is essential to differentiate between the physical (true) and the spurious solutions. For a physical mode, mathematically, its eigenvector satisfies the condition $\nabla.\mathbf{H} = 0$. So it is possible to identify the spurious solution from the physical ones by calculating the $\nabla.\mathbf{H}$ for each solution over the waveguide cross section. The solution with low values of $\nabla.\mathbf{H}$ are the real modes whilst those with high values are the spurious modes.

Based on this phenomenon, Rahman and Davies [35] developed the so called *Penalty function* method. It is a useful way of imposing certain constraints on solution variables. The method has been used in structural engineering problems to impose specific boundary conditions. This method was used to successfully eliminate these spurious solutions in problems of microwave or optical waveguides; improving the quality of the field. In this approach, an additional integral is added to the variational formulation equation (3.22), which satisfies the condition $\nabla.\mathbf{H} = 0$. The penalty term can be thus written as [35]

$$\omega^2 = \frac{\int\left[(\nabla\times\mathbf{H})^*.\varepsilon^{-1}.(\nabla\times\mathbf{H})\partial\Omega + \left[\frac{\alpha}{\varepsilon_0}\right](\nabla\times\mathbf{H})^*.(\nabla.\mathbf{H})\right]\partial\Omega}{\int\mathbf{H}^*.\mu.\mathbf{H}\,d\Omega} \qquad (3.25)$$

where α is the dimensionless penalty number, the element matrix $[A]_e$ can be introduced in a separate subroutine to implement the additional penalty term in the numerator of the equation (3.25). The value of the penalty function α can be approximated as $1/\varepsilon_g$, where ε_g is the dielectric constant of the core guide. The advantage of using the penalty term is that it does not increase the matrix order and additional computational time is negligible. For higher values of the penalty coefficient a further reduction of spurious modes exists, but may deteriorate the accuracy of the eigenvalues.

3.9 Mathematical Formulation of FEM

Firstly, the FEM discretize the entire problem domain into a finite number of triangular sub-regions, called *elements*, so that the continuous field problem is reduced to finding fields at discrete nodes, where the unknown field values in only coupled to the field values of neighbouring nodes. Using many elements, we can approximate any continuum with a complex boundary and with an arbitrary index distribution so that an accurate analysis can be carried out. The field functions are defined by a set of algebraic polynomials over each element in the transverse plane, and longitudinal dependence $\exp(-j\beta z)$ is assumed, for given β.

3.9.1 Shape Function

For the approximation of the field over each element, it is important to consider a continuous function that is allowed to vary in a linear manner over the element region. The function varying is constrained by the fact that at the nodal points, the function should take values equal to the nodal values ϕ_1, ϕ_2 and ϕ_3. In this perspective, the functions have to be expressed in terms of its nodal values. These functions are referred to as the "*shape functions*".

The continuous field function $\phi(x,y)$ in the problem domain can be replaced by a set of discrete values ($\phi_i, i = 1,2,3,\ldots\ldots,m$), where m is the total number of nodes. Across the adjacent triangles this function will be continuous. For these functions to be

admissible, they must satisfy some conditions between the element; usually the continuity of the field across the boundaries is preferred.

For each first order triangular element, ϕ is interpolated continuously, this is shown in Fig. 3.4. This can be achieved by introducing the *nodal shape function (interpolation function)*, $N_i(x,y)$. When considering $\phi_k(x,y)$ to be the field inside the element, the interpolation functions for $i = 3$, can be represented as

$$\phi_k(x,y) = \sum_{i=1}^{3} N_i(x,y).\phi_i \tag{3.26}$$

where ϕ_i are the nodal field values. The equation (3.26) can also be represented in a matrix form as

$$\phi_k(x,y) = \begin{bmatrix} N_1 & N_2 & N_3 \end{bmatrix} \begin{Bmatrix} \phi_1 \\ \phi_2 \\ \phi_3 \end{Bmatrix} \tag{3.27}$$

therefore,

$$\phi_k(x,y) = [N]\{\phi_k\} \tag{3.28}$$

where N is referred to as the *shape function matrix* and ϕ_k is the vector corresponding to the element nodal field values at the three vertices of the triangular (i.e the nodal field values).

The first-degree polynomial ($a + bx + cy$) is used over each element for a simple first order triangular element. The element shape function can be represented in a matrix notation as

$$\{N\}^T = \begin{bmatrix} N_1 \\ N_2 \\ N_3 \end{bmatrix} = \frac{1}{2A_e} \begin{bmatrix} x_2y_3 - x_3y_2 & y_2 - y_3 & x_3 - x_2 \\ x_3y_1 - x_1y_3 & y_3 - y_1 & x_1 - x_3 \\ x_1y_2 - x_2y_1 & y_1 - y_2 & x_2 - x_1 \end{bmatrix} \begin{bmatrix} 1 \\ x \\ y \end{bmatrix} \tag{3.29}$$

where T denotes a transpose, x_1, x_2, x_3, y_1, y_2 *and* y_3 are the x and y coordinates of the three nodes respectively. A_e is the area of the triangular element given as

$$A_e = \frac{1}{2}\begin{vmatrix} 1 & x_1 & y_1 \\ 1 & x_2 & y_2 \\ 1 & x_3 & y_3 \end{vmatrix} = \frac{1}{2}\left(x_2y_3 - x_3y_2\right) + \left(x_3y_1 - x_1y_3\right) + \left(x_1y_2 - x_2y_1\right) \qquad (3.30)$$

The shape function matrix can also be written as

$$\{N\}^T = \begin{bmatrix} N_1 \\ N_2 \\ N_3 \end{bmatrix} = \begin{bmatrix} a_1 + b_1x + c_1y \\ a_2 + b_2x + c_2y \\ a_3 + b_3x + c_3y \end{bmatrix} \qquad (3.31)$$

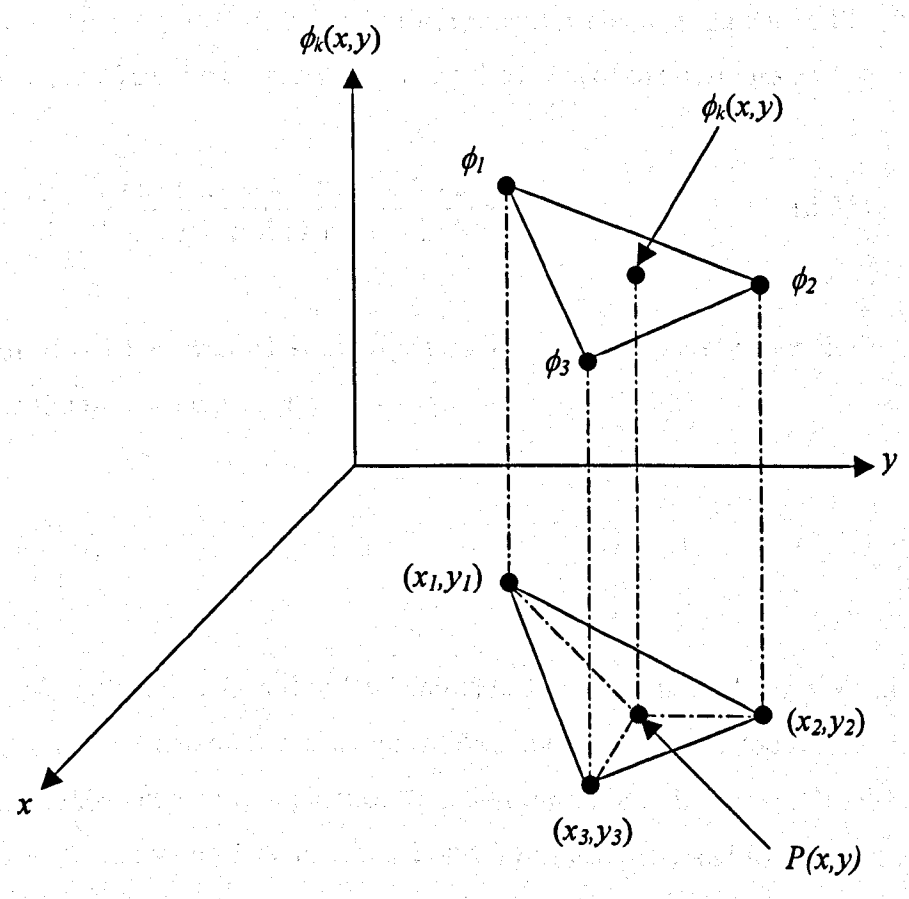

Fig. 3.4 The First-order triangular element showing the coordinates and node numbers.

With respect to equations (3.30) and (3.31), a_i, b_i, and c_i (i = 1,2,3) are constants, which are calculated as

$$a_1 = \frac{x_2 y_3 - x_3 y_2}{2A_e} \tag{3.32}$$

$$b_1 = \frac{y_2 - y_3}{2A_e} \tag{3.33}$$

$$c_1 = \frac{x_3 - x_2}{2A_e} \tag{3.34}$$

The values of a_2, b_2, c_2, a_3, b_3 and c_3 can be obtained by a cyclic exchange in equations (3.32), (3.33) and (3.34) simultaneously.

Also, if we consider a typical point inside the triangular element shown in Fig. 3.4. The shape functions N_i can be expressed by using the areas of the triangles as

$$N_1 = \frac{\text{area of the sub - triangle P - 2 - 3}}{\text{area of full triangle 1 - 2 - 3}} \tag{3.35}$$

N_2 and N_3 can also be expressed similarly, this yields immediately that the shape function N_i has the following property

$$\sum_{i=1}^{3} N_i = 1 \tag{3.36}$$

The shape function N_1 yields the value 1 when evaluated at the node 1 (x_1, y_1) and the value 0 at nodes 2 and 3 and all the other points passing through the nodes on the line. This is the unique first-degree interpolation function for node 1. In terms of the shape functions N_2 and N_3, the value 1 is at nodes 2 and 3 respectively, and the other nodes are 0.

3.9.2 Element and Global Matrices

The matrices **A** and **B** in equation (3.19*b*) are known as the *global matrices*, and are built up with triangular element matrices of the discretised cross section of the waveguide. The derivation of the element matrices based on the full vectorial **H**-field variational expression of equation (3.22) will be discussed in this section.

Considering each triangular element, the three unknown **H**-field components, H_x, H_y and H_z of the magnetic field can be written as

$$H_x(x,y) = [N_1 \quad N_2 \quad N_3] \begin{Bmatrix} H_{x_1} \\ H_{x_2} \\ H_{x_3} \end{Bmatrix} \tag{3.37}$$

$$H_y(x,y) = [N_1 \quad N_2 \quad N_3] \begin{Bmatrix} H_{y_1} \\ H_{y_2} \\ H_{y_3} \end{Bmatrix} \tag{3.38}$$

$$H_z(x,y) = [N_1 \quad N_2 \quad N_3] \begin{Bmatrix} H_{z_1} \\ H_{z_2} \\ H_{z_3} \end{Bmatrix} \tag{3.39}$$

where, H_{x_i}, H_{y_i} and H_{z_i} (i = 1,2,3) represents the x, y and z components of the nodal magnetic fields. The nodal magnetic field vector $[H]_e$ for each element can then be written as

$$[H_e] = \begin{bmatrix} H_x(x,y) \\ H_y(x,y) \\ H_z(x,y) \end{bmatrix} \tag{3.40}$$

$$[H_e]=\begin{bmatrix} N_1 & N_2 & N_3 & 0 & 0 & 0 & 0 & 0 & 0 \\ 0 & 0 & 0 & N_1 & N_2 & N_3 & 0 & 0 & 0 \\ 0 & 0 & 0 & 0 & 0 & 0 & N_1 & N_2 & N_3 \end{bmatrix} \begin{Bmatrix} H_{x_1} \\ H_{x_2} \\ H_{x_3} \\ H_{y_1} \\ H_{y_2} \\ H_{y_3} \\ H_{z_1} \\ H_{z_2} \\ H_{z_3} \end{Bmatrix} \tag{3.41}$$

Equation (3.41) can also be expressed as

$$[H]_e=[N]\{H\}_e \tag{3.42}$$

where $\{H\}_e$ is the column vector which contains the three components of the nodal field values of the element and $[N]$ is the shape function matrix.

The factor $(\nabla \times H)_e$ can be substituted in equation (3.42) to define each element, and can be written as

$$(\nabla \times H)_e = [\nabla]\times[N][H]_e = \begin{bmatrix} 0 & \frac{-\partial}{\partial z} & \frac{\partial}{\partial y} \\ \frac{\partial}{\partial z} & 0 & \frac{-\partial}{\partial x} \\ \frac{-\partial}{\partial y} & \frac{\partial}{\partial x} & 0 \end{bmatrix} [N]\{H\}_e = [Q]\{H\}_e \tag{3.43}$$

where the matrix $[Q]$ can be written as

$$[Q]=\begin{bmatrix} [0] & \frac{-\partial[N]}{\partial z} & \frac{\partial[N]}{\partial y} \\ \frac{\partial[N]}{\partial z} & [0] & \frac{-\partial[N]}{\partial x} \\ \frac{-\partial[N]}{\partial y} & \frac{\partial[N]}{\partial x} & [0] \end{bmatrix}=\begin{bmatrix} [0] & j\beta[N] & j\frac{\partial[N]}{\partial y} \\ -j\beta[N] & [0] & -j\frac{\partial[N]}{\partial x} \\ \frac{-\partial[N]}{\partial y} & \frac{\partial[N]}{\partial x} & [0] \end{bmatrix} \tag{3.44}$$

therefore

$$[0]=[0 \quad 0 \quad 0] \tag{3.45}$$

$$[N]=[N_1 \quad N_2 \quad N_3] \tag{3.46}$$

$$\frac{\partial[N]}{\partial x}=[b_1 \quad b_2 \quad b_3] \tag{3.47}$$

$$\frac{\partial[N]}{\partial y}=[c_1 \quad c_2 \quad c_3] \tag{3.48}$$

In equations (3.33) and (3.34) the coefficients of the shape functions b_1, b_2, b_3, c_1, c_2 and c_3 have been defined.

When an isotropic media is assumed and equations (3.42) and (3.43) are substituted in the variational expression equation (3.22) for an element, we obtain the following

$$J_e = \int_{\Omega}\{H\}_e^T[Q]^*\varepsilon^{-1}[Q]\{H\}_e d\Omega - \omega^2 \int_{\Omega}\{H\}_e^T[N]^T\mu[N]\{H\}_e d\Omega \tag{3.49}$$

the integration done over the element domain is represented by Ω, T and $*$ denotes the transpose and the complex conjugate transpose, respectively.

By summing J_e of all the elements, the total function, J, associated with the whole cross section of the waveguide can be obtained as

$$J = \sum_{e=1}^{n} J_e \tag{3.50}$$

When Rayleigh-Ritz procedure is employed in equation (3.50), (differentiating with respect to the nodal values and equating zero) i.e.,

$$\frac{\partial J}{\partial \{H\}_e} = 0 \qquad \textit{where, } e = 1,2,3.....,n$$

The following eigenvalue equation is obtained

$$[\mathbf{A}]\{H\} - \omega^2 [\mathbf{B}]\{H\} = 0 \tag{3.51}$$

where

$$[\mathbf{A}] = \sum_{e=1}^{n} [\mathbf{A}]_e = \sum_{e=1}^{n} \int_{\Omega} \varepsilon^{-1} [Q]^T [Q] d\Omega \tag{3.52}$$

$$[\mathbf{B}] = \sum_{e=1}^{n} [\mathbf{B}]_e = \sum_{e=1}^{n} \int_{\Omega} \mu [N]^T [N] d\Omega \tag{3.53}$$

$[\mathbf{A}]$ and $[\mathbf{B}]$ are the global matrices of the eigenvalue equation, while $[\mathbf{A}]_e$ and $[\mathbf{B}]_e$ represent the element matrices. Column matrix $\{H\}$ contains all **H**-field nodal values over the whole cross section of the waveguide structure. The evaluation of the elements $[\mathbf{A}]_e$ and $[\mathbf{B}]_e$ are shown in the Appendix 1.

3.10 The Infinite Elements

An infinite element is a finite element that indeed extends to infinity, and the shape functions for such an element should be realistic to represent the fields and should be square integrable over the infinite element area, to satisfy the radiation condition.

Open-type waveguide has the property of the finite fields existing in the region outside the guide. Outside the guide core, the field decays and the region of interest extends to infinity. The extension of the problem domain is significant for solutions near to cut-off, as the fields decay slowly and the region of significant field value can be arbitrarily large.

In an Orthodox finite element discretisation of the waveguide, as shown in Fig. 3.5, the region cannot be extended to infinity. Yeh *et al.*, [30] used boundary elements considering an exponential decay outside the guide core. Due to non-conformity of the two co-ordinate systems, the field used were not continuous. Mabaya [87] suggested an artificial electric or magnetic wall boundary condition to this problem, but it needs to consider large active domain to minimise the perturbation error or introduces a significant error. Another technique [94] involves shifting the virtual boundary wall to satisfy a given criterion for the maximum field strength at that wall. The recursion approach is another technique, which is used to generate the matrix representing the region outside the main domain. It is possible to find the internal and external solutions and match them on an imaginary boundary, some sort of integral solution being possible for the outside region [95].

Rahman and Davies [36] then developed a very useful and efficient approach which involves the extending the domain of interest to infinity keeping the same matrix value, as shown in Fig. 3.5. The method doesn't increase the order of the matrices and is quite simple to implement.

Elements can be extended in either or both transverse direction, when extending in one transverse direction, we consider an exponential shape function in that direction and conventional polynomial shape function in the other direction. For instance, as shown in Fig. 3.6, if an element is extending towards infinity in the x-direction, we can assume exponential decay in x and conventional shape function dependence in the y-direction. Thus, the shape function can be expressed as

$$N_i(x,y) = f_i(y).\exp(-x/L) \tag{3.54}$$

where, L is the decay length. The infinite elements extending towards the y-direction can be obtained by considering the exponential decay in y. Similarly, by assuming exponential decay in both x and y, we can consider a rectangular or quadrant element extending towards infinity in both x and y-directions. Integration of these shape functions or their derivatives over the infinite elements are finite, and can be easily carried out.

Lets assume any field component, for example, H_x, it can be written as

$$H_x = f(x,y)\,H_{x_i} = \sum_{i=1}^{2} N_i(x,y).H_{x_i} \tag{3.55}$$

$$H_x = f_1(y).e^{(-x/L)}.H_{x_1} + f_2(y).e^{(-x/L)}.H_{x_2} \tag{3.56}$$

$$H_x = \begin{bmatrix} N_1 & N_2 \end{bmatrix} \begin{Bmatrix} H_{x_1} \\ H_{x_2} \end{Bmatrix} \tag{3.57}$$

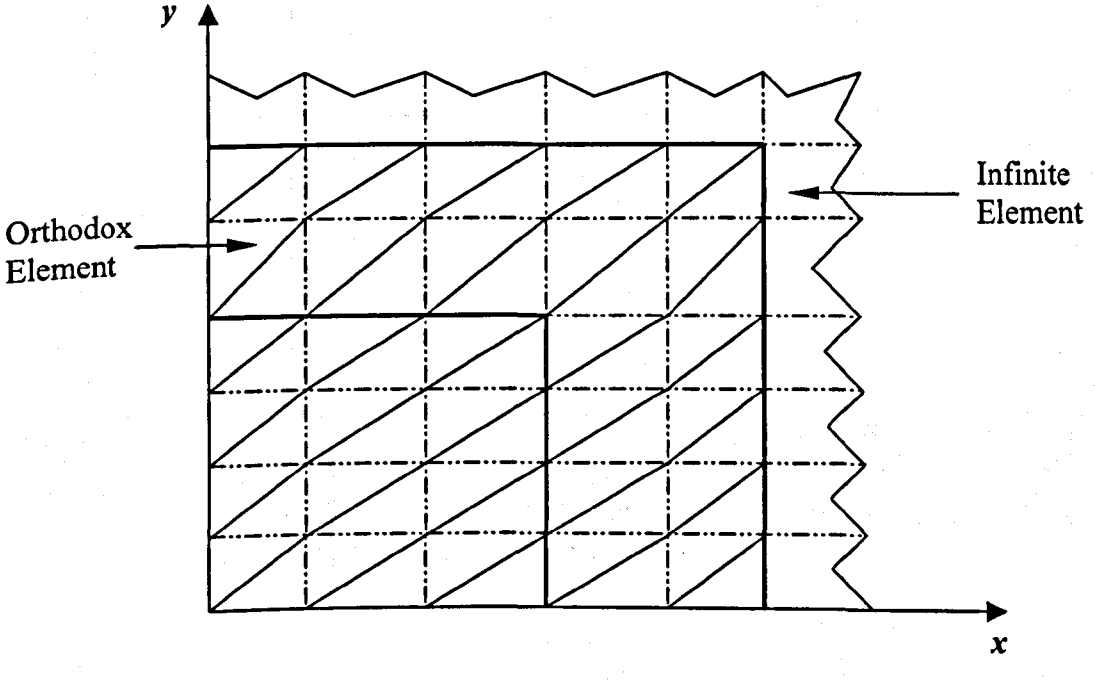

Fig. 3.5 Rectangular dielectric waveguide discretised into orthodox and infinite elements.

where H_{x_1} and H_{x_2} are the values of H_x at the nodes 1 and 2, respectively. In its simplest form, N_1 and N_2 can be expressed as

$$N_1 = \frac{y}{b} e^{(-x/L)} \tag{3.58}$$

$$N_2 = \left(1 - \frac{y}{b}\right) e^{(-x/L)} \tag{3.59}$$

where b is the width of the infinite element in the y-direction. Similarly, the other field components, H_y and H_z can be expressed in the same manner.

Indeed, combining all the infinite elements along with the conventional finite element, we can represent any open-type waveguide cross-sectional domain very conveniently with each field component being continuous over the whole infinite domain.

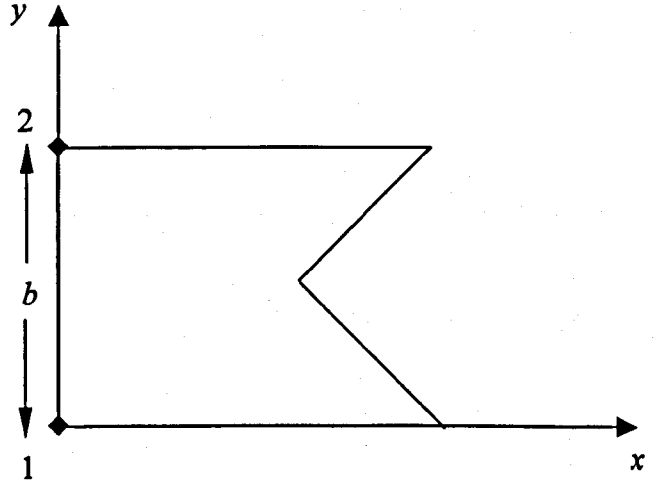

Fig. 3.6 Infinite Element of width b in the y direction and extending to infinity in the x direction.

3.11 Summary

The application of the finite element technique based on the vectorial principle for solving optical waveguide problems has been presented in this chapter. A brief history

of the method and the steps involved in the analysis of the technique has been described. The aspects involved including different scalar and vector formulations, natural boundary conditions, shape functions and infinite elements have also been detailed. Since the vector formulation suffers from the appearance of spurious solutions the use of the penalty function method was also discussed to eliminate these non-physical modes. This chapter incorporated with the beam propagation method presented in the next chapter forms the numerical basis for this research work for the analysis of optical waveguide problems involved in subsequent chapters.

4.0 The Beam Propagation Method

4.1 Introduction

One of the fundamental aspects in integrated optics is the analysis and simulation of electromagnetic wave propagation in photonics devices based on waveguide geometries, including optical waveguides. Most of the photonic integrated devices cannot be accurately analysed by simple analytical techniques. Also, even where analytical techniques are available, numerical techniques are employed to verify the designs before proceeding to invest serious effort in making new structures. In fact, numerical techniques are becoming increasingly available and user-friendly.

Optoelectronics is an emerged technology that combines the capability of photonics and microelectronics and has produced a diverse novel and useful devices for interconnections and telecommunications. The lack of powerful computerised design tools, though have made it difficult for engineering, manufacturing as well as research the development of optoelectronic devices for system applications. Development and engineering of optoelectronic devices follow a pattern of design, fabrication, characterisation and re-design process that is not adequate for optimisation and engineering of sophisticated optoelectronic devices to the desired specifications. Therefore, it is imperative to develop powerful computer-aided modelling and simulation tools that are efficient, robust and accurate.

In the previous chapter, the finite element method, which is useful in the modal solution of optical waveguide problems, has been discussed. But, this method is not capable of simulating how light is propagating and interacting with media in longitudinally non-uniform structures and for this purpose; researchers have developed various methods. For instance, the Beam Propagation Method (BPM), which is a step-by-step method of simulating the guidance of light through any waveguiding medium, allowing us to track the optical field at any point as it propagates along the guiding structures. The calculations are repeated for each step in a manner of step like calculation of the propagating field. The Beam Propagation

Method is a powerful modelling technique for optical wave-guiding structures. It is particularly useful for waveguides that change slowly in the propagation direction, although it has also been extended to structures with longitudinal interfaces.

4.2 Brief history of the Beam Propagation Method

Feit and Fleck first introduced the Beam propagation method for the study of fibre optics in 1978 [38,96] to calculate the mode properties of optical fibres. Ever since researchers have developed many other optical waveguide structures.

In 1983, Hermansson, Yevick and Danielsen [97] analysed tapers with a parabolic graded index transverse profile and various longitudinal profiles with the aid of the propagating beam method. With the implementation of both, analytical and numerical techniques, they described the optimal profiles for tapers and demonstrated the standard first-order local normal perturbation theory for such structures.

Danielsen [98], succeeded in reducing the three-dimensional problem of calculating the field distribution in an integrated optic circuit to a two-dimensional problem, which was solved by applying the propagating beam method. On the basis of his work he used a Y-branch electro-optic modulator as an example, which agreed with the pertubation theory.

The Beam Propagation Method was also employed to demonstrate the characteristics of active as well as passive integrated optics X-structures, both single mode and multimode, and it has been shown that the results were readily understood in terms of mode interference [99]. Since then many other optical waveguide structures such as the bends [100], gratings [101], fibre couplers [102,103] and non-linear directional couplers [104] have been analysed and modelled by using this method.

4.3 Overview of Propagation Algorithms

The Beam Propagation Method (BPM) is one of the most commonly used numerical methods for analysis and simulation of guided-wave propagation in axially non-uniform structure media. In the literature to formulate the BPM, basically, four numerical approaches have been presented. These approaches are

a) Fast Fourier Transform Method
b) Finite Difference Method
c) Modal Propagation Method
d) Finite Element Method

These four numerical approaches will be studied briefly in the following subsections outlining their respective advantages and disadvantages.

4.3.1 Fast Fourier Transform Beam Propagation Method

The Fast Fourier Transform Beam Propagation Method (FFT-BPM) is the first BPM algorithm. In this method, the optical propagation is modelled as a plane wave spectrum in the spatial frequency domain, and the effect of the medium inhomogeneity is interpreted as a correction of the phase in the spatial domain at each propagation step [38]. The use of the *fast Fourier techniques* connects the spatial and spectral domains, and this method is therefore called *Fast Fourier transform Beam Propagation Method* (FFT-BPM). This method is also referred to as *Split-Operator FFT-BPM* and can be expressed mathematically as

$$\psi(x,y,z+\Delta z) = PQP\psi(x,y,z) \tag{4.1}$$

where $\psi(x,y,z)$ and $\psi(x,y,z+\Delta z)$ are the field distributions at two subsequent propagation steps, P is a propagator which can be solved by the FFT, and Q is a phase correction.

The limitations of using the conventional FFT-BPM are

a) A paraxial approximation has been made in the derivation; therefore the FFT-BPM is accurate only when the beam propagates in the direction with a small angle to the z-axis.

b) The formulation of the method is under the assumption that the refractive index difference in the transverse directions is very small so that the phase error term can be expressed by the first term in a Taylor series. Therefore, structures with large index discontinuities that are a common feature in modern optoelectronics based on semiconductor materials FFT-BPM is difficult to solve.

c) The FFT-BPM cannot describe the vectorial properties such as the polarisation coupling and polarisation dependence of guided-wave devices as it can only trace the scalar wave propagation.

However the distinct advantages of the method are

a) It applies to a structure with an arbitrary cross section.

b) In the analysis both the guided and radiation waves are included. As long as input field is given, the FFT-BPM is capable of tracing the wave propagation in the given structure.

4.3.2 Finite Difference Beam Propagation Method

The beam propagation method that solves the paraxial form of the scalar wave equation in inhomogeneous medium using the finite difference method is called the *Finite Difference Beam Propagation Method* (FD-BPM). This requires choosing a computational window in the transverse dimension (x, y) as well as choosing a grid in the z-direction. The computational window must be large enough to contain the desired field distribution all along the propagation path.

However, since radiated fields can always be present, setting the field values to zero at the boundaries of the computational window can create difficulties. Since this boundary condition effectively creates a reflecting boundary, the radiated fields will reflect back and create spurious field distribution.

One way to eliminate this difficulty is to use absorbing boundaries. This is achieved by introducing an artificial complex index distribution around the computational window to generate a lossy boundary. The radiated fields are then absorbed before reaching the edge of the window [105].

Hedow and Shakir [106] developed a finite difference method beam propagation method to solve the paraxial wave equation by the finite difference method to improve the efficiency and flexibility. The original application of FD-BPM, though, has been limited to cylindrically symmetric structures. Chung and Dagli [39] introduced the FD-BPM to the Cartesian coordinate system.

Due to the limitations of the conventional FFT-BPM, some efforts has been made to adapt BPM to treat strongly guided waveguides [107-110]. For example, a split-step FD-BPM has been developed by Yevick and Hermanson [111,112] to stimulate strongly guiding semiconductor-based rib waveguides. Instead of using the FFT, they used the split-step FD-BPM to solve the propagator by the finite difference method. The conventional phase correction is still retained in the algorithm.

The numerical advantages of FD-BPM over the conventional FFT-BPM are

a) To stimulate integrated photonic devices the FD-BPM is clear, since it admits larger propagation steps, and also behaves quite well managing structures with large discontinuities in the refractive index.

b) If the computational window is reduced in such a way that the optical field reaches the computational boundaries, it is necessary to implement additional algorithms to avoid the optical fields reflecting at the boundaries and re-entering the computational window; otherwise, the simulation of the optical devices will not be correct. This problem can be adequately solved in the case of FD-BPM, but is cumbersome when using FFT-BPM.

c) For a given cross-section, the FD-BPM computation is proportional to the number of mesh points, N, instead of NlogN in FFT-BPM, therefore the number of mesh points, N, can be arbitrary number in

FD-BPM, while it is restricted to a power of 2 in the conventional FFT-BPM.

d) An additional advantage of FD-BPM, besides the lower memory and time consuming in modelling complex structures, is the possibility of incorporating wide-angle propagation and full vector algorithms [113,114].

Some researchers devoted on developing semi and full-vectorial beam propagation method algorithms based on the finite difference method. These propagation algorithms are capable of predicting the polarisation dependence and coupling of guided-wave optical devices, but, since they are based on finite difference scheme, they suffer the following shortcomings

a) The finite difference method suffers from inefficiency in the discretisation of the waveguide cross-section. They instead rely on uniform grids, which results in high computational efforts, and for curved boundaries, they present very crude approximation.

b) Some authors have noticed that if an arbitrary input field is used, for vectorial propagation algorithms based on finite differences, some unphysical gain (lossless structure is assumed) is observed during the propagation [115]. The explanation of the occurrence of the unphysical gain may be that the propagation matrices involved in the FD-BPM algorithms are complex non-Hermitian, which gives the chance to unphysical spurious modes to appear. Specifically, the inadequate description of the interface boundary conditions through truncated Taylor series expansion [116] may lead to that complex non-Hermitian propagation matrices, and hence to the unphysical gain effect.

4.3.3 Modal Propagation Method

Some analytical approaches have been proposed to describe the wave propagation in optical devices, since the FD-BPM needs a large computational effort. One of these is the Least Squares Boundary Residuals (LSBR) [117,118]. The LSBR method was introduced as an alternative to point-matching (and Galerkin) methods, satisfying the

boundary conditions in the usual least-squares sense over the interface. The method is rigorously convergent, the error minimization being global rather than sampled, and has the flexibility of introducing an electric/magnetic-weighting factor.

The LSBR method has been used to study scattering coefficients at the discontinuity planes. [119-121]. Other very similar approaches to LSBR have also been proposed [122,123]. All these approaches also depend on the same principle of matching the transverse electric and transverse magnetic field components using the conventional mode matching technique to treat problems of one- and two-dimensional dielectric waveguide discontinuities. Since these approaches basically, depend on expanding the field components in terms of the guided and/or radiation modes, they are termed as *Modal Propagation Methods.*

The advantages of these methods includes

a) They are very computationally efficient compared with the FD-BPM.
b) They are capable of determining the reflected waves which is not available in some of the FD-BPM algorithms.

On the other hand, accurate characterisation of optical devices using the modal propagation methods needs the determination of all guided and radiation modes. Finding the radiation modes using very powerful numerical methods like Vector **H**-field finite element method in one-dimensional problems is a difficult process and many radiation modes are needed to be found in order to get accurate numerical results.

For photonic devices which contain large number of discontinuities, like structures such as the tapered waveguide, numerically approximated by a series of very small longitudinal sections, the process of finding both the guided and radiation modes must be repeated at each propagation step. This situation will be more difficult when working with two-dimensional problems.

4.3.4 Finite Element Beam Propagation Method

The Finite Element Beam Propagation Method (FE-BPM) is a more computationally efficient propagation algorithm based on the finite element scheme, as an alternative to the conventional FFT-BPM and FD-BPM. In literature, Koch and Davies presented one of the first FE-BPM algorithms [124,125]. In their approach, a variational method is used to solve the scalar wave equation, under the paraxial approximation; with the finite element method applied to the transverse cross section and the finite difference Crank-Nicolson method applied to the longitudinal axis to propagation.
Koshiba [126,127] have presented a beam propagation method (BPM) based on the finite element method (FEM) for longitudinally varying three-dimensional (3-D) optical waveguides. In his approach, in order to avoid non-physical reflections from the computational window edges, the transparent boundary condition was introduced. Using the Pade approximation, a wide-angle finite element beam propagation method for 3-D waveguide structures was established. The FE-BPM was derived via the application of Galerkin's procedure, to solve the scalar wave equation.

All the FE-BPM algorithms explained above are solving scalar wave equations, hence, they are not adequate in predicting the polarisation properties and coupling of strongly guiding optical devices based on semiconductor materials.

Montanari, Selleri, Vincetti and Zoboli [128,129] presented a vectorial approach, which is based on the paraxial approximation, and also not using the rigorous absorbing boundary condition. This vectorial FE-BPM approach demands large computational effort and storage requirements for solving three magnetic field components.

Obayya, Rahman, and El-Mikati [43,130] presented a full-vectorial beam propagation algorithm based on the versatile-finite element method, in order to accurately characterize three-dimensional (3-D) optical guided-wave devices. The computationally efficient formulation was based on the two transverse components of the magnetic field without destroying the sparsity of the matrix equation. The robust perfectly matched layer (PML) boundary condition was incorporated into the formulation so as to effectively absorb the unwanted radiation out of the

computational domain. In this Chapter this particular finite element beam propagation formulation will be discussed and presented.

Indeed, the finite element method has some advantages, when it comes to discretisation, over the FD and/or FFT schemes. These methods are inefficient in the discretisation of the transverse section relying on rectangular, and often even uniform, grids. In contrast, the finite elements, allow a better description of curved geometrics and an efficient distribution of nodal points; furthermore they permit adaptive techniques to be used and allows one to deal with media with high index step.

The advantages of the vectorial FE-BPM considered in this work are

a) Ability to solve only for the transverse components of the magnetic field; hence it minimises the computational effort and the storage requirements.
b) Wide-angle approximation; hence it is capable of tracking waves propagating off the propagation axis.
c) Rigorous perfectly matched layer boundary condition.

4.4 Perfectly Matched Layer Boundary Condition

Due to the fact that the computational domain in BPM calculations is finite, it is necessary to specify boundary conditions for the optical field at the limits of the computational window. These boundary conditions must be adequately chosen, in such a way that the effect of the boundaries does not introduce errors in the propagation description of the optical field. If these conditions are not well specified, the radiation tends to reflect on the limits of the computational window and comes back to the region of interest, and unwanted interference is produced when the propagation is performed by FD-BPM. In the case of wave propagation based on FFT-BPM, the results is the disappearance of the optical field through a boundary, but the appearance of a new perturbation from the opposite window boundary.

The most common way of preventing boundary reflection using FFT-BPM is the insertion of artificial absorption regions adjacent to the pertinent boundaries [38,131]. Usually, the absorption coefficient is ramped from zero at the region's leading edge to some maximum value at the boundary node. Thus, the thickness of the region, the maximum absorption coefficient, and the functional shape must all be carefully chosen for the method to work properly. However, if the gradient in the absorption coefficient is too large, that gradient itself will generate reflections. Although the artificial absorption procedure is accurate provided that the absorption region is adequately tailored, ensuring that this condition is fulfilled for each new problem is often difficult and time-consuming process. Even when successful, the addition of extra problem zones results in computational penalties of run-time and storage space.

When using FD-BPM for simulating optical propagation we find that the field at points $j = 0$ and $j = N + 1$ are not defined, but are necessary for calculating the field in the interior points ($j = 1$ *to* N), and we need two extra equations to determine them. *Dirichlet* boundary conditions provide the simplest possibility by specifying the boundary values μ_0 and μ_{N+1} directly, for instance by setting their value to zero; other possibilities are the *Neumann* or even the *periodic* boundary conditions [132].

Unfortunately, none of these boundary conditions gives satisfactory results, and the implementation causes optical field "reflections" at the window limits, because the condition of zero field at the boundaries is not realistic when the optical perturbation reaches the limits of the computational window. One alternative to this dilemma consists in trying to implement realistic boundary conditions from a physical point of view, that is, an algorithm that allows the wave to leave the computational region when it reaches the window limits, without any reflection coming back to the domain. This algorithm is known as *transparent boundary condition* (TBC), and simulates a non-existent boundary [105,133]. Radiation is allowed to freely escape the problem region without appreciable reflection, whereas radiation flux back into the region is prevented. This TBC employs no adjustable parameters, and thus is problem independent, and can be directly applied to any waveguide structure. In addition, it is easily incorporated into a standard Crank-Nicolson differencing scheme in both two

and three dimensions, and it is applicable to longitudinally varying structures of importance for integrated photonic devices [133].

In TBC, the idea is to approximate the wave near the boundary of the computational domain as a plane wave, which satisfies

$$\frac{\partial \phi}{\partial \rho} = -jk\phi \tag{4.2}$$

where ϕ is the field near the boundary, k is the transverse wave-vector and ρ is the distance in the direction normal to the boundary. However, for TBC, the plane wave approximation of the outgoing wave near the boundary is not sufficient to suppress large radiation. Also, some numerical instability will occur, when many field values inside the computational domain are involved in estimating k [134,135].

Berenger [136] has introduced the concept of the Perfectly Matched Layer (PML) as an alternative to the absorbing or transparent boundary conditions. The objective was to synthesise an absorbing layer for the Finite Difference Time Domain (FDTD) method. The PML concept has been successfully applied in one- dimensional FD-BPM [137] and has proved to be more robust than the transparent boundary condition.

The original form of PML introduced by Berenger needs the splitting of the field components into two sub-components. When this happens, it leads to non-Maxwell's equations, which is not the desired form for the application of finite elements. Pekel and Mittra [138,139] have introduced a new form of the PML, for treating free space scattering problems, which does not involve the field splitting, maintaining the desired form of the Maxwell's equation for the finite element application.

Obayya, Rahman and El-Mikati [43], incorporated the robust perfectly matched layer (PML) boundary condition into the finite element based BPM formulations, but either considering a simple scalar formulation [140] or the E-field formulation [141], which considers all the three field components. In this approach, the sparsity of the global matrices is retained, as no matrix inversion is needed, hence, a numerically efficient sparse matrix solver is used which is the main advantage of the present formulation.

The PML boundary condition effectively absorbs the unwanted radiation waves without reflection. The PML form has been introduced into the vectorial FE-BPM equations.

Consider the optical waveguide cross section as shown in Fig. 4.1, where x and y are the transverse directions, regions Ω_1 and Ω_2 are the PML regions normally faced with x and y directions, respectively, regions Ω_3 corresponds to the four corners of the PML, z is the direction of propagation, Ω corresponds to the computational domain region, W is the width (or height) of the PML, and W_x and H_y are the width and height of the computational domain in the x and y directions, respectively.

With PML form, Maxwell's curl equations can take the form

$$\nabla \times H = \varepsilon \frac{\partial E}{\partial t} + J \tag{4.3}$$

$$\nabla \times E = -\mu \frac{\partial H}{\partial t} \tag{4.4}$$

Lets assume the time dependence to be exp ($j\omega t$), where j is the imaginary part, ω is the angular frequency (radians), and t is the time, for convenience purposes. Thus the differential form of Maxwell's equations can be written as

$$\nabla \times H = j\omega \varepsilon_o n^2 E \tag{4.5}$$

$$\nabla \times E = -j\omega \mu_o H \tag{4.6}$$

where E and H are the electric and magnetic field vectors, respectively, n^2 is the square of the refractive index, and ∇ is the modified differential operator defined as

$$\nabla = x\alpha_x \frac{\partial}{\partial x} + y\alpha_y \frac{\partial}{\partial y} + z\frac{\partial}{\partial z} \tag{4.7}$$

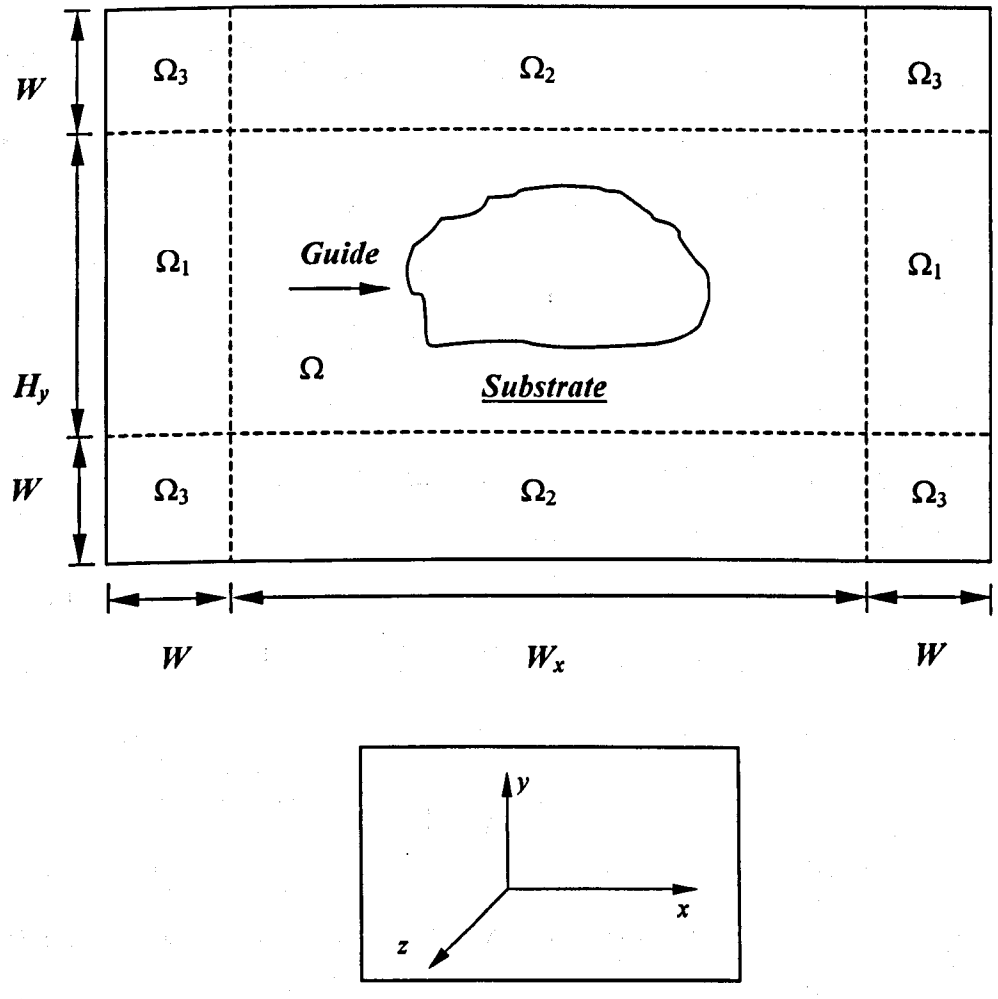

Fig. 4.1 Different PML regions along an optical waveguide cross-section.

where

$$\alpha_t(t = x \text{ or } y) = \frac{1}{1 - j\dfrac{\sigma_e}{\omega\varepsilon_o n^2}} = \frac{1}{1 - j\dfrac{\sigma_m}{\omega\mu_o}} \tag{4.8}$$

In this case σ_e and σ_m are the electric and magnetic conductivities of the PML, respectively. The equation (4.8) shows that the PML satisfies the impedance matching

condition with an adjacent medium in the computational domain with refractive index n and wave impedance $\sqrt{\frac{\mu_o}{\varepsilon_o n^2}}$.

In the regions the values of the parameters α_x and α_y are defined as

a) region Ω (computational domain)

$\alpha_x = 1$ and $\alpha_y = 1$

b) region Ω_1

$\alpha_x = \alpha_t$ and $\alpha_y = 1$

c) region Ω_2

$\alpha_x = 1$ and $\alpha_y = \alpha_t$

d) region Ω_3

$\alpha_x = \alpha_t$ and $\alpha_y = \alpha_t$

The electric conductivity profile can be assumed as

$$\sigma_e(\rho) = \sigma_{\max}\left[\frac{\rho}{W}\right]^m \tag{4.9}$$

ρ is the distance inside the PML, which is measured from the interface of the computational domain and the PML, σ_{max} is the maximum value of the electric conductivity, and m is the power of the conductivity profile and will be taken as 2. For this conductivity profile, the theoretical reflection coefficient, R, at the interface between the PML and the computational domain is [137]

$$R = exp\left[-2\frac{\sigma_{\max}}{cn\varepsilon_o}\int_0^W\left(\frac{\rho}{W}\right)^2 \partial\rho\right] \tag{4.10}$$

where c is the velocity of light in free space. Integrating equation (4.10), σ_{max} can be given as

$$\sigma_{max} = \frac{3cn\varepsilon_o}{2d} \ln\left(\frac{1}{R}\right) \tag{4.11}$$

When the value of the theoretical coefficient is chosen, R (set to very small value), the maximum electric conductivity, σ_{max}, is calculated using the equation (4.11). The electric conductivity profile $\sigma(\rho)$ and the PML parameters α_x and α_y will be determined for the different PML areas. Such PML arrangements will force any non-physical radiation wave leave freely the computational domain whatever the angle and/or the strength it hits the boundary of the computational domain.

4.5 The Wave Equations

When considering Maxwell's curl equations (4.5) and (4.6), to derive the vectorial wave equations. Taking the curl equation (4.5) and using equation (4.6) yields [40]

$$\nabla \times \left(n^{-2} \nabla \times \boldsymbol{H}\right) - k_0^2 \boldsymbol{H} = 0 \tag{4.12}$$

k_o is the free space wavenumber and is given as

$$k_0 = \omega\sqrt{\mu_o \varepsilon_o} = \frac{2\pi}{\lambda} \tag{4.13}$$

where λ is the free space wavelength. The full vectorial wave equation shown in equation (4.12) contains the three components of the magnetic field vector, $\boldsymbol{H}$. By the use of the zero divergence condition this wave equation can be reduced to only the two transverse components, i.e., H_x or H_y as

$$\alpha_x \frac{\partial H_x}{\partial x} + \alpha_y \frac{\partial H_y}{\partial y} + \frac{\partial H_z}{\partial z} = 0 \tag{4.14}$$

Substituting equation (4.14) into equation (4.12) gives the following two coupled wave equations

$$\frac{\partial}{\partial z}\left(n^{-2}\frac{\partial H_x}{\partial z}\right)+\alpha_y\frac{\partial}{\partial y}\left(n^{-2}\alpha_y\frac{\partial H_x}{\partial y}\right)+n^{-2}\alpha_x\frac{\partial}{\partial x}\left(\alpha_x\frac{\partial H_x}{\partial x}\right)+$$

$$k_0^2H_x+n^{-2}\alpha_x\frac{\partial}{\partial x}\left(\alpha_y\frac{\partial H_y}{\partial y}\right)-\alpha_y\frac{\partial}{\partial y}\left(n^{-2}\alpha_x\frac{\partial H_y}{\partial x}\right)=0 \qquad (4.15)$$

$$\frac{\partial}{\partial z}\left(n^{-2}\frac{\partial H_y}{\partial z}\right)+\alpha_x\frac{\partial}{\partial x}\left(n^{-2}\alpha_x\frac{\partial H_y}{\partial x}\right)+n^{-2}\alpha_y\frac{\partial}{\partial y}\left(\alpha_y\frac{\partial H_y}{\partial y}\right)+$$

$$k_0^2H_y+n^{-2}\alpha_y\frac{\partial}{\partial y}\left(\alpha_x\frac{\partial H_x}{\partial x}\right)-\alpha_x\frac{\partial}{\partial x}\left(n^{-2}\alpha_y\frac{\partial H_x}{\partial y}\right)=0 \qquad (4.16)$$

The assumption that the refractive index is slowly varying in the direction of propagation $\left(\frac{\partial n^{-2}}{\partial z}\right)=0$, has been made in deriving the wave equations (4.15) and (4.16). Solving equations (4.15) and (4.16) is more convenient than equation (4.12), because it has a less number of unknown components and also because the zero divergence condition is automatically satisfied through the derivation, thus, there is no possibility for spurious solutions to propagate. Assuming the wave travels along the $+z$ direction, the fields can be separated as slowly varying envelopes and a fast-oscillating phase term as

$$\begin{Bmatrix}H_x\\H_y\end{Bmatrix}=\begin{Bmatrix}\psi_x\\\psi_y\end{Bmatrix}\exp(-jn_0k_0z) \qquad (4.17)$$

ψ_x and ψ_y are the slowly-varying envelopes of the H_x and H_y components, respectively and n_0 is a reference index of refraction which should be chosen such that the envelope varies very slowly in the $+z$ direction. For this purpose, n_0 should be chosen very close to the effective index of the guided mode(s) of the concerned structures. In case of monomode waveguides, n_0 can be set equal to the effective index of the

fundamental mode. But, for multimode waveguides, the situation will be complicated, as the effective indices of all guided modes have to be determined in order to set n_0 to the proper value. In this particular case, a better approximation is to set n_0 as the average of the guide and substrate refractive indices [142].

The following two coupled unidirectional wave equations will be obtained when substituting equation (4.17) into equations (4.15) and (4.16);

$$n^{-2}\frac{\partial^2\psi_x}{\partial^2 z^2}-2jn_0k_0n^{-2}\frac{\partial\psi_x}{\partial z}+\alpha_y\frac{\partial}{\partial y}\left(n^{-2}\alpha_y\frac{\partial\psi_x}{\partial y}\right)+n^{-2}\alpha_x\frac{\partial}{\partial x}\left(\alpha_x\frac{\partial\psi_x}{\partial x}\right)+$$

$$+k_0^2\left(1-n^{-2}n_0^2\right)\psi_x+n^{-2}\alpha_x\frac{\partial}{\partial x}\left(\alpha_y\frac{\partial\psi_y}{\partial y}\right)-\alpha_y\frac{\partial}{\partial y}\left(n^{-2}\alpha_x\frac{\partial\psi_y}{\partial x}\right)=0 \qquad (4.18)$$

$$n^{-2}\frac{\partial^2\psi_y}{\partial^2 z^2}-2jn_0k_0n^{-2}\frac{\partial\psi_y}{\partial z}+\alpha_x\frac{\partial}{\partial x}\left(n^{-2}\alpha_x\frac{\partial\psi_y}{\partial x}\right)+n^{-2}\alpha_y\frac{\partial}{\partial y}\left(\alpha_y\frac{\partial\psi_y}{\partial y}\right)+$$

$$+k_0^2\left(1-n^{-2}n_0^2\right)\psi_y+n^{-2}\alpha_y\frac{\partial}{\partial y}\left(\alpha_x\frac{\partial\psi_x}{\partial x}\right)-\alpha_x\frac{\partial}{\partial x}\left(n^{-2}\alpha_y\frac{\partial\psi_x}{\partial y}\right)=0 \qquad (4.19)$$

The following section of this chapter will use equations (4.18) and (4.19) to solve the slowly varying envelope by the application of the finite element method.

4.6 Formulation of the Finite Elements

Lets assume that the waveguide cross section shown in Fig. 4.1 is discretised into a patchwork of first order triangular elements. Considering equations (4.18) and (4.19), the application of the standard Galerkin's procedure gives

$$\int_e n^{-2}\frac{\partial^2\psi_x}{\partial z^2}N_i ds - \int_e 2jn_0k_0n^{-2}\frac{\partial\psi_x}{\partial z}N_i ds + \int_e \alpha_y^2\frac{\partial}{\partial y}\left(n^{-2}\frac{\partial\psi_x}{\partial y}\right)N_i ds +$$

$$\int_e \alpha_x^2 n^{-2}\frac{\partial^2\psi_x}{\partial x^2}N_i ds + \int_e k_0^2(1-n^{-2}n_0^2)\psi_x N_i ds + \int_e \alpha_x\alpha_y n^{-2}\frac{\partial^2\psi_y}{\partial x\partial y}N_i ds -$$

$$\int_e \alpha_x\alpha_y\frac{\partial}{\partial y}\left(n^{-2}\frac{\partial\psi_y}{\partial x}\right)N_i ds = 0 \qquad (4.20)$$

$$\int_e n^{-2}\frac{\partial^2\psi_y}{\partial z^2}N_i ds - \int_e 2jn_0k_0n^{-2}\frac{\partial\psi_y}{\partial z}N_i ds + \int_e \alpha_x^2\frac{\partial}{\partial x}\left(n^{-2}\frac{\partial\psi_y}{\partial x}\right)N_i ds +$$

$$\int_e \alpha_y^2 n^{-2}\frac{\partial^2\psi_y}{\partial y^2}N_i ds + \int_e k_0^2(1-n^{-2}n_0^2)\psi_y N_i ds + \int_e \alpha_x\alpha_y n^{-2}\frac{\partial^2\psi_x}{\partial x\partial y}N_i ds -$$

$$\int_e \alpha_x\alpha_y\frac{\partial}{\partial x}\left(n^{-2}\frac{\partial\psi_x}{\partial y}\right)N_i ds = 0 \qquad (4.21)$$

N_i are the shape functions with i = 1,2,3 over the first order triangular element, e, and $\int_e (.)\,ds$ stands for the integration over the element area. In writing equations (4.20) and (4.21), it has been assumed that the refractive index, n, and the PML parameters, α_x and α_y, are fixed to constant values within each element. Thus, for step index waveguides, the discontinuity of the refractive index and the associated interface boundary conditions will not be accounted for. Therefore, by using the Green's theorem for integration by parts will result in line integrations, around each element, which can be used to satisfy the following interface boundary conditions

a) Continuity of E_z,

$$E_z \propto n^{-2}\left(\frac{\partial\psi_y}{\partial x} - \frac{\partial\psi_x}{\partial y}\right)$$

b) Discontinuity of $n^{-2}\frac{\partial \psi_x}{\partial x}$ and $n^{-2}\frac{\partial \psi_y}{\partial y}$ along the horizontal and vertical interfaces between two different media.

Using the Green's theorem for integration by parts and applying it to equations (4.20) and (4.21) taking the above interface boundary conditions into consideration yields

$$\int_e n^{-2}\frac{\partial^2 \psi_x}{\partial z^2}N_i ds - 2jn_0k_0\int_e n^{-2}\frac{\partial \psi_x}{\partial z}N_i ds - \int_e \alpha_y^2 n^{-2}\frac{\partial \psi_x}{\partial y}\frac{\partial N_i}{\partial y}ds - \int_e \alpha_x^2 n^{-2}\frac{\partial \psi_x}{\partial x}\frac{\partial N_i}{\partial x}ds +$$

$$\oint_{\Gamma_e}\alpha_x^2 n^{-2}\frac{\partial \psi_x}{\partial x}N_i n_x d\Gamma_e + \int_e k_0^2\left(1-n^{-2}n_0^2\right)\psi_x N_i ds - \int_e \alpha_x\alpha_y n^{-2}\frac{\partial \psi_y}{\partial y}\frac{\partial N_i}{\partial x}ds +$$

$$\oint_{\Gamma_e}\alpha_x\alpha_y n^{-2}\frac{\partial \psi_y}{\partial y}N_i n_x d\Gamma_e + \int_e \alpha_x\alpha_y n^{-2}\frac{\partial \psi_y}{\partial x}\frac{\partial N_i}{\partial y}ds = 0 \qquad (4.22)$$

$$\int_e n^{-2}\frac{\partial^2 \psi_y}{\partial z^2}N_i ds - 2jn_0k_0\int_e n^{-2}\frac{\partial \psi_y}{\partial z}N_i ds - \int_e \alpha_x^2 n^{-2}\frac{\partial \psi_y}{\partial x}\frac{\partial N_i}{\partial x}ds - \int_e \alpha_y^2 n^{-2}\frac{\partial \psi_y}{\partial y}\frac{\partial N_i}{\partial y}ds +$$

$$\oint_{\Gamma_e}\alpha_y^2 n^{-2}\frac{\partial \psi_y}{\partial y}N_i n_y d\Gamma_e + \int_e k_0^2\left(1-n^{-2}n_0^2\right)\psi_y N_i ds - \int_e \alpha_y\alpha_x n^{-2}\frac{\partial \psi_x}{\partial y}\frac{\partial N_i}{\partial x}ds +$$

$$\oint_{\Gamma_e}\alpha_x\alpha_y n^{-2}\frac{\partial \psi_x}{\partial x}N_i n_y d\Gamma_e + \int_e \alpha_x\alpha_y n^{-2}\frac{\partial \psi_x}{\partial y}\frac{\partial N_i}{\partial x}ds = 0 \qquad (4.23)$$

where n_x and n_y represent the direction cosines between the normal element boundary Γ_e and the x and y directions, respectively, and $\oint_{\Gamma_e}(.)d\Gamma_e$ represents the line integration around the element boundary, Γ_e. The line integrals in equations (4.22) and (4.23), introduced to account for the interface boundary conditions, are also responsible for the coupling and polarisation dependence. In order to get a true vectorial formulation, the inclusion of these integral into the formulation is

mandatory. Over each element, e, and in terms of the shape functions, N_j, the transverse magnetic field envelopes can be represented as

$$\psi_x^e(x,y,z)=\sum_{j=1}^{3}h_{xj}(z)N_j(x,y) \tag{4.24}$$

$$\psi_y^e(x,y,z)=\sum_{j=1}^{3}h_{yj}(z)N_j(x,y) \tag{4.25}$$

where $h_{xj}(z)$ and $h_{yj}(z)$ express the element nodal values of the x and y components of the magnetic field, respectively, at any propagation distance. Substituting equations (4.24) and (4.25) into equations (4.22) and (4.23) and collecting the contribution from all the elements gives

$$[M]\frac{d^2\{h_t\}}{dz^2}-2jn_0k_0[M]\frac{d\{h_t\}}{dz}+\left([K]-n_0^2k_0^2[M]\right)\{h_t\}=\{0\} \tag{4.26}$$

where $\{0\}$ is a column vector with all zero entries, and

$$\{h_t\}=\begin{Bmatrix}h_x(z)\\h_y(z)\end{Bmatrix}=\sum_e\begin{Bmatrix}h_{x1}\\h_{x2}\\h_{x3}\\h_{y1}\\h_{y2}\\h_{y3}\end{Bmatrix} \tag{4.27}$$

where $h_x(z)$ and $h_y(z)$ are the nodal values of the x and y components of the magnetic field over the whole domain. The global matrices $[M]$ and $[K]$ can be represented as a summation of the corresponding matrices as

$$[M]=\sum_e[M]_e=\sum_e\begin{bmatrix}[M_{xx}] & [0]\\ [0] & [M_{yy}]\end{bmatrix} \tag{4.28}$$

$$[K]=\sum_e [K]_e=\sum_e \begin{bmatrix} [K_{xx}] & [K_{xy}] \\ [K_{yx}] & [K_{yy}] \end{bmatrix} \tag{4.29}$$

where $\sum_e$ represents the contribution of all element matrices $[M]_e$ and $[K]_e$ into the global ones and $[0]$ is a 3×3 zero matrix. The matrices $[M_{xx}]$ and $[M_{yy}]$ have the same form as

$$[M_{xx}]=[M_{yy}]=n^{-2}\begin{bmatrix} \int_e N_1^2 ds & \int_e N_1 N_2 ds & \int_e N_1 N_3 ds \\ \int_e N_2 N_1 ds & \int_e N_2^2 ds & \int_e N_2 N_3 ds \\ \int_e N_3 N_1 ds & \int_e N_3 N_2 ds & \int_e N_3^2 ds \end{bmatrix} \tag{4.30}$$

Also, matrices $[K_{xx}]$ and $[K_{yy}]$ can be expressed in the form

$$[K_{xx}]=[K_{tt}]+[K_{xx}]_{\Gamma_e} \tag{4.31}$$

$$[K_{yy}]=[K_{tt}]+[K_{yy}]_{\Gamma_e} \tag{4.32}$$

where

$$[K_u] = k_0^2 \begin{bmatrix} \int_e N_1^2 ds & \int_e N_1 N_2 ds & \int_e N_1 N_3 ds \\ \int_e N_2 N_1 ds & \int_e N_2^2 ds & \int_e N_2 N_3 ds \\ \int_e N_3 N_1 ds & \int_e N_3 N_2 ds & \int_e N_3^2 ds \end{bmatrix} - n^{-2}\alpha_y^2 \begin{bmatrix} \int_e N_{1y}^2 ds & \int_e N_{1y} N_{2y} ds & \int_e N_{1y} N_{3y} ds \\ \int_e N_{2y} N_{1y} ds & \int_e N_{2y}^2 ds & \int_e N_{2y} N_{3y} ds \\ \int_e N_{3y} N_{1y} ds & \int_e N_{3y} N_{2y} ds & \int_e N_{3y}^2 ds \end{bmatrix}$$

$$- n^{-2}\alpha_x^2 \begin{bmatrix} \int_e N_{1x}^2 ds & \int_e N_{1x} N_{2x} ds & \int_e N_{1x} N_{3x} ds \\ \int_e N_{2x} N_{1x} ds & \int_e N_{2x}^2 ds & \int_e N_{2x} N_{3x} ds \\ \int_e N_{3x} N_{1x} ds & \int_e N_{3x} N_{2x} ds & \int_e N_{3x}^2 ds \end{bmatrix} \tag{4.33}$$

where N_{ix} and N_{iy} denotes the x and y derivatives of the shape function N_i, respectively. The matrices $[K_{xx}]_{\Gamma_e}$ and $[K_{yy}]_{\Gamma_e}$ are related to the line integrals and expressed as

$$[K_{xx}]_{\Gamma_e} = n^{-2}\alpha_x^2 \begin{bmatrix} \oint_{\Gamma_e} N_1 N_{1x} n_x d\Gamma_e & \oint_{\Gamma_e} N_1 N_{2x} n_x d\Gamma_e & \oint_{\Gamma_e} N_1 N_{3x} n_x d\Gamma_e \\ \oint_{\Gamma_e} N_2 N_{1x} n_x d\Gamma_e & \oint_{\Gamma_e} N_2 N_{2x} n_x d\Gamma_e & \oint_{\Gamma_e} N_2 N_{3x} n_x d\Gamma_e \\ \oint_{\Gamma_e} N_3 N_{1x} n_x d\Gamma_e & \oint_{\Gamma_e} N_3 N_{2x} n_x d\Gamma_e & \oint_{\Gamma_e} N_3 N_{3x} n_x d\Gamma_e \end{bmatrix} \tag{4.34}$$

$$[K_{yy}]_{\Gamma_e} = n^{-2}\alpha_y^2 \begin{bmatrix} \oint_{\Gamma_e} N_1 N_{1y} n_y d\Gamma_e & \oint_{\Gamma_e} N_1 N_{2y} n_y d\Gamma_e & \oint_{\Gamma_e} N_1 N_{3y} n_y d\Gamma_e \\ \oint_{\Gamma_e} N_2 N_{1y} n_y d\Gamma_e & \oint_{\Gamma_e} N_2 N_{2y} n_y d\Gamma_e & \oint_{\Gamma_e} N_2 N_{3y} n_y d\Gamma_e \\ \oint_{\Gamma_e} N_3 N_{1y} n_y d\Gamma_e & \oint_{\Gamma_e} N_3 N_{2y} n_y d\Gamma_e & \oint_{\Gamma_e} N_3 N_{3y} n_y d\Gamma_e \end{bmatrix} \tag{4.35}$$

Also, the matrices $[K_{xy}]$ and $[K_{yx}]$ can be represented as

$$[K_{xy}] = [K_1] - [K_2] + [K_{xy}]_{\Gamma_e} \tag{4.36}$$

$$[K_{yx}] = [K_2] - [K_1] + [K_{yx}]_{\Gamma_e} \tag{4.37}$$

where

$$[K_1] = n^{-2}\alpha_x\alpha_y \begin{bmatrix} \int_e N_{1y}N_{1x}ds & \int_e N_{1y}N_{2x}ds & \int_e N_{1y}N_{3x}ds \\ \int_e N_{2y}N_{1x}ds & \int_e N_{2y}N_{2x}ds & \int_e N_{2y}N_{3x}ds \\ \int_e N_{3y}N_{1x}ds & \int_e N_{3y}N_{2x}ds & \int_e N_{3y}N_{3x}ds \end{bmatrix} \tag{4.38}$$

$$[K_2] = n^{-2}\alpha_x\alpha_y \begin{bmatrix} \int_e N_{1x}N_{1y}ds & \int_e N_{1x}N_{2y}ds & \int_e N_{1x}N_{3y}ds \\ \int_e N_{2x}N_{1y}ds & \int_e N_{2x}N_{2y}ds & \int_e N_{2x}N_{3y}ds \\ \int_e N_{3x}N_{1y}ds & \int_e N_{3x}N_{2y}ds & \int_e N_{3x}N_{3y}ds \end{bmatrix} \tag{4.39}$$

$$[K_{xy}]_{\Gamma_e} = n^{-2}\alpha_x\alpha_y \begin{bmatrix} \oint_{\Gamma_e} N_1N_{1y}n_x d\Gamma_e & \oint_{\Gamma_e} N_1N_{2y}n_x d\Gamma_e & \oint_{\Gamma_e} N_1N_{3y}n_x d\Gamma_e \\ \oint_{\Gamma_e} N_2N_{1y}n_x d\Gamma_e & \oint_{\Gamma_e} N_2N_{2y}n_x d\Gamma_e & \oint_{\Gamma_e} N_2N_{3y}n_x d\Gamma_e \\ \oint_{\Gamma_e} N_3N_{1y}n_x d\Gamma_e & \oint_{\Gamma_e} N_3N_{2y}n_x d\Gamma_e & \oint_{\Gamma_e} N_3N_{3y}n_x d\Gamma_e \end{bmatrix} \tag{4.40}$$

$$[K_{yx}]_{\Gamma_e} = n^{-2}\alpha_x\alpha_y \begin{bmatrix} \oint_{\Gamma_e} N_1N_{1x}n_y d\Gamma_e & \oint_{\Gamma_e} N_1N_{2x}n_y d\Gamma_e & \oint_{\Gamma_e} N_1N_{3x}n_y d\Gamma_e \\ \oint_{\Gamma_e} N_2N_{1x}n_y d\Gamma_e & \oint_{\Gamma_e} N_2N_{2x}n_y d\Gamma_e & \oint_{\Gamma_e} N_2N_{3x}n_y d\Gamma_e \\ \oint_{\Gamma_e} N_3N_{1x}n_y d\Gamma_e & \oint_{\Gamma_e} N_3N_{2x}n_y d\Gamma_e & \oint_{\Gamma_e} N_3N_{3x}n_y d\Gamma_e \end{bmatrix} \tag{4.41}$$

The shape function integrals used in the calculation of the element matrices $[M]_e$ and $[K]_e$ can be evaluated using the following formulae

$$\int_e N_1^i N_2^j N_3^k ds = \frac{i!.j!.k!.2!}{(i+j+k+2)!} A_e \tag{4.42}$$

$$\int_{\Gamma_{12}} N_1^i N_2^j d\Gamma_e = \frac{i!.j!.}{(i+j+1)!} l_{12} \tag{4.43}$$

The element area related to the nodal coordinates of the element is expressed as, A_e, and Γ_{12} and l_{12} are the part and length of the element boundary connecting the nodes 1 and 2, respectively.

It can be noted that the element matrix $[K]_e$, from the above formulation of the element matrices is responsible for coupling and polarisation dependence. The inclusion of the line integrals in the matrices $[K_{xx}]$ and $[K_{yy}]$ make them unequal, and thus, the polarisation dependence is accounted for. But, since the matrices $[K_{xy}]$ and $[K_{yx}]$ are not zeros, the coupling between the polarisation states is taken into account.

This formulation considers only two transverse components of the magnetic field. The resulting global matrices $[M]$ and $[K]$ are *sparse*, hence, only non-zero elements have to be stored, and also computationally-efficient matrix solver based on LU-decomposition can be based. This is a major strength of the formulation, since other vector formulations based on this phenomenon of transverse field components lead to dense matrices. In some optical devices, the hybrid nature of the field is not strong; hence, the polarisation coupling is very weak. The matrices $[K_{xy}]$ and $[K_{yx}]$ can be neglected so that the formulation reduce to two decoupled wave equations for H_x and H_y, hence referred to as a *semi-vectorial* one. However, for some weakly guiding optical devices, even the polarisation dependence may be neglected, thus, matrices $[K_{xx}]$and $[K_{yy}]$ will reduce to one matrix $[K_n]$ so that the formulation reduces to only one wave equation for H_x and H_y. In this case, the formulation reduces to a scalar one.

The exact non-paraxial vectorial wave equation to be solved in a step-by-step procedure in z direction is shown in equation (4.26). The neglection of the z-second derivative term reduces to the approximate paraxial equation which is *valid* only for

wave propagating very near to the axis of propagation, z. Hence, by application of the Pad'e approach [143] gives a better approximation. The equation (4.26) can be re-written as

$$-2jn_0k_0[M]\frac{d\{h_t\}}{dz_{i+1}} = -\frac{([K]-n_0^2k_0^2[M])\{h_t\}}{1-\frac{1}{2jn_0k_0}\frac{d}{dz_i}} \tag{4.44}$$

where, $\frac{d}{dz_0} = 0$

By utilising the first Pad'e approximation (Pad'e (1,0)) by putting $i = 0$ in the recurrence Pad'e relation as shown in equation (4.44), yields

$$-2jn_0k_0\left[\hat{M}\right]\frac{d\{h_t\}}{dz} + ([K]-n_0^2k_0^2[M])\{h_t\} = \{0\} \tag{4.45}$$

where

$$\left[\hat{M}\right] = [M] + \frac{1}{4n_0^2k_0^2}([K]-n_0^2k_0^2[M]) \tag{4.46}$$

The paraxial equation is easily obtained from equation (4.45) by replacing matrix $\left[\hat{M}\right]$ by $[M]$. Since equation (4.45) can trace wave propagating off the propagation axis, z, with accuracy than the paraxial equation, it is called the *wide–angle equation.* Moreover, to solve equation (4.45) in a finite range of the z-domain, we divide it into sections each of a width Δz. Over the kth section (shown in Fig. 4.2), the finite element method can also be used to approximate the field as

$$\{h_t(\zeta)\} = L_k(\zeta)\{h_t(\zeta_k)\} + L_{k+1}(\zeta)\{h_t(\zeta_{k+1})\} \tag{4.47}$$

where ζ is the local coordinate of the kth section, $\{h_t(\zeta_k)\}$ and $\{h_t(\zeta_{k+1})\}$ are the column vectors containing the field nodal values over the whole cross section at k^{th}

and $(k+1)^{th}$ propagation steps, respectively, while $L_k(\zeta)$ and $L_{k+1}(\zeta)$ are the shape functions given as

$$L_k(\zeta) = 1 - \zeta \tag{4.48}$$

$$L_{k+1}(\zeta) = \zeta \tag{4.49}$$

Applying Galerkin's procedure, with weighting functions W_m, and substituting equations (4.47), (4.48) and (4.49) into equation (4.45) yields

$$[A]_k \{h_t\}_{k+1} = [B]_k \{h_t\}_k \tag{4.50}$$

where

$$[A]_k = -2jn_0k_0\left[\hat{M}\right]_k + \theta\,\Delta z\left([K]_k - n_0^2k_0^2[M]_k\right) \tag{4.51}$$

$$[B]_k = -2jn_0k_0\left[\hat{M}\right]_k + (\theta - 1)\,\Delta z\left([K]_k - n_0^2k_0^2[M]_k\right) \tag{4.52}$$

where subscripts k and $k+1$ denote the quantities related to the kth and $(k+1)^{th}$ propagation steps, respectively and Δz is the propagation step size, θ is the scheme parameter given as

$$\theta = \frac{\int_0^1 W_m \zeta d\zeta}{\int_0^1 W_m d\zeta} \tag{4.53}$$

Once the initial field has been specified, equation (4.51) can be solved to get the field at the successive propagation steps. The value of the scheme parameter, θ, depends on the choice of the weighting functions W_m. The value of, θ, decides the stability and the numerical losses of the propagation algorithm. It has been reported that when $\theta \geq 0.5$, then the algorithm will be unconditionally stable [144]. Moreover, when $\theta = 0.5$, which corresponds to the finite difference Crank-Nicolson algorithm, the algorithm will be stable and conserving the propagating beam power too.

However, for Crank-Nicolson algorithm, some high frequency oscillations may appear in the field distribution. The use of the rigorous PML boundary conditions can eliminate these high frequency oscillations. The high frequency oscillations can also be eliminated by using higher values of the scheme parameter, θ, but this has a drawback of appearance of non-physical numerical losses.

Therefore, we can conclude that the vectorial propagation algorithm used in this section is unconditionally stable ($\theta = 0.5$) and power conserving too.

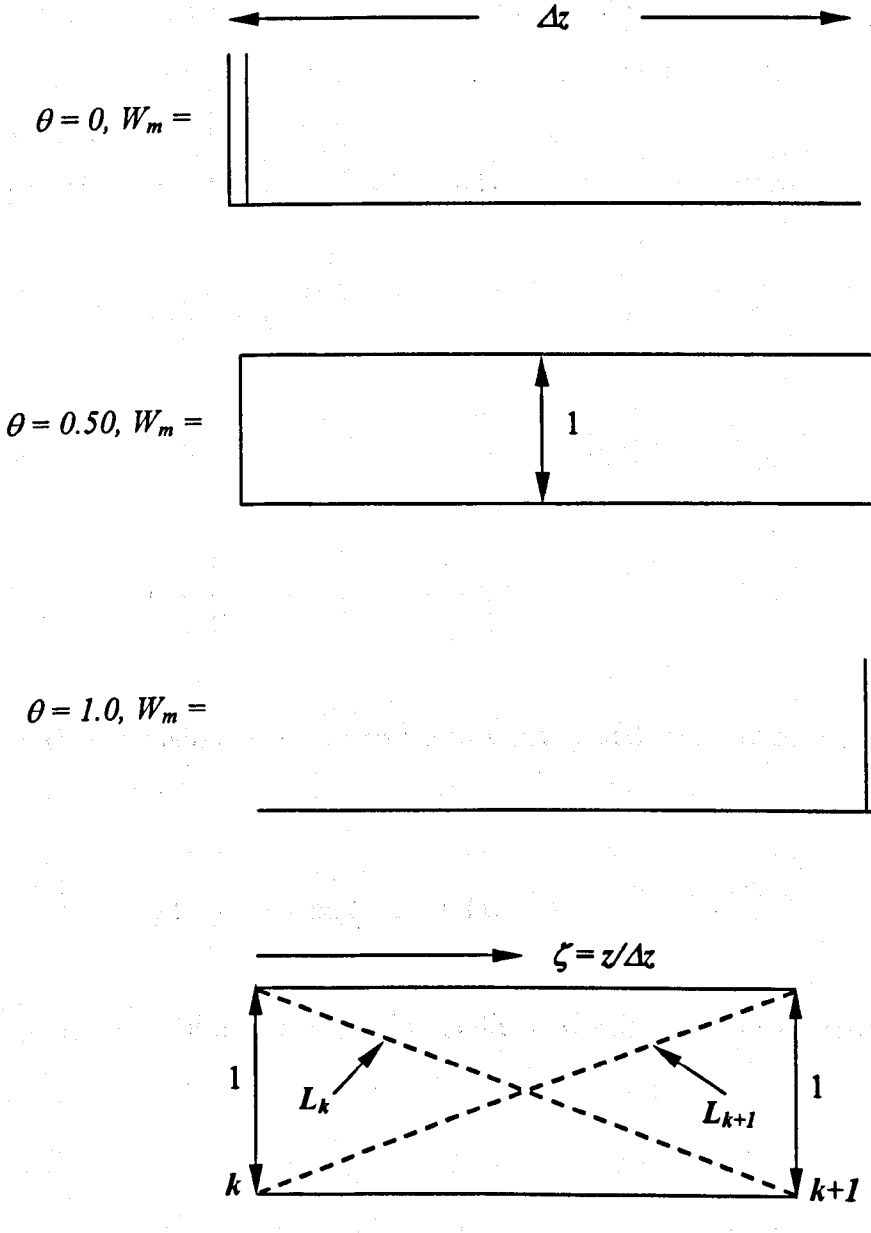

Fig. 4.2 Shape functions and different cases of weighting functions for discretisation along the longitudinal z-axis.

4.7 The Imaginary Axis Propagation

BPM offers an accurate description of spatial (near-field) and angular (far-field) properties of the electric field, but it can also generate information relevant to a purely modal description of the field [100]. The method is very efficient in tracing wave propagation in guided wave optical devices. The modal solution of uniform optical waveguides using the vector **H**-field finite element method has been discussed in the previous Chapter. Furthermore, it has been proven that BPM is capable of calculating the guided modes of a uniform optical waveguide if any arbitrary field is allowed to propagate in the direction of an imaginary axis [145,146]. The inclusion of the imaginary axis propagation will be incorporated in the context of the developed vectorial FEBPM algorithm.

The paraxial form of equations (4.18) and (4.19) can be expressed as

$$\frac{\partial \psi}{\partial z} = -j\boldsymbol{Q}\psi \tag{4.54}$$

where

$$\psi = \begin{Bmatrix} \psi_x \\ \psi_y \end{Bmatrix} \tag{4.55}$$

where $\boldsymbol{Q}$ is a matrix of transverse directions, x and y, operators affecting the field envelope, ψ. Equation (4.54) can also be expressed in the form

$$\psi(x,y,z) = \exp(-jz\boldsymbol{Q})\psi(x,y,0) \tag{4.56}$$

where $\psi(x,y,0)$ is an arbitrary initial field, which can also be represented as the summation of the waveguide modes (both guided and radiated) as

$$\psi(x,y,0) = \sum_{n=0}^{\infty} c_n \phi_n(x,y) \tag{4.57}$$

where $\phi_n(x,y)$ are the eigenvectors of the operator $\boldsymbol{Q}$, and the associated eigenvalues, λ_n, which can be in the order

$$\lambda_0 > \lambda_1 > \ldots\ldots\ldots\ldots > \lambda_n > \ldots\ldots\ldots\ldots \tag{4.58}$$

The eigenvectors and eigenvalues of the operator $\boldsymbol{Q}$ should satisfy

$$\boldsymbol{Q}\phi_n(x,y) = \lambda_n \phi_n(x,y) \tag{4.59}$$

The relation between the eigenvalues λ_n and the propagation constant of the nth order mode β_n of the paraxial wave equation is

$$\lambda_n = \beta_n - n_0 k_0 \tag{4.60}$$

Applying Taylor's series expansion to exp(-$jz\boldsymbol{Q}$) and using equation (4.57), we can write equation (4.56) in the form

$$\psi(x,y,z) = \sum_{n=0}^{\infty} c_n \exp(-j\lambda_n z)\phi_n(x,y) \tag{4.61}$$

When the field propagates along an imaginary axis ($z = j\xi$), equation (4.61) becomes

$$\psi(x,y,\xi) = \sum_{n=0}^{\infty} c_n \exp(\lambda_n \xi)\phi_n(x,y) \tag{4.62}$$

When n_0 is chosen close to $\frac{\beta_0}{k_0}$, then $\lambda_0 \approx 0$ and all other eigenvalues will be negative. This means that, all higher order modes will exponentially decay as the field propagates and only the fundamental mode will propagate with very slight decaying. Therefore, after some distance of propagation along the imaginary axis, ξ, the propagating field will eventually be similar to the profile of the fundamental mode whose propagation constant can be obtained from

$$\beta(\xi) = n_0 k_0 + \frac{\ln\left(\int \psi(x,y,\xi+\Delta\xi)d\Omega\right) - \ln\left(\int \psi(x,y,\xi)d\Omega\right)}{\Delta\xi} \tag{4.63}$$

Once the nodal values of the field are obtained, the integrals in equation (4.63) can be obtained by summing the contributions of each element as discussed in the previous section.

4.8 Power Calculation

The calculation of the propagating beam power is an essential parameter for characterising many photonic devices. For instance, for bent or leaky mode waveguides, the estimation of power losses is important as the fundamental to understand and minimise these losses.

The power associated with a beam propagating in the $z+$ direction (Poynting's theorem) is given as [147]

$$P = \frac{1}{2} R_e\left(\int E \times H^* . \overset{\bullet}{z}\, d\Omega\right) = \frac{1}{2} R_c\left[\int \left(E_x H_y^* - E_y H_x^*\right) d\Omega\right] \tag{4.64}$$

where R_e represents the real part, $\overset{\bullet}{z}$ is the unit vector in the z direction, and the integration is carried over the surface of the computational domain. The transverse electric field components can be given in terms of the magnetic field components as

$$E_x = \frac{n_0 k_0}{\omega \varepsilon_0} n^{-2} H_y \tag{4.65}$$

$$E_y = -\frac{n_0 k_0}{\omega \varepsilon_0} n^{-2} H_x \tag{4.66}$$

The second order derivatives with respect to the transverse coordinates, x and y have been neglected, in deriving E_x and E_y. Substituting from equations (4.65) and (4.66) into equation (4.64) gives

$$P = \frac{n_0 Z_0}{2} \int n^{-2} \left(|H_x|^2 + |H_y|^2 \right) d\Omega \tag{4.67}$$

where Z_0 is the free space wave impedance ($Z_0 \approx 377$ ohms). Substituting from equations (4.17), (4.24) and (4.25) yields

$$P = \frac{n_0 Z_0}{2} \{h_t\}^T [M] \{h_t\} \tag{4.68}$$

where $\{h_t\}$ represents the nodal values of the propagating field, T is the complex conjugate transpose and $[M]$ is the global matrix defined earlier in the previous section.

4.9 Summary

In this chapter the vectorial propagation algorithm based on the finite element technique has been presented. The formulation does not only consider the minimum number of components for a real vector formulation, but also, satisfies the interface boundary conditions satisfying the zero divergence condition, therefore, the existence of non-physical modes during propagation is not possible. The approach is truly vectorial as it accounts for the polarisation dependence and coupling.

The concept of the perfectly matched layer and inclusion of the imaginary axis propagation with the developed vectorial algorithm has also been outlined. The propagation algorithm will be used to investigate and analyse photonic devices in subsequent chapters.

5.0 The Beam Propagation Method Analysis of SOA Waveguides

5.1 Introduction

High-power and low-cost semiconductor laser sources have significant potential for use in applications that are currently dominated by expensive solid-state lasers. The direct application of high-power semiconductor lasers for free-space and satellite communications, visual displays, biomedical applications and remote sensing, optical recording, spectroscopy, optical data storage, laser printers, laser radar and also for materials processing is becoming increasingly attractive due to the remarkable improvement in performance of high-power laser diodes. In addition, high-power spatially and spectrally coherent sources are required for the efficient pumping of solid-state and fiber lasers and efficient nonlinear frequency conversion to the short-wavelength part of the visible spectrum, which is not readily available with semiconductor sources directly.

In edge-emitting semiconductor lasers, the possibility of catastrophic optical damage limits the power density to several tens of milliwatts per micrometer width of the active layer. One of the approaches available to increase the total power is by increasing the width of the active area for broad-area lasers, but these usually exhibit non-coherent multiple lateral mode operation, thus degrading the beam quality and leading to filamentation. Alternatively, by using many parallel coupled lasers, the overall total power can also be increased [148]: however, poor gain discrimination and the early onset of spatial mode oscillations limits the total power, and these arrays often exhibit an undesirable two-lobed far-field pattern, indicative of a phase shift between the adjacent emitting elements.

Another alternative approach for obtaining higher output power is to amplify the output power of a single-mode laser, where the coherent output is more readily scaled to high power, retaining good beam quality. Semiconductor optical amplifiers (SOAs)

[149] with a tapered gain region have proven to be very efficient to reach the diffraction limited high output powers with high efficiency. In such high-power lasers, the optical mode size of the laser source has to be expanded in order to reduce both the junction temperature and nonlinear effects and the optical power density at the laser facets. Broad-area tapered devices have been proposed to yield high output power, together with achieving better quantum efficiency and higher beam quality [150], and in recent years, similar semiconductor laser amplifiers with tapers have been studied extensively. In the taper design, the width is gradually increased [146, 150] to expand the optical beam, which consequently lowers the power density, and thus the effect of the gain saturation is reduced.

On the other hand, if the width is progressively reduced, in a similar way to the design of a spot-size converter [151], the optical beam would expand only when the waveguide reaches its modal cut-off condition. This design may be useful for a low-power amplifier to couple efficiently this device to a single-mode fibre with a larger spot size. However, since its spot-size would be smaller along most of the tapered structure, except near the end where the cut-off condition is approached, for a high-power optical amplifier an increased power density along the amplifier would reduce the overall gain due to early onset of gain saturation. Although significant progress has been made in the use of wider tapered waveguides, one of the most significant issues remaining is beam filamentation, which can limit the output power and degrade the beam quality. Often, a Gaussian output beam profile is preferred to couple the optical beam more efficiently. The modal field profile of the fundamental mode of an expanded tapered waveguide may be close to a Gaussian profile. However, with such a large waveguide being multimoded, the beam shape often deteriorates due to the mode beating between the fundamental mode and the higher order modes. This beam filamentation has been attributed to different mechanisms, including the carrier [152] and thermally induced index change [153], amplified spontaneous emission [154], the line-width enhancement factor [155], and defocusing-type nonlinearities [156].

This section focuses on the evolution of the optical beam along tapered semiconductor laser structures, by using rigorous vectorial numerical approaches based on the finite-element method (FEM).

5.2 Modal Solution by Beam Propagation Method

In this phase of the project, the generated Gaussian and mode input (from FEM) field profiles were used to investigate the properties of the propagating field along the waveguide by the use of the beam propagation method (BPM).

In Fig. 5.1(a)-(d) a uniform guide was developed with an axial distance of $z = 200$ μm for a Gaussian input width, $W_o = 1.0$ μm. In this work, re-meshing is carried out after every ten z steps i.e., at 10-μm intervals ($m = 10$), unless otherwise stated. The height of the waveguide (H) is taken as 1 μm, and its width (W) is adjusted along the tapered structure. For the structure considered here, the quaternary InGaAsP core and InP cladding indexes are taken as $n_g = 3.39$ and $n_s = 3.17$, respectively, at the operating wavelength of 1.50 μm. The generated Gaussian input field is shown in Fig. 5.1 (a), although it appears to be oval in shape, which is due to change of scale in the vertical direction (Height). Although its actual spatial profile is circular in nature, the variation of the normalized power along the axial direction is shown in Fig. 5.1 (b). It is clearly observed that the power undergoes faster loss along the axial direction when $z < 50$ μm and when $z > 50$ μm the power loss was much slower. Gaussian field was not identical as the mode field, but can be considered as superposition of the fundamental mode and many higher order modes, which are not guided. The launch field settles to the fundamental mode and other higher order modes radiates out, contributing to the loss.

When $z > 100$ μm the power loss (normalised) stabilises and settles around 0.74 dB, further increase in the propagation distance had a limited effect on the power loss. In Fig. 5.1 (c) the total power loss experiences similar characteristics as in Fig 5.1 (b), however it stabilises and settles around –1.29 dB. During propagation the Gaussian input field settles to generate the output field profile as shown in Fig. 5.1 (d) which is much smaller compared to the original input field profile. The output field profile obtained from the Gaussian input field appears identical with the mode output field obtained when the actual mode input was launched from FEM as shown in Fig. 5.1 (e).

The variation of the spot-size along the axial direction is shown Fig. 5.1 (f). It is clearly seen that the spot-size starts from $\sigma = 2.65\ \mu m^2$, then decreases rapidly to $\sigma = 0.62\ \mu m^2$, however these abrupt changes in the spot-size reduce when $z > 50\ \mu m$. The damped oscillations in the spot-size appear to settle around $0.96\ \mu m^2$. When the mode input is used instead of the Gaussian input the spot-size increased from $0.96\ \mu m^2$ to $0.98\ \mu m^2$ as shown in Fig. 5.1 (g). Due to a magnified view on the vertical direction the difference appears to be large but it is actually very small around $0.020\ \mu m^2$. However when $z > 25\ \mu m$ the damped oscillations in the spot-size area appear to settle around $0.97\ \mu m^2$, which correlates with the Gaussian input result.

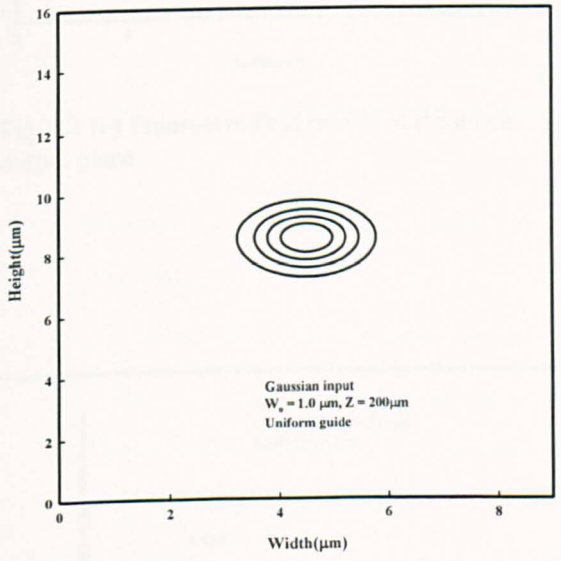

Fig. 5.1 (a) Transverse field profile of the Gaussian input plane.

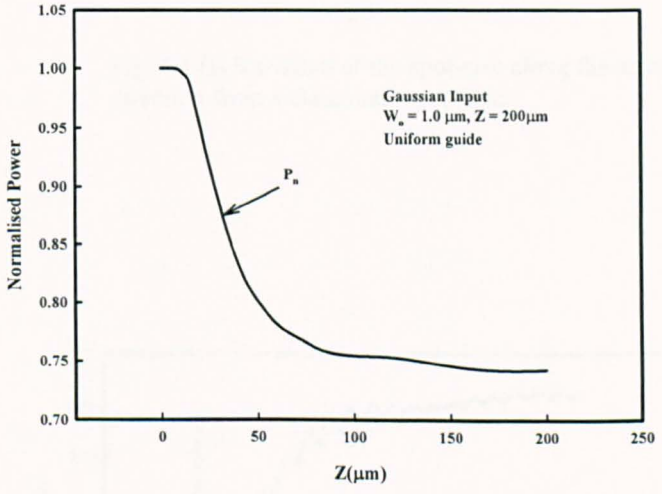

Fig. 5.1 (b) Variation of the normalised power along the axial direction from a Gaussian input field.

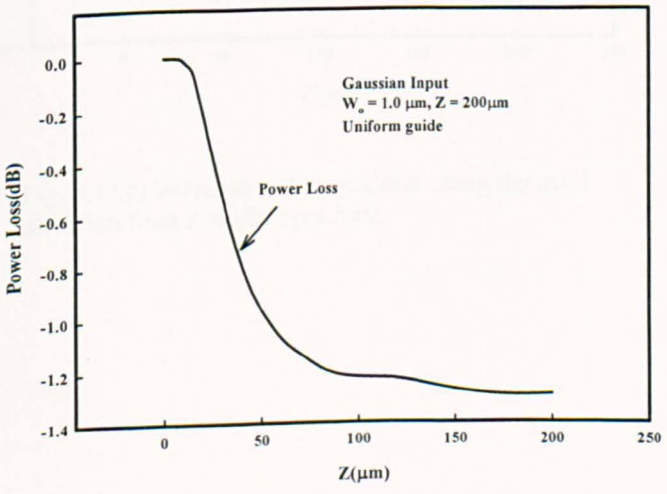

Fig. 5.1 (c) Variation of the power loss along the axial direction from a Gaussian input field.

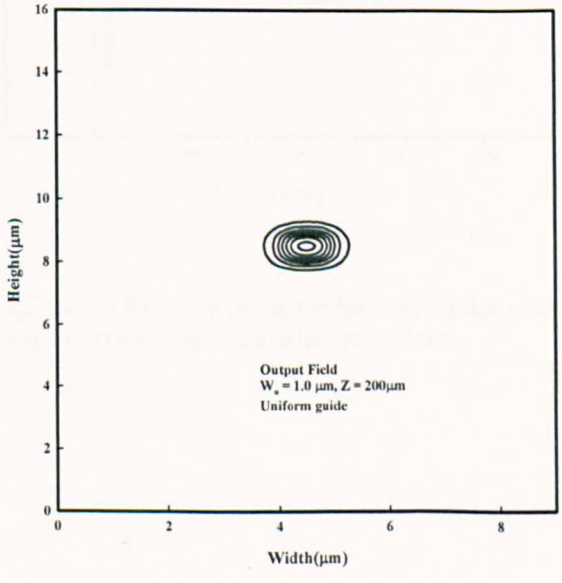

Fig. 5.1 (d) Transverse output field profile due to Gaussian input field.

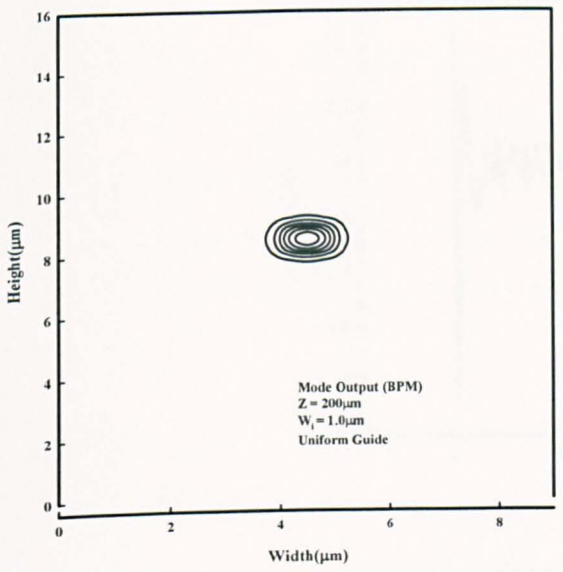

Fig. 5.1 (e) Transverse field profile of the mode output plane.

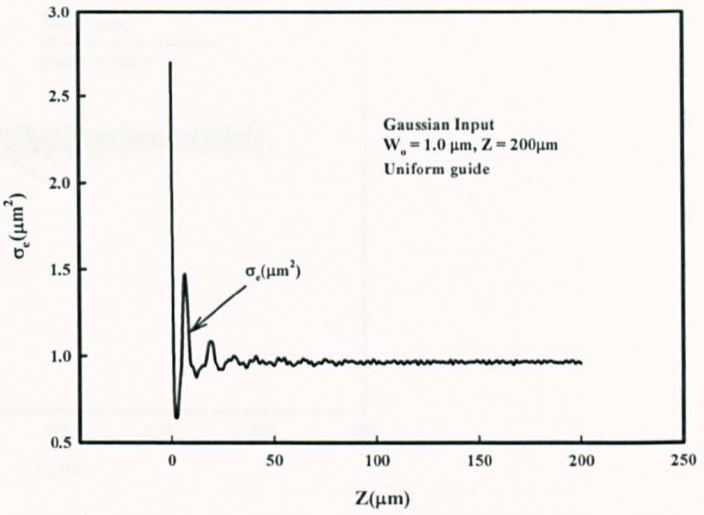

Fig. 5.1 (f) Variation of the spot-size along the axial direction from a Gaussian input field.

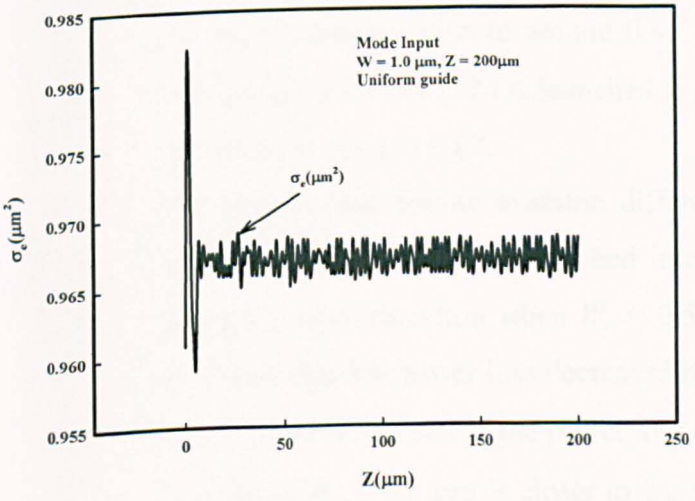

Fig. 5.1 (g) Variation of the spot-size along the axial direction from a mode input field.

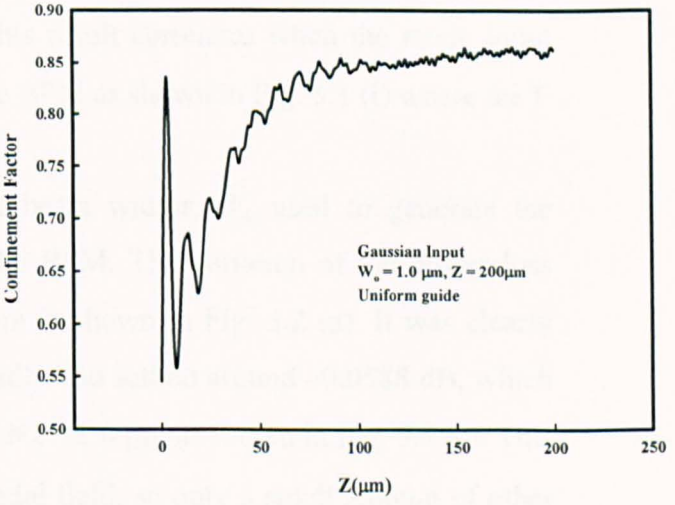

Fig. 5.1 (h) Variation of the confinement factor along the axial direction from a Gaussian input field.

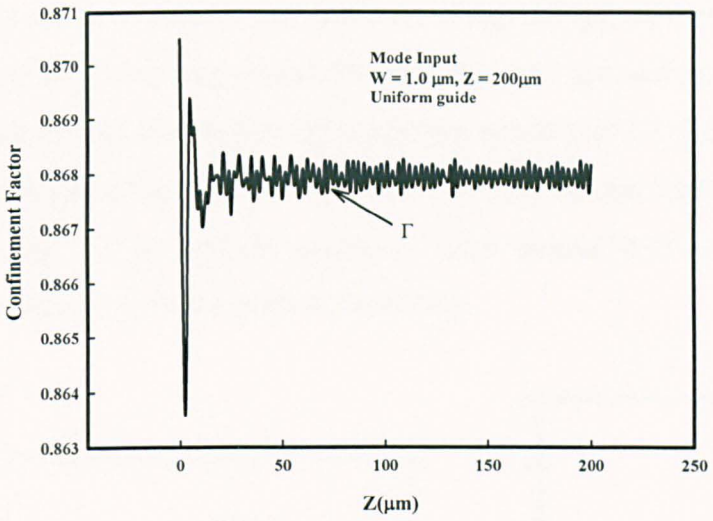

Fig. 5.1 (i) Variation of the confinement factor along the axial direction from a Gaussian input field.

Variation of the confinement factor (Γ) along the axial direction when the Gaussian input is launched is shown in Fig. 5.1 (h). It is clearly observed that at the beginning, Γ = 0.55, which increases rapidly to 0.84 then decreases again. However, when z > 100 μm the Γ, settles down to around 0.86. This result correlates when the mode input field generated from FEM is launched to the BPM as shown in Fig. 5.1 (i) where the Γ settles down around 0.87.

The results that follow examine different beam widths, W_o used to generate the Gaussian input field, then launched into the BPM. The variation of the power loss along the axial direction when W_o = 0.5 μm is shown in Fig. 5.2 (a). It was clearly observed that the power loss decreased rapidly and settled around –0.0588 dB, which is much less compared to the power loss of W_o = 1.0 μm as shown in Fig. 5.1 (c). This is because W_o = 0.5 μm is closer to the modal field, so only a small amount of other modes were generated. The output field from the Gaussian input is also shown in Fig. 5.2 (b), which shows clearly that the mode has settled, and this is very close to the modal field. The variations of the spot size and confinement factor along the axial direction are shown in Fig. 5.2 (c) and (d) respectively.

The trend appears to be the same with comparison to W_o = 1.0 μm, however for W_o = 0.5 μm the damped oscillations in the spot size appear which settles around 0.97 μm^2,

and the Γ settles around 0.87. When a much smaller width, W_o = 0.3 μm is examined, the power loss increases rapidly and is shown in Fig. 5.3 (a), and settles around –1.59 dB which is much higher than compared when W_o = 0.5 μm and more closer to W_o = 1.0 μm. To understand this feature the maximum power loss for different widths was investigated and plotted in Fig. 5.4. However, the spot size and confinement factor (Γ) as shown in Fig. 5.3 (a) and (b) appear to settle around 0.97 μm² and 0.87 μm² respectively, correlating with the previous results.

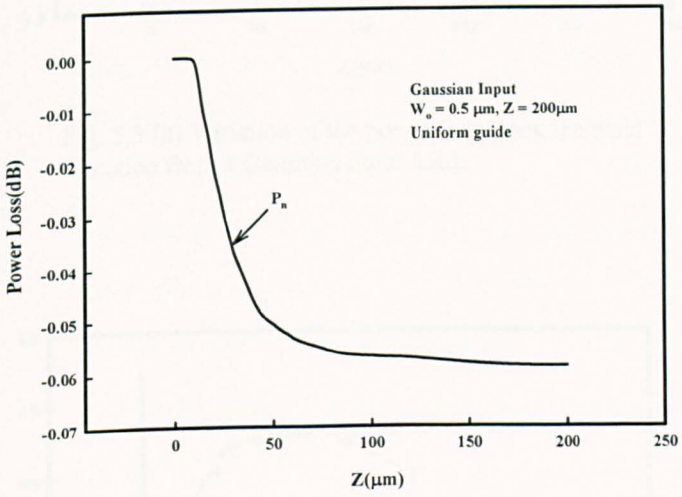

Fig. 5.2 (a) Variations of the power loss along the axial direction from a Gaussian input field.

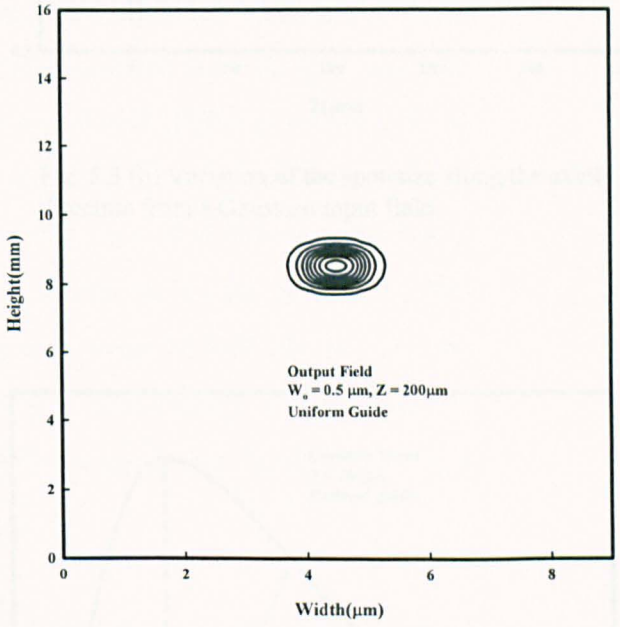

Fig. 5.2 (b) Transverse field profile of the Gaussian output plane.

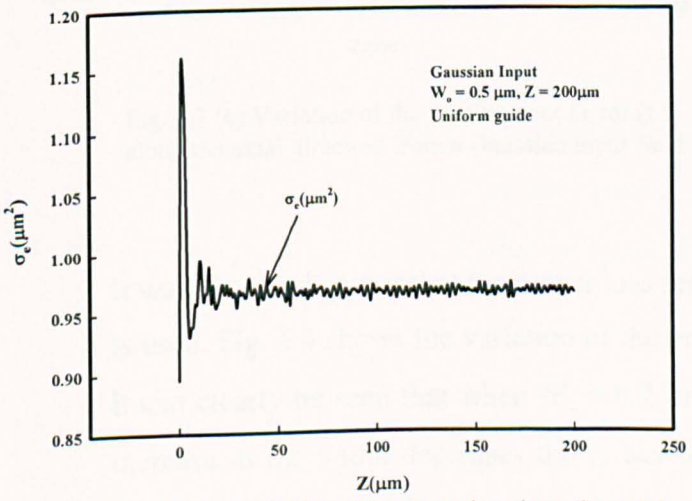

Fig. 5.2 (c) Variation of the spot-size along the axial direction from a Gaussian input field.

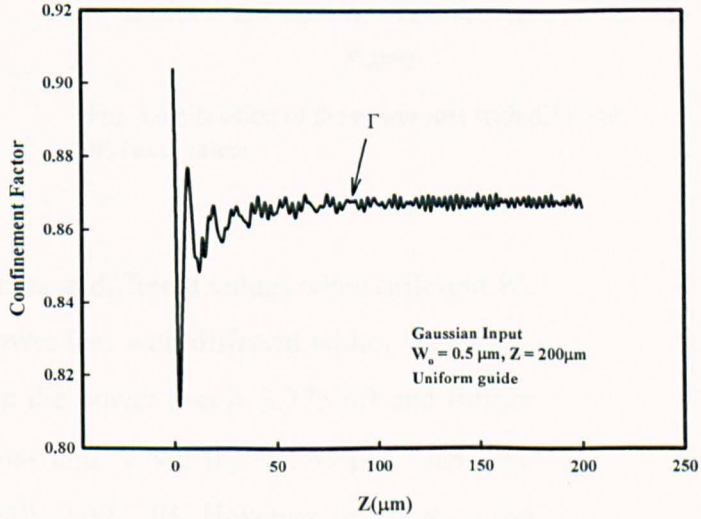

Fig. 5.2 (d) Variation of the confinement factor along the axial direction from a Gaussian input field.

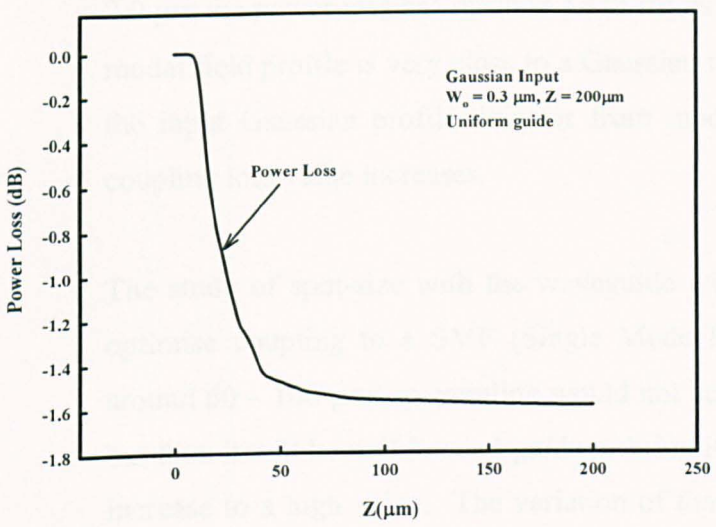

Fig. 5.3 (a) Variation of the power loss along the axial direction from a Gaussian input feild.

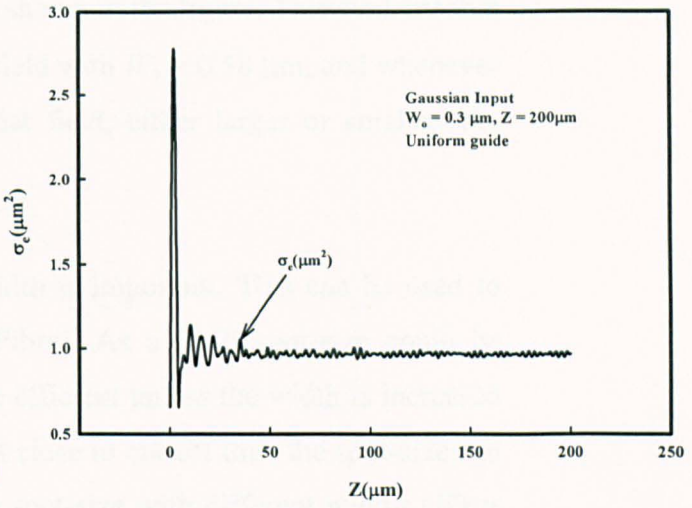

Fig. 5.3 (b) Variation of the spot-size along the axial direction from a Gaussian input field.

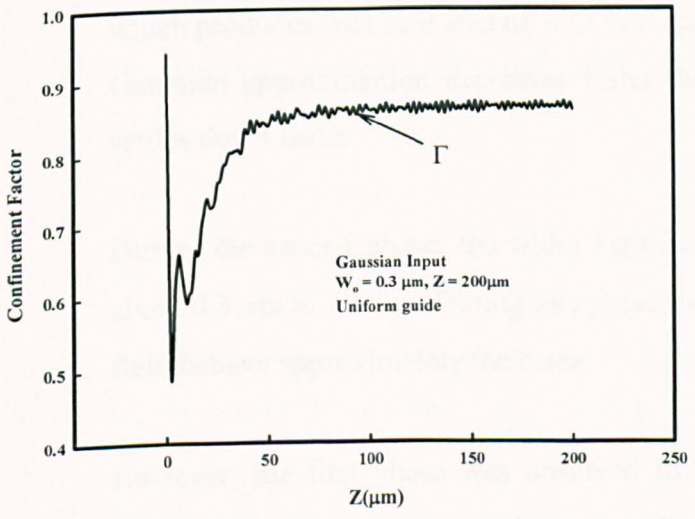

Fig. 5.3 (c) Variation of the confinement factor (Γ) along the axial direction from a Gaussian input field.

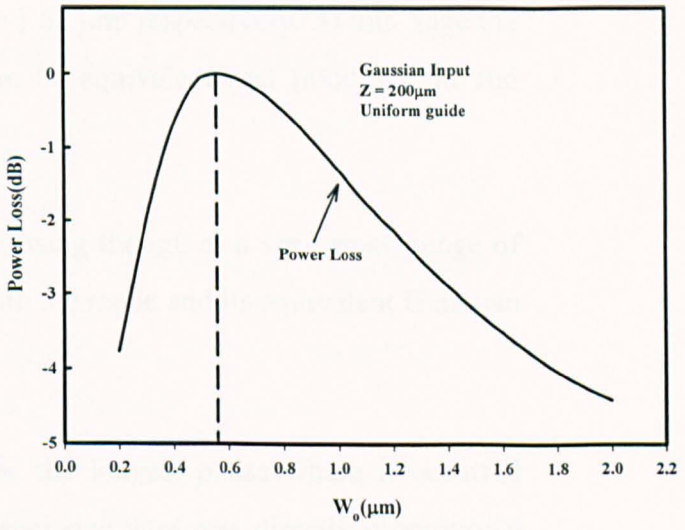

Fig. 5.4 Variation of the power loss with different W_o (μm) values.

It was observed earlier that the power loss settles at different values when different W_o is used. Fig. 5.4 shows the variation of the power loss with different width, W_o values. It can clearly be seen that when W_o = 0.2 μm the power loss is 3.775 dB and further increase in the width decreases the power loss until when W_o = 0.58 μm where the minimum power loss is attained which is only 0.002 dB. However, increase in the

width from henceforth, results in further increase in power loss respectively. At W_o = 2.0 μm the power loss has reached 4.411 dB as shown in the figure. This explains that modal field profile is very close to a Gaussian field with W_o = 0.58 μm, and whenever the input Gaussian profile deviates from modal field, either larger or smaller, the coupling loss value increases.

The study of spot-size with the waveguide width is important. This can be used to optimise coupling to a SMF (Single Mode Fibre). As a SMF spot-size could be around 60 – 100 μm² so coupling would not be efficient unless the width is increased but then it will be multimoded guide or bring it close to cut-off then the spot-size can increase to a high value. The variation of the spot-size with different widths (W) is shown in Fig. 5.5. It is clearly observed that there are three distinct phases that occur when the waveguide width is varied. When W reduces spot size reduces, reaches a minimum value and as W is reduced more, it approaches the modal cut-off and the spot-size expands. This occurs when the width is at a range of 0.02 μm to 0.1 μm, which produces spot-size area of 7.75 μm² and 1.62 μm² respectively. At this stage the Gaussian approximation decreases faster than its equivalent real (mode) field and settles down faster.

During the second phase, the width kept increasing though at a very small range of about 0.3 μm to 1.5 μm. During this phase, both the mode and its equivalent Gaussian field behave approximately the same.

However, the first phase was observed to be the longest phase where it occurred between 10 μm to 2 μm. At this stage, the spot-size area was directly proportional towards the width, hence increase in the width caused an increase in the spot-size area. The highest value of the spot-size area obtained at this phase was 25.87 μm². During this phase the Gaussian approximation decreases slower than its equivalent real field and settles down.

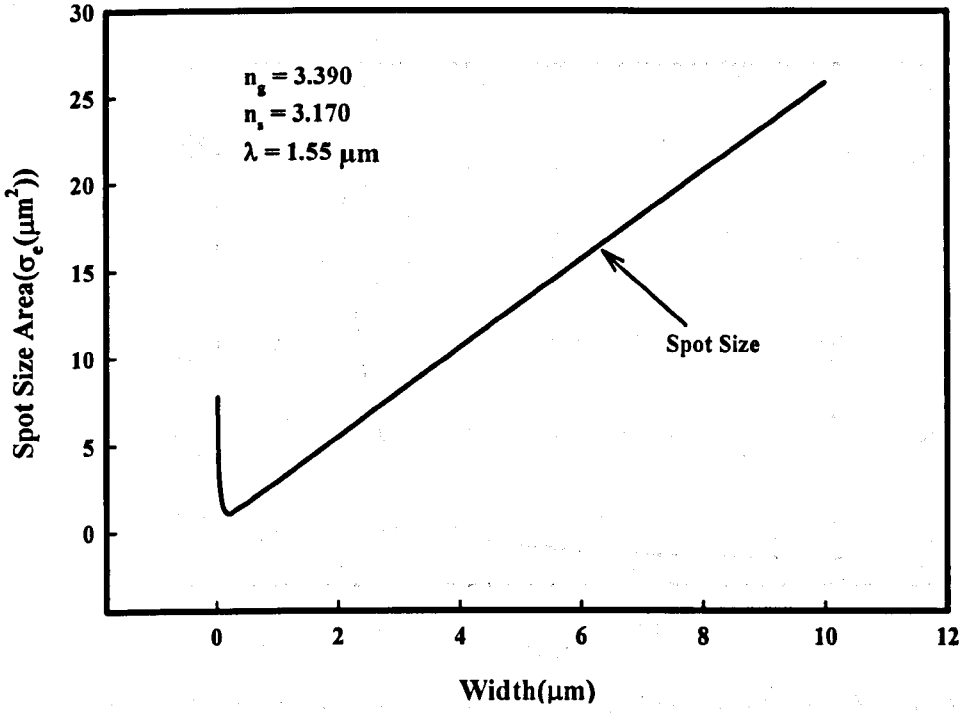

Fig. 5.5 Variation of the spot size for different widths (W).

The variation of the modal birefringence for different widths is shown in Fig. 5.6, which implies that the effective index n_e^x of the H_x^{11} mode is lower than the effective index n_e^y of the mode H_y^{11}. This yields to a positive modal birefringence, B expressed as $B = n_e^y - n_e^x$, where $n_e = \frac{\beta}{k_o}$ and $k_o = \frac{2\pi}{\lambda}$. However, in some cases a negative modal birefringence has also been reported [157]. It should be noted that in this example $W <$ H, but for larger W, mode is well confined so the difference is smaller.

When the width of the waveguide is decreased beyond the cut-off, the modal birefringence stays steady until the width is 2 μm, where it increases rapidly as W increases further. In this case the birefringence values obtained for the whole range of widths considered are positive since $n_e^y > n_e^x$.

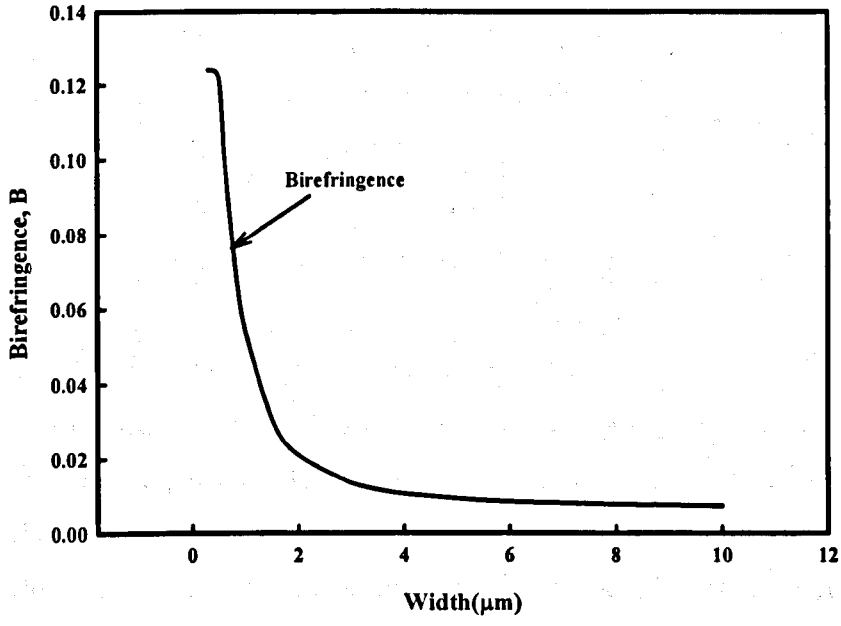

Fig. 5.6 Variation of the modal birefringence for different widths (W).

5.3 Tapered Semiconductor Optical Amplifier Waveguides

Tapered waveguides are important components in integrated optics. They can be used to interconnect optical devices of different cross-sectional dimensions such as lasers, fibres, and waveguides. The development of tapered amplifiers has raised a lot of interest recently due to the emergence of various applications like frequency doubling, pumping of fiber amplifiers or free space communication. Optical guided-wave devices often contain tapered structures [158-160] to achieve a highly efficient power coupling between two different optical devices. It is desirable that a well-designed taper possesses the capacity to convert optical mode sizes adiabatically. In general, to reduce the radiation loss, the dimensional variation along the propagation direction of a tapered waveguide must be small, so that the device length is therefore increased. In recent years, semiconductor optical amplifiers (SOAs) with linear [161] or exponential tapers [76,161] and other combinations [162,163] have been studied intensively as they provide higher saturation output power and better quantum efficiency.

5.3.1 Design of the SOA Tapered Waveguides

The need for high output power and good spatial and spectral purity often required by applications in ultra fast nonlinear optics or communication systems has led in recent years to device designs for high-power high-brightness semiconductor laser sources and to the realization of new laser amplifiers with improved beam quality. The laser amplifier system consisting of a laser pulse source and a semiconductor amplifier is a very commonly used configuration since it allows the separate optimisation of device properties responsible for pulse properties and output power. The spatial and spectral properties of a pulsed signal that has been amplified in a high-power semiconductor laser thereby depend particularly strongly on both the geometry of the laser (in particular the waveguide geometry) and the specific realization of the current injection. More recent investigations on tapered laser amplifiers have revealed the influence of the tapered angle and the length of the waveguide section on beam quality and power of the amplified signal [164].

The first structure studied was a simple rectangular waveguide as shown in Fig. 5.7. The properties of the waveguide are uniform in the x-direction; n_g is the refractive index of the core and n_s is the refractive index of the substrate. The refractive indices of the quanternary InGaAsP core and InP cladding are taken as $n_g = 3.39$ and $n_s = 3.17$, respectively. The free space wavelength λ, considered here is 1.50 μm. W_i represents the initial width and h represents the height (thickness) of the core region, taken as 1 μm and 0.1 μm, respectively. The final width (W_f) was taken as 3 μm. However, in the later stage, W_i and W_f were taken as 4 μm and 100 μm, respectively, as will be discussed in detail in this chapter.

An initial 100 μm uniform section was considered prior to the tapered section as shown in Fig. 5.7 (b). The TE mode of the input signal generated from the FEM is launched in this structure and the guided beam is investigated as it propagates along the waveguide.

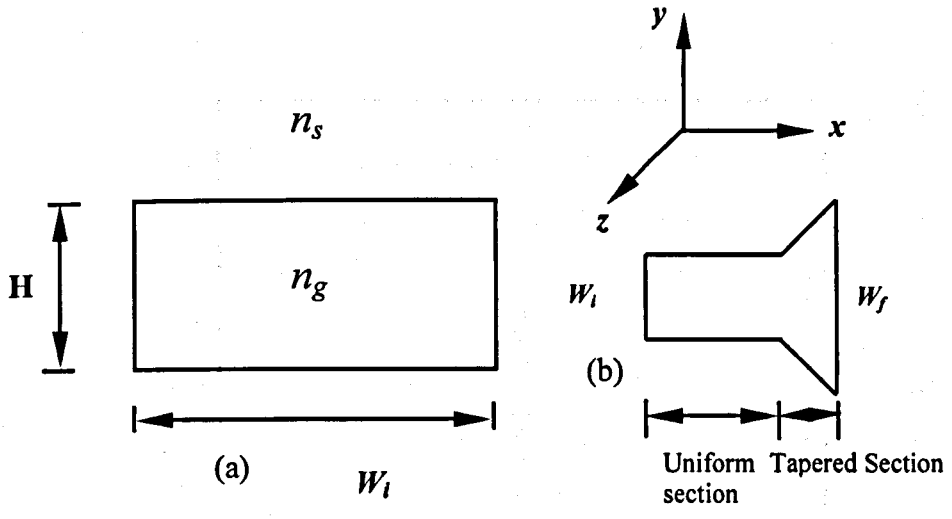

Fig. 5.7 Schematic diagram of a rectangular waveguide.

Later in this chapter the contribution of this waveguide structure to the evolving beam profile will be examined and discussed.

5.3.2 Propagation Analysis of the Modal Field

In this section, the evolving beam will be examined as it propagates along the waveguide structure. However, it should be noted that for the first 100 μm a uniform section was developed. The refractive indexes were taken as $n_g = 3.39$ and $n_s = 3.17$, respectively, at the operating wavelength of 1.50 μm. In this work, the tapered angle θ is large i.e., $\theta = 6.0^0$, and this is varied symmetrically to achieve a final width (W_f) of 100 μm from an initial $W_i = 4.0$ μm.

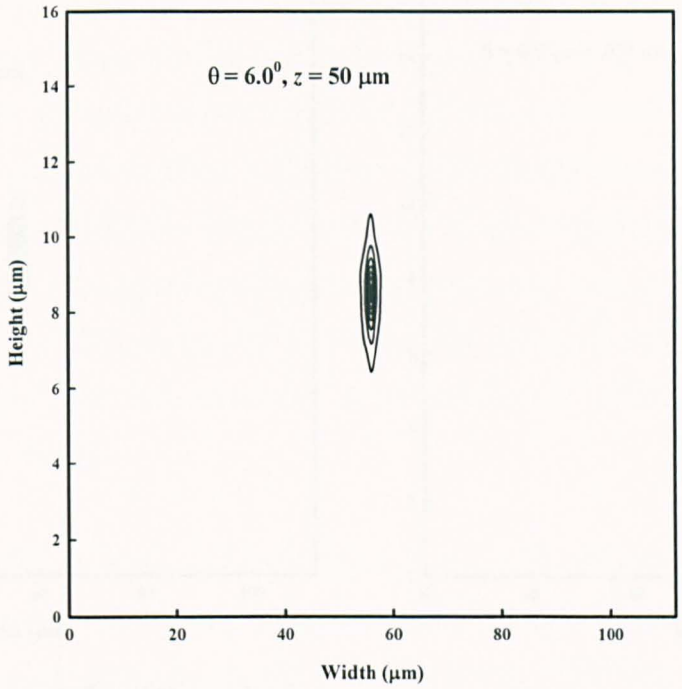

Fig. 5.8 (a) Transverse electric field profile of the evolved beam at z = 50 μm.

For the initial 100 μm the structure was uniform, therefore the evolving beam at z = 50 μm and z = 100 μm as shown in Fig. 5.8 and Fig. 5.9, respectively, appeared identical, during propagation. This is mainly because the width of the waveguide was constant at 4.0 μm, however after z = 100 μm, further increased in the width increased the size of the evolving beam as seen in the figures below (It should be noted here that the horizontal and vertical scales are different). However, it should be noted here that the height of the evolving beam always remained constant in both the uniform and tapered sections, as waveguide height, H, was not changed.

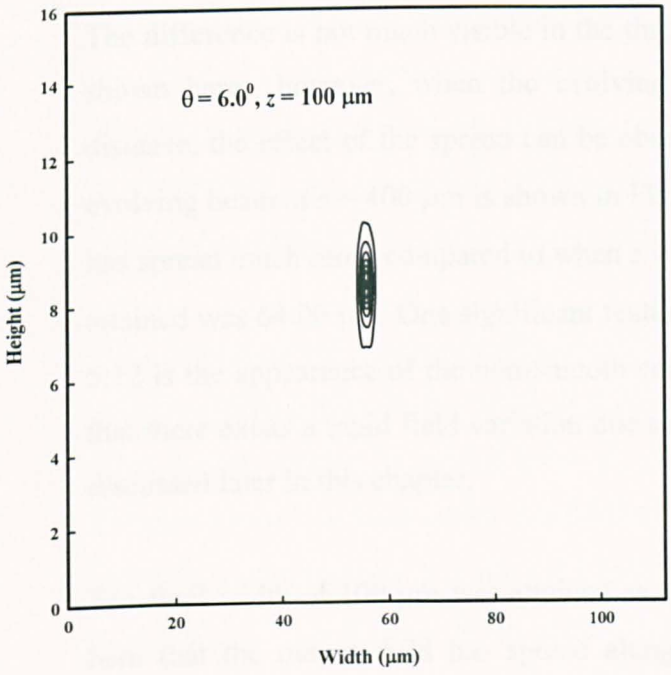

Fig. 5.9 Transverse field profile of the evolved beam at z = 100 μm.

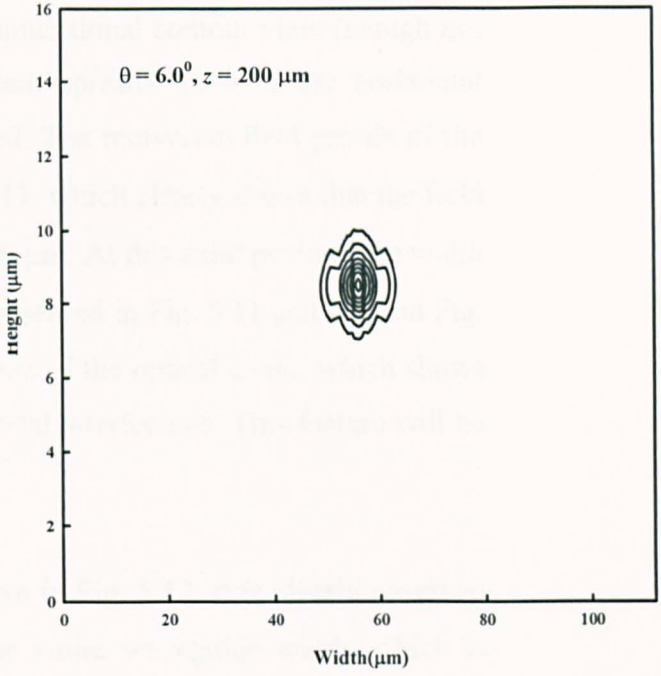

Fig. 5.10 Transverse field profile of the evolved beam at z = 200 μm.

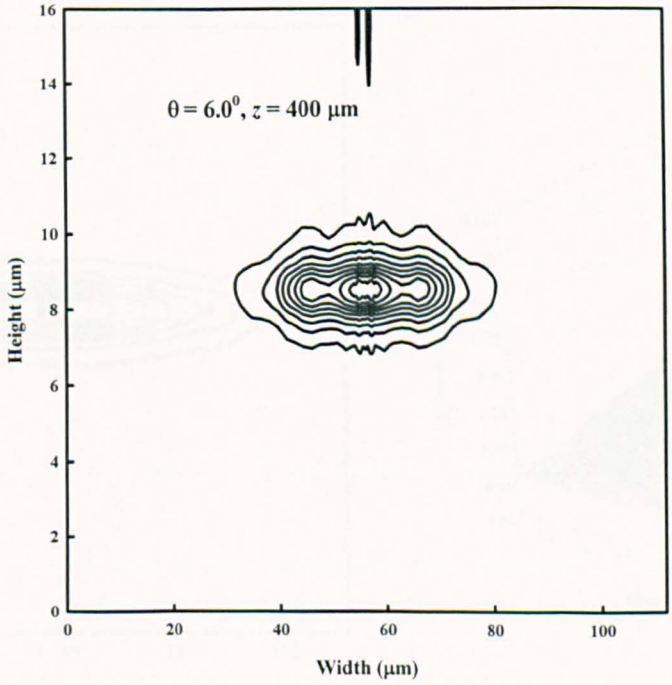

Fig. 5.11 Transverse field profile of the evolved beam at z = 400 μm.

In Fig. 5.10 it can clearly be observed that evolving beam has started to spread out due to the contribution of the tapered region, and the effect of the tapered angle is

clearly visible. When z = 200 μm, at this particular axial position the width of the field has increased from the initial 4.0 μm to 22.02 μm, to allow the expansion of the field. The difference is not much visible in the three dimensional contour view (though not shown here), however, when the evolving beam spreads all over the horizontal distance, the effect of the spread can be observed. The transverse field profile of the evolving beam at z = 400 μm is shown in Fig. 5.11, which clearly shows that the field has spread much more compared to when z = 200 μm. At this axial position the width attained was 64.06 μm. One significant feature observed in Fig. 5.11 and later on Fig. 5.12 is the appearance of the non-smooth contours of the optical beam, which shows that there exists a rapid field variation due to modal interference. This feature will be discussed later in this chapter.

The final width of 100 μm was attained as shown in Fig. 5.12. It is clearly observed here that the output field has spread along the entire waveguide width, which is clearly visible when a 3D view was plotted as shown in Fig. 5.13. This was attained when z = 557 μm.

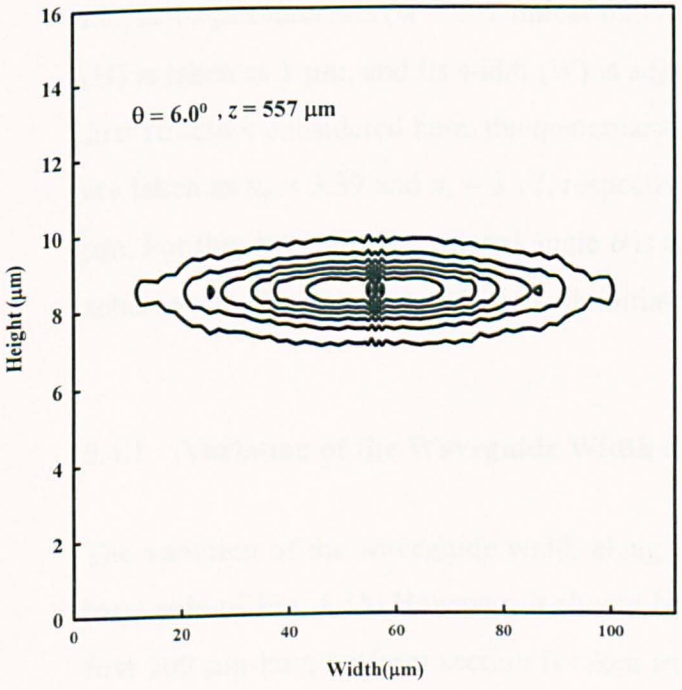

Fig. 5.12 Transverse field profile of the evolved beam at z = 557 μm.

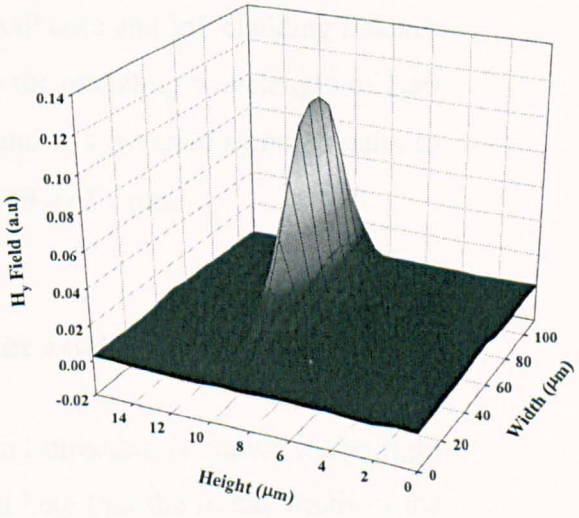

Fig. 5.13 The 3D view of the evolved beam at z = 557 μm.

5.4 Study of the Evolution Beam along Tapered waveguides

Initially, a small tapered structure is considered to study rigorously the resulting mode expansion and the optical power loss by using the full-vectorial FEBPM [43]. A schematic diagram of the beam expander considered here is shown in Fig. 5.14. In the BPM approach, an input optical field profile is needed as the exciting field, this being generated by employing a fully vectorial **H**-field-based FEM (VFEM) [93].

Often, a high-power semiconductor amplifier is preceded by a master oscillator [165] or preamplifier [166]. In this work, a uniform section, represented here by an initial 100-μm-long section, is added prior to the tapered section, which stabilizes the launched beam. For high-power applications, the output waveguide could be several hundreds of micrometers in width [165,166], and the corresponding taper angles could be as high as 10° [166,167]. In this study, the longitudinal propagation step Δz is taken as 1 μm. The z-dependent tapered guided-wave structure is required to be remeshed along the axial direction as its width is continuously changed. However, rather than remeshing at every propagation step, this is carried out at a finite interval to reduce the computational cost. In this study, remeshing is carried out after every ten z steps i.e., at 10-μm intervals (m = 10), unless otherwise stated. The height of the waveguide (H) is taken as 1 μm, and its width (W) is adjusted along the tapered structure. For the first structure considered here, the quaternary InGaAsP core and InP cladding indexes are taken as n_g = 3.39 and n_s = 3.17, respectively, at the operating wavelength of 1.50 μm. For this structure, the tapered angle θ is small, and this is varied symmetrically to achieve a final width (W_f) of 3 μm with initial width (W_f) of 1 μm.

5.4.1 Variation of the Waveguide Width along the axial direction

The variation of the waveguide width along the axial direction is shown in the right hand side of Fig. 5.15. However, it should be noted here that the initial width of the first 100-μm-long uniform section is taken as, W_i = 1 μm, and after this section, it is expanded in a staircase fashion. The horizontal steps are of 10 μm, as dictated by the remeshing steps (m = 10), and its slope is governed by the tapered angle θ. In this

particular case, for a tapered angle $\theta = 0.3^{\circ}$ and an axial step Δz = 1 μm, the lateral width step used ΔW was 0.1 μm.

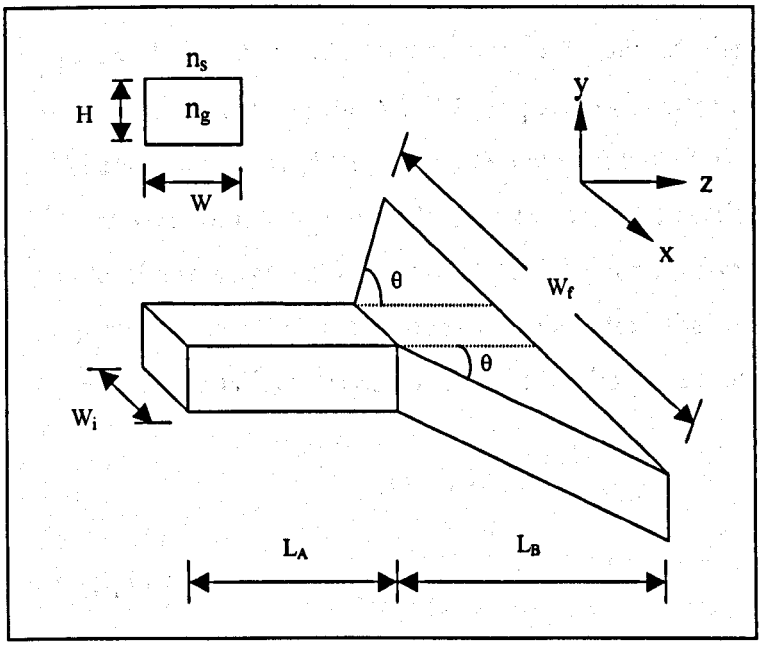

Fig. 5.14 Schematic diagram of the tapered semiconductor amplifier, including a short uniform section at the beginning.

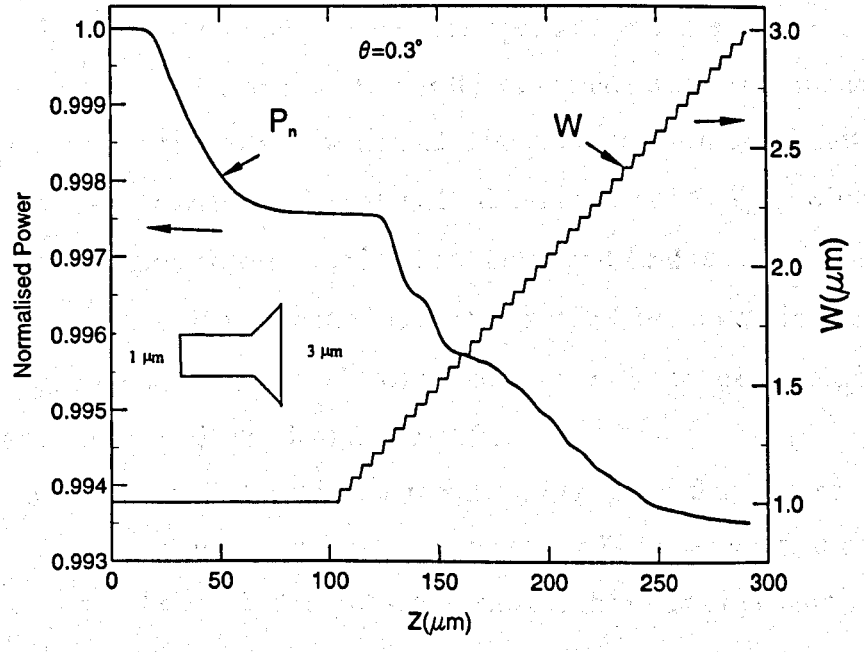

Fig. 5.15 Variations of the normalized power and local width along the axial direction.

5.4.2 Variation of the Normalised Power along the axial direction

The variation of the total guided power along the axial distance is shown in the left hand side of Fig. 5.15. It can be noted that the total normalized power reduces *monotonically* along the axial distance. Within the first 100 μm of the uniform section, the mode shape obtained by using the VFEM [19] settles down to a similar mode shape (but for BPM approach, so slightly different) that is obtained by using the FEBPM, with only 0.3% power loss. The power loss in the tapered section is also clearly visible. The mode shape requires approximately 20 propagation steps to evolve or stabilize in a particular section. It has been observed that the total power loss increases as the tapered angle is increased, which will be discussed later in this chapter.

5.4.3 Variations of the Spot-Size along the axial direction

The evolution of the optical beam along the tapered structure can be identified by its spot-size, and its variation along the axial direction as shown in Fig. 5.16. In this case, the spot-size is defined as the area, which has more than $1/e^2$ of the maximum intensity (i.e., the field intensity $1/e$). It can clearly be observed that in the first 100-μm-long and uniform (1-μm-wide) section, the spot-size remains constant, and subsequently it expands in the tapered section as the waveguide width is continuously increased. The input beam profile and the expanded output beam profiles are shown in Fig. 5.17. It can be clearly seen that the output field has increased to 3 μm when z = 291 μm, from initially 1 μm, however the height of the output field remained constant all through the propagation. For a shorter distance of z = 291 μm, to attain the final width a smaller tapered angle of $\theta = 0.3°$ was used. Hence, the tapered angle has a significant effect on the overall length of the amplifier.

However, one new feature that could be readily observed is that the spot-size expansion is not *monotonic* but goes through a strong oscillation process. It can be seen that at positions B, D, and Y the spot size is smaller than that of positions A, C and X, respectively, even though the local waveguide width is wider at these positions (positions B, D and Y). Expansions of the spot-size along the axial direction for $\theta =$ 0.2° and 0.4° are also shown in Fig. 5.18.

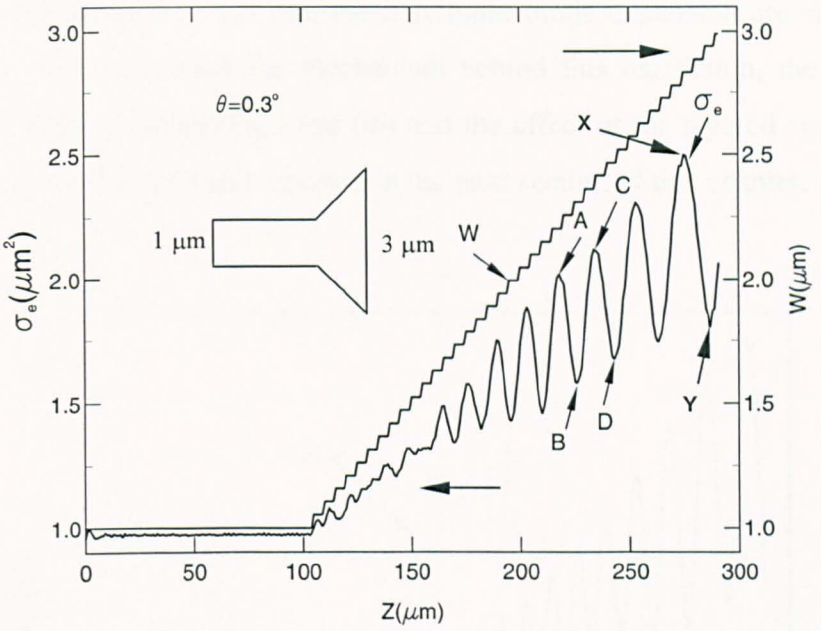

Fig. 5.16 Variations of the spot size and local width along the axial direction.

Oscillations in the spot-size variations, similar to that shown in Fig. 5.16, are also visible here. However, it can be observed that for a smaller tapered angle, such as $\theta =$ 0.2°, the overall rate of the spot-size expansion is slower, compared to that of for $\theta =$ 0.4°.

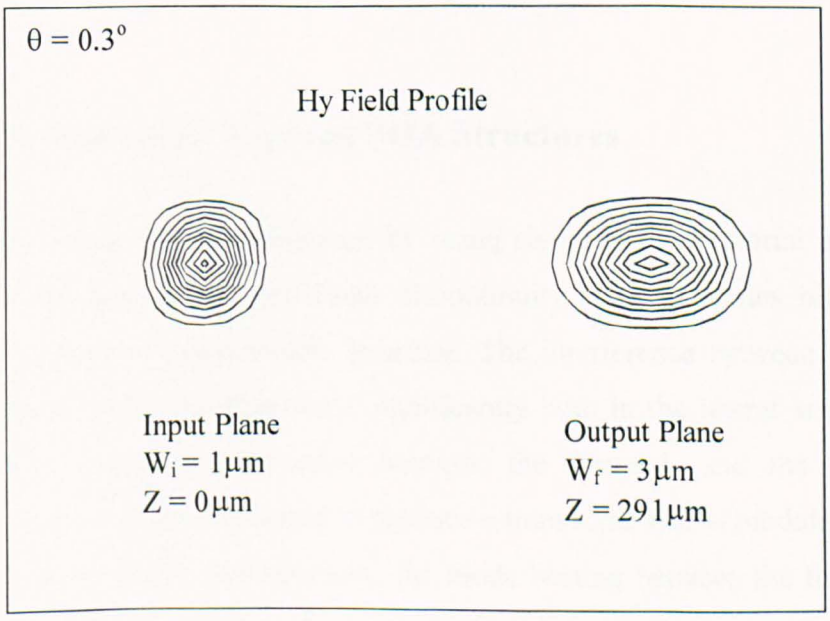

Fig. 5.17 Input and output beam profiles.

However, in both the cases, although their lengths were different, and since the final waveguide width is fixed at 3.0 μm, the maximum mode expansion are similar for both the cases. To understand the mechanism behind this oscillation, the resultant beam shapes, effect of remeshing steps (m) and the effect of the tapered angle, θ are then thoroughly investigated and reported in the next section of this chapter.

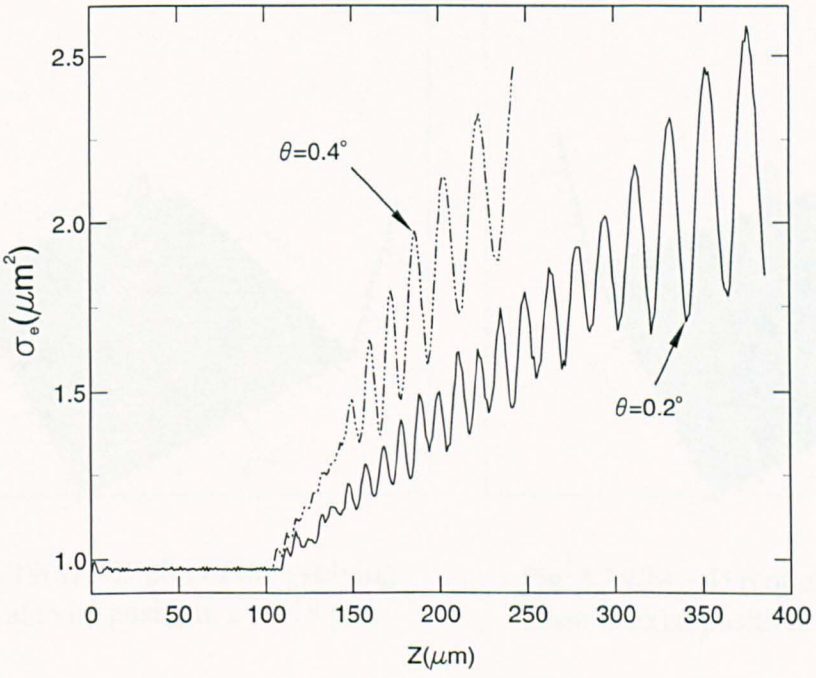

Fig. 5.18 Variations of the spot-sizes for two different tapered angles.

5.5 Mode Beating in Tapered SOA Structures

Numerically simulated results obtained by using rigorous full-vectorial approaches indicate that the presence of the finite discontinuity steps generates higher order modes along a tapered guided-wave structure. The interference between the modes allows the beam quality to deteriorate significantly both in the lateral and the axial directions. The nonlinear interaction between the forward- and the backward-propagating waves has been reported to produce a transverse spatial modulation of the phase and intensity [168], and similarly, the mode beating between the fundamental mode and the higher order modes may also contribute towards the beam filamentation.

The 3-D plots of the evolving beam at four different axial positions were examined and illustrated in Fig. 5.19. From the 3-D plots there was no significant observation to the evolving beam, as at all the different axial positions, the fields appeared to be similar.

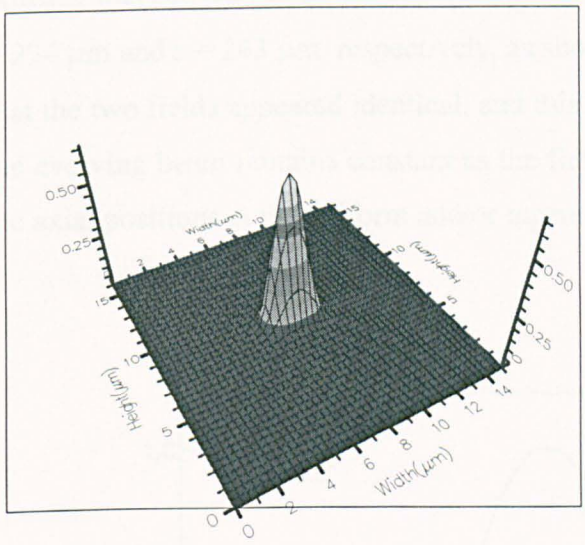

Fig. 5.19(a) 3-D plot of the evolving beam at axial position, $z = 218$ μm.

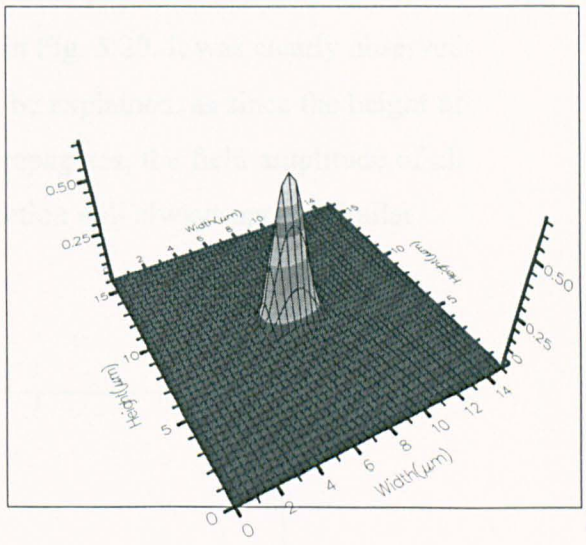

Fig. 5.19(b) 3-D plot of the evolving beam at axial position, $z = 225$ μm.

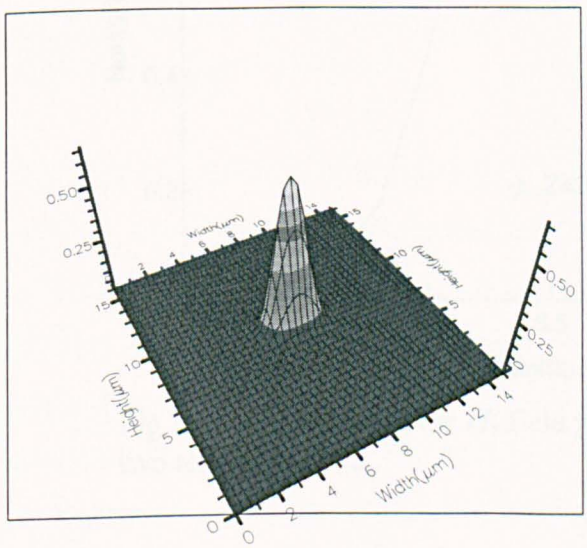

Fig. 5.19(c) 3-D plot of the evolving beam at axial position, $z = 234$ μm.

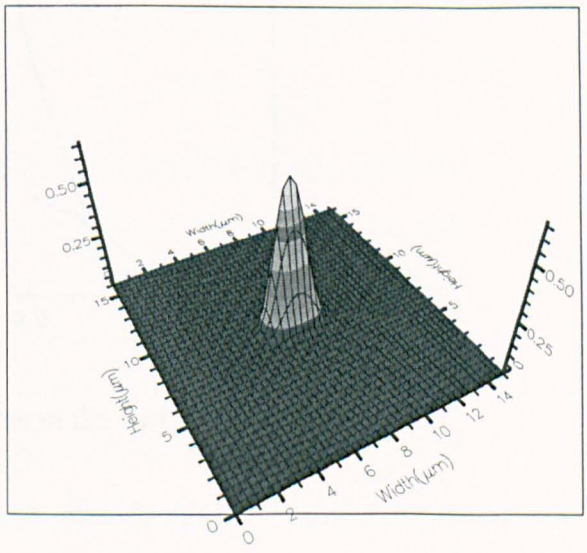

Fig. 5.19(d) 3-D plot of the evolving beam at axial position, $z = 243$ μm.

Fig. 5.19 3-D plots of the evolving beam at different axial positions.

However, it should be noted that as the field propagates along the tapered section there was always a slight increase to the width of the field and the height remained constant at H = 1 μm.

Further investigation was carried out on the field amplitude at the selected axial positions and some significant results were observed. The variations of the $\boldsymbol{H}_y$ field profiles was carried out in the vertical direction at axial positions 'C' and 'D' when z = 234 μm and z = 243 μm, respectively, as shown in Fig. 5.20. It was clearly observed that the two fields appeared identical, and this can be explained, as since the height of the evolving beam remains constant as the field propagates, the field amplitude of all the axial positions at the uniform and/or tapered section will always appear similar.

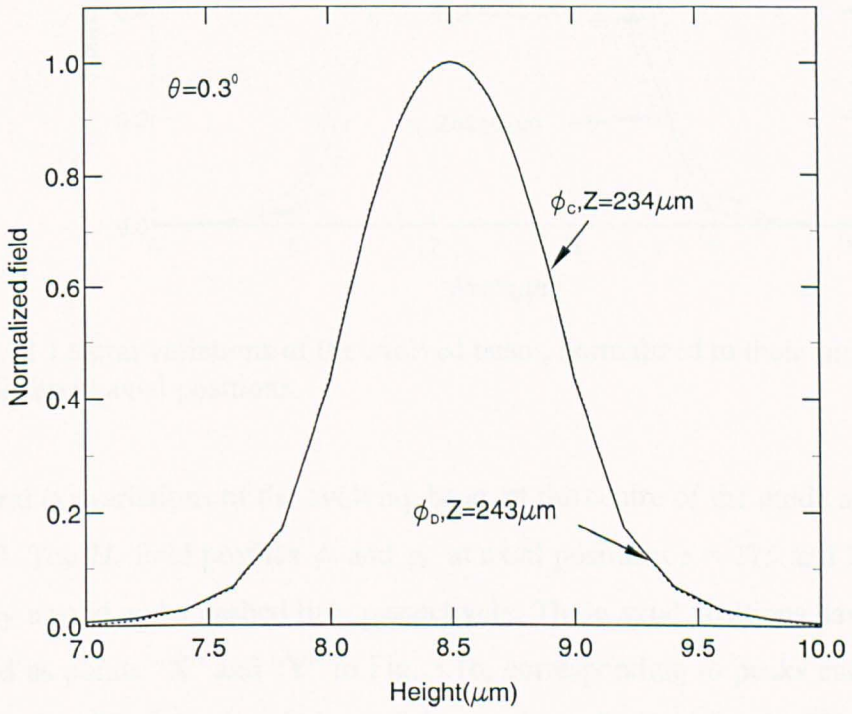

Fig. 5.20 Variations of the $\boldsymbol{H}_y$ field profiles in the vertical direction at two axial positions.

Fig. 5.21 shows the variations of the evolving beam along the horizontal (x) direction for $\theta = 0.3^{\circ}$. The dominant $\boldsymbol{H}_y$ field profiles, ϕ_A, ϕ_B, ϕ_C and ϕ_D at axial positions, z = 218μm, 225μm, 234μm, and 243μm, respectively, are shown here. These axial positions have also been identified as points 'A', 'B', 'C' and 'D' in Fig. 5.16,

corresponding to peaks and troughs in their spot-sizes. In these cases the maximum values of the H_y fields have been normalized to unity to enable a closer comparison of their profiles. It can be observed that the beam profile expands and contracts periodically in the lateral direction. At z = 218μm the field is narrow then expands at z = 225μm, then when z =234μm reduces then again at z =243μm it expands.

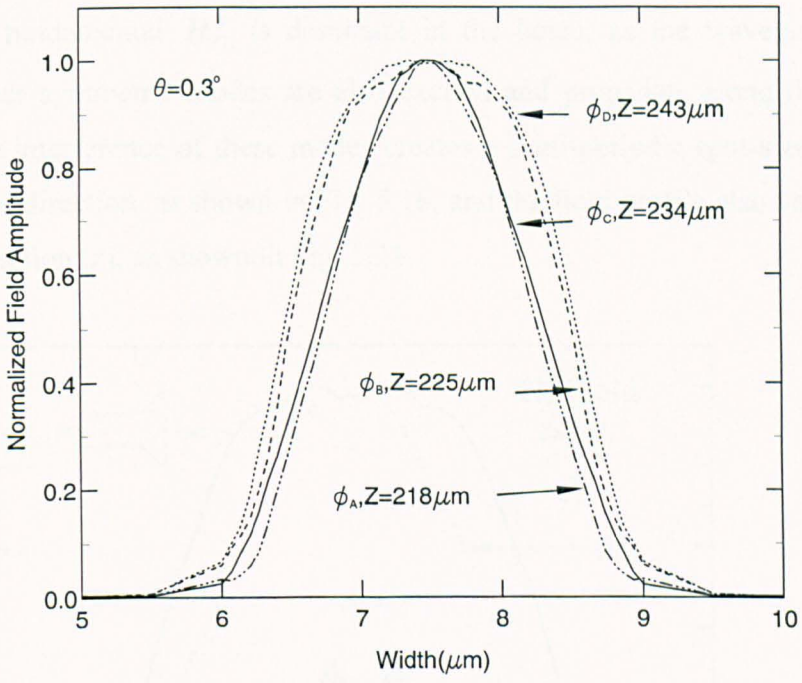

Fig. 5.21 Lateral variations of the evolved beam, normalized to their amplitudes, at four different axial positions.

The lateral (x) variations of the evolving beam at the centre of the guide are shown in Fig. 5.22. The H_y field profiles ϕ_X and ϕ_Y, at axial positions z = 275 and 287 μm, are shown by a solid and a dashed line, respectively. These axial positions have also been identified as points "**X**" and "**Y**" in Fig. 5.16, corresponding to peaks and troughs in their spot size. The lateral variations of the dominant H_y field for the TE mode along the center of the waveguide clearly indicate the interference between the fundamental $\left(H_{11}^{y}\right)$and the higher order modes. Since the structure is symmetric and the input beam was also symmetric, no anti-symmetric mode (H_{pq}^{y}, where p is even) is generated, and the evolving beam remains symmetric, as is shown in this figure. To identify the origin of the interference, the difference between the optical fields at these positions, ϕ_X - ϕ_Y, has also been plotted. This difference clearly shows the existence of the H_{31}^{y}

mode. The beat length shown in Fig. 5.16 does clearly correlate with the beat distance or with the $\Delta\beta(\Delta\beta = \beta_{11} - \beta_{31})$, where β_{11} and β_{31} are the propagation constants of the H_{11}^{y} and H_{31}^{y} modes, respectively.

The overlap integrals of these modes with the evolved beam were also obtained at these positions. At position "**X**", the modal coefficients of the normalized H_{11}^{y}, H_{31}^{y} and H_{51}^{y} modes were 0.93, 0.26, and 0.06, respectively. This clearly proved that although the fundamental H_{11}^{y} is dominant in the beam, as the waveguide width increases, other symmetric modes are also excited and propagate along the tapered structure. The interference of these modes creates a semi-periodic spot-size variation along the axial direction, as shown in Fig. 5.16, and the field profile also varies along the lateral direction (x), as shown in Fig. 5.21.

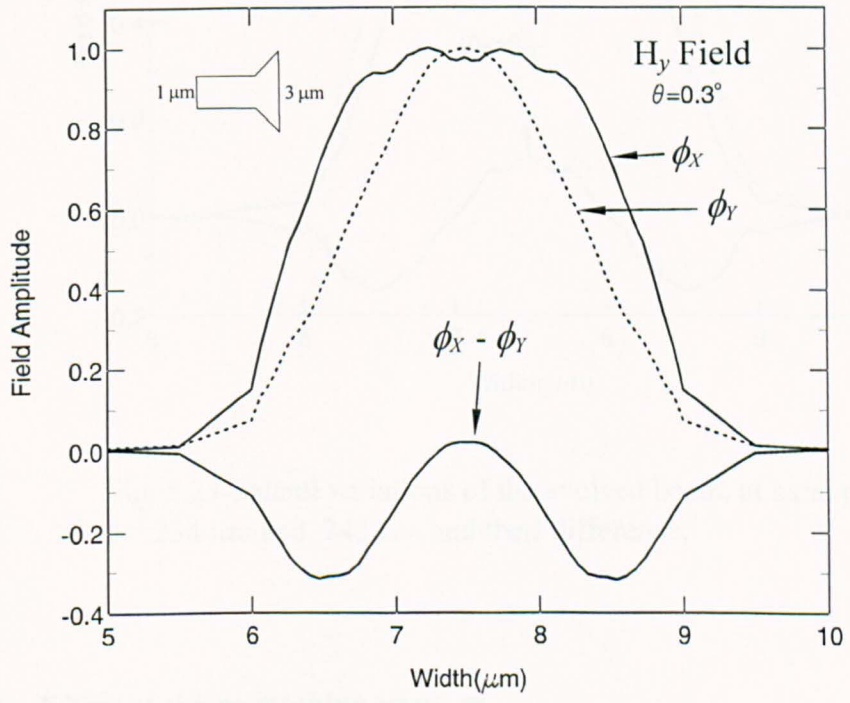

Fig.5.22 Variations of the $\mathbf{H}_y$ field profile for the TE polarized optical beam at axial positions, z = 275 μm and 287 μm and their difference.

The axial positions 'C' and 'D' were also investigated. For this type of field presentation, the peak field value z = 234 μm is higher than of z = 243 μm, as at this position the lateral spreading was smaller as shown in Fig. 5.23. The difference between the field values of these two positions, ϕ_D - ϕ_C, has also been plotted, which shows the existence of the H_{31}^{y} mode. The local width increases along the axial

direction and the values of β_{11} and β_{31} also increase with the local width. However, their difference reduces and consequently the beat length slowly increases. At position 'D' the modal coefficients of the normalized H_{11}^{y} and H_{31}^{y} modes were 0.95 and 0.20, respectively. This also shows that amplitude of the higher order modes increase along the z – direction.

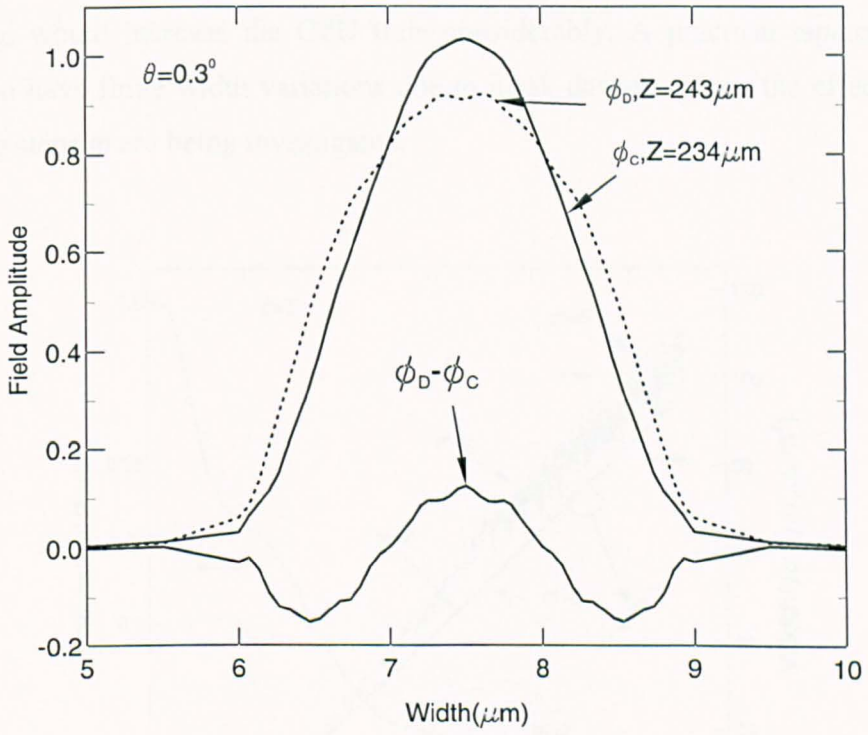

Fig. 5.23 Lateral variations of the evolved beam, at axial positions z = 234 μm and 243 μm and their difference.

5.5.1 Effect of the re-meshing steps, *m*

Subsequently, a more typical tapered structure with a large waveguide width [21], suitable for high-power semiconductor amplifiers, has been considered. In this case, the initial width of the guide is taken as 4 μm, with its core height being 1 μm. The core and the cladding indexes are taken as n_g = 3.22 and n_s = 3.17, respectively, at the operating wavelength of 1.50 μm. A much reduced index contrast for the diluted In-

GaAsP core $\Delta n = n_g - n_s = 0.05$ has been used in this case to reduce the number of the guided modes when the waveguide is expanded to a much wider width. Again, an initial 100-μm uniform section is considered prior to the tapered section so that the input field stabilizes before the start of the actual tapered section.

Although the change in the waveguide width could be considered at each propagating step (which, in this case, is 1 μm), the associated matrix calculation at each remeshing, would increase the CPU time considerably. A practical tapered device would also have finite width variations due to mask designs. Here, the effects of the remeshing steps m are being investigated.

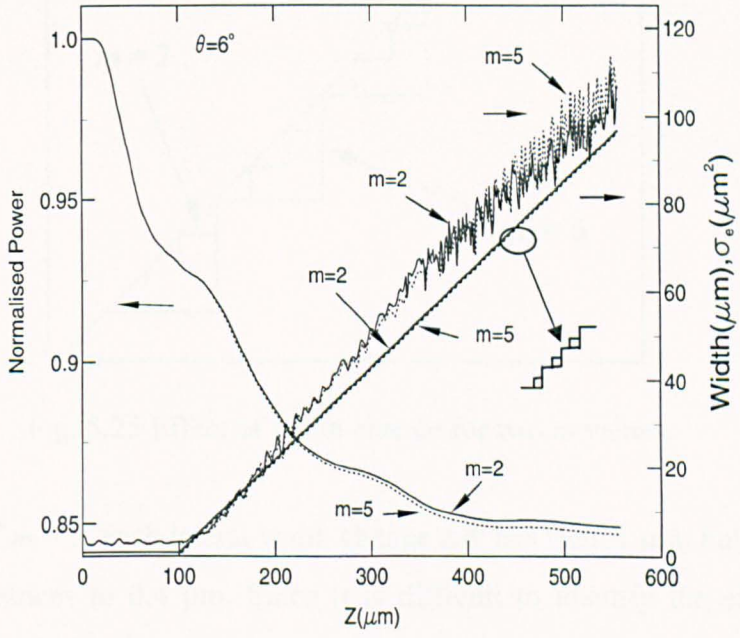

Fig. 5.24 Variations of the spot-size, local width and normalized power for two different remeshing schemes.

The variations of the spot-size, local width and the normalized power along the axial direction for the two different values of m are shown in Fig. 5.24. In this case, the tapered angle is 6°, and the tapered section is 457 μm long to achieve the 100 μm final width from its 4 μm initial width. It can be observed that the spot-size expands as the width of the tapered section increases: however, both the curves (for m = 2 and 5) are almost identical. Although the oscillations are clearly visible, it can be noted that their

periodicity is much less pronounced than that of the curve shown in Fig. 5.16 for the earlier structure. The reason for such a less pronounced variation is that a waveguide with a large width can support a large number of guided modes, and the rapid change in its width excites a large number of these modes. However, the modal interference between such a large number of modes, with their different beat lengths, makes the spot-size variation much less prominent, although it does still exist. It can also be noted that the optical power loss is almost the same for both cases, but for $m = 5$, this is slightly larger due to a larger discontinuity step as shown in Fig. 5.24.

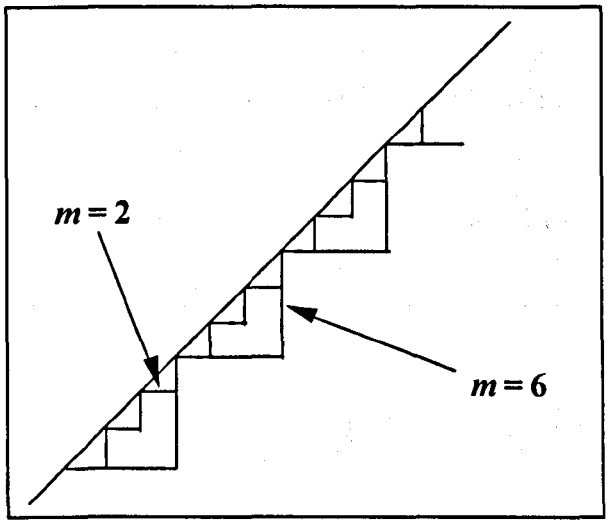

Fig. 5.25 Effect of width change for two m values.

For the case of $m = 5$, each lateral width change ΔW has been 1 μm, but in the case of $m = 2$, this reduces to 0.4 μm. Since it is difficult to identify the effect of width changes from the staircase-like line, a magnified view of the line is shown in Fig. 5.25 (it should be noted, however, that in this figure, m was taken as 2 and 6, respectively to show clearly the effect of the discontinuity).

5.5.2 Effect of the Tapered Angle

The optical loss depends on the taper angle. The variations of the optical power with the axial distance for three different taper angles are shown in Fig. 5.26. In this case, the lengths of the tapered sections are 1375, 686, and 457 μm (beyond the first 100 μm uniform section), for taper angles of 2^0, 4^0, and 6^0, respectively, to achieve the

100 μm final width. It can be noted that in all three cases, the power loss in the first 100 μm were the same, since these uniform sections were identical for all the cases. Subsequently, the rate of power loss becomes higher for a larger tapered angle. Although such a larger angle requires a shorter tapered section to achieve the 100 μm final width, however, the total loss is higher, due to larger discontinuity step encountered.

The variations of the spot-size for these three different tapered angles are shown in Fig. 5.27. The diffraction angle, ϕ, was calculated using equation (2.37). Therefore, for $W_i = 4$ μm, diffraction angle, $\phi = \frac{\lambda z}{\pi W_o} = \frac{1}{8} radians$ (approximately 7.0^0), where λ is the wavelength, W_o is the width of the beam which increases with z, z is the propagation distance. It should be noted that the rate of increase in the width is proportional to the wavelength and inversely proportional to the initial width of the beam.

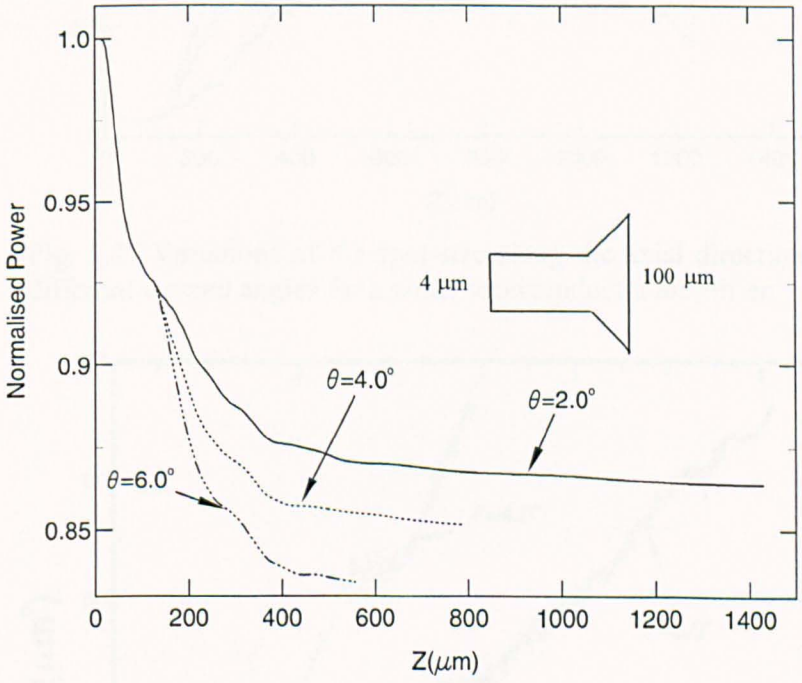

Fig. 5.26 Variations of the normalized power for three different tapered angles.

It can be noted that for the smaller tapered angle, the rate of the spot-size increase is smaller. However, for the same final width ($W_f = 100$ μm), the final spot- sizes at the end of the tapered sections are very similar for all the three cases.

Oscillations are also clearly visible, but because of the interference between many of these modes (with their different beat lengths), the periodicity is less pronounced, but

in general, the oscillations amplitudes are lower for smaller angles. However, it has been noticed that if θ is larger than 10.0^0, then the spot-size expansion is limited by the diffraction angle, ϕ, which depends on the waveguide aperture and this being equal to 7.0^0, when the taper angle increased faster than this, spot size did not expand at a faster rate as shown in Fig. 5.28.

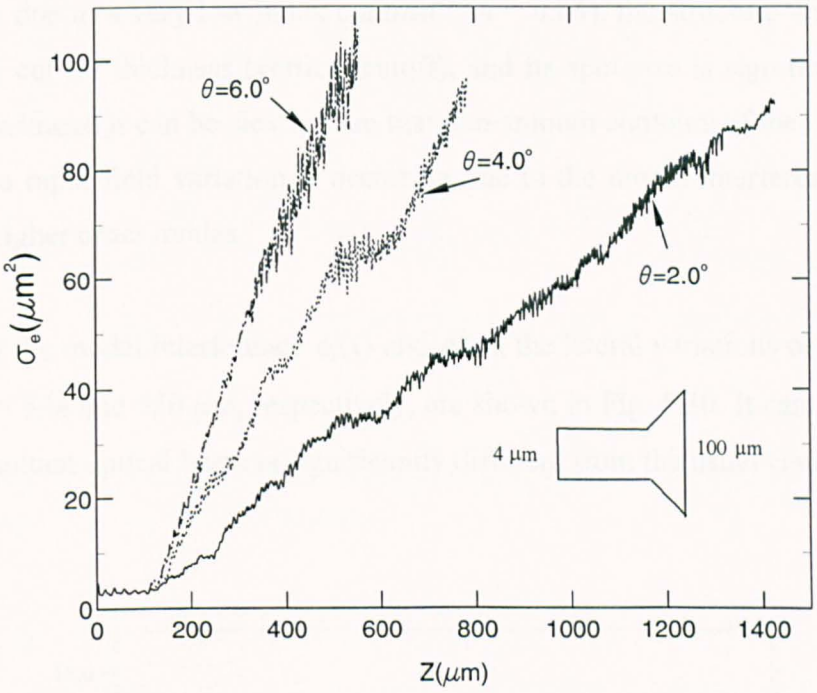

Fig. 5.27 Variations of the spot-size along the axial direction for three different tapered angles for a wider semiconductor amplifier.

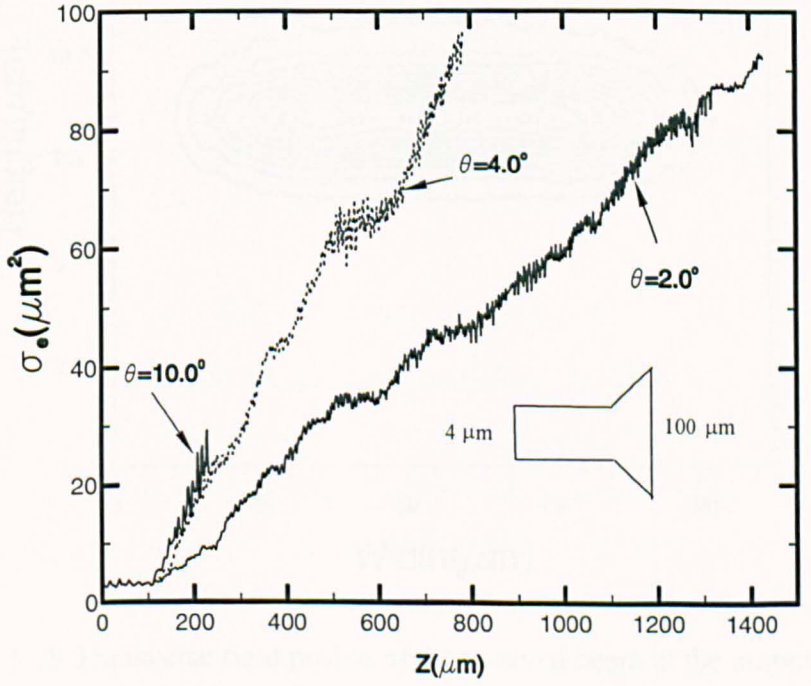

Fig. 5.28 Spot-size expansion limited by the diffraction angle.

5.5.3 The Output Field Profile

The output field profile at the end of the tapered section when W_f = 100 μm is shown in Fig. 5.29. In this case, the horizontal spot-size is clearly controlled by the local width, which was 100 μm at the end of the tapered structure. Its vertical spot-size was constant, fixed by the core thickness, and in this case, although the core thickness was only 1 μm, due to a very low index contrast (Δn = 0.05), the structure was operating close to its cut-off thickness (vertical cutoff), and its spot-size is significantly larger than the thickness. It can be clearly seen that non-smooth contours of the optical beam show that a rapid field variation is occurring due to the modal interference between the many higher order modes.

To identify the modal interference $\phi_1(x)$ and $\phi_2(y)$, the lateral variations of the evolved beam at z = 534 and 550 μm, respectively, are shown in Fig. 5.30. It can be observed that the resultant optical beam is significantly different from the usual Gaussian

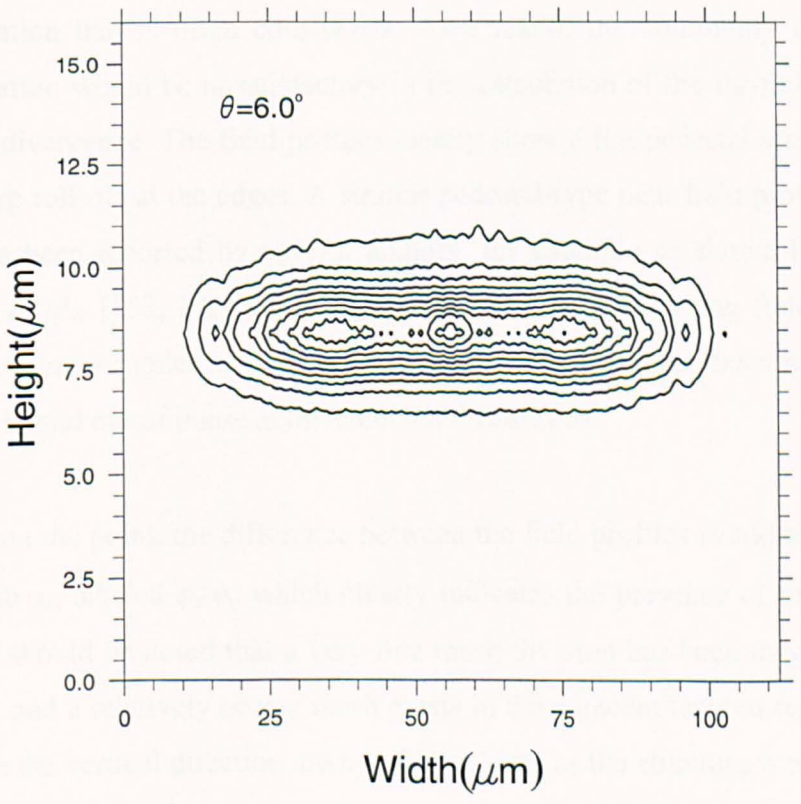

Fig. 5.29 Transverse field profile of the evolved beam at the output plane.

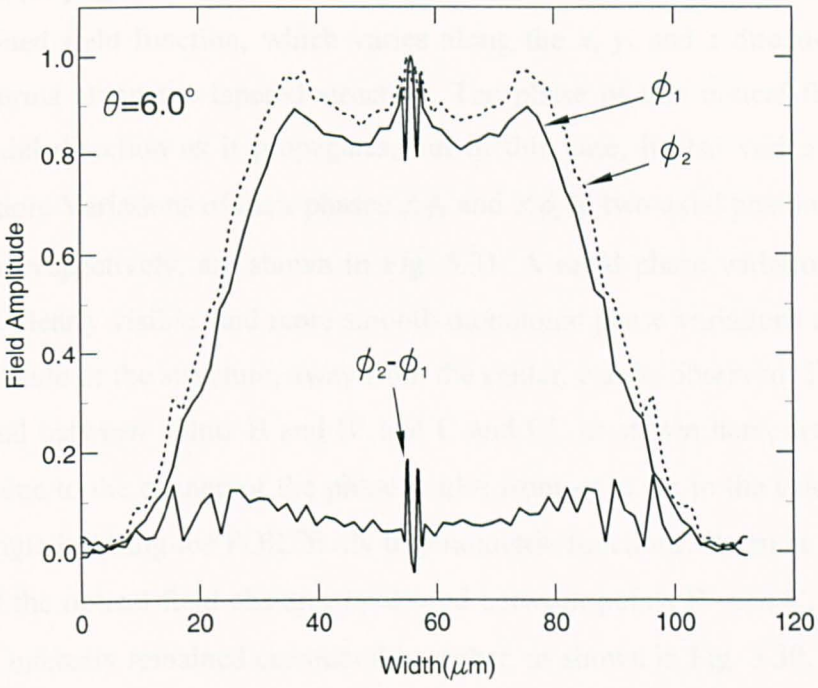

Fig. 5.30 Lateral variation of the evolved beam at two different axial positions and their difference.

approximation that is often considered. As a result, the commonly used Gaussian approximation would be unsatisfactory in the calculation of the far-field profiles and the beam divergence. The field profiles clearly show a flat pedestal area in the centre and a sharp roll-off at the edges. A similar pedestal-type near field profile with many spikes has been reported by several authors, for example as shown in the work of Goldberg *et al.*, [153, Fig. 19]. However, some sharp oscillating fields, originating from higher order modes, are also visible near the centre. It has been noted that these peaks are in and out of phase at different axial positions.

To illustrate the point, the difference between the field profiles ϕ_1 and ϕ_2 is also shown in by a curve, labeled ϕ_2-ϕ_1, which clearly indicates the presence of the higher order modes. It should be noted that a very fine mesh division has been used in the central core area, and a relatively coarse mesh exists in the adjacent tapered region. The field profiles in the vertical direction are not shown here, as the structure was single-moded in the vertical direction, and thus the associated vertical beam profile remains unchanged along the tapered structure.

In the beam-propagation approach, the evolving optical field is considered as a complex valued field function, which varies along the x, y, and z directions as the beam transforms along the tapered structure. The phase of this optical field varies along the axial direction as it propagates, but in this case, it also varies along the lateral direction. Variations of their phases $\angle\phi_1$ and $\angle\phi_2$ at two axial positions $z = 534$ and 550 μm, respectively, are shown in Fig. 5.31. A rapid phase variation near the center (A) is clearly visible, and more smooth monotonic phase variations in both the left and right side of the structure, away from the center, can be observed. The sudden phase reversal between points B and B' and C and C', as shown here, are artificial, these being due to the change of the phase angles from $-\pi$ to $+\pi$ in the calculation of the arctan angle by using the FORTRAN trigonometric functions. It can be noted that the phase of the optical field changes by 2π rad between points B' and C, where the optical field intensity remained considerably higher, as shown in Fig. 5.30. It has also been observed, but not shown here, that inside the guide core, the phase angle is constant along the vertical direction; however, outside the core region, there is a rapid π rad phase change in the cladding region.

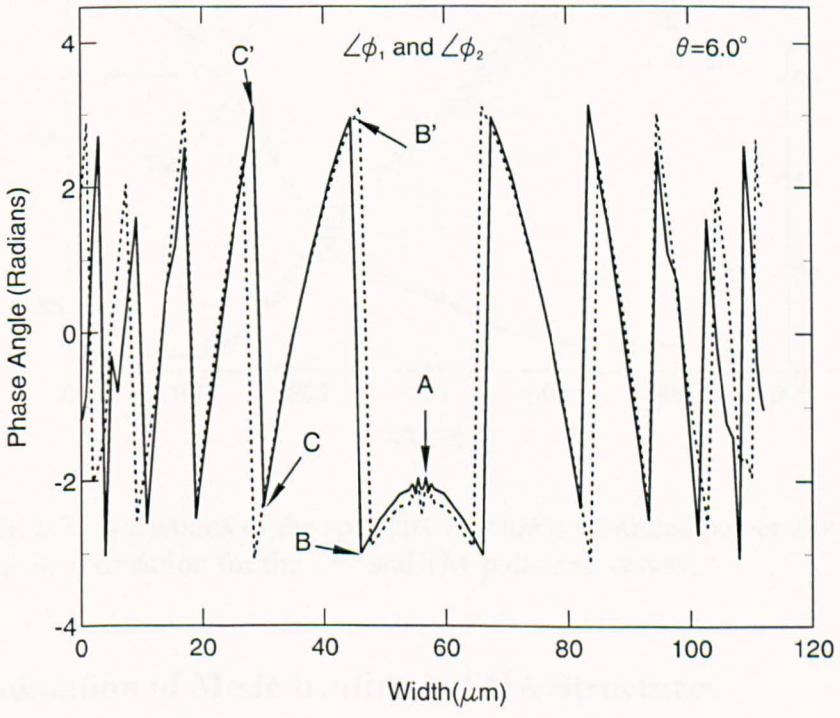

Fig. 5.31 Variations of the phase angle of the evolved beam along the lateral direction (x) at two different axial positions.

5.6 Comparison between the TE- and TM-polarized modes

A hybrid transverse-magnetic (TM) mode is also launched into the same structure with a taper angle $\theta = 6^0$. The variations of the spot-size and the normalized power along the axial direction (z) are shown in Fig. 5.32 by solid and dashed lines, for the TM and TE modes, respectively. It can be observed that the power loss and the spot variations are almost similar for both the polarizations. In this case, the index contrast (Δn) of the waveguide in both the lateral and vertical directions were very small and equal to 0.05. However, for an optical guided-wave structure with a higher index contrast, or a slanted sidewall, or a curved section, it is expected to show a higher polarization-dependent performance.

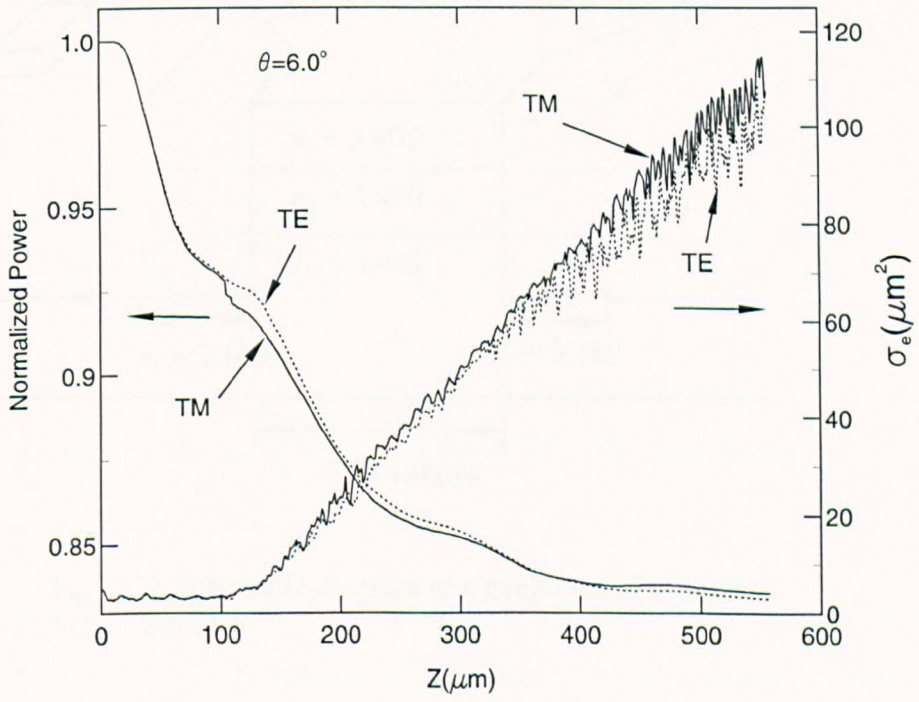

Fig. 5.32 Variations of the spot-size and the normalized power along the axial direction for the TE- and TM-polarized waves.

5.7 Elimination of Mode Beating in SOA Structures

In this work, a deep-etched semiconductor optical amplifier [149] was considered to study rigorously the mode beating in SOA. Furthermore, an approach has been used to

eliminate the mode beatings, however, the approach was seen to be costly and generally, increase the computational time.

The deep-etched tapered SOA is shown in Fig. 5.33. In this particular case the core height (h) is taken as 0.1 μm, with an initial width (W_i) of the guide as 1.0 μm and this width is adjusted along the tapered structure. The core and cladding indices at the operating wavelength of 1.55 μm were taken as n_g = 3.480 and n_s = 3.402, respectively, generating an index contrast, $\Delta n = n_g - n_s$ = 0.078. Based on this structure, initially, the tapered angle, θ, is taken as 0.3° and the width is varied symmetrically to achieve the final width (W_f) of 8 μm. An initial 100 μm uniform section is considered prior to the tapered section, before the actual tapered section.

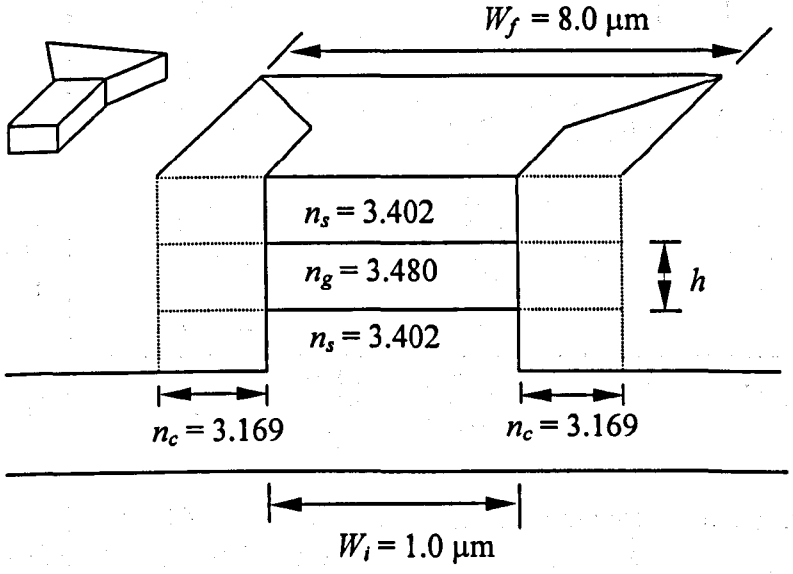

Fig. 5.33 Schematic diagram of a deep-etched tapered SOA Structure.

The spot-size and its variation along the axial direction can illustrate the evolution of the optical beam along the tapered waveguide. The variations of the spot-size along the axial direction with different m values are shown in Fig. 5.34. It can be clearly seen that for higher m values (i.e., m = 30) the oscillations were visible compared to m = 5. However, for m = 5 the amplifier length was shorter and the oscillations were reduced dramatically as the evolving beam propagates, which clearly indicates the non-existence of the higher order modes with the fundamental (H_{11}^{y}) mode. However,

one significant feature was observed when m = 5, the spot-size expansion stabilizes and settles down before further expansion as shown in the inset on the left side of Fig. 5.34. This feature will be discussed in a later stage of this chapter.

To prove the existence of mode beating when a large value of m = 30 was used, the peaks and troughs of the spot-size were plotted with their differences at different axial positions i.e., z = 530 μm, 538 μm and 546 μm.

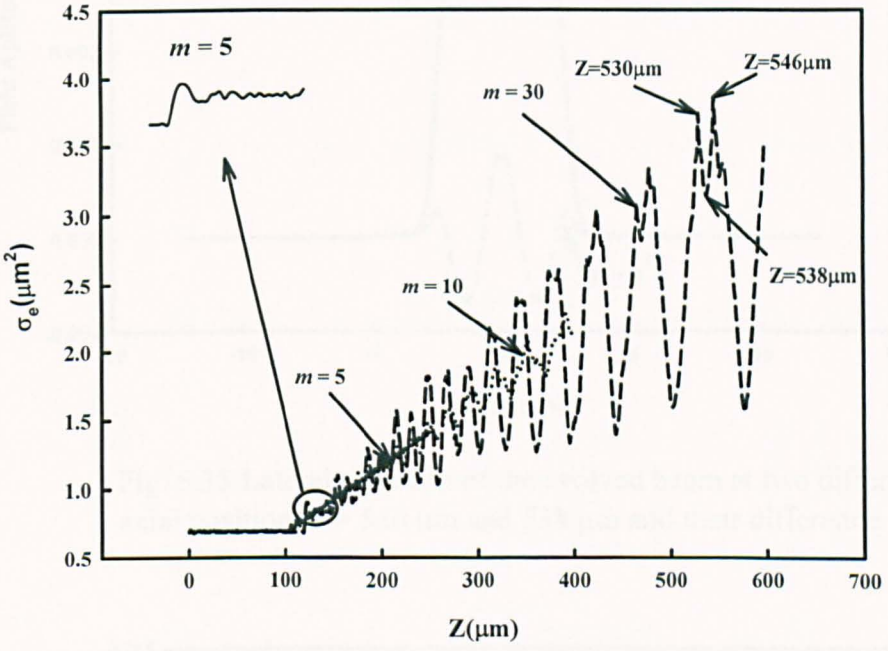

Fig. 5.34 Variations of the spot-size along the axial direction with different m values.

The H_y field profiles ϕ^1 and ϕ^2 at axial positions, z = 530 μm and 538 μm, are shown by a solid and dotted lines, respectively, in Fig. 5.35. As explained earlier in this chapter the field profile at centre of the waveguide clearly indicates the interference between the fundamental (H_{11}^y) and higher order modes. The difference between these two points, ϕ^1 and ϕ^2, has also been plotted as dashed line in the figure, which shows clearly the existence of the H_{31}^y mode. Furthermore, when the variations of the evolving beam at axial positions z = 538 μm and 546 μm and their difference plotted as shown in Fig. 5.36, it clearly indicated the existence of the H_{51}^y mode. This

hypothesis proved the interference between the higher order modes and the fundamental (H_{11}^{y}) mode, which occurs during the field propagation.

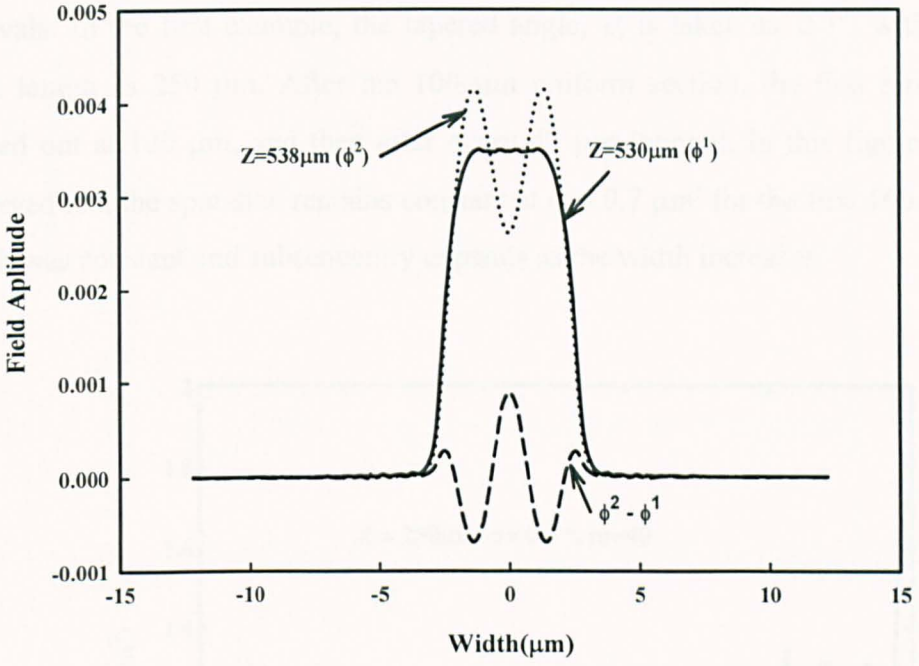

Fig. 5.35 Lateral variation of the evolved beam at two different axial positions z = 530 μm and 538 μm and their difference.

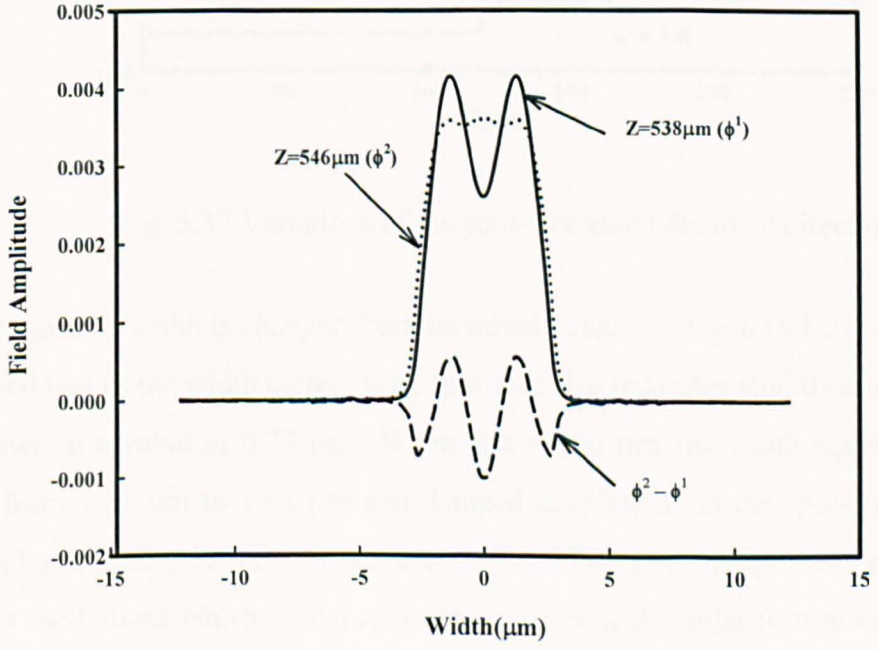

Fig. 5.36 Lateral variation of the evolved beam at two different axial positions z = 538 μm and 546 μm and their difference.

The variation of the spot-size along the axial direction (z) is shown again in Fig. 5.37. In this case to see the effect of the width change initially a large remeshing step, m, was used. In this work the axial step, Δz, is taken as 1.0 μm, and if the m is taken as 40, then the remeshing along the axial direction is carried out at every 40 μm intervals. In the first example, the tapered angle, θ, is taken as 0.3^0, with the total SOA length as 250 μm. After the 100 μm uniform section, the first remeshing is carried out at 120 μm, and then after every 40 μm interval. In this figure it can be observed that the spot-size remains constant at $\sigma = 0.7$ μm² for the first 100 μm as the width was constant and subsequently expands as the width increases.

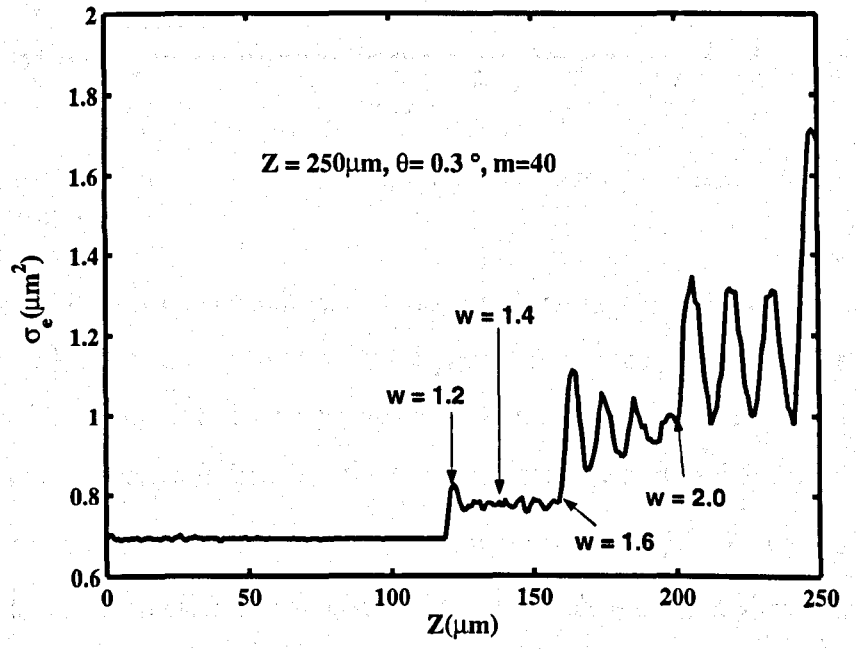

Fig. 5.37 Variations of the spot-size along the axial direction.

At z = 120 μm, its width is changed from its initial value of 1.0 μm to 1.21 μm. It can be observed that as the width increases its spot-size also increases slightly and quickly settles down to a value of 0.77 μm². When at z = 160 μm, the width again changes abruptly from 1.21 μm to 1.63 μm and damped oscillations in the spot-size appear which settles around 0.91 μm². At the next step, z = 200 μm, the spot-size expansion undergoes oscillations which do not appear to stabilize and similar feature can also be noted at 240 μm.

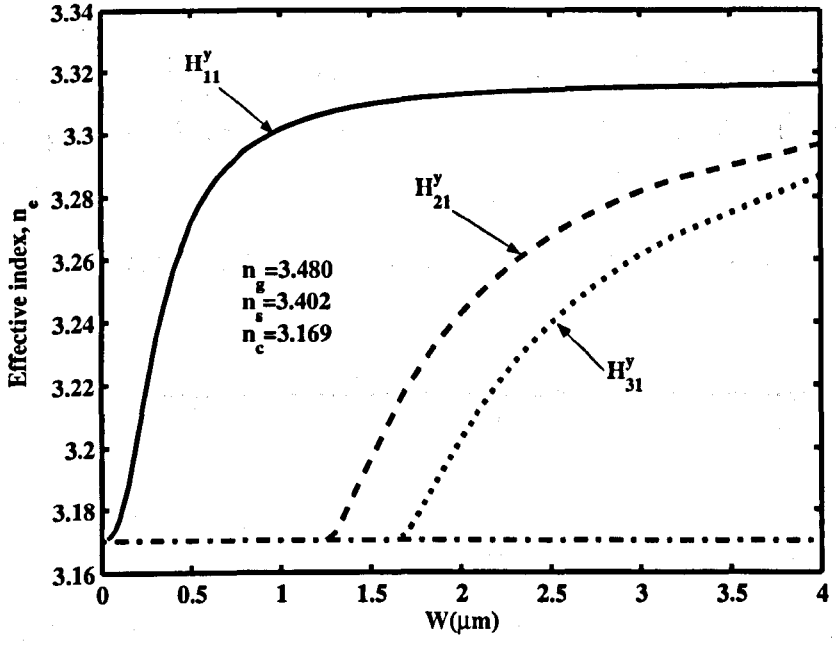

Fig.5.38 Variations of the effective indices with the waveguide width (W).

The interference between the fundamental mode and the higher order modes is clearly seen in Fig. 5.37. Next, a thorough investigation is carried out to understand the mechanism of the spot-size during propagation through the stepped tapered section. Variations of the effective indices for the fundamental H_{11}^{y} and higher order H_{21}^{y} and H_{31}^{y} modes with the waveguide widths, W, are shown in Fig. 5.38 with a solid, a dashed and a dotted lines, respectively. A horizontal chained line shows the cutoff conditions for these modes. It can be observed that the second H_{21}^{y} and the third H_{31}^{y} modes reach their cutoff conditions when the waveguide widths are 1.31 μm and 1.6 μm respectively.

When z = 120 μm, the higher order modes were generated at the discontinuity plane, as it was necessary to satisfy the boundary conditions. However, these modes attenuate rapidly, as shown in Fig. 5.37, since at local W = 1.21 μm, these higher order modes are below their cut-off conditions. Due to the symmetrical nature of the tapered structure, no asymmetric higher order mode (H_{mn}^{y}) where m is even, is excited when a symmetrical input field is used. When z = 160 μm, the local width changed to

1.63 μm, the generated H_{31}^{y} is very lossy by being close to the cutoff condition and attenuates rapidly with damped oscillations, as shown clearly in Fig. 5.37. However, beyond 200 μm, as $W > 2.05$ μm, the generated H_{31}^{y} will not dissipate, as this mode is now well guided. This yields more pronounced oscillations due to the interference between the H_{11}^{y} and H_{31}^{y} modes and the beat length strongly correlates with the local Δβ between the H_{11}^{y} and H_{31}^{y} as shown in the Figs. 5.39 and 5.40.

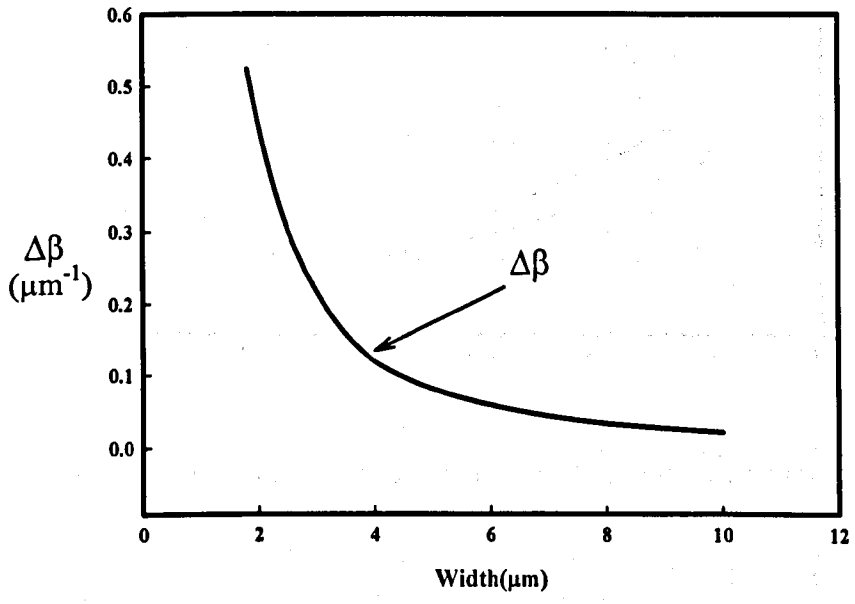

Fig. 5.39 Variations of the local Δβ as the width (W) increases.

In Fig. 5.39 when the width of the waveguide is increased beyond the cut-off, it is clearly observed that $\Delta\beta = \beta_{11} - \beta_{31}$, for the H_{11}^{y} and H_{31}^{y} respectively, decreases sharply as the width increases, however when $W = 6.0$ μm, it decreases slowly as W increases further. This is mainly because when a much smaller waveguide width is used only the fundamental and second order modes are excited, but if the width is increased further it excites other higher order modes as shown in Fig. 5.40 which leads to a more complex mode beating as discussed earlier.

The variations of the beat length, expressed as $L_B = \frac{\pi}{\Delta\beta}$, with width are shown in Fig. 5.40. Due to the different cutoff regions for the modes H_{11}^{y}, H_{31}^{y} and H_{51}^{y} the L_B obtained from different Δβ varied. However, they all appeared to have started from a

similar L_B value and increased steadily as the width was increased. It shows that even though the fundamental mode propagates along the waveguide, the excitation of higher order modes were observed, especially for tapered structures as the width will be constantly changing in the tapered section.

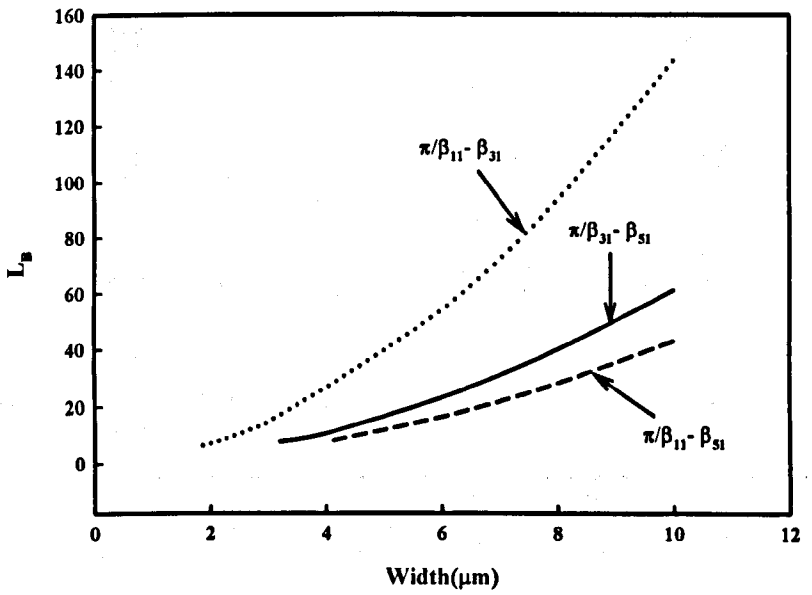

Fig. 5.40 Variation of beat length (L_B) to the width (W).

Variations of the beat length along the axial direction for different m values are shown in Fig. 5.41. It is clearly observed that as the evolved beam propagates the beat length for m = 20 and 30 are mostly identical, however after z = 800 μm, for m = 30 the beat length is slightly lower compared to m = 20. To link the beat length, as obtained from the BPM simulation, its variation with the local waveguide width is also calculated and shown in Fig. 5.42. Moreover, when the width increases the beat length for both the m values were identical and increased steadily as shown in the figure.

This result showed that the m value has no significant impact in this particular case to the evolving mode along the axial direction. However, it should be noted that a finer mesh should be used for better results. For comparison, the variations of the beat length when the width increases from FEM calculation ($L_B = \frac{\pi}{\Delta\beta}$) and BPM analysis are shown together in Fig. 5.43. It should be noted here that a similar waveguide with identical refractive indices were used. From the BPM result the L_B started at

z = 216 μm with a width of 2.047 μm. At this axial position, the excitation of H_{31}^{y} was observed which contributed to the β_{31} value that yields the first $\mathbf{L_B}$ approximation.

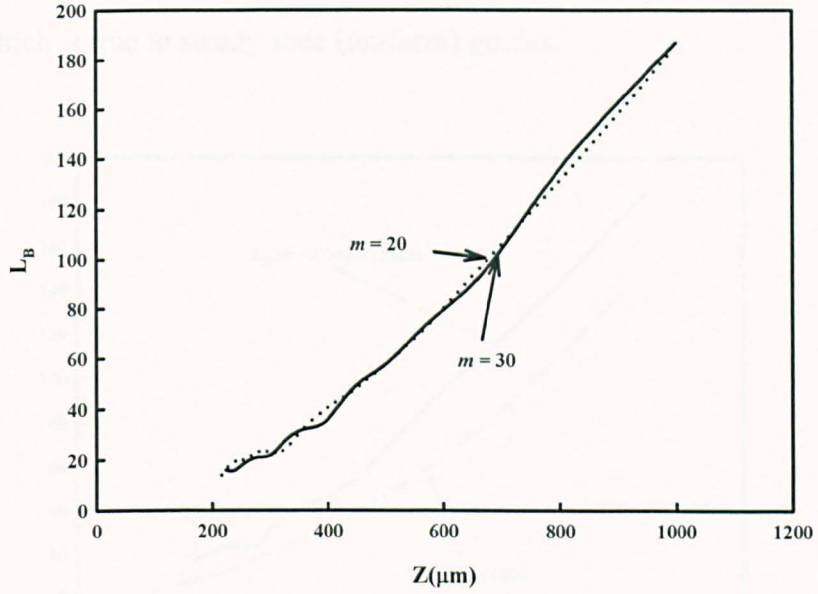

Fig. 5.41 Variations of the beat length along the axial direction for different values of m.

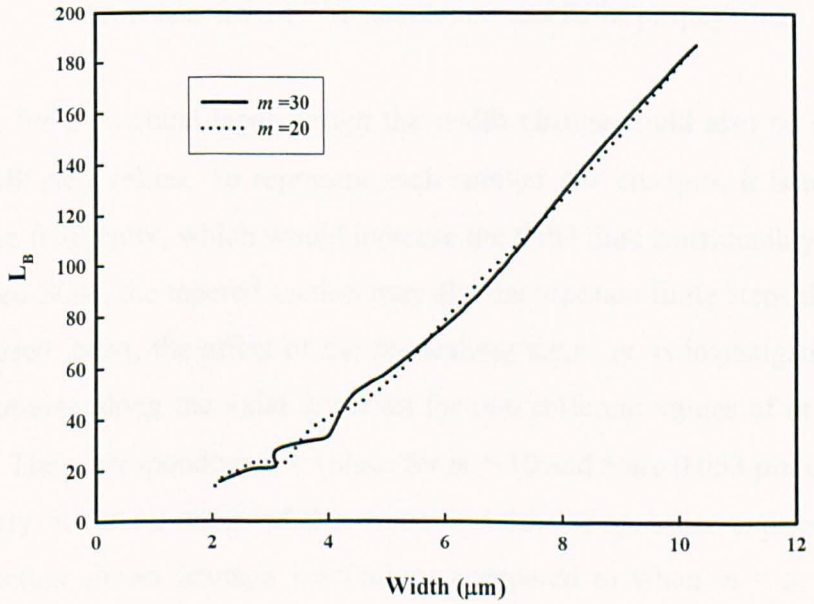

Fig. 5.42 Variations of the beat length as the width increases along the axial direction for different values of m.

It can clearly be seen that both curves increases as the width increased. However, the fundamental mode stabilizes and settles during propagation along the waveguide, this causes the L_B in the BPM analysis to appear unsteady at the start before settling down as shown in Fig. 5.43. The agreement between the curves is true, however, it should be noted that local width of BPM can only roughly correlate with the FEM modal solution, which is true to steady state (uniform) guides.

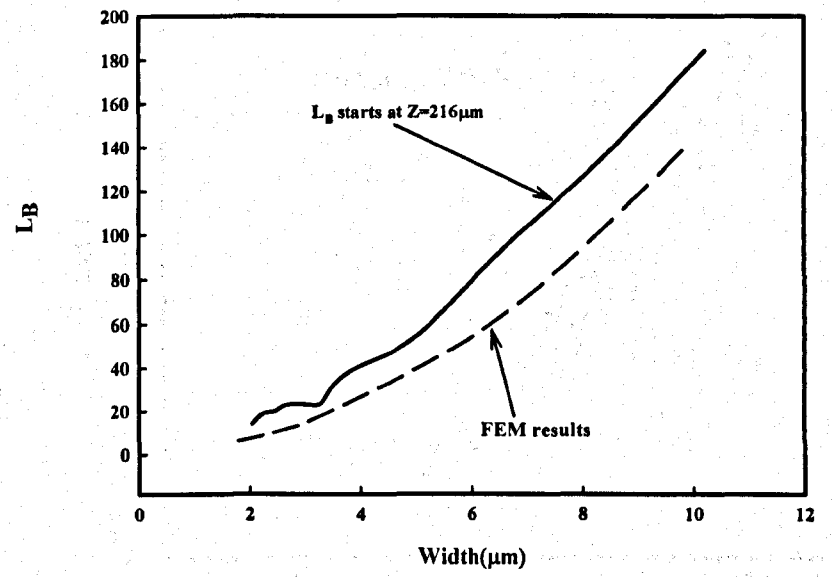

Fig. 5.43 Variations of the beat length when the width increases from FEM calculation and BPM propagation.

However, for a practical taper design the width change could also be slower with a smaller ΔW step values. To represent such smaller ΔW changes, it is required to re-mesh more frequently, which would increase the CPU time considerably. However, in a fabricated SOA, the tapered section may also incorporate finite steps due to the type of mask used. Next, the effect of the re-meshing steps, m, is investigated. Variations of the spot-size along the axial direction for two different values of m are shown in Fig. 5.44. The corresponding ΔW values for m = 10 and 5 are 0.053 μm and 0.026 μm, respectively. It can be observed that when m = 10, the spot-size expansion along the axial direction shows stronger oscillations compared to when m = 5, which shows significantly smooth variations and the peaks and troughs of the spot-size expansion were reduced dramatically. It was observed that any further reduction of the re-meshing step, m, did not modify the spot-size expansion property, as shown in Fig.

5.45. It has also been observed, that for m = 5, when the difference between the fields at two axial positions z = 206 and 207 μm almost identical were plotted and compared as shown in Fig. 5.46, no *stronger* existence of higher order modes was visible. The magnitude of the higher order field is very small and it should be noted that the highly magnified scale is used on the right hand side to plot the field differences. To understand this an approach has been proposed.

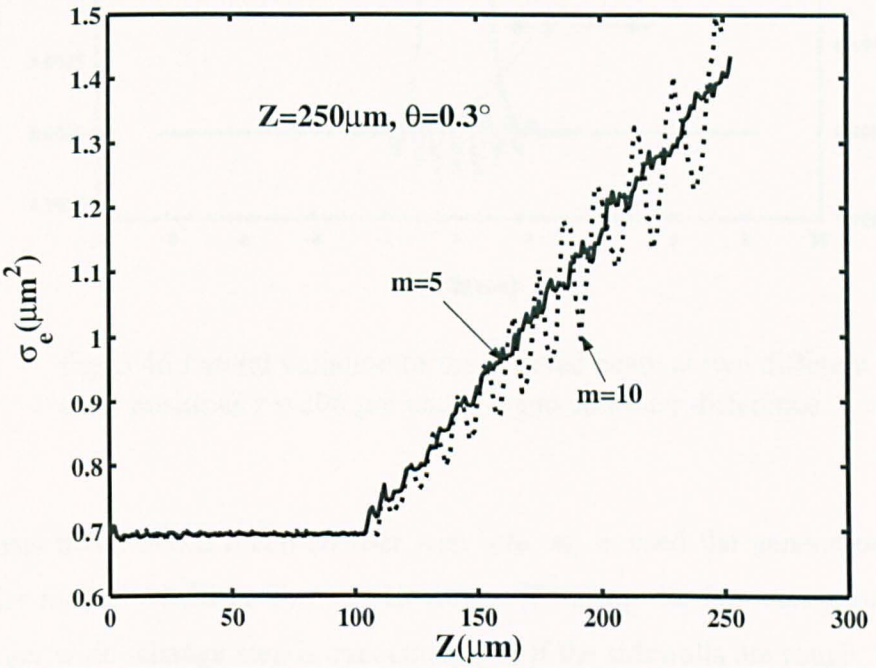

Fig.5.44 Variations of the spot-size along the axial direction with different step size (m) values.

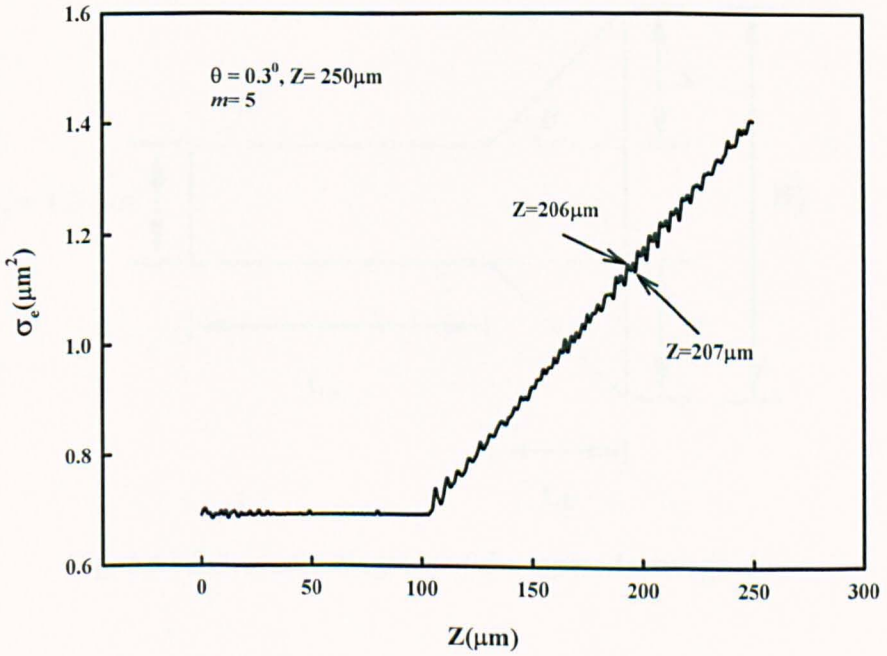

Fig. 5.45 Variations of the spot-size along the axial direction.

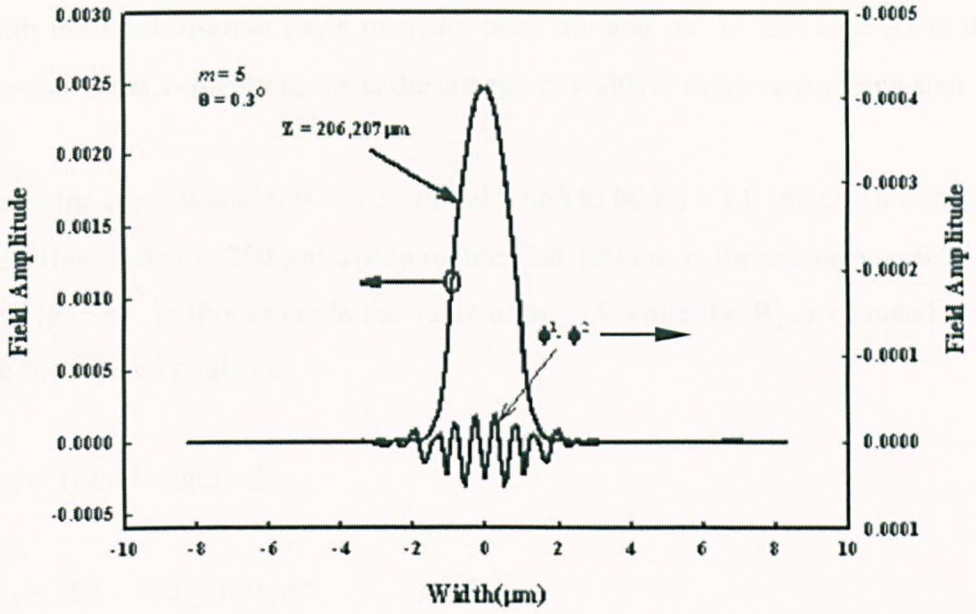

Fig. 5.46 Lateral variation of the evolved beam at two different axial positions z = 206 μm and 207 μm and their difference.

This suggests that when a much smaller step size, m, is used the generation of the higher order modes would be limited. However, if during the fabrication of such a SOA, a larger width change step is encountered or if the sidewalls are rough, then the modal interference between the modes could exist.

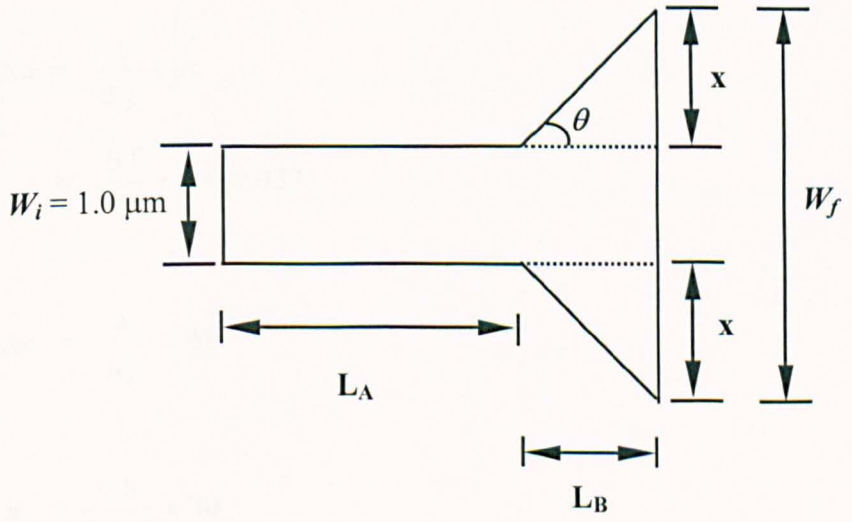

Fig. 5.47 Schematic diagram of the tapered waveguide.

During this study, it was also identified that at every remeshing stage, it should also match with the discretisation steps in width both Δw and Δx. In this case Δx is the mesh division in the x-direction, Δw is the change in width at every re-meshing step.

Lets assume the tapered angle, $\theta = 0.3^0$, initial width to be $W_i = 1.0$ μm and the length of the amplifier to be $z = 250$ μm assuming the first 100 μm is the uniform section as shown in Fig. 5.47. In this example the value of $m = 5$ while the W_f is changed with respect to the tapered angle i.e.,

$$\mathbf{L_B} = \text{Total Length} - \mathbf{L_A}$$

$$\mathbf{L_B} = 250 - 100 = 150\ \mu\text{m}$$

$$\mathbf{x} = \tan 0.3^0 * 150 \approx 0.8\ \mu\text{m}$$

$$\therefore \quad W_f = 2\left(\tan 0.3^0 * 150\right) + W_i$$

$$\therefore \quad W_f \approx 2.6\ \mu\text{m}$$

In this approach, to eliminate the excitation of higher order modes and limit the oscillations we assume, $\Delta w = \Delta x$;

$$\Delta w = \frac{x}{L_B} \times m$$

$$\therefore \quad = \frac{0.8}{150} \times 5 = 0.027$$

$$\Delta x = \frac{x}{n_x} = \Delta w$$

$$\therefore \quad n_x = \frac{0.8}{0.027} \approx 30$$

where $\mathbf{L_A}$ is the uniform section of the amplifier, $\mathbf{L_B}$ is the tapered section, W_f is the final width, x is the x-dimension where the field widens as the evolving beam propagates along the axial direction, and n_x is the number of horizontal (x), mesh divisions in the flared part, x. For this approach to be efficient and effective for longer tapered sections the tapered angle, θ and the value of m should be small, mainly because if a higher tapered angle and/or m value is used the value of n_x tends to be high, this will demand considerable CPU computational time and can only be solved by supercomputers which allows a much increased mesh distribution.

Variations of the spot-size along the axial direction when m = 10 is shown in Fig. 5.48. The H (height) = 1.0 μm, initial and final width as, W_i = 1.0 μm and W_f = 3.0 μm, respectively. The tapered angle was taken as, $\theta = 0.3^0$. It can clearly be observed that the spot-size was uniform at the first 100 μm, thereafter appearances of oscillations. The mesh distribution was 80*70, with finer mesh used in the core region of the structure. It should be noted here that $\Delta x = 0.067$, while $\Delta w = 0.052$ (discussed in section 5.7).

To understand the effect of the re-meshing steps and its contribution to the oscillations a smaller m value was used i.e., m = 5 as shown in Fig. 5.49. In this case the mesh distribution was kept constant at 80*70 with finer mesh used at the core.

Again $\Delta x \neq \Delta w$, since m = 5, $\Delta w = 0.026$ while $\Delta x = 0.067$. For the first 100 μm to 180 μm, the oscillations were slightly reduced; thereafter they appeared consistent all through the propagation distance. It can be concluded here that even though the re-meshing step was reduced, as long as $\Delta x \neq \Delta w$, the appearance of oscillations on the tapered section was very likely.

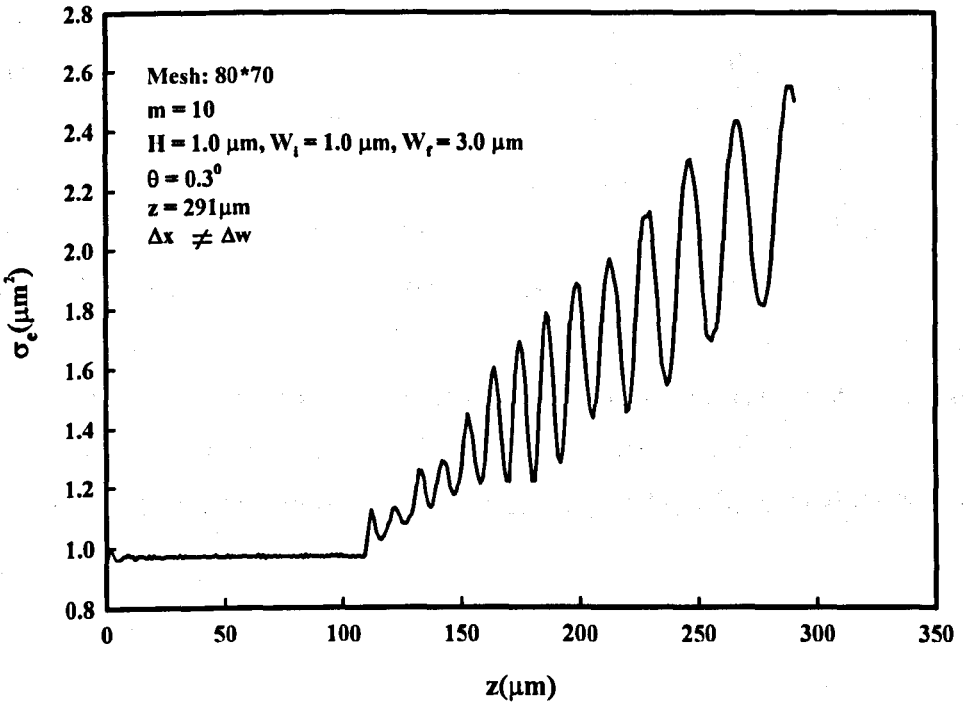

Fig. 5.48 Variations of the spot size along the axial direction for re-meshing step, $m = 10$.

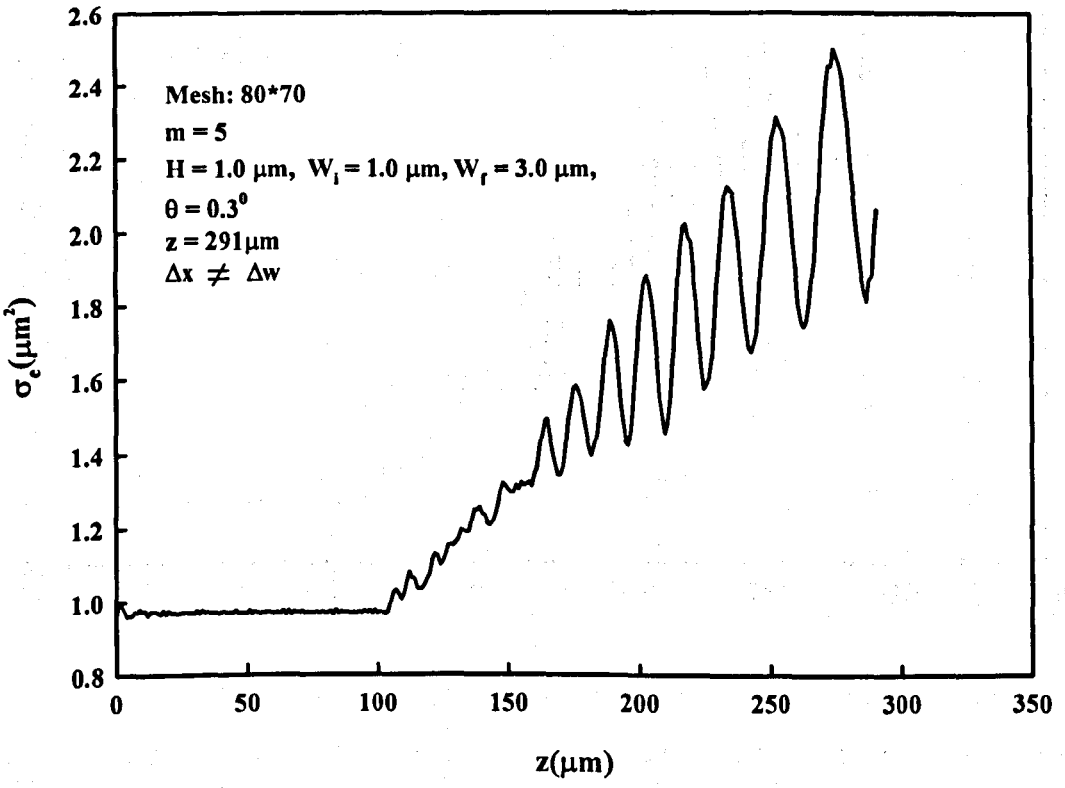

Fig. 5.49 Variations of the spot size along the axial direction for re-meshing step, $m = 5$.

The variation of spot-size along the axial direction when m = 10 with higher mesh distribution is shown in Fig. 5.50. In this case, the mesh distribution was increased to 126*70, with all other parameters kept constant. There was no significant change observed during the propagation at the tapered section, as the oscillations were still consistent. Therefore, increase in the mesh with no consideration on the Δx value, did not improve the results either.

A smaller m value i.e., m = 7, with higher mesh distribution (126*70) was used as shown in Fig. 5.51. Again, all the parameters were kept constant. It can be observed that at the tapered section the oscillations have been significantly reduced. The peaks and troughs were reduced and the oscillations inconsistent. It should be noted that in this case $\Delta x \neq \Delta w$, however, since the mesh was increased and the m value reduced, the difference between Δx and Δw was small i.e., 0.011, where Δx = 0.026 and Δw = 0.037.

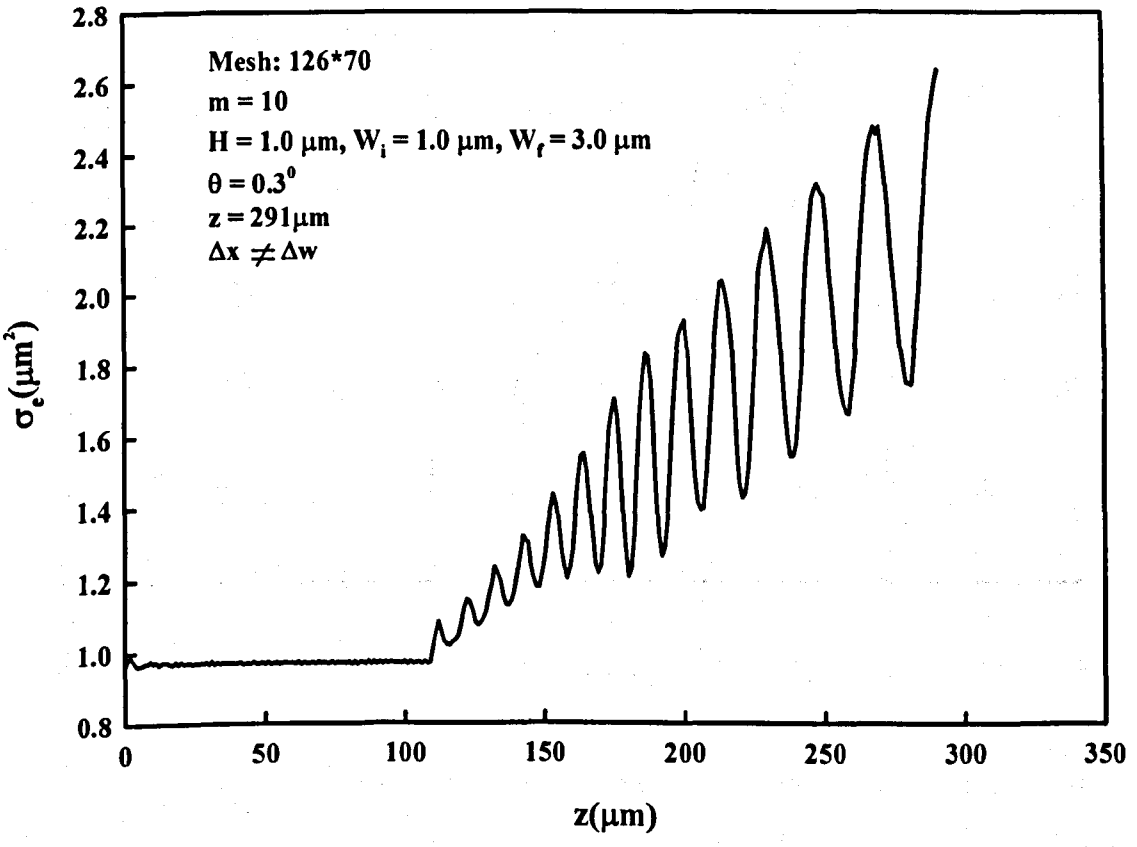

Fig. 5.50 Variations of the spot size along the axial direction for re-meshing step, m = 10.

To understand the above result thoroughly and make sound conclusion a smaller m value, i.e., $m = 5$ was used with the same mesh distribution (126*70) as shown in Fig. 5.52. However, it should be noted here that, $\Delta x = \Delta w$, where $\Delta x = 0.026$. The oscillations were eliminated significantly on the tapered section of the propagation distance. Therefore, purely based on these results we can conclude that the oscillations can be indeed avoided by using finer mesh and smaller value of re-meshing step, m, which will correlate with $\Delta x = \Delta w$. However, for longer propagation distances for devices such as amplifiers, a higher mesh distribution may be required, which will take considerably CPU computational time and can only be solved by supercomputers.

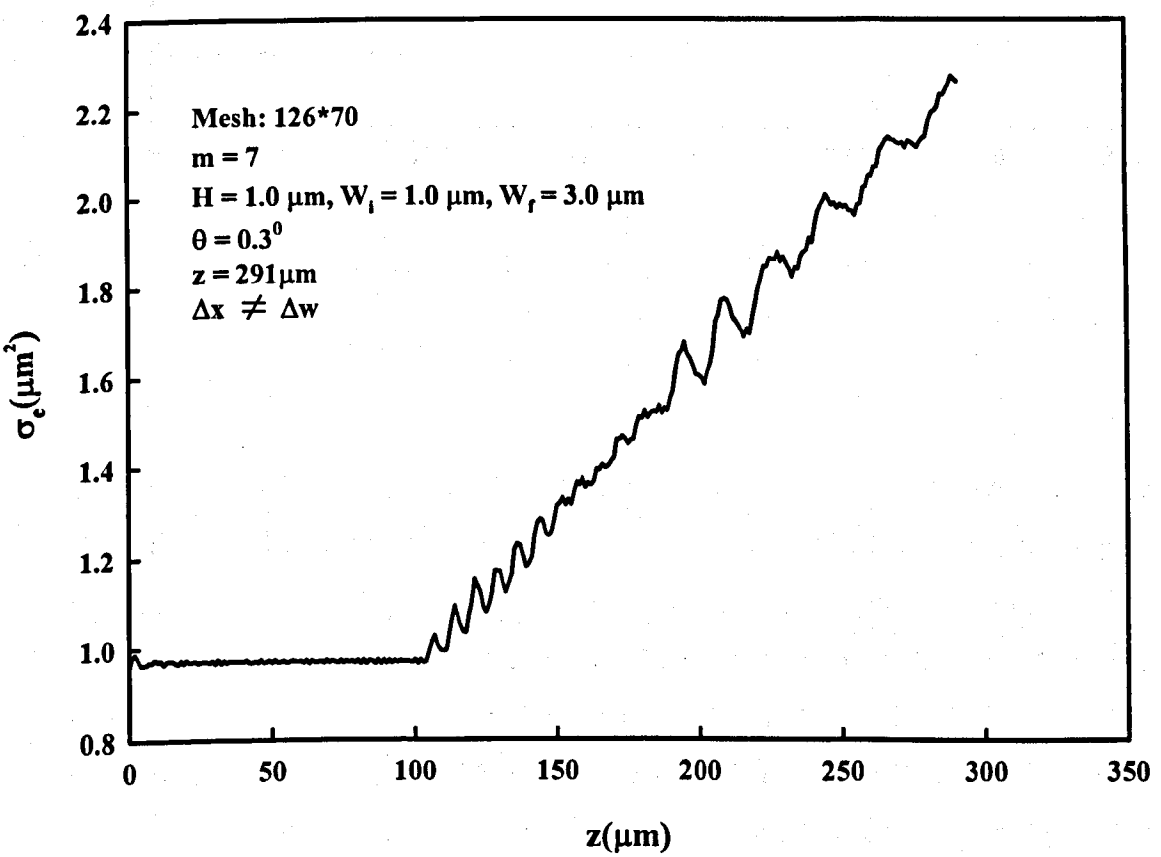

Fig. 5.51 Variations of the spot size along the axial direction for re-meshing step, $m = 7$.

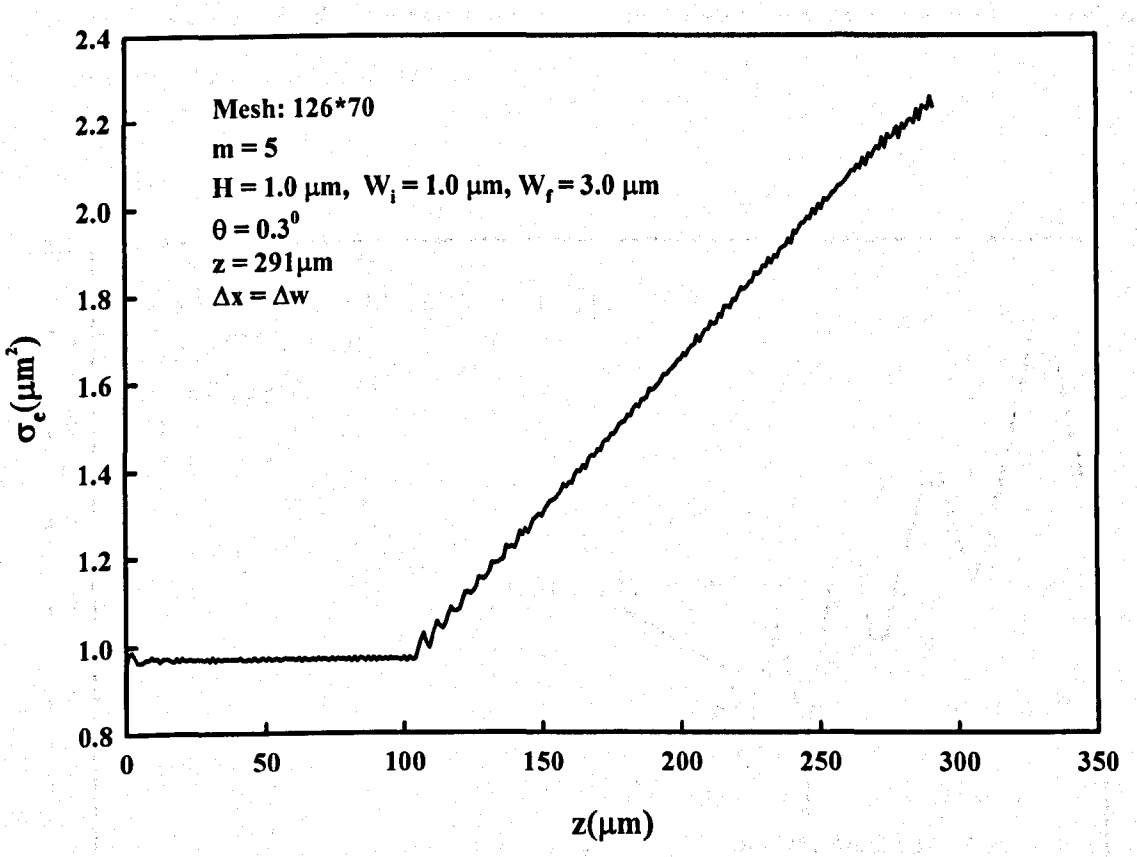

Fig. 5.52 Variations of the spot size along the axial direction for re-meshing step, $m = 5$, where $\Delta x = \Delta w$.

The variation of the spot-size area along the axial direction is shown in Fig. 5.53. Here, the initial and final widths were taken as 1.0 μm and 8.0 μm, respectively. The tapered angle, $\theta = 0.5^0$, and the n_i, carrier gain at low power was taken as 0.005, and the amplitude coefficient, b, as 1.0. It should be noted here that, $\Delta x \neq \Delta w$. In this case two m values were used, i.e., $m = 5$ and 10, and the mesh was distributed accordingly to achieve the final width of 8.0 μm. For $m = 5$, the mesh distribution used was 120*90 while for $m = 10$, it was 140*90. It can be clearly observed that the spot-size area remains constant for the first 100 μm (uniform section).

From the figure it can be seen that for $m = 5$, the oscillations drastically reduced at the start of the tapering section and became apparent again after $z = 180$ μm, this is mainly because the mesh distribution was high to allow room for the expanding field and the difference between Δx and Δw was small, however on further tapering the

effect of the oscillations was observed. On the other hand, for m = 10, the oscillations appeared as early as the start of the tapered section which was due a high re-meshing step along the propagating distance.

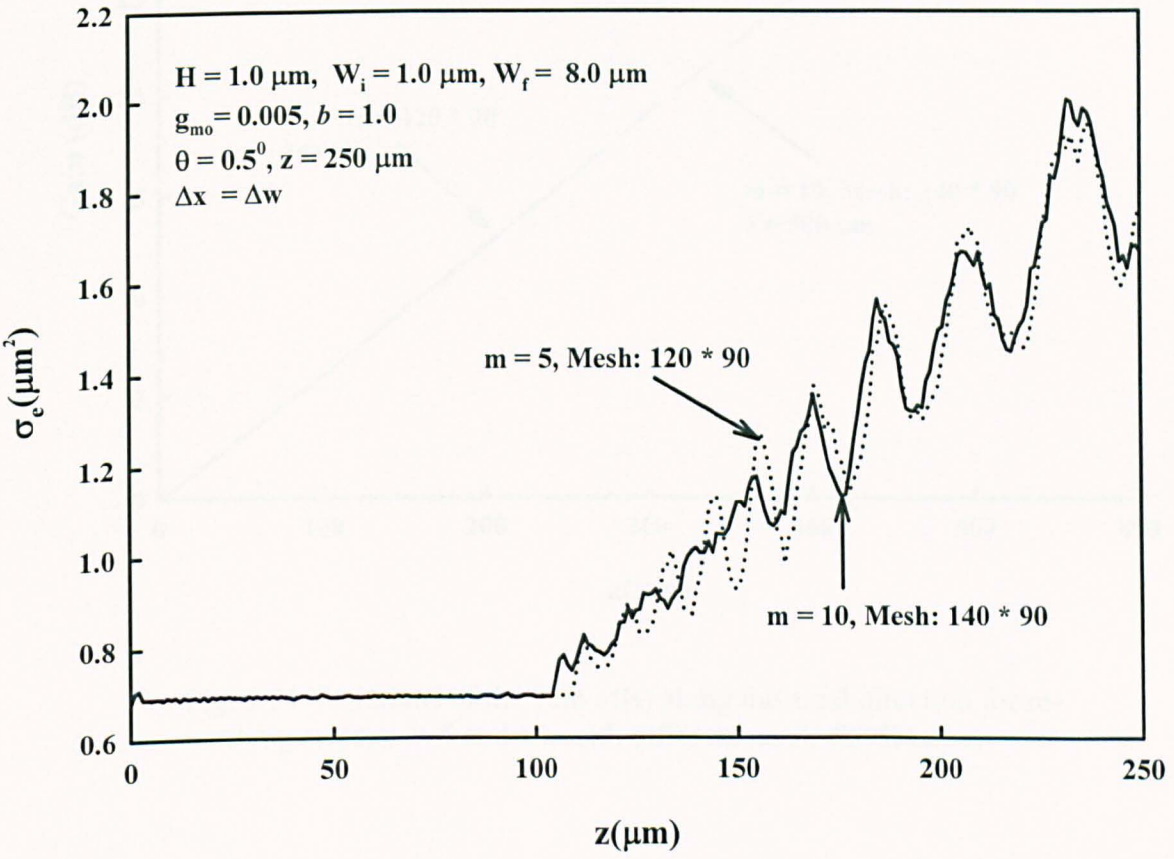

Fig. 5.53 Variations of the spot size along the axial direction for re-meshing steps, m = 5 and 10, with different mesh distribution.

The presence of oscillations had no significant effect on the overall gain as shown in Fig. 5.54. It should be noted here that for m = 10, the amplifier length was taken as 501 μm to achieve the W_f = 8.0 μm. It can be clearly seen that from the start of the propagation gain verses z is almost linear. Furthermore, for both m values with different mesh distribution the gain at each axial position was identical. It can be concluded here that the re-meshing step and the mesh used has no significant effect on the overall gain of the amplifier.

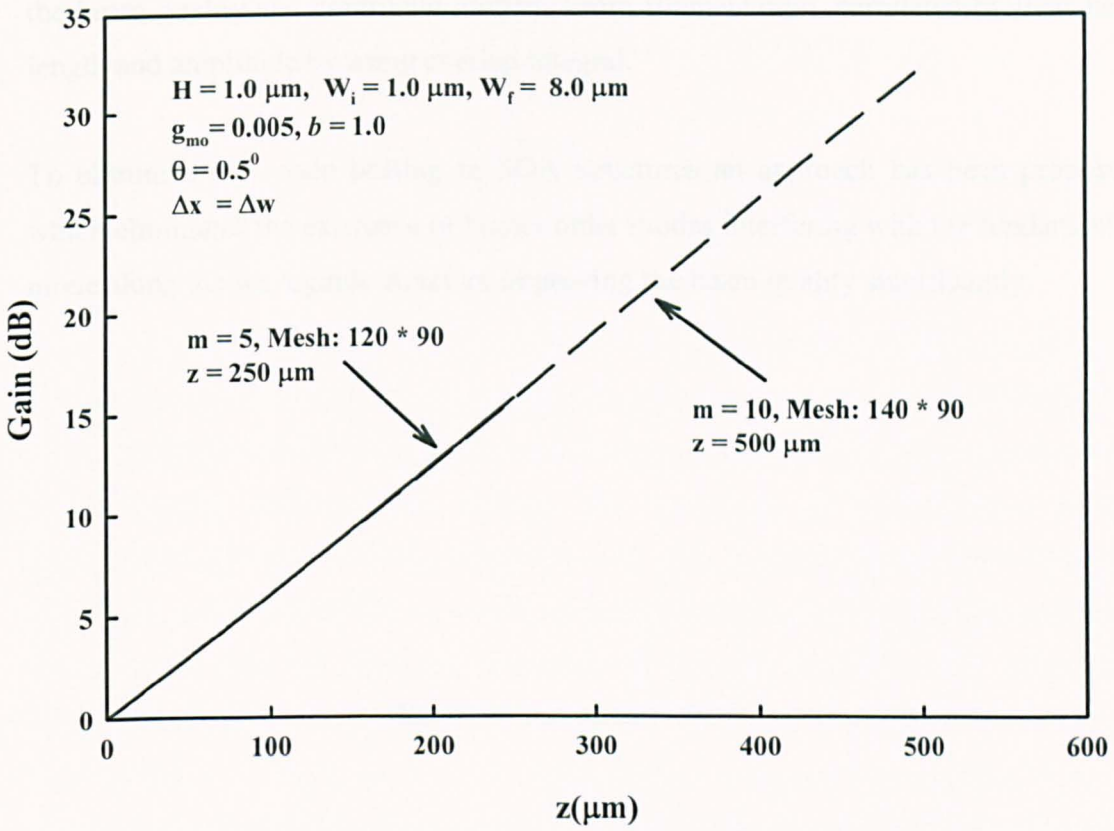

Fig. 5.54 Variations of the gain (dB) along the axial direction for re-meshing steps, m = 5 and 10, with different mesh distribution.

5.8 Summary

In this chapter, the study of the evolution of the optical beam along various waveguide structures by using the rigorous vectorial numerical approaches based on the versatile finite element technique has been presented. Initially the Gaussian and mode fields were used as the input field to investigate the properties of the propagating field along the waveguide with the beam propagation method.

The variations of the waveguide width, normalised power, power loss, expansion of the beam shape and spot-size area were thoroughly investigated. One significant observation discussed in this chapter was the appearance of higher order modes, which caused significant modal interference with the fundamental mode along the

propagation distance. The mode beating is likely to contribute to the degradation of the beam quality and contribute towards beam filamentation, correlated by their beat length and amplitude by using overlap integral.

To eliminate the mode beating in SOA structures an approach has been proposed which eliminates the existence of higher order modes interfering with the fundamental mode along the waveguide structure improving the beam quality significantly.

6.0 The Carrier Rate Equation, Gain Analysis and Gain Saturation in SOA Structures

6.1 Introduction

In recent years, there has been increased attention towards semiconductor laser amplifiers (SLAs) due to their unique feature to be easily integrated with other photonic devices and feasibility of performing sophisticated multifunctions such as pulse-shape regeneration, signal tapping, switching and routing. The advantages of semiconductor optical amplifiers, includes; potentially low cost, wide gain bandwidth, and possibilities for monolithic integration with laser diodes and/or photodetectors. It is therefore significant to understand how the saturation characteristics of these amplifiers may affect their performance in future applications.

The tapered structure of a laser amplifier has been shown to provide better saturation performance [161], used to amplify picosecond pulses with very little distortion [169] and also generating mode-locked [170] and Q-switched [171] short pulses with high peak values. SLAs have been developed mainly to replace complex optoelectronic regenerating systems. Some of their main functions are to act as

(a) Post-amplifiers for the optical transmitter
(b) In-line amplifiers, and
(c) Preamplifier for optical receivers

Recently, the development of EDFAs has challenged many applications of SLAs. The limitation of SLA is the difficulties in achieving high gain, low polarisation sensitivity, low noise figure and low coupling loss at the same time [172]. However, SLAs have the advantage of small size, low power consumption and low cost (when mass produced), and can be integrated monolithically with other photonic devices like lasers or detectors. Moreover, they are also available at a wavelength of 1.3 μm and perform other functions such as pulse-shape regeneration, switching and wavelength conversion.

Gain saturation in travelling wave- semiconductor optical amplifiers (TW-SLAs) severely limits many of its applications. In a wavelength division-multiplexing system, the gain saturation is determined by the total power of all the channels involved. As a result, the number of channels in WDM system for a given gain is limited by the gain saturation. This also results in undesirable effects, such as gain saturation induced channel cross-talk [173], and nearly degenerates four-wave mixing [174]. When SLAs are used as in-line amplifiers, the gain provided by each amplifier (which also determines the number of required amplifiers) is limited by the gain saturation of the amplifier. Many other applications, such as booster amplifiers, also require high gain saturation.

One method of obtaining high gain saturation in a SLA is to increase the cross-section area of the active region. There are two aspects that result in an improvement in gain saturation. Firstly, by increasing the cross-sectional area of the active region, the intensity is reduced for a given optical power. Secondly, there are more carriers available for providing gain since the active volume is bigger. Increasing the width of the active region enhances the cross-sectional area. The cross-section area of conventional TW-SLA is limited by the condition for single mode propagation, which is desirable for high coupling efficiency to single mode fibre [175]. To achieve both high gain saturation and single-mode propagation simultaneously, the width of the TW-SLA can be increased gradually from the input to the output so that conversion to higher order modes can be minimised [76]. The performance of tapered TW-SLAs has been investigated in [163,176], where, it was found that linearly tapered TW-SLA gave a better gain saturation performance and a higher normalised fundamental mode output power.

6.2 The Carrier Rate Equation Analysis

In this section, the analysis of carrier rate equation and its contribution to the optical modal gain will be discussed. To study the carrier density, modal gain and gain saturation through a tapered guided-wave structure, an etched semiconductor optical amplifier is considered and a schematic diagram of such a deep-etched SOA is shown in Fig. 6.1. In this particular case the core height (H) is taken as 0.1 μm, with an initial

width (W_i) of the guide as 1.0 μm and this width is adjusted along the tapered structure as shown in Fig. 6.1. The core and cladding indices at the operating wavelength of 1.55 μm were taken as n_g = 3.480 and n_s = 3.402, respectively, generating an index constant, $\Delta n = n_g - n_s = 0.078$. For a non-uniform structure, its width is varied symmetrically with a tapered angle, θ, to achieve the wider final width, W_f. An initial 100 μm uniform section is considered, which often can represent a preceding laser, before the actual tapered section.

The power gain in an active photonic device, such as a laser or an amplifier is due to the presence of the imaginary part of the complex refractive index in the core. The injected current generates *carrier density* and when this density is above the transparent carrier density then the optical field can be amplified. A complex refractive index, $n_g = n_r + jn_i$, has been considered in the waveguide core to mimic the optical gain of a semiconductor optical amplifier. The local gain parameter, g_i, is related to the imaginary part of the refractive index, n_i, by $g_i = k_o n_i$. The imaginary part of the refractive index, which provides the necessary gain is often taken as a constant value in the core region, but in reality this is not constant but its local profile depends on the local optical power density. Since this profile depends on the total optical power and as the total optical power continuously increases along the axial distance, so this parameter, $n_i(z)$, also changes nonlinearly along the propagation distance. The transverse optical intensity profile also depends on the mode field profiles, so this parameter, $n_i(x,y)$, also changes continuously in the transverse direction as well as along the axial direction, $n_i(x,y,z)$, as the power density changes with the modal gain.

The TW-SOA structure considered in this study is shown in Fig. 6.2. The z dependence of the width $W(z)$ of this structure can be expressed as

$$W(z) = W_i + \left(\frac{W_f - W_i}{L}\right) z \qquad (6.1)$$

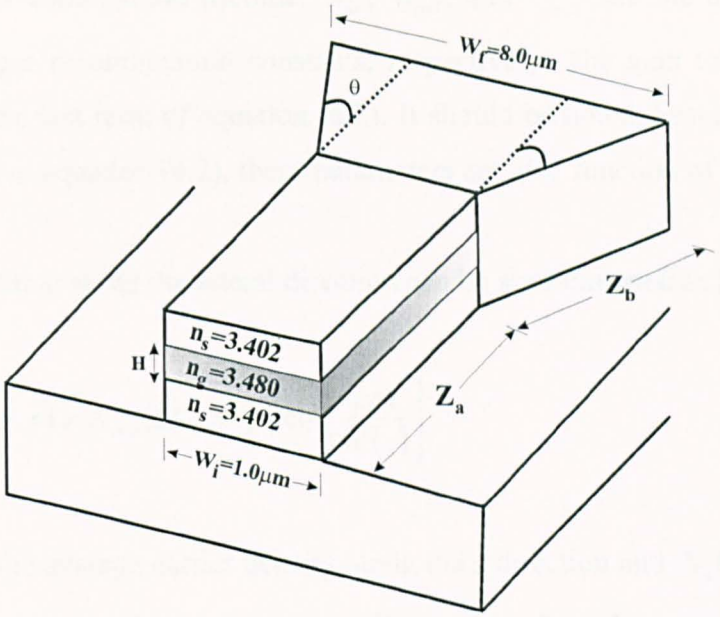

Fig. 6.1 Schematic diagram of the deep-etched tapered semiconductor amplifier.

where W_i and W_f are the input and output widths, respectively. The rate equation for the carrier density in the TW-SOA can be expressed as [177]

$$\frac{\partial N}{\partial t} = D\frac{\partial^2 N}{\partial x^2} + \frac{J}{ed} - \frac{N}{\tau_s(N)} - g_m(N)\frac{S(x,y)}{hf} \tag{6.2}$$

where

$$\tau_s(N) = \frac{1}{A_{nr} + B_{rad}N + C_{Aug}N^2} \tag{6.3}$$

$$g_m(N) = a(N - N_o) \tag{6.4}$$

where N is the carrier density, D is the diffusion coefficient, J is the current density, e is the electron charge, d is the active layer thickness, x is the distance along the lateral direction, $S(x,y)$ is the optical field, hf is the photon energy, $g_m(N)$ is the

material gain, a is the gain coefficient, N_o is the carrier density at transparency, $\tau_s(N)$ is the carrier combination lifetime, A_{nr}, B_{rad}, and C_{Aug} are the nonradiative, radiative, and Auger recombination constants, respectively. The gain term has also been included in the last term of equation (6.2). It should be noted, besides the time-dependence stated in equation (6.2), these parameters are also function of their spatial positions.

The carrier distribution along the lateral direction can be approximated as [161]

$$N(x,z)=N_{ave}(z)-N_1(z)\cos\left[\frac{2\pi x}{W(z)}\right] \tag{6.5}$$

where $N_{ave}(z)$ is the average carrier density along the z direction and $N_1(z)$ accounts for the amplitude of the spatial carrier density distribution along the x-direction. It can be assumed that carrier profile is uniform along the y-direction inside the active region.

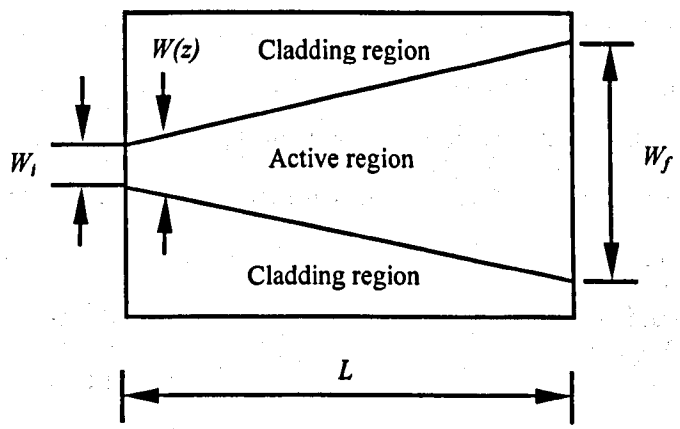

Fig. 6.2 Schematic diagram of the active region of a linear TW SOA.

Since the maximum field intensity is at the centre of the waveguide, often a simple transverse variation of the local gain coefficient can be used in the numerical simulation of the optical amplifier and this can be expressed as [169].

$$g(x)=n_i(1-b*\cos 2\pi x/W) \tag{6.6}$$

The term n_i is the carrier gain at a low power, and the amplitude coefficient, b, depends on the maximum power intensity. Here x is the lateral position (from the centre of the guide), and W is the local width of the amplifier.

The transverse gain profile, $g(x)$, along the horizontal direction is shown in Fig. 6.3. For a fixed value of n_i, the overall optical gain strongly depends on the value of b. As the value of b is increased, the local gain is reduced and hence the overall optical gain is also reduced.

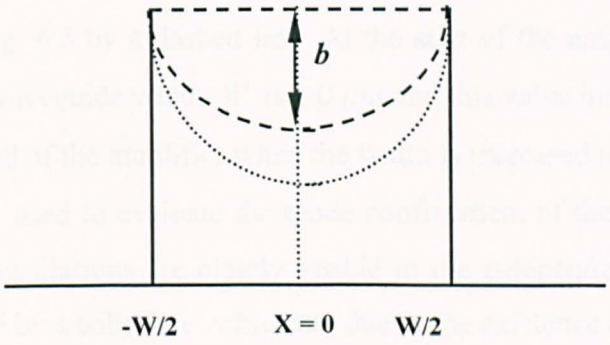

Fig. 6.3 Transverse gain profile ($g(x)$) along the horizontal direction.

It has been observed that the overall gain depends strongly on the value of b and the gain is only 0.2 when the value of b is 1, compared to that when $b = 0$ as shown in Fig. 6.4. Gain verses z is almost linear, however, close observation from the numerical data yields that gain between 800 – 900 μm was about 5% higher than that of between 100 – 200 μm, which was due to the slight increased confinement factor (in the wider guide). It was also observed that increase in the value of n_i with b value kept constant causes the overall gain to be increased.

It has been mentioned earlier that in the simplified numerical approaches the modal confinement factor, Γ, expressed as

$$\Gamma = \frac{Power\ in\ the\ active\ area}{Total\ guided\ power} \tag{6.7}$$

have been used instead of the detailed transverse variation of the optical parameters. Although in this work the detailed two-dimensional variations of the field profiles, power density, carrier profiles, gain profiles, and their nonlinear interactions have

been considered, but the confinement factor for the stationary modal fields and for the evolutionary propagating beam have also been calculated. It should also be noted that for a tapered SOA, the confinement factor is not constant but changes along the SOA as the local width varies. The variation of the confinement factor, Γ, for the fundamental H_{11}^{y} mode along the axial direction is shown in Fig. 6.5. In this case, the total length of the SOA, is taken as 500 μm and the tapered angle, $\theta = 0.5^{0}$.

For this optical structure, the stationary value of the power confinement factor in the active area has also been calculated by using the finite element method (FEM) and also shown in Fig. 6.5 by a dashed line. At the start of the amplifier, this value Γ = 0.183 when the waveguide width, W, is 1.0 μm and this value increases monotonically to 0.206 at the end of the amplifier when the width is increased to 8.0 μm.

The BPM is also used to evaluate the mode confinement of the optical beam. In this case, the sharp oscillations are clearly visible in the z-dependent BPM solutions, as shown in Fig. 6.5 by a solid line, which are due to the existence of higher order modes and mode beating during propagation. For a smaller waveguide width, the generated higher order modes are quickly radiated out. At a longer axial position, z, when the width is bigger, the generated higher order modes are guided.

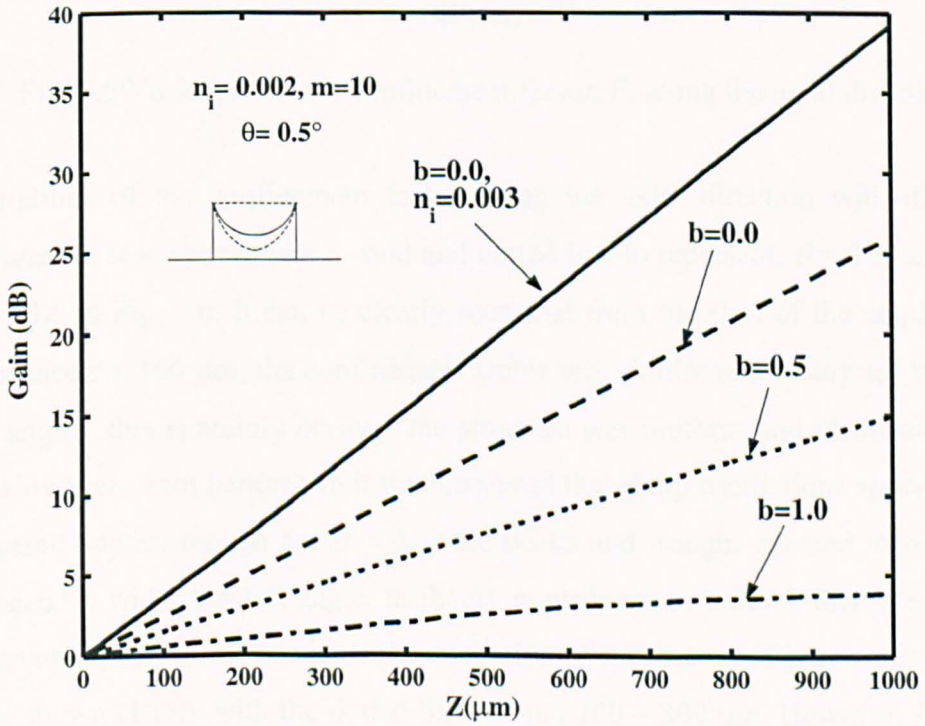

Fig. 6.4 Variations of the Gain (dB) along the axial direction with different b values and the effect of n_i.

The near periodic variation of the confinement factor strongly correlates with the beat length between the propagating H_{11}^{y} and H_{31}^{y} modes. Overall, the BPM solution shows a slightly lower value of Γ as compared to FEM solutions in the tapered section. The slight reduction in its value could be due to the contributions from the higher order modes, which are generated and have lower modal confinement values.

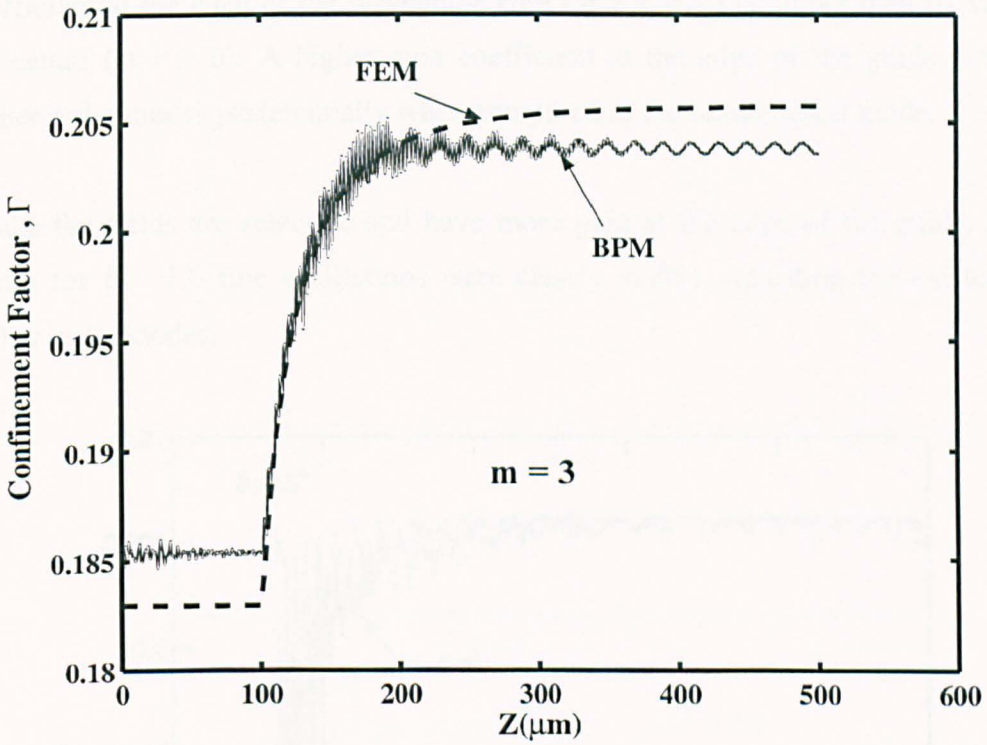

Fig. 6.5 Variations of the confinement factor, Γ, along the axial direction.

The variations of the confinement factor along the axial direction with different tapered angles, θ, is shown with a solid and dotted line to represent, $\theta = 0.3^{0}$ and 0.5^{0}, respectively, in Fig. 6.6. It can be clearly seen that from the start of the amplifier to axial distance $z = 100$ μm, the confinement factor was similar and steady for both the tapered angles, this is mainly because the structure was uniform and identical in this region. However, from henceforth it was observed that sharp oscillations appeared for both tapered angles, though for $\theta = 0.5^{0}$ the peaks and troughs seemed to be much pronounced. A wider tapered angle, in theory contributes to a much increased width of the structure, this however yields the excitation of much more higher order modes, which is shown clearly with the dotted line around 100 – 300 μm. However, for both the tapered angles, the confinement factor settles down around 0.206.

The normalised field profiles along the transverse direction for $b = 0$ and $b = 1$, are shown in Fig. 6.7, by a dashed and a solid line respectively. As shown in Fig. 6.7 the field at the edge of the guide when $b = 1.0$ are relatively higher than the field in the centre compared to that of $b = 0$. In the case of $b = 0$ it experienced a uniform gain, while for $b = 1.0$ the gain at the edge of the guide was higher. Besides the reduction of gain, the evolved modal optical beam profile is also slightly different, as the gain coefficient at the edge of the waveguide core (at $x = W/2$) is higher than its value at the centre (at $x = 0$). A higher gain coefficient at the edge of the guide amplifies higher order modes preferentially when compared to the fundamental mode.

Hence the fields are selective and have more gain at the edge of the guide. At the centre for $b = 1.0$ fine oscillations were clearly visible indicating the existence of higher order modes.

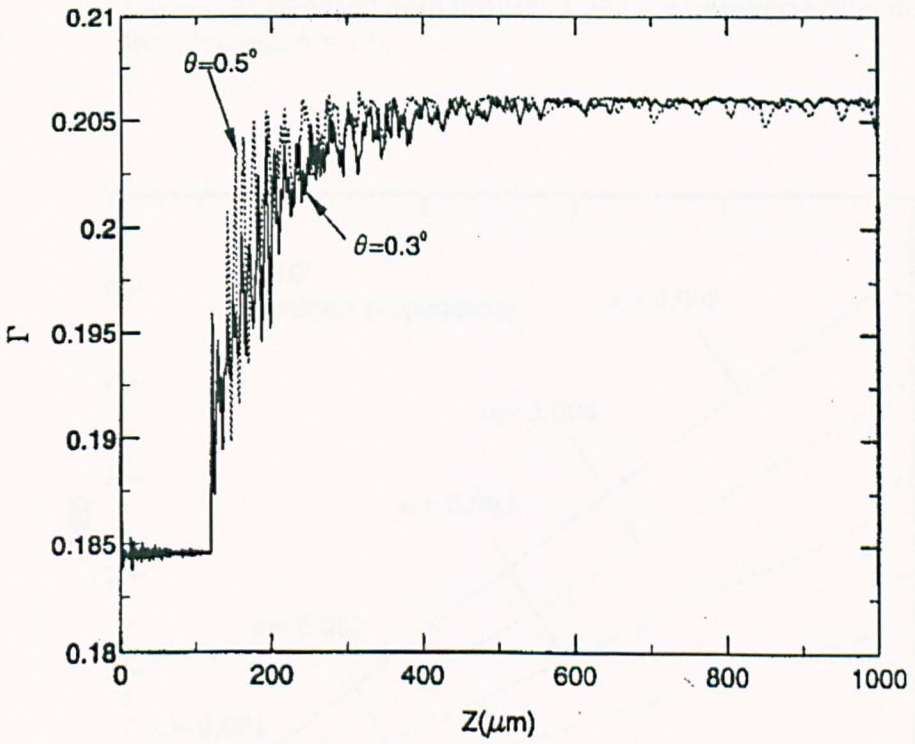

Fig. 6.6 Variations of the confinement factor, Γ, along the axial direction for different tapered angles, θ.

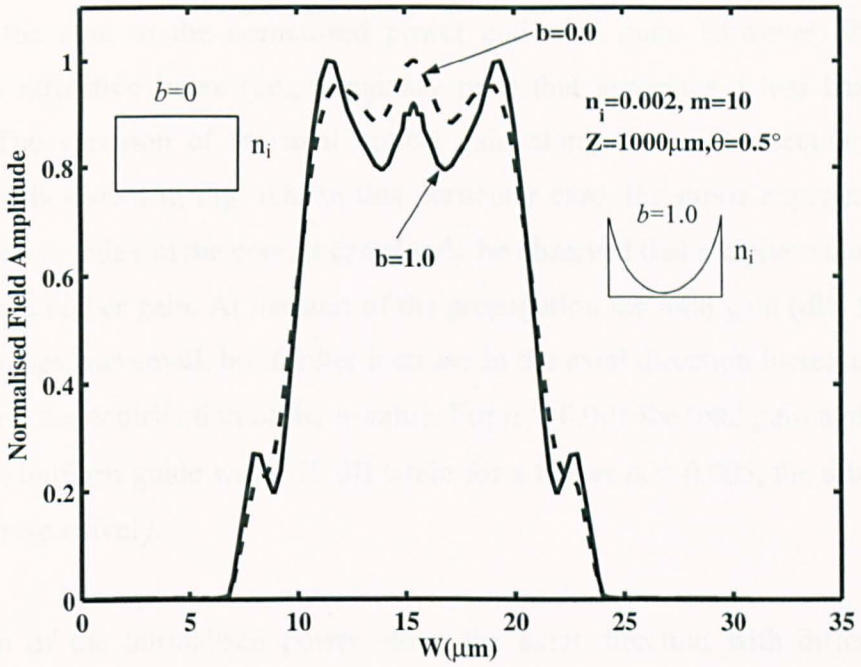

Fig. 6.7 Normalised field profiles along the transverse direction for $b = 0$ and $b = 1.0$.

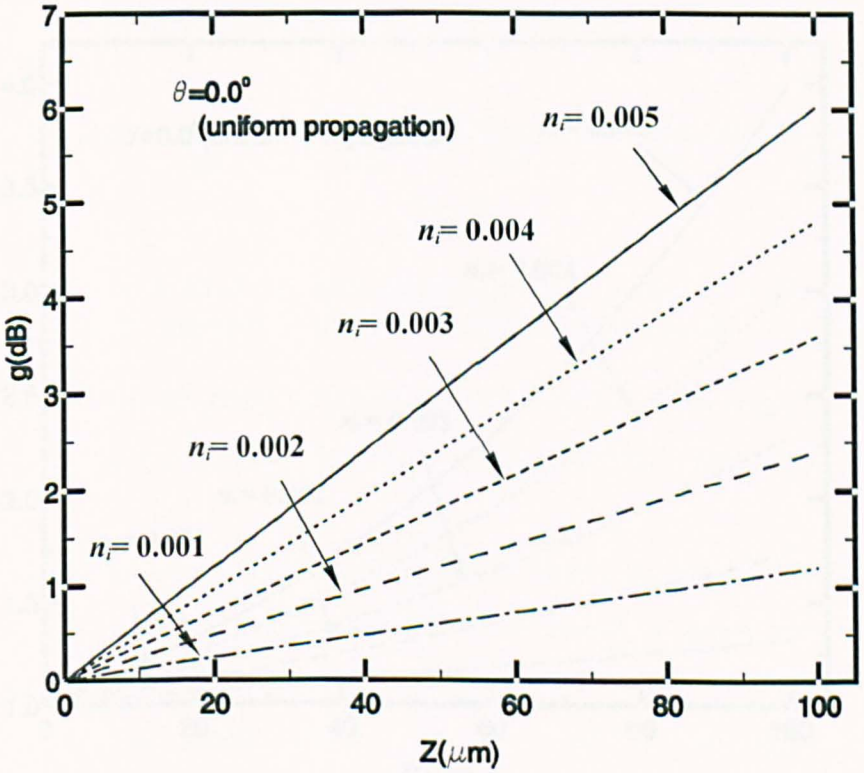

Fig. 6.8 Variation of the total optical gain (dB) along the axial direction with different n_i values for a uniform guide (Gain).

We shall also investigate the effect of the local refractive index (only the imaginary part, n_i), in the core to the normalised power and total gain. However, for this experiment a refractive index (i.e., imaginary part) that generates a loss has been considered. The variation of the total optical gain along the axial direction for a uniform guide is shown in Fig. 6.8. In this particular case, the guide experienced a positive refractive index in the core. It can clearly be observed that a higher value of n_i contributed to a higher gain. At the start of the propagation the total gain (dB) for the different n_i values was small, but further increase in the axial direction increases gain dependently on the contribution of the n_i value. For $n_i = 0.001$ the total gain at the end of z =100 μm uniform guide was 1.27 dB while for a higher $n_i = 0.005$, the total gain was 3.98 dB respectively.

The variation of the normalised power along the axial direction with different n_i values for a uniform guide is shown in Fig. 6.9. It can clearly be observed that the power at the start of the guide is the same but as the field propagates along the axial direction there is an increase in the normalised power, however it should be noted that for a lower n_i value the increase is slower.

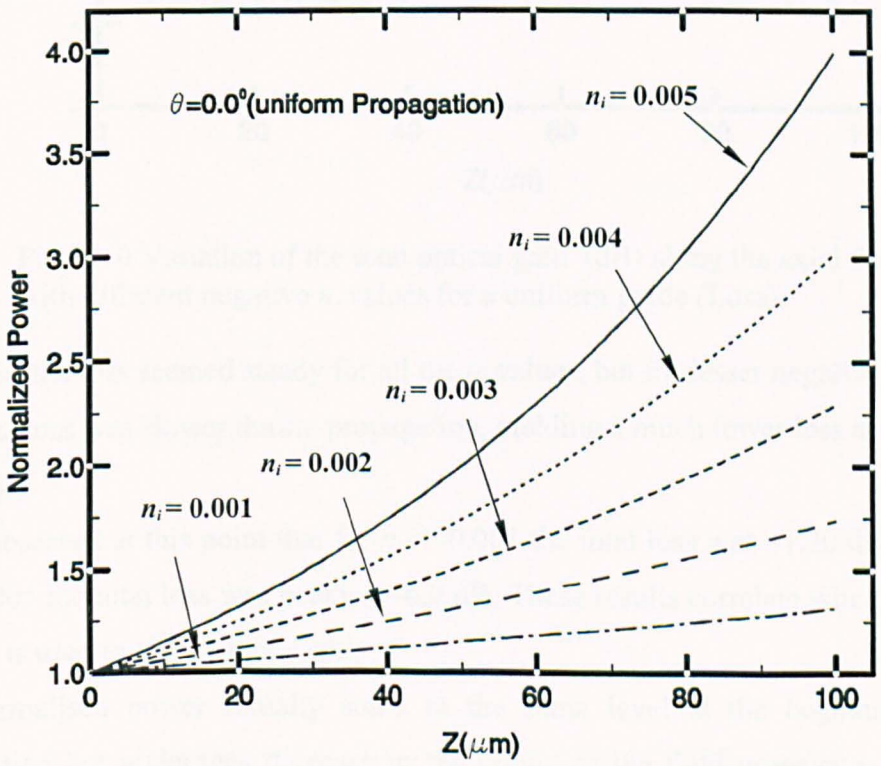

Fig. 6.9 Variation of the normalised power along the axial direction with different n_i values for a uniform guide (Gain).

It is observed that for n_i = 0.001 the normalised power peaked 1.30 with comparison to n_i = 0.005 which was 4.0 at 100μm distance.

To understand the contribution of the local refractive index, a negative n_i value was plotted as shown in Fig. 6.10, to demonstrate the total loss along the waveguide. At the start, the total loss was zero but reduces along the axial direction. It can be observed that the loss is less when a higher n_i value is used.

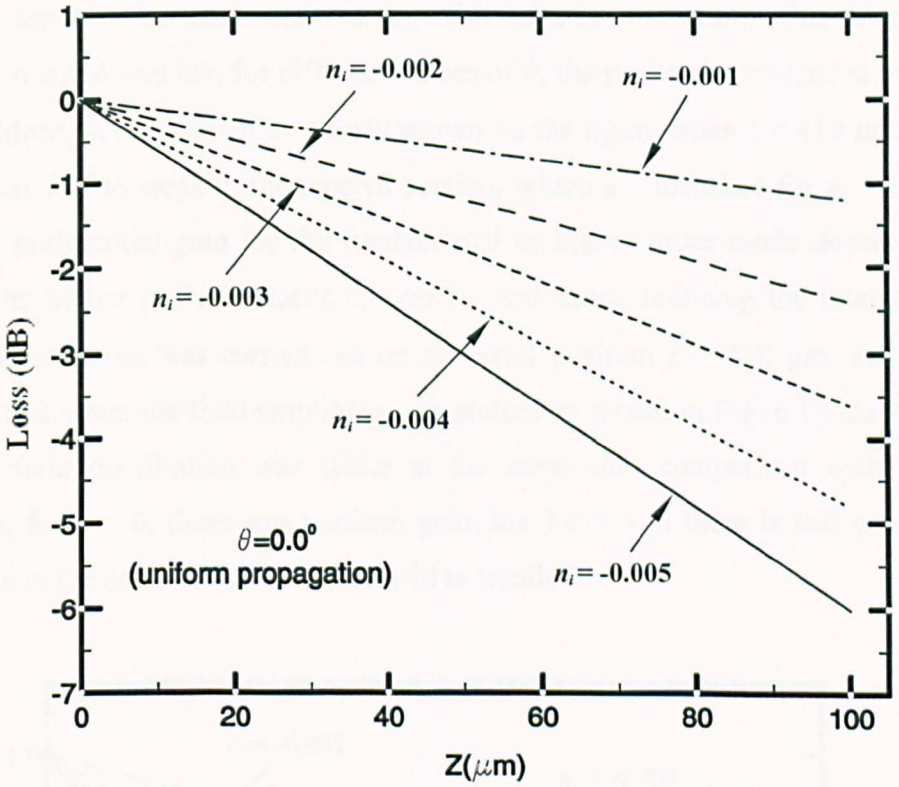

Fig. 6.10 Variation of the total optical gain (dB) along the axial direction with different negative n_i values for a uniform guide (Loss).

However, the loss seemed steady for all the n_i values, but for lesser negative refractive index the loss was slower during propagation, yielding a much lower loss at the end of the guide.

It was observed at this point that for n_i = -0.001 the total loss was –1.20 dB while for n_i = -0.005 the total loss was peaking –6.0 dB. These results correlate when a positive n_i value is used to obtain a gain (dB).

The normalised power initially starts at the same level at the beginning of the propagation but undergoes decrease in the power as the field propagates along the axial direction since it is experiencing a loss as shown in Fig. 6.11. However, it was

clearly observed that for lower negative n_i value the power loss was slower (in real scale, but uniform rate in dB scale) and lower at the end of the propagation. It was recorded that for n_i = -0.001 and -0.005 the total normalised power at z =100 μm was 0.75 and 0.25, respectively, indicating clearly that the loss was high when n_i = -0.005 was used.

It was observed as shown in Fig. 6.12 that for the first 100 μm (uniform section) the spot-size remains constant and varies with change in width. One significant observation noted was that for different values of b, the peaks and troughs at different axial positions were different as clearly shown on the figure when z = 410 μm. Mode beating was due to steps in the tapered section, which are identical for m = 10 used here. But preferential gain for the fundamental or higher order mode depends on b values. The higher power reduces the carrier and hence reducing the total gain. A further investigation was carried out on the axial position z = 410 μm, and it was observed that when the field amplitude was plotted as shown in Fig. 6.13 that when b = 0, the field distribution was wider at the edge with comparison with b = 1. Therefore, for b = 0, there was uniform gain, but for b = 1, there is less gain at the edges than at the center that's why the field is smaller.

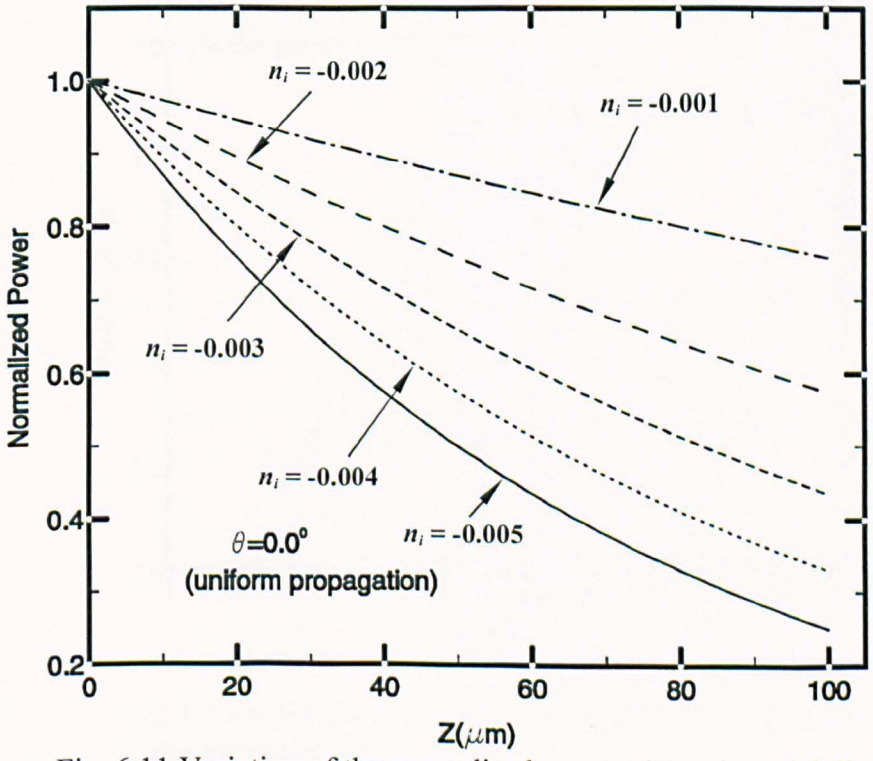

Fig. 6.11 Variation of the normalised power along the axial direction with different negative n_i values for a uniform guide (Loss).

This is mainly because as the field propagates power is higher on the edge with respect to the centre and this was brought about due to the formation of the structure.

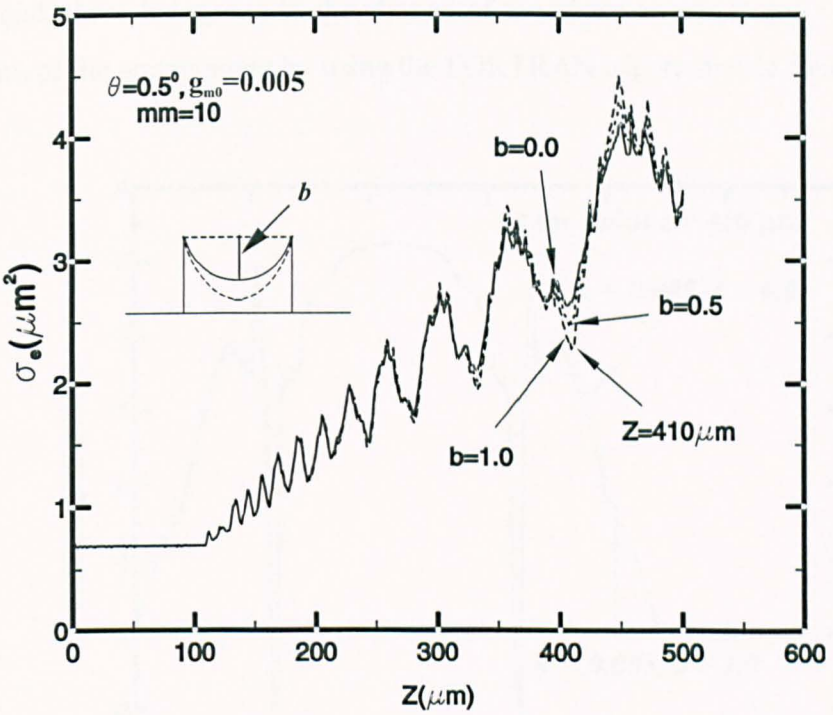

Fig. 6.12 The variation of the spot-size along the axial direction for different values of *b*.

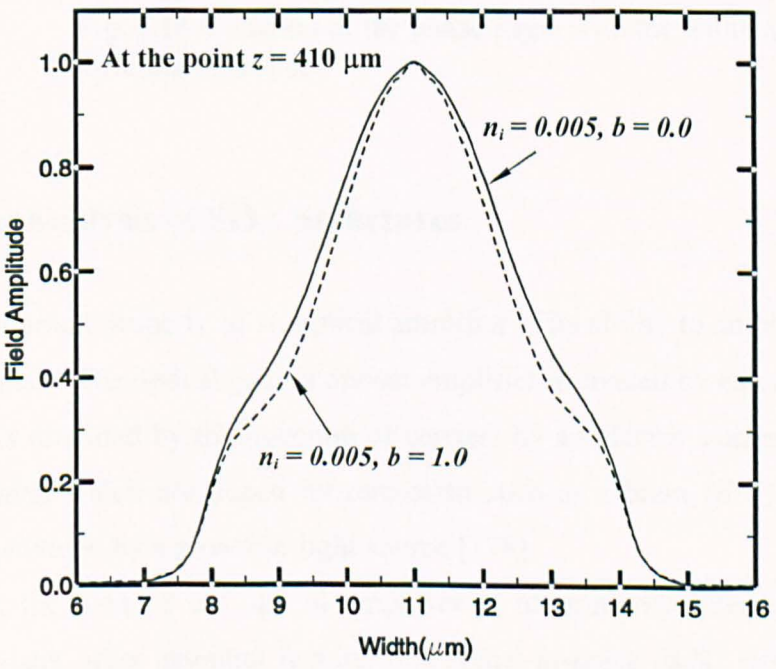

Fig. 6.13 Variation of the field amplitude with the width for different values of *b*.

However, when the phase at that axial position was plotted as shown in Fig. 6.14, where $b = 0$ and $b = 1.0$ represented by a dotted and solid lines respectively, there was no significant change between the two different b values. The sudden phase reversal are artificial, these being due to the change of the phase angles from $-\pi$ to $+\pi$ in the calculation of the arctan angle by using the FORTRAN trigonometric functions.

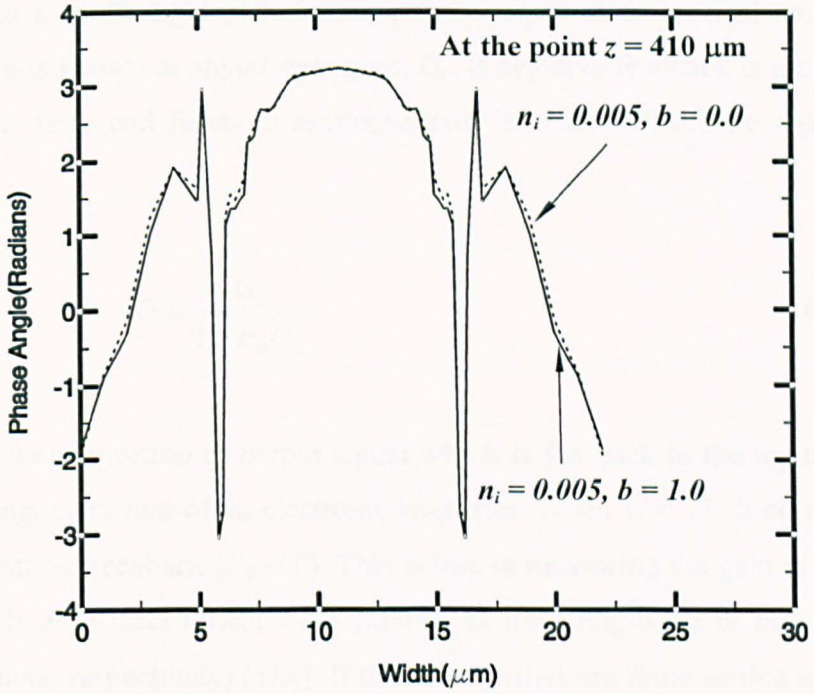

Fig. 6.14 Variation of the phase angle with the width at different values of b.

6.3 Gain Analysis of SOA Structures

The most important property of an optical amplifier is its ability to amplify the power of optical signals. The optical gain in optical amplifier is created by external pumping. In SLAs, it is provided by the injection of carriers by an electric current, whereas in fibre amplifiers, which are doped by rare-earth such as erbium (Er^{3+}), the external pumping is provided by a powerful light source [178].

In any case, the gain of the optical amplifier is of primarily interest [179], as it determines many other essential factors, like signal-to-noise (S/N) ratio, when they are incorporated into systems [180]. The signal gain, G of an optical amplifier is given in decibels, and expressed as

$$G = 10\log_{10}[P_{out} / P_{in}] \tag{6.8}$$

where P_{out} is the light power measured at the output of the optical amplifier, and P_{in} is that measured at the input end [181]. One can further refine definition of signal gain G by considering the light path. If equation (6.8) describes the input and output light power due to a single light path from input to output of the optical amplifier, the resulting gain is known as *signal pass gain*, G_s. If negative feedback is provided (i.e., by reflections from end facets in semiconductor laser amplifiers) the signal gain G becomes;

$$G = \frac{G_s}{1 + F_B G_s} \tag{6.9}$$

where F_B is the proportion of output signal which is fed back to the input. Equation (6.9) is analogous to that of an electronic amplifier. When $G = G_s$, it corresponds to amplifiers without feedback ($F_B = 0$). This is true in measuring the gain in SLAs with zero or nearly zero facet reflectivities (known as travelling-wave or near travelling-wave amplifiers, respectively) [182]. If the reflectivities are finite so that some sort of optical feedback is provided to the amplifier, then F_B is finite and the resulting amplifier structure becomes a Fabry-Perot amplifier.

Ideally, an optical amplifier should have as high a gain as possible. Physically, optical amplifiers with infinite gain are impossible to achieve. Furthermore, an amplifier with infinite gain will actually generate an output without an input. This is equivalent to the condition for oscillations where the amplifier becomes a laser [183]. Therefore, the performance limit of the gain in any optical amplifier is that the amplifier gain is not so large that self-sustained oscillations will be excited. This is complicated by the fact that stray reflections in the system can provide additional feedback in the amplifier [184], pushing the overall gain of the amplifier. In addition, the maximum gain, which can be obtained in optical amplifier, is further restricted by *gain saturation* mechanisms. This subsequently affects the dynamic range of the amplifier, limiting the maximum optical power, which can be input to and output from the amplifier

[185]. In the next section of this chapter the gain saturation mechanism will be discussed and investigated.

6.4 Gain Saturation in SOA Structures

It is well known that the total gain of a semiconductor amplifier also depends on the input power to the SOA. When the input power is higher, the resulting optical field reduces the carrier density and ultimately saturates the overall gain. The optical gain coefficient is a function of the intensity of the optical wave travelling in the gain medium, it decreases as the optical signal intensity increases.

Often the saturation power density, S_s, along with the confinement factor, Γ, have been used to find the effect of the gain saturation. In this case it is assumed that a fraction of the power, $\Gamma.S_s$, is uniformly distributed in the core, which reduces the carrier density uniformly in the core. However, it is clear that the power density is not constant and its effect on the modification of the local gain coefficients would not also be uniform. This physical effect can be modelled by introducing a saturation power density expressed as [77]

$$g(x,y,z)=\frac{g_{mo}}{1+\dfrac{S(x,y,z)}{S_s}} \tag{6.10}$$

where g_{mo} is the unsaturated material gain coefficient equal to $n_i k_o$, $S(x,y,z)$ is the local power density profile, which not only depends on the transverse (x and y) profile of the optical beam, but also on the axial (z) position as the total optical power increases. It should be noted that in the case of a conventional laser amplifier where the input and output widths are equal, the saturation power intensity S_s, is constant. However, in a tapered amplifier structure this is not the case and the saturation power intensity also depends on the design of the active layer width and depends on the active layer width, given as

$$S_s = S_i(x,y,z)f(w) \tag{6.11}$$

The contribution of the active layer width on S_s is given as function *f(w)*, which can be easily obtained by varying the local gain along the active region.

When the local optical power density, $S_i(x,y,z)$ is equal to the saturation power density, S_s, then the local gain, g_l, is reduced to half its unsaturated gain value, g_{mo}.

The device parameters used for the work to follow are shown in Table 6.1.

6.5 Simulation Results

In this section the variations of the field profiles, power density, carrier profiles, gain profiles, gain saturation and their properties, with their nonlinear interactions will be considered and investigated. The variation of the gain coefficient propagating along the axial direction is shown in Fig. 6.15. It was clearly observed as shown in the figure that as the field was propagating along the axial direction (*z*) as the total power increases, so does the power density (*S(x,y,z)*), resulting the gain coefficient $g(x,y,z)$ to be reduced drastically.

The parameters values used in the tapered amplifier model.

W_i	Input active region width	1 μm
W_f	Output active region width	30-50 μm
L	Amplifier length	1000 μm
L_A	Length of the uniform region	100 μm
L_B	Length of the tapered region	900 μm
d	Active region thickness	0.1 μm
n_g	Refractive index in the core region	3.480
n_s	Refractive index in the cladding region	3.402
d_{uw}	Upper cladding thickness	0.2 μm
d_{lw}	Lower cladding thickness	0.2 μm
λ	Operating wavelength	1.55 μm
A_{nr}	Non-radiative recombination constant	$0\ s^{-1}$
B_{rad}	Spontaneous recombination constant	$8 \times 10^{-17}\ m^3s^{-1}$
C_{aug}	Auger recombination constant	$9 \times 10^{-41}\ m^6s^{-1}$
ε	Gain compression factor	0
a	differential gain coefficient	$1.64 \times 10^{-20} m^{-2}$
N_o	Transparent carrier density	$10^{24}\ m^{-3}$
θ	Tapered angle	0.5°(unless stated)
Γ	Optical confinement factor	0.2

Table 6.1 Device parameters for the tapered model [161].

As clearly seen in Fig. 6.15 a further increase in the z causes decrease in the slope. The variation of the power density at particular axial position is shown in Fig. 6.16. As stated the power density ($S(x,y,z)$) is clearly observed to increase as the z distance increases as shown in the figure. In this case, the g_{mo} used was 0.005, while the S_s = 0.002 W/μm². This figure illustrates clearly the effect of power and its contribution to the gain coefficient as stated earlier.

The investigation of the gain saturation of different g_{mo} (unsaturated material gain coefficient) is shown in Fig. 6.17. It was observed initially up to z = 200 μm that the curve was linear as it was going through constant gain as power is small since the width is larger. Around z = 600 μm it slopes downward, which means the rate of power increase is smaller due to the effect of gain saturation. For higher, g_{mo}, gain is higher, so the effect of gain saturation is higher as power was also high. The saturation power was maintained constant, at S_s = 0.002 W/μm², and g_{mo} was varied. For different values it is seen that the gain saturation level was reached on a respective, g_{mo}, thus it can be said that the power density increases along the axial direction but the rate is reduced when higher, reducing the total gain.

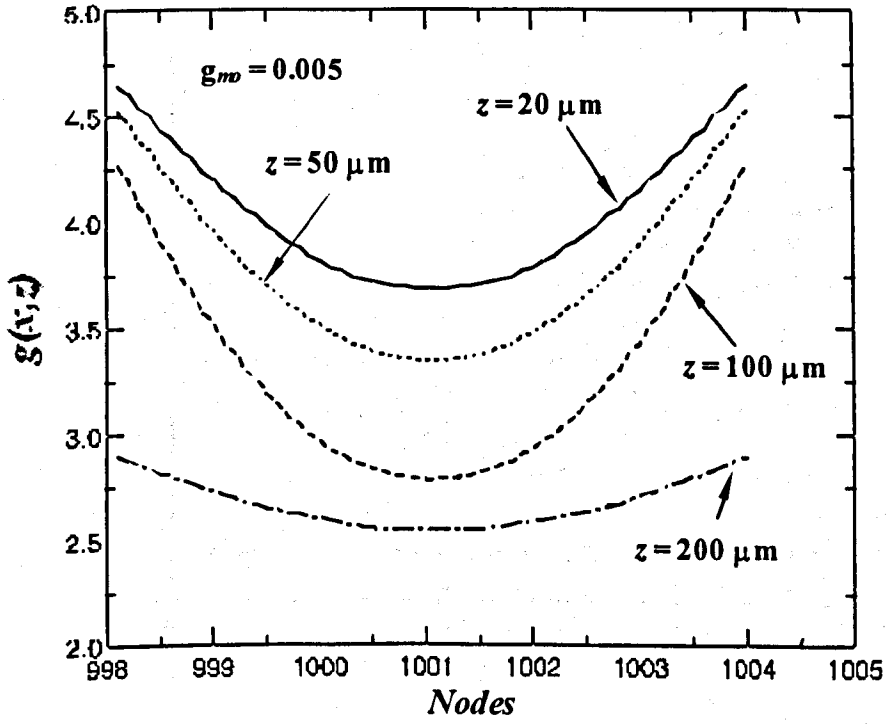

Fig. 6.15 The transverse variation of the gain coefficient, $g(x,y,z)$, at different axial position.

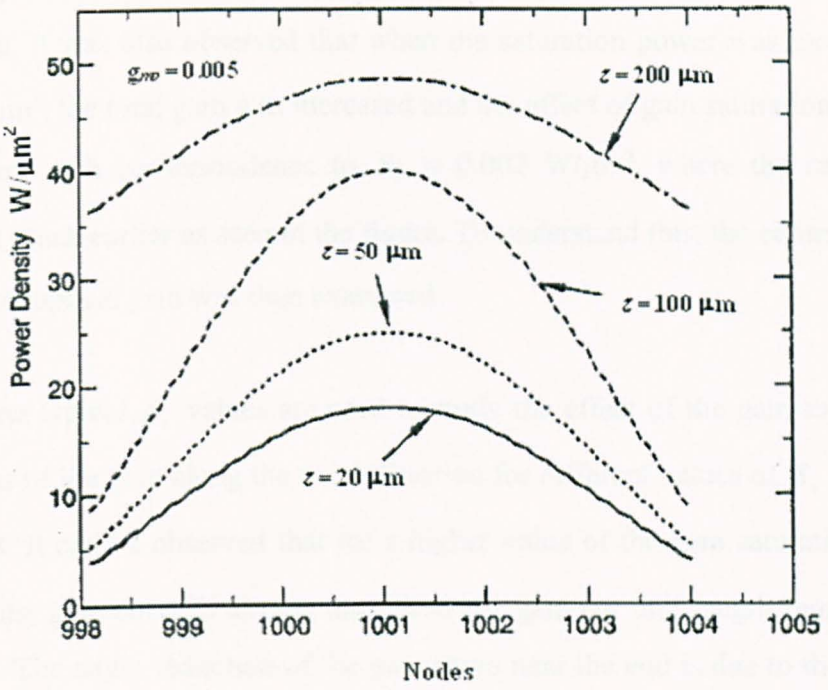

Fig. 6.16 The transverse variation of the power density ($S(x,y,z)$) at different axial position.

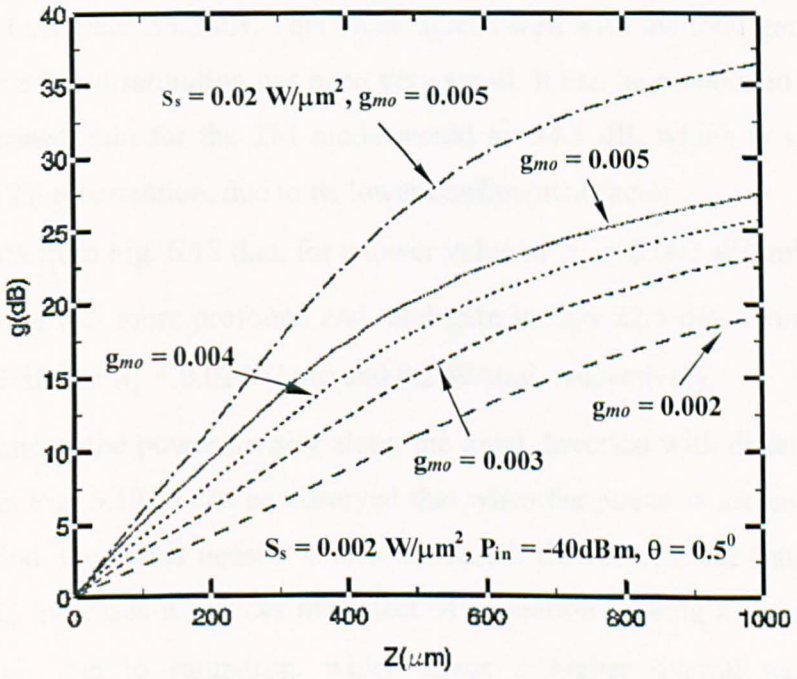

Fig. 6.17 Variations of gain with different gain coefficients (g_{mo}) and the effect of gain saturation.

Hence, as gain increases, power increases, effect of gain saturation increases gain per unit length/rate slows down but when it reaches z = 1000 μm, the increase is minimum. It was also observed that when the saturation power was increased, S_s = 0.02 W/μm², the total gain was increased and the effect of gain saturation was not that significant, with correspondence to S_s = 0.002 W/μm², where the saturation was observed much earlier as seen in the figure. To understand this, the contribution of S_s to the total optical gain was then examined.

Here some typical S_s values are used to study the effect of the gain saturation. The variations of the gain along the axial direction for different values of S_s are shown in Fig. 6.18. It can be observed that for a higher value of the gain saturation, S_s = 0.2 W/μm², the gain curve is almost linear and the gain per unit length remained almost constant. The slight reduction of the gain slope near the end is due to the higher total power affecting the gain near the output section.

It has also been shown earlier in Fig. 6.5 that, for this structure the average confinement factor is 0.195 and if the gain saturation can be neglected then the total gain would have been 35.3 dB. This value agrees well with the total gain of 35.5 dB as the effect of gain saturation has been very small. It can be mentioned here that the total unsaturated gain for the TM mode would be 34.8 dB, which is slightly lower than that of TE polarization, due to its lower confinement factor.

It can be seen from Fig. 6.18 that, for a lower value of S_s = 0.002 W/μm² the effect of gain saturation was more profound and total gain is only 22.5 dB, compared to 30.0 dB and 35.5 dB for S_s = 0.02 W/μm² and 0.2 W/μm², respectively.

The variations of the power density along the axial direction with different S_s values are shown in Fig. 6.19. It can be observed that when the power is increased along the axial direction, the power density is also increased. However, if the saturation power intensity (S_s) increases it reduces the effect of saturation causing a smaller reduction of $g(x, y, z)$, due to saturation, which gives a higher overall gain. Although oscillation peak for S_s = 0.2 W/μm² appear to be higher than that for S_s = 0.002 W/μm², but their percentage of variation are of similar order. At a given axial position

z, higher power gives increased power density. However, there are some oscillations that are shown here which are mainly due to the existence of higher order modes excitation.

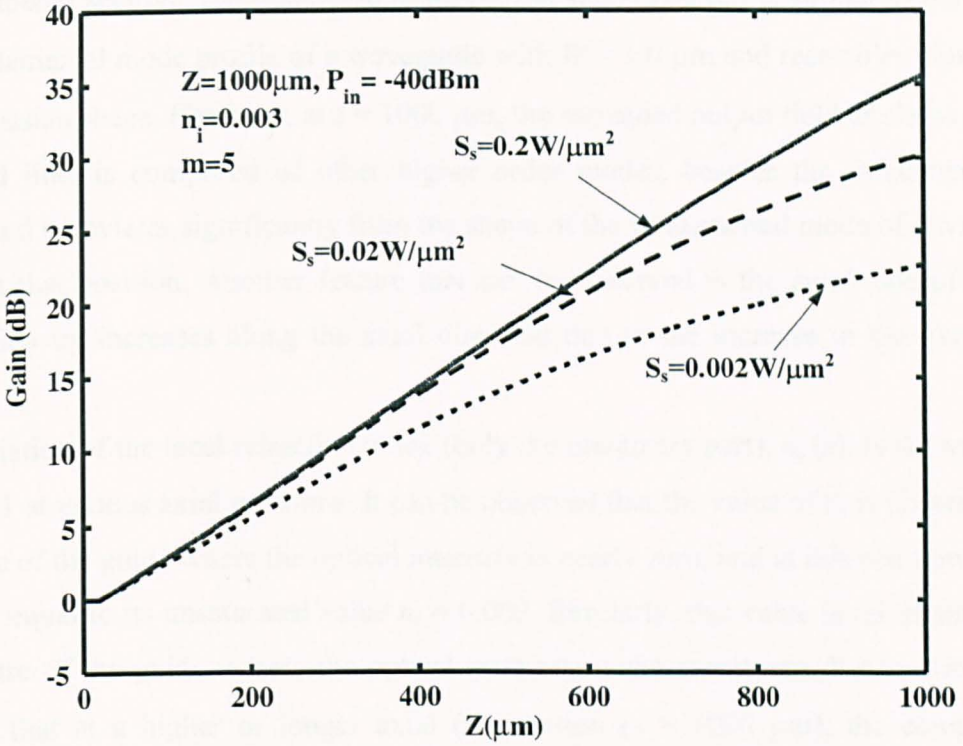

Fig. 6.18 Variations of the gain (dB) along the axial direction for different S_s values.

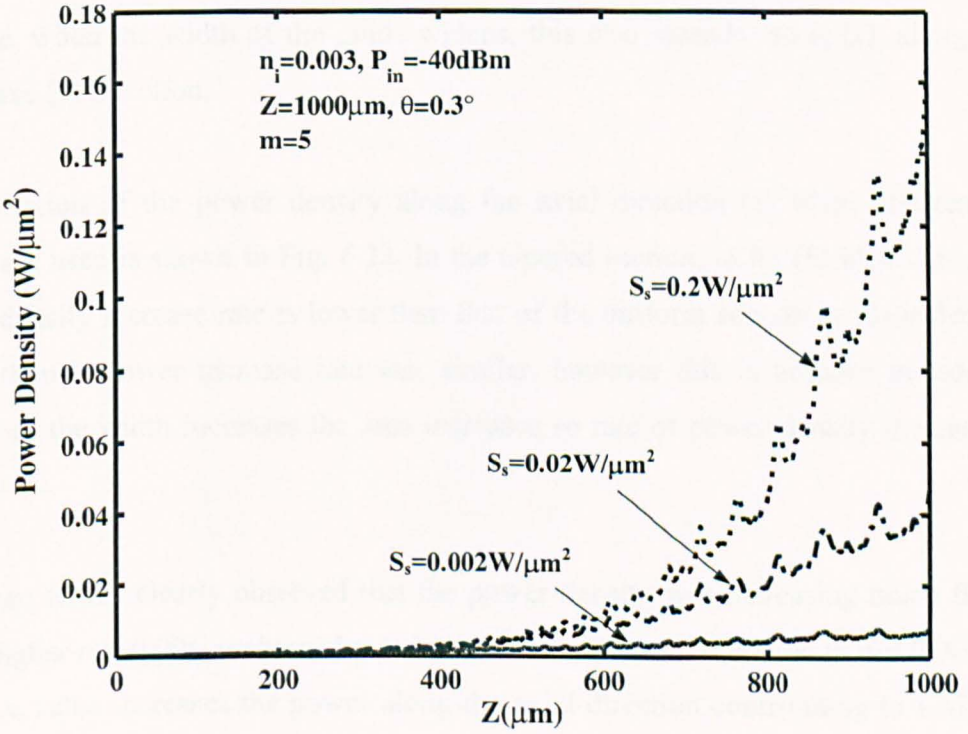

Fig. 6.19 Variations of the power density along the axial direction with different S_s values.

Variations of the power density along the transverse (x) direction at different axial positions are shown in Fig. 6.20. It can be observed that the optical field expands in the lateral direction as the axial distance increases, which is due to the increased width in the tapered section. The transverse beam profile at z = 100 μm is similar to that of the fundamental mode profile of a waveguide with W = 1.0 μm and resembles closely to a Gaussian shape. However, at z = 1000 μm, the expanded output field as shown by a dotted line, is composed of other higher order modes, besides the fundamental mode, and it deviates significantly from the shape of the fundamental mode of a wider guide at that position. Another feature that can be observed is the amplitude of the power density increases along the axial direction due to the increase in the overall gain.

The variation of the local refractive index (only the imaginary part), n_i (x), is shown in Fig. 6.21 at various axial positions. It can be observed that the value of n_i is highest at the edge of the guide where the optical intensity is nearly zero, and at this position the n_i (x) is equal to its unsaturated value n_i = 0.003. Similarly, this value is minimum at the centre of the guide, where the optical intensity is the maximum. It can also be noticed that at a higher or longer axial (z) position (z = 1000 μm), the complex refractive index profile is significantly lower, since the optical power is higher at this location, which reduced n_i (x) further. It is clearly visible that at a larger axial distance, when the width of the guide widens, this also spreads the n_i (x), along the transverse (x) direction.

The variation of the power density along the axial direction (z) when different n_i values are used is shown in Fig. 6.22. In the tapered section, as by (b) identified, the power density increase rate is lower than that of the uniform section as identified by (a). Although power increase rate was similar, however this is because in tapered section as the width increases the area increases so rate of power density increase is slower.

However, it was clearly observed that the power density was increasing much faster when higher n_i = 0.006 as shown by a chained line was used compared to n_i = 0.003. A higher n_i value increases the power along the axial direction contributing to a higher power density. For the dashed line as shown in the figure, when n_i = 0.003, there is no

gain in the uniform section, the rates are similar to the tapered structure of the same n_i, but due to no power increase in the uniform section the total power density is lower.

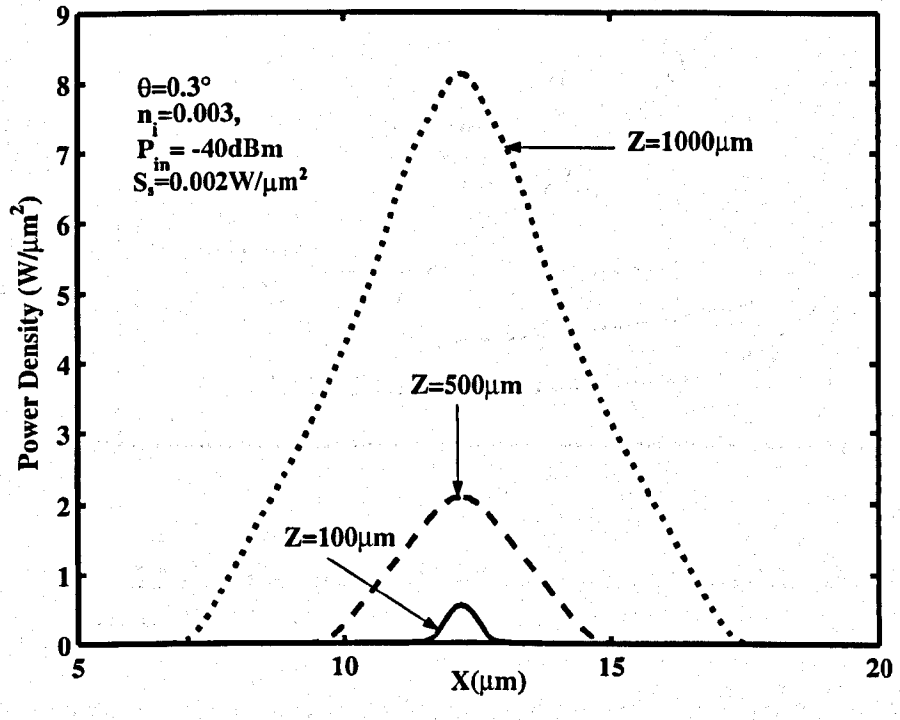

Fig. 6.20 Variations of the power density at different axial positions (z) along the transverse (x) direction.

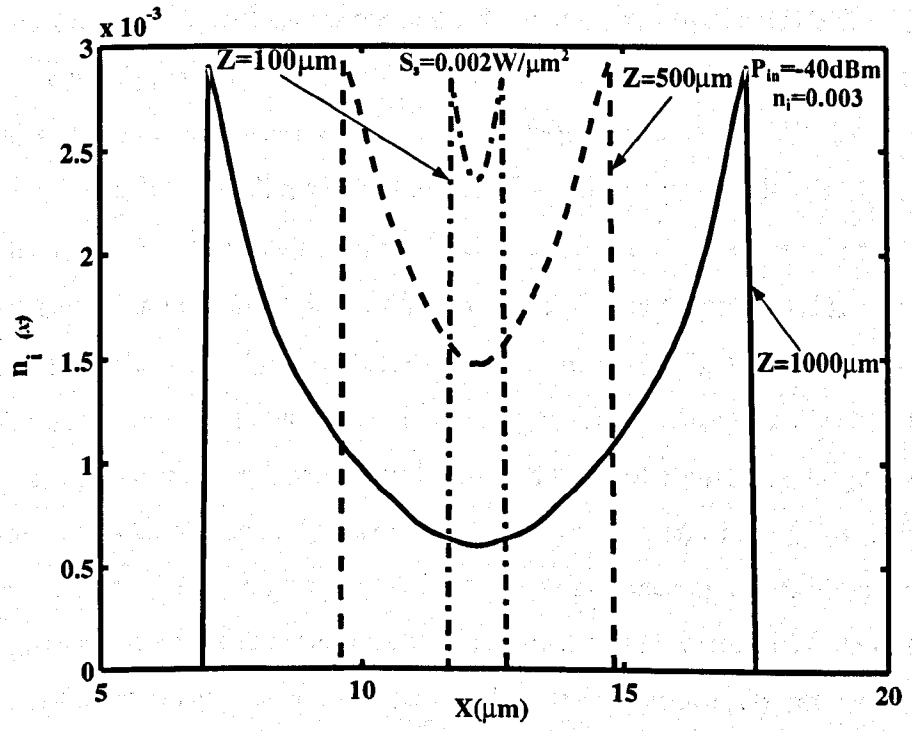

Fig. 6.21 Transverse variation of the $n_i(x)$ at different axial positions (centre of the active area).

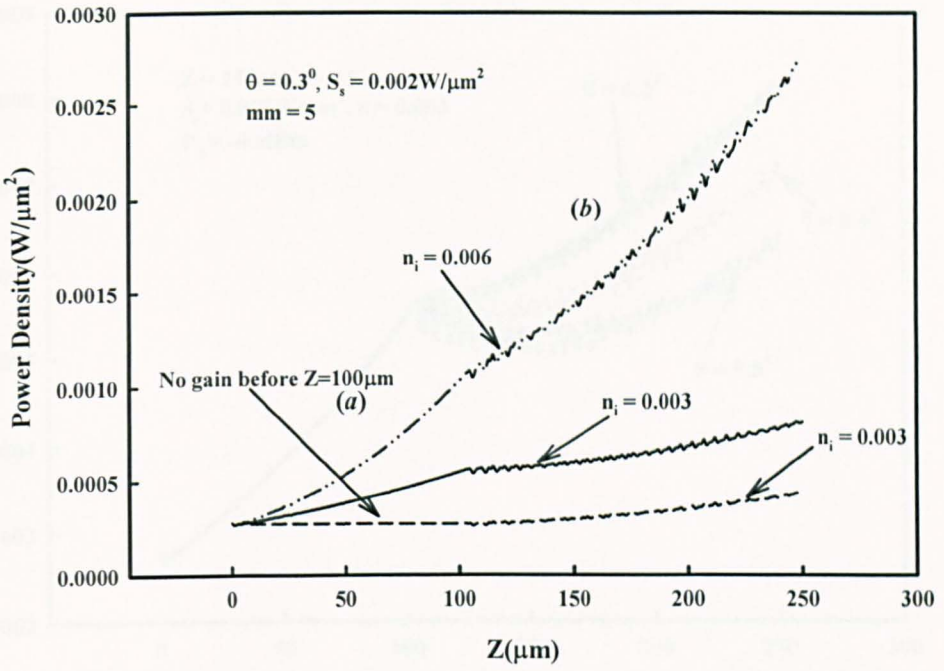

Fig. 6.22 Variation of the power density along the axial direction (z) when different n_i values are used.

The effect on the power density is visible when different tapered angles are used, and next the effect of tapered angle is studied. The variation of the power density along the axial direction for different tapered angles is demonstrated and shown in Fig. 6.23. In this case, the P_{in}, S_s, and n_i was maintained constant at –40 dBm, 0.002 W/μm^2, and 0.003 respectively, while the tapered angle is varied. In both cases, since the input power is very low, the power density is increasing but very slowly. However, it is clearly seen that for a smaller tapered angle, $\theta = 0.3^0$ the power density is increasing much faster, therefore, overall attaining the saturation much earlier. Variation of the power density along the axial direction (z) when different tapered angles, θ, with high input power is shown in Fig. 6.24, however this time the P_{in} = 10 dBm, being very large, for both the tapered angles it is clearly observed after the z = 100 (uniform section), the power density drops rapidly. In this particular case, the large drop in the power density is almost entirely due to the lateral expansion of the SOA. However, it is clearly observed that higher tapered angles experience much more drop on the overall power density. If the cross-section area of the SOA increases (due to tapering) faster than the power increase, then, power density is reduced. By proper design, the power density can be adjusted by controlling gain parameter and taper angle.

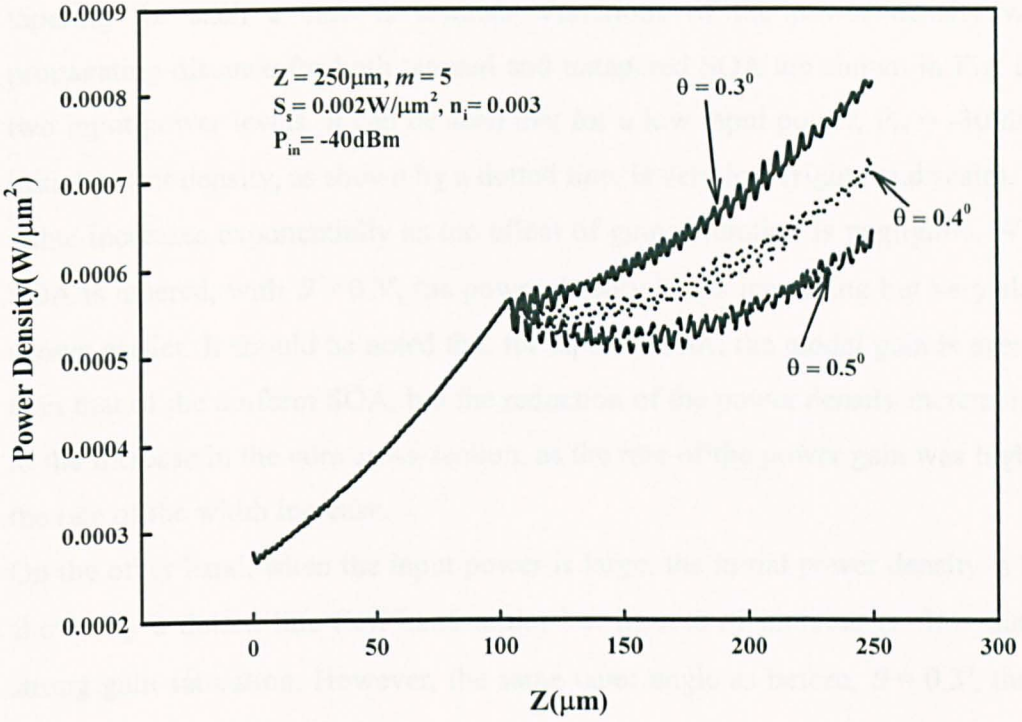

Fig. 6.23 Variation of the power density along the axial direction (z) when different tapered angles, θ, with low input power.

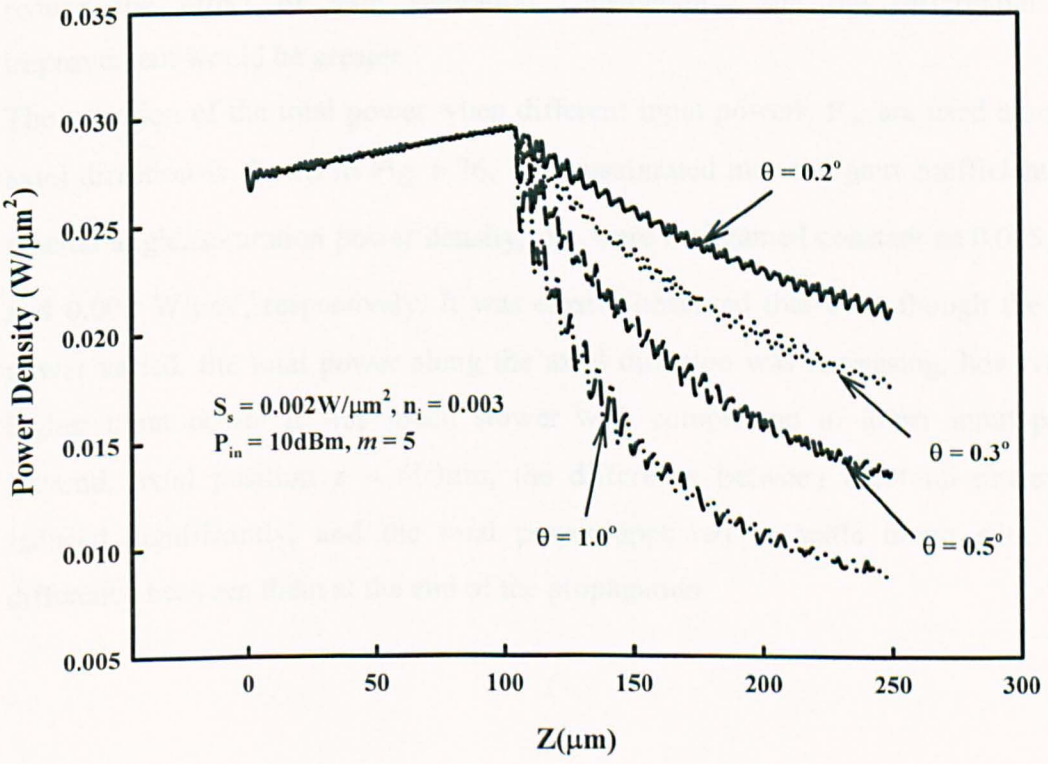

Fig. 6.24 Variation of the power density along the axial direction (z) when different tapered angles, θ, with high input power.

The effect of gain saturation is severe when input power is high and next the effect of tapering for such a case is studied. Variations of the power density with the propagating distance for both tapered and untapered SOA are shown in Fig. 6.25 for two input power levels. It can be seen that for a low input power, P_{in} = -30 dBm, the initial power density, as shown by a dotted line, is very low (right hand scale), but this value increases exponentially as the effect of gain saturation is negligible. When the SOA is tapered, with $\theta = 0.3^0$, the power density keeps increasing but very slowly as shown earlier. It should be noted that for tapered SOA, the modal gain is even higher than that of the uniform SOA, but the reduction of the power density increment is due to the increase in the core cross-section, as the rate of the power gain was higher than the rate of the width increase.

On the other hand, when the input power is large, the initial power density is high, as shown by a dotted line (left hand scale) but its rate of increase is slow due to the strong gain saturation. However, the same taper angle as before, $\theta = 0.3^0$, the power density drops rapidly.

In this case, since the power gain was very slow, the large drop in the power density is almost entirely due to the lateral expansion of the SOA as stated earlier. This would reduce the effect of gain saturation considerably, and the differential gain improvement would be greater.

The variation of the total power when different input powers, P_{in}, are used along the axial direction is shown in Fig. 6.26. The unsaturated material gain coefficient, g_{mo}, tapered angle, saturation power density, S_s, were maintained constant as 0.005, 0.5^0, and 0.002 W/μm², respectively. It was clearly observed that even though the input power varied, the total power along the axial direction was increasing, however for higher input power it was much slower with comparison to lower input power. Beyond, axial position z = 600μm, the difference between the total power was reduced significantly, and the total power appeared to settle down with slight difference between them at the end of the propagation.

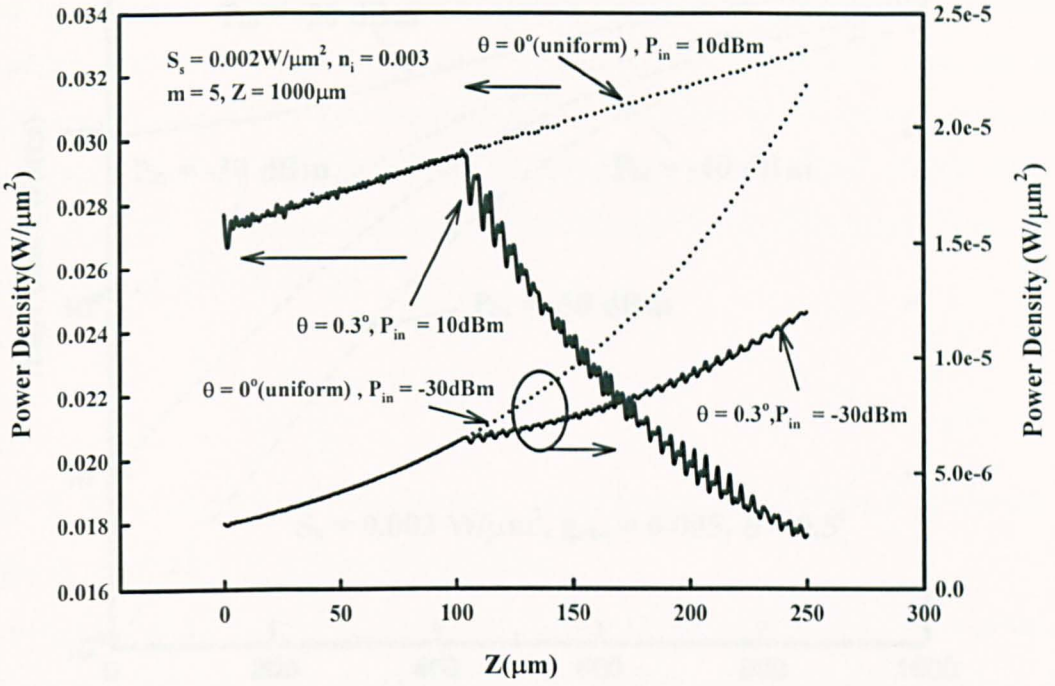

Fig. 6.25 Variations of the power density along the axial direction with different input power, for both tapered and untapered SOA.

The variations of the gain along the axial direction for different tapered angle are shown in Fig. 6.27, when S_s, n_i, and P_{in} were maintained constant at 0.002 W/μm², 0.003, and –40 dBm, respectively. It can be observed that the tapered angle has significant impact on the final gain value. This is mainly because smaller angles yield a narrower width, which progressively increases local power density and reduces gain coefficients due to saturation. It was clearly observed that the total gain for $\theta = 0.3^0$ was 22.5 dB, compared to 27.5 dB when $\theta = 1.5^0$. This clearly shows that a wider tapered angle makes the SOA cross-section larger, reduces the effect of gain saturation in comparison to smaller tapered angles. Hence the higher the tapered angle, lower is the effect of saturation causing the overall gain to be high. Now, the variation of the overall power gain with the tapered angle is shown in Fig. 6.28 for two different gain saturation values. It can be observed that as the tapered angle, θ, is increased the total gain is also increased due to smaller effect of the gain saturation. In this case the input signal is taken as –40 dBm. It can also be observed that when the S_s value is increased, then the overall gain is also increased.

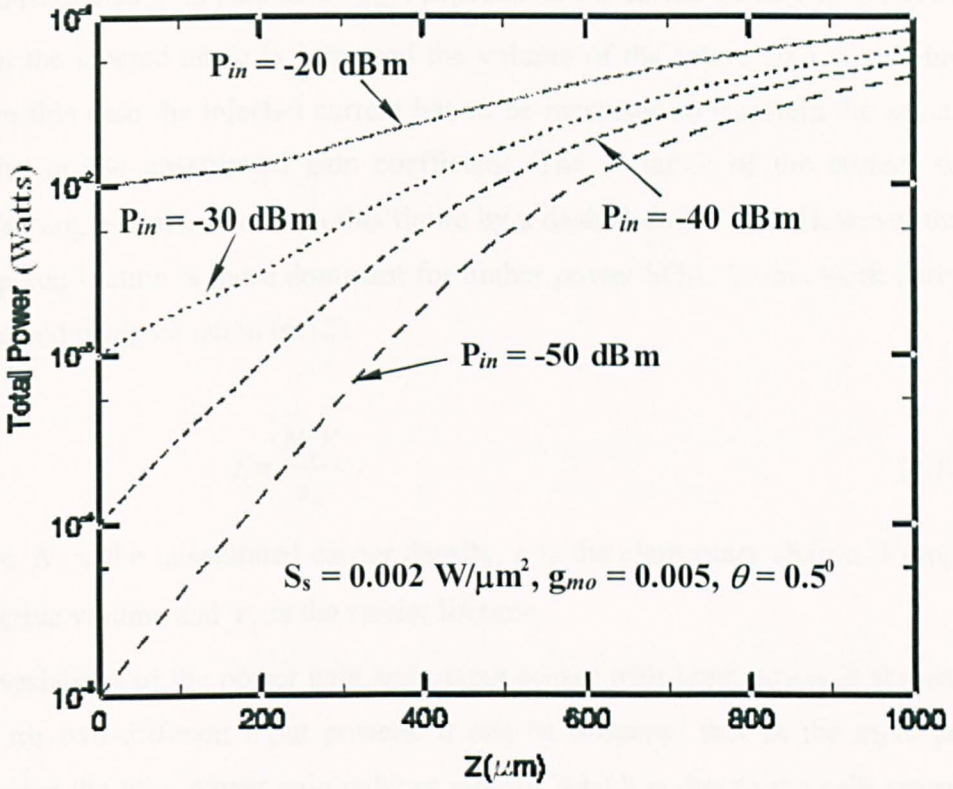

Fig. 6.26 Variations of the total power along the axial direction with different input powers.

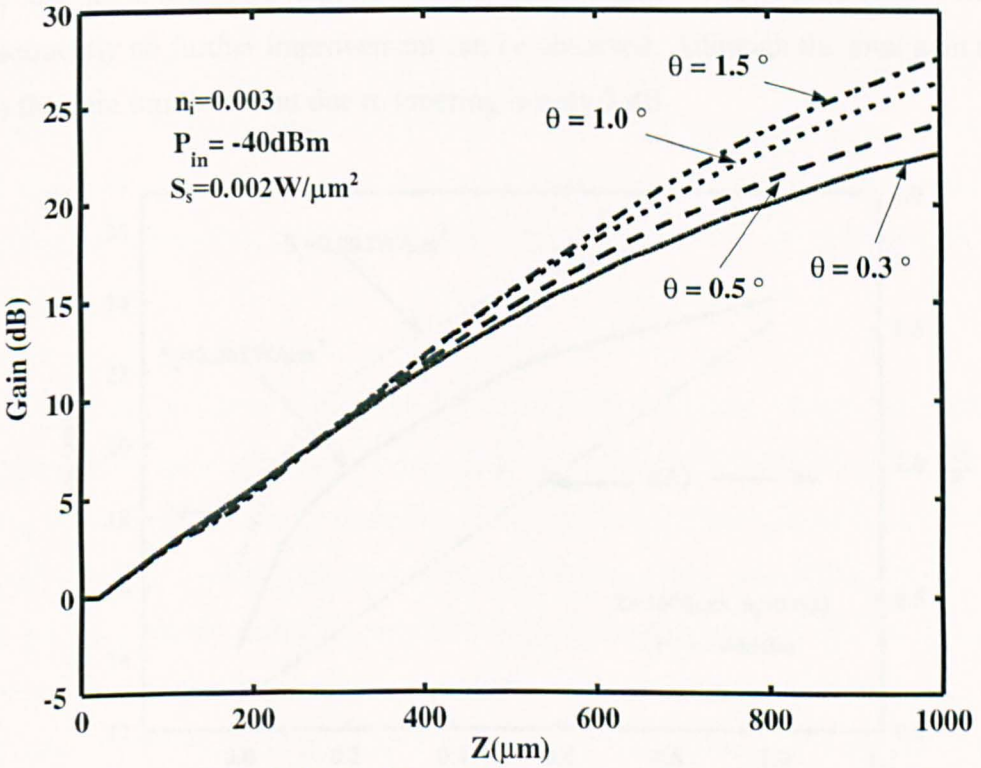

Fig. 6.27 Variations of the gain along the axial direction with different tapered angles for a wider semiconductor amplifier.

The unsaturated gain parameter, g_{mo}, depends on the carrier density in the active area. When the tapered angle is increased the volume of the active area is also increased and in this case the injected current has to be increased to maintain the same carrier density or the unsaturated gain coefficient. The variation of the current with the tapered angle is also shown in this figure by a dashed-dotted line. However the effect of tapered section is more dominant for higher power SOA. In this work current was calculated using equation (6.12)

$$I = \frac{N_q V}{\tau_s} \tag{6.12}$$

where N is the unsaturated carrier density, q is the elementary charge, V represents the active volume and τ_s is the carrier lifetime.

The variations of the power gain and output power with input power is shown in Fig. 6.29 for two different input powers. It can be observed that as the input power is increased the total power gain reduces rapidly, which is due to the gain saturation. It can also be observed that for a low input power, P_{in} = -40 dBm, as shown by a dashed line, the gain increases rapidly as the taper angle, θ, is increased to 0.1^0 and subsequently no further improvement can be observed. Although the total gain is very high the gain improvement due to tapering is only 3 dB.

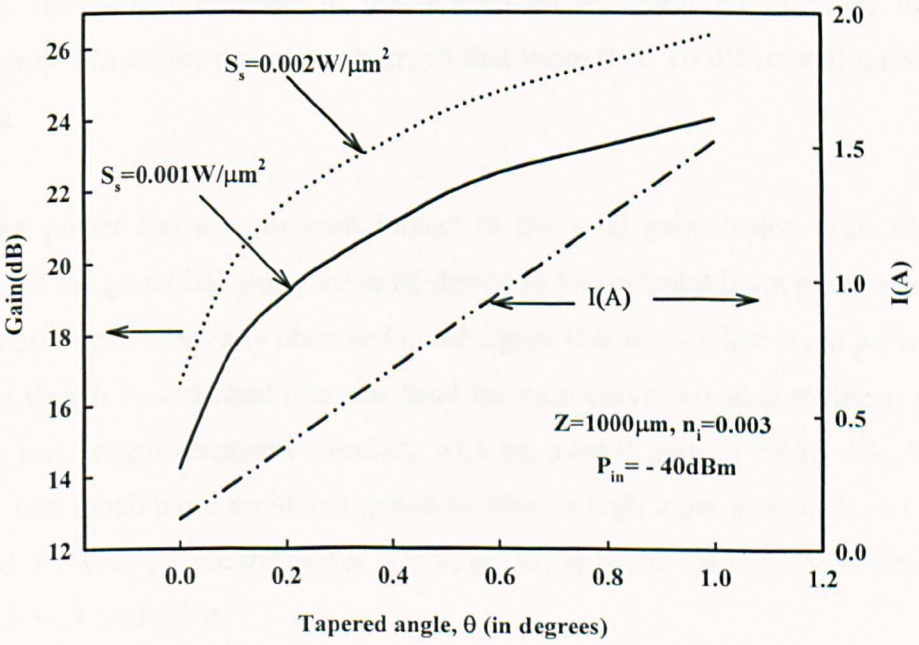

Fig. 6.28 Variations of gain (dB) and current (A) against tapered angle with different S_s values.

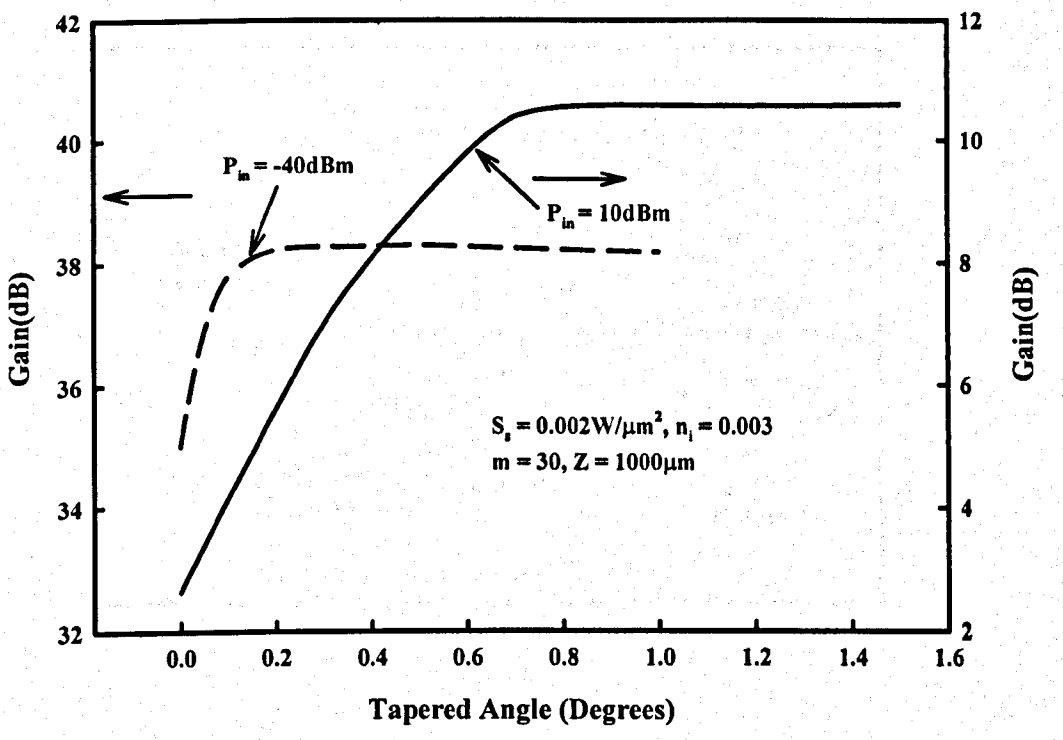

Fig. 6.29 Effect of the tapered angles (degrees) on the overall gain with different input power.

On the other hand, for a larger input power, P_{in} = 10 dBm, the total gain is very low, but this value increases monotonically and reaches its maximum value around θ = 0.7^0 and any further increase in the tapered angle would not increase the gain significantly. However, it can be observed that more than 10 dB overall gain can be achieved.

The input power has a significant impact to the total gain, hence examined. The variation of the gain (dB) along the axial direction for different input powers is shown in Fig. 6.30. It can be clearly observed in the figure that when a low input power, P_{in} = -40 dBm shown by a dashed line was used the gain curve was almost linear, and the gain per unit length remained constant, with an overall gain of 38.28 dB. Also the increase was much more rapid, compared to when a high input power, P_{in} = 10 dBm, was used. However, since the power is low, so power density is low, the effect of gain saturation was negligible.

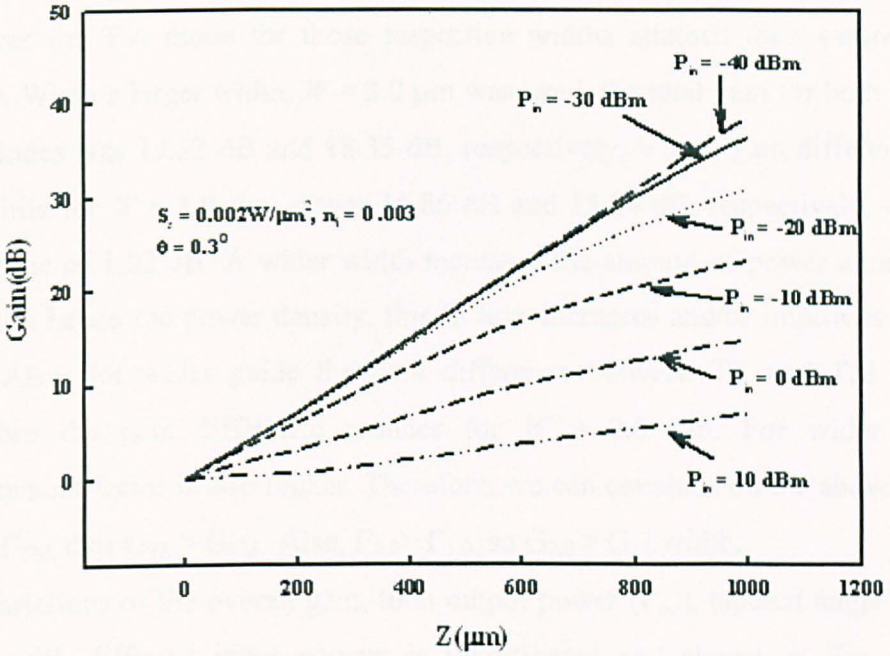

Fig. 6.30 Variations of the gain (dB) along the axial direction for different input powers.

On the other hand, when a high input power was used, the gain increase along the axial direction was very slow, but since the power density was high, the effect of saturation was attained earlier, with a small overall gain of 7.0 dB. Another significant observation made was that when the input powers were P_{in} = -30 dBm and -40 dBm, the gain along the axial direction was nearly the same, until when z > 800μm, when P_{in} = -40 dBm had a slight increase in the overall gain. It was also observed though not shown here that when the input power was further reduced the effect of gain was minimum, for the axial distance of z = 1000 μm.

The effect of the polarization dependence on the total gain along the axial direction was also examined. In this experiment a uniform guide structure was established, with the tapered angle, $\theta = 0^0$. It is clearly seen in Fig. 6.31 that initially the gain for all the TE and TM modes was zero, however further increase along the axial direction contributed to increase in the gain with slight difference before reaching their respective saturation levels.

For both widths, i.e., W = 1.0 μm and 2.0 μm, the TE mode shown by the dashed and solid lines, respectively, their overall gain was slightly higher than for the TM mode, however the TM mode for those respective widths attained their saturation much earlier. When a larger width, W = 2.0 μm was used, the total gain for both the TE and TM modes was 19.32 dB and 18.35 dB, respectively, with a gain difference of 0.97 dB, while for W = 1.0 μm, it was 16.86 dB and 15.84 dB, respectively, with a gain difference of 1.02 dB. A wider width increases the amount of power along the axial direction hence the power density, this in turn increases and/or improves the overall gain. Also, for wider guide the gain difference between TE and TM is smaller, therefore the gain difference reduces for W = 2.0 μm. For wider guide the confinement factor is also higher. Therefore, we can conclude on the above work that, $\Gamma_{TE} > \Gamma_{TM}$, thus $G_{TE} > G_{TM}$. Also, $\Gamma_{2.0} > \Gamma_{1.0}$, so $G_{2.0} > G_{1.0}$ width.

The variations of the overall gain, total output power (P_{out}), tapered angle or uniform guide with different input powers is investigated and shown in Fig. 6.32. It is observed that when the input power decreases, the overall gain increases as shown in the left hand side of the figure caused by increase in the power density as stated earlier. However for a uniform guide structure the saturation was reached earlier, with an overall gain of 35.01 dB, compared to the tapered structures which was 38.28 dB and 38.30 dB for $\theta = 0.3^0$ and 0.5^0, respectively. It can also be seen that for the tapered angles the difference in the overall gain when different input powers were used was minimum. However for the higher tapered angle, $\theta = 0.5^0$, the gain was slightly higher due to the effect of the guide width. At input power, P_{in} = -40 dBm both structures attained their saturations. The overall gain will always be high, when a large tapered angle is used, as long as the input power is low.

On the other hand, the total P_{out} results shown in the right hand side of the figure reflects the gain curve; when the guide was uniform increase in P_{in} increases the total P_{out}, with a total output power, P_{out} = 12.63 dBm at the end of the propagation when 10 dBm input power was used. When a tapered structure was implemented, the total output power was increased significantly with a total P_{out} = 17.00 dBm and 18.98 dBm for $\theta = 0.3^0$ and 0.5^0, respectively, thus it can be concluded here that increase in tapered angle increases the overall output power, as long as the input power is high.

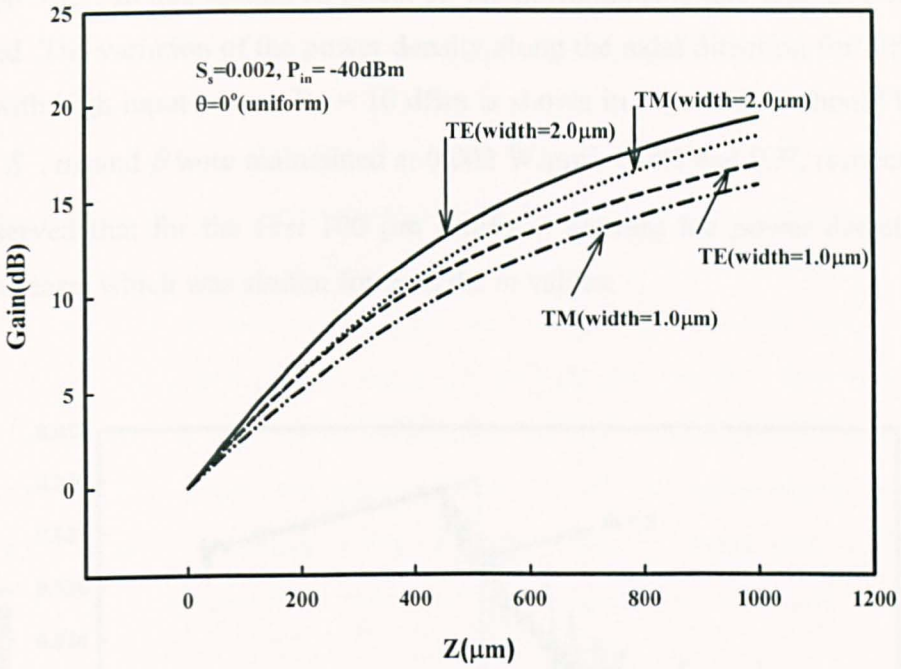

Fig. 6.31 Variations of gain (dB) along the axial direction for the TE and TM polarized modes at different input widths.

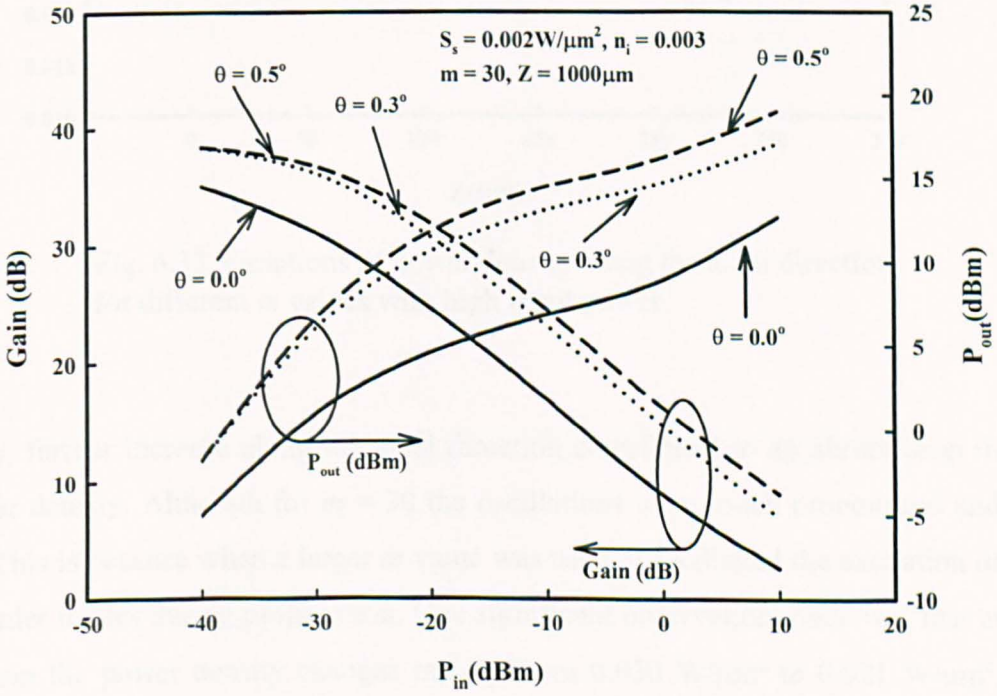

Fig. 6.32 Variations of the gain and total output power for different tapered angles with different input powers.

The effect of remeshing steps (m) plays a great role to the spot-size area as explained in section 5.5.1. In this section its effect on the power density and total power will be examined. The variation of the power density along the axial direction for different m values with high input power, P_{in} = 10 dBm is shown in Fig. 6.33. It should be noted that the S_s, n_i, and θ were maintained at 0.002 W/μm², 0.003 and 0.3°, respectively. It was observed that for the first 100 μm (uniform section) the power density had a slight increase, which was similar for both the m values.

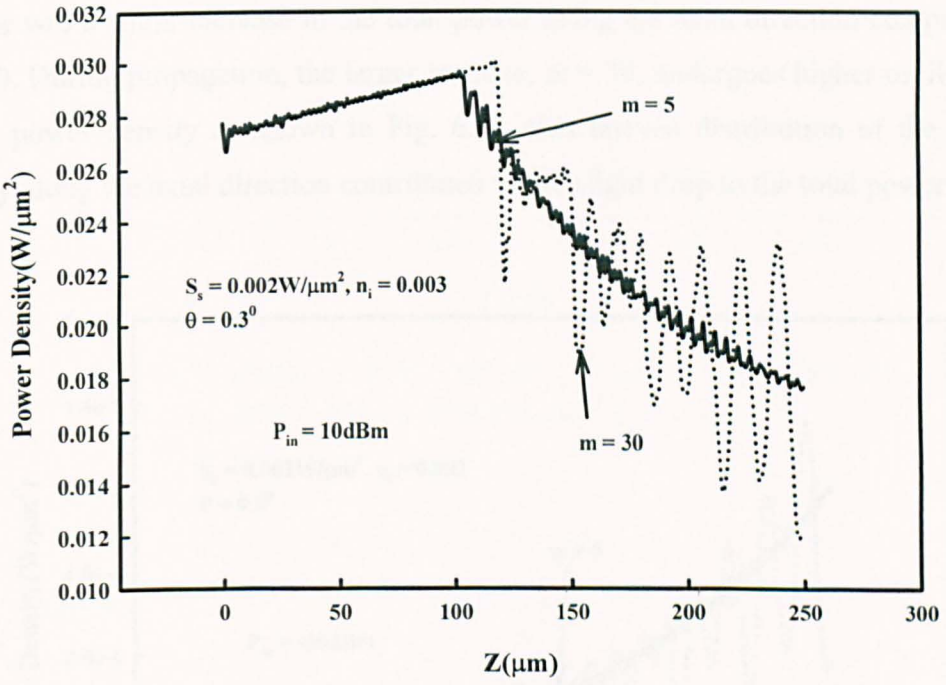

Fig. 6.33 Variations of power density along the axial direction for different m values with high input power.

However, further increase along the axial direction contributed to an abrupt drop in the power density. Although for m = 30 the oscillations were much pronounced and visible. This is because when a larger m value was used, it facilitated the excitation of higher order modes during propagation. One significant observation made was that at z =120 μm the power density changes rapidly from 0.030 W/μm² to 0.021 W/μm², before it settles down to 0.025 W/μm², this feature has also been observed previously in the spot-size expansion in Fig. 5.37. However, when z = 150 μm, the power density undergoes oscillations which does not appear to settle down, to the end of the

propagation. When a low input power, P_{in} = -30 dBm was used and the parameters maintained as before as shown in Fig. 6.34, it was observed that when $z > 100$ μm, the power density increases exponentially along the axial distance and the effect of m was the same as the previous figure.

The variations of the total power along the axial distance when different m values, were used is shown in Fig. 6.35. It can clearly be observed that for the uniform section the total power was the same for both the remeshing steps, however further increase varied the total power between the two m values. It is seen that for a low m value, m = 5, their was a slight increase in the total power along the axial direction compared to m = 30. During propagation, the larger m value, m = 30, undergoes higher oscillations in the power density as shown in Fig. 6.34, this uneven distribution of the power density along the axial direction contributed to the slight drop to the total power.

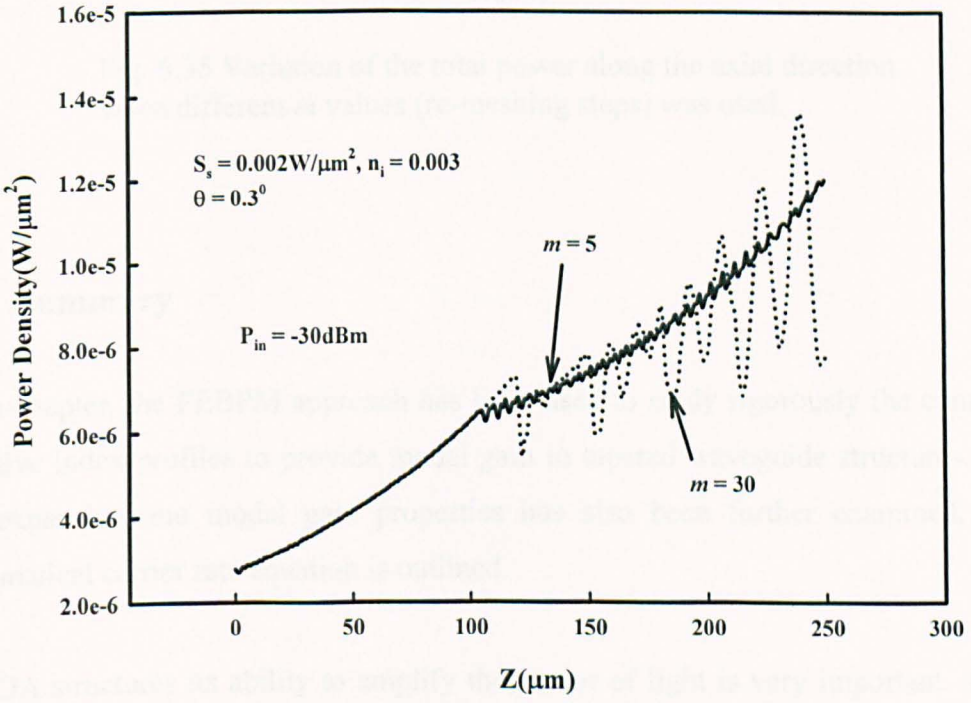

Fig. 6.34 Variations of power density along the axial direction for different m values with low input power.

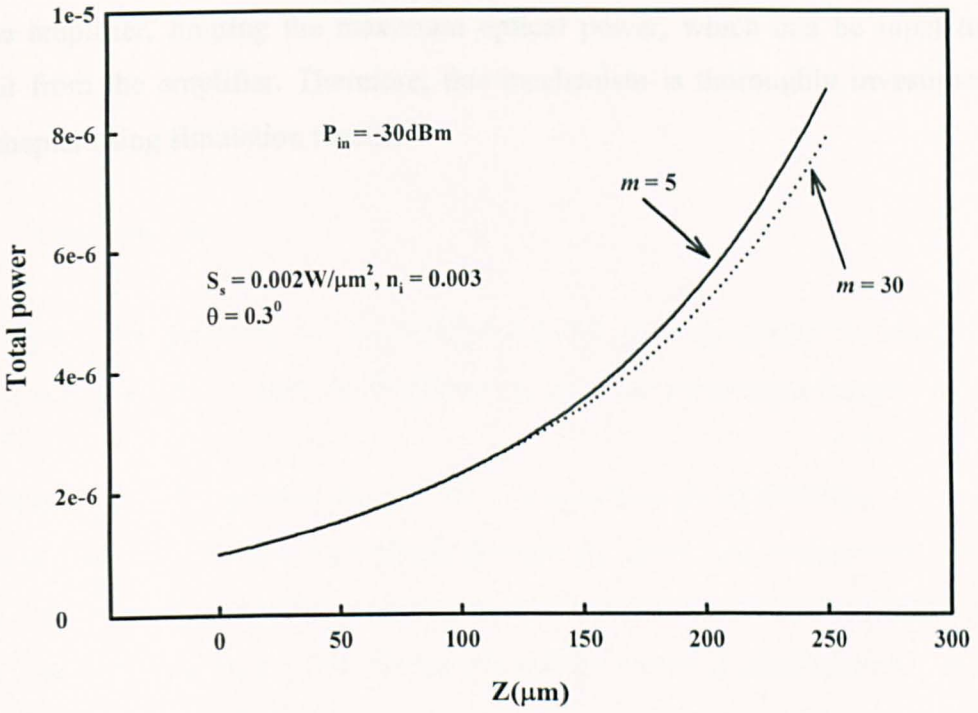

Fig. 6.35 Variation of the total power along the axial direction when different *m* values (re-meshing steps) was used.

6.6 Summary

In this chapter, the FEBPM approach has been used to study rigorously the complex refractive index profiles to provide modal gain in tapered waveguide structures. The field expansion and modal gain properties has also been further examined. The mathematical carrier rate equation is outlined.

For SOA structures its ability to amplify the power of light is very important. Thus, the gain of the SOA is of primarily interest, as it determines other essential factors, such as signal-to-noise ratio when incorporated into systems [186]. In this chapter the gain analysis of SOA structures is described which includes the variation of the gain, tapered angle, current, input power and power saturation along the axial direction.

It is well known that the maximum gain, which can be obtained in these structures is restricted by gain saturation mechanisms. This subsequently affects the dynamic range of the amplifier, limiting the maximum optical power, which can be input to and output from the amplifier. Therefore, this mechanism is thoroughly investigated in this chapter using simulation results.

7.0 Far field Patterns and Birefringence in SOA Structures

7.1 Introduction

In Chapter 2, we discussed the Far field profile theory in this chapter we shall discuss the mode expansion principle and furthermore, demonstrate some simulation results.

The optical wave transmitted through the waveguide is partly reflected at the facet; simultaneously, it is partly transmitted through the facet and radiates into the free space. The transmitted wave, observed just outside the facet, is in a form proportional to the lateral mode E (x,y) of the waveguide and the intensity distribution is called the *near-field pattern* (NFP).
The output wave propagates in free space, with evolution of the wavefront and the intensity distribution. The intensity distribution observed at a plane sufficiently away from the facet is called the *far-field pattern* (FFP).

Analysis of the wave-front and the intensity distribution in the far field provides important insights useful for the design of focussing, collimating and coupling into optical fibre of semiconductor laser light for practical applications.

The dimensions of a convenient test range can be reduced by making measurements in the near field, and then using the analytical methods to transform the measured near-field data to compute the far field radiation characteristics [187-189]. These are referred to as *near field* or *far field* (NF/FF) methods. Generally, implementation of NF/FF transformation techniques begin with measuring the magnitude and phase of the tangential electric field components radiated at regular intervals over a well-defined surface in the near field. By the principle of *modal expansion*, the sampled E-field data is used to determine the amplitude and phase of an angular spectrum of plane, cylindrical or spherical waves. Expressing the total field in terms of modal expansion allows the calculation of the field at any distance, solving for the fields at

infinite distance results in the far field pattern. However, the planar-near field transformation has a principal advantage over the cylindrical and spherical techniques, due to its mathematical simplicity.

In the next section of this chapter we shall discuss the mode expansion method for planar waveguides.

7.2 Mode Expansion Method for Planar Waveguides

The mathematical formulations of the planar NF/FF method are based on the plane wave (modal) method. Simply stated, any monochromatic, but otherwise arbitrary, wave can be represented as a superposition of plane wave travelling in different directions, with different amplitudes, but all of the same frequency. The objective of the plane wave expansion is to determine the unknown amplitudes and directions of propagation of the plane waves. Similarly, cylindrical wave and spherical wave expansions are used to determine far field patterns from fields measured in the near field over cylindrical and spherical surfaces, respectively.

The relationship between the near–zone ***E***-field measurement and the far-zone fields for planar waveguides can be expressed as

$$E(x,y,z)=\frac{1}{4\pi^2}\int_{-\alpha}^{\alpha}\int_{-\alpha}^{\alpha} f(k_x,k_y)e^{-jk.r}\,dk_x dk_y \qquad (7.1)$$

where

$$f(k_x,k_y)=\hat{a}_x f_x(k_x,k_y)+\hat{a}_y f_y(k_x,k_y)+\hat{a}_z f_z(k_x,k_y) \qquad (7.2)$$

$$k=\hat{a}_x k_x+\hat{a}_y k_y+\hat{a}_z k_z \qquad (7.3)$$

$$r=\hat{a}_x x+\hat{a}_y y+\hat{a}_z z \qquad (7.4)$$

where $f(k_x, k_y)$ represents the plane wave spectrum of the field. The x and y components of the electric field measured over a plane surface ($z = 0$) are expressed as

$$E_{xa}(x, y, z = 0) = \frac{1}{4\pi^2} \int_{-\alpha}^{\alpha} \int_{-\alpha}^{\alpha} f_x(k_x, k_y)\, e^{-j(k_x x + k_y y)} dk_x dk_y \qquad (7.5)$$

$$E_{ya}(x, y, z = 0) = \frac{1}{4\pi^2} \int_{-\alpha}^{\alpha} \int_{-\alpha}^{\alpha} f_y(k_x, k_y)\, e^{-j(k_x x + k_y y)} dk_x dk_y \qquad (7.6)$$

The x and y co-ordinates of the plane wave spectrum, $f_x(k_x, k_y)$ and $f_y(k_x, k_y)$, in terms of the near-zone electric field is given as

$$f_x(k_x, k_y) = \int_{-b/2}^{+b/2} \int_{-a/2}^{+a/2} E_{xa}(x', y', z' = 0)\, e^{+j(k_x x' + k_y y')} dx' dy' \qquad (7.7)$$

$$f_y(k_x, k_y) = \int_{-b/2}^{+b/2} \int_{-a/2}^{+a/2} E_{ya}(x', y', z' = 0)\, e^{+j(k_x x' + k_y y')} dx' dy' \qquad (7.8)$$

The far field pattern, in terms of the plane wave spectrum function, f, is then expressed as

$$E(r, \theta, \phi) \cong j \frac{k e^{-jkr}}{2\pi r} [\cos\theta\, f(k_x, k_y)] \qquad (7.9)$$

or

$$E_\theta(r, \theta, \phi) \cong j \frac{k e^{-jkr}}{2\pi r} (f_x \cos\phi + f_y \sin\phi) \qquad (7.10)$$

$$E_\phi(r, \theta, \phi) \cong j \frac{k e^{-jkr}}{2\pi r} \cos\theta (-f_x \sin\phi + f_y \cos\phi) \qquad (7.11)$$

The procedure then to determine the far field from near field is as follows:

1) Obtain the electric field components $E_{xa}(x, y, z = 0)$ and $E_{ya}(x, y, z = 0)$ in the near field.

2) Find the plane wave spectrum function f_x and f_y using equations (7.7) and (7.8), respectively.

3) Determine the far field electric field using equations (7.10) and (7.11), respectively.

Similar procedures are used for cylindrical and spherical measuring systems except that the constant surfaces are, respectively, cylinders and spheres. However, their corresponding analytical expressions have different forms.

It is apparent once again, that if the tangential field components are known along a plane, the plane wave spectrum can be found, more convenient if the evaluation is restricted to the far field region.

7.3 Simulation Results

In this section the far field patterns will be studied and demonstrated. The near field was obtained from the Beam Propagation Method (BPM) input and output fields. These were then investigated and their far field patterns plotted. It should be noted here that tapered waveguide structures were used.

The variation of the farfield pattern with different angles for both the absolute and real and imaginary inputs are shown in Fig. 7.1. It should be noted here that a tapered waveguide structure was used with a tapered angle, $\theta = 0.3^0$. The dashed and solid lines represent the absolute input and real and imaginary parts, respectively. It was observed that when the real and imaginary parts were read and launched to generate the near field, the farfield pattern generated was similar to when the absolute field was launched. However, in this figure we can see clearly that there was a slight mismatch between the two, which is insignificant. It should be noted that, the farfield pattern when the imaginary and real values were obtained never expanded to their maximum due to the size of the window.

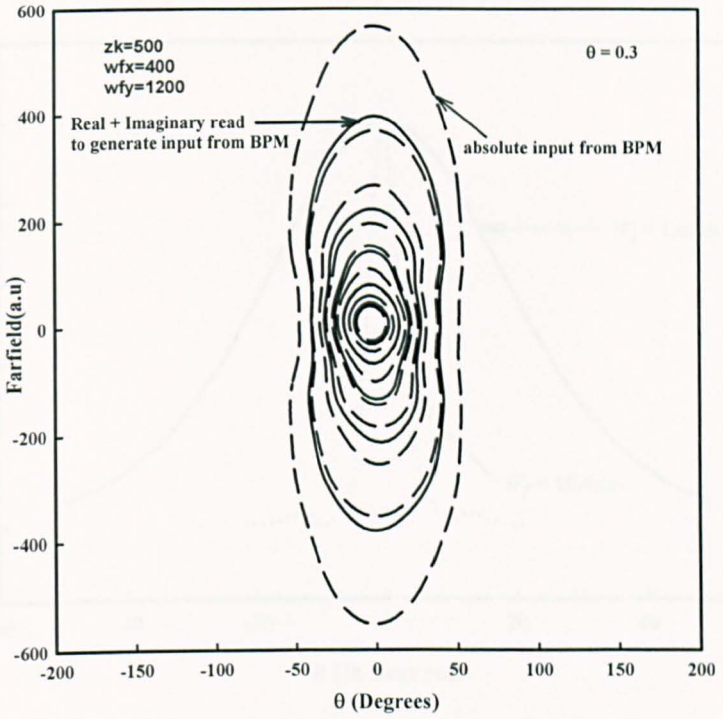

Fig. 7.1 Variation of the farfield with different angles, for both absolute and real and imaginary inputs.

The variations of the farfield when the mode field was launched at the start of the waveguide (before tapering) and after tapering were investigated and shown in Fig. 7.2. It should be noted here that at the start the initial width of the guide was W_i = 1.0 μm and expanded to W_f = 10.4 μm at the end of the propagation. It can be clearly seen that when the near field was W_i = 1.0 μm, the farfield pattern widens from θ = -50° to 50°. However, when the output field was launched the farfield beam was reduced to θ = -20° to 20° and the appearance of ripples were visible. It should be noted here that when a Gaussian near field input was used the farfield pattern was similar to the near field, but in this case the modal field as the input profile was used. The presence of ripples was due to the mode expansion after propagation and phase change, which was contributed due to the excitation of higher order modes with the fundamental mode during propagation in the tapered section.

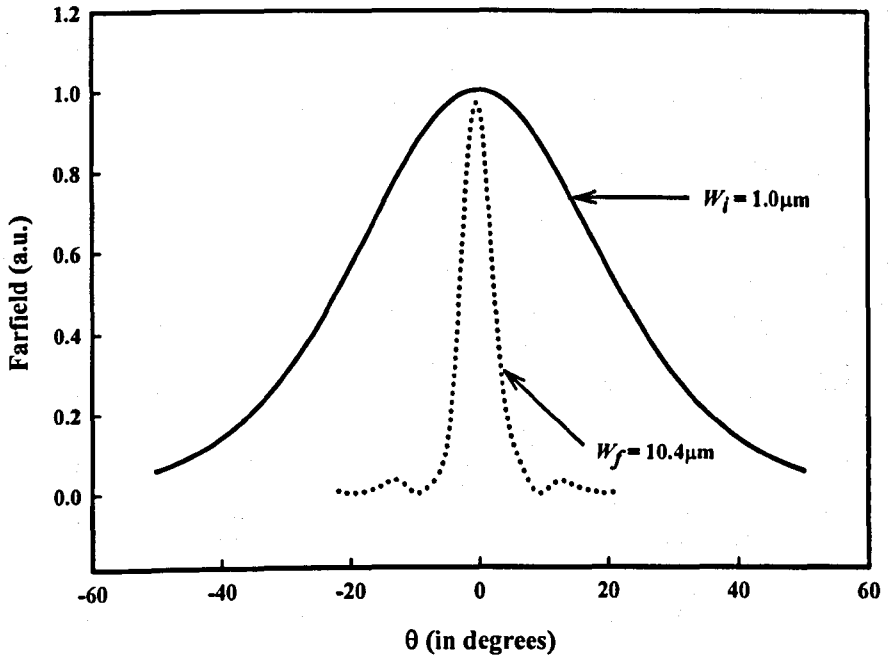

Fig. 7.2 Variation of the farfield at different width locations.

In the following figure the investigation of the vertical and horizontal angles of the farfield pattern were investigated and shown as Fig. 7.3. The near field used was the output field obtained at the end of the tapered section in BPM. It can be observed that the farfield pattern on the vertical direction (θ_y) is more similar to the one plotted earlier when W_i = 1.0 μm, this is mainly because the width of the mode at the tapered section kept on changing during propagation while the height remained constant. However, the field pattern was not as smooth as before due to mode interference. The ripples observed may also be due to the near field being very wide, and this yields a very narrow far field, which can have side lobes and nulls similar as antenna's radiation pattern [190,191].

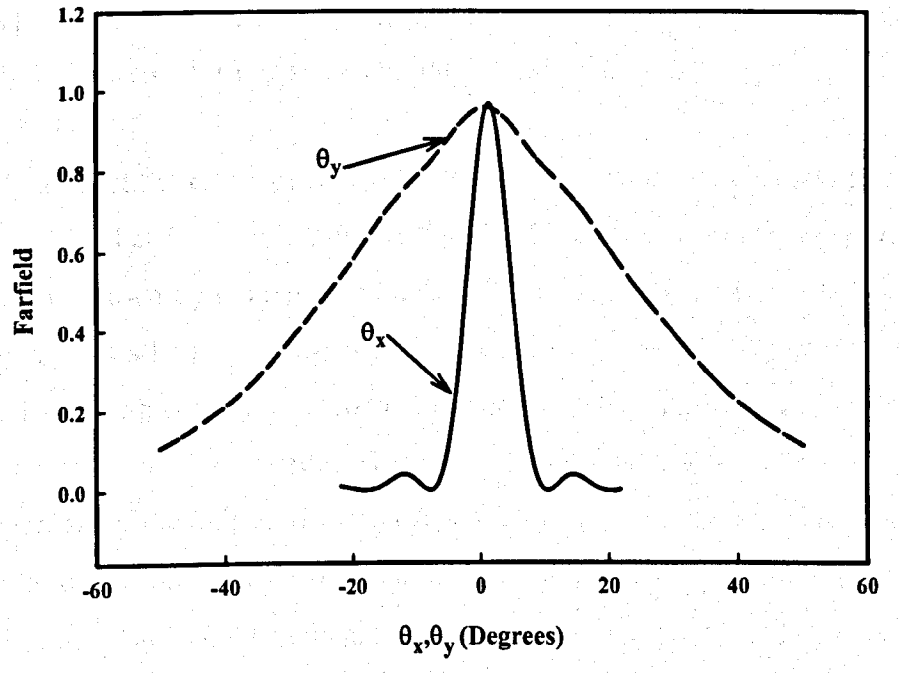

Fig. 7.3 Variation of the farfield at different angles.

In Fig. 7.4 the variation of the farfield on the vertical direction with different angles has been plotted. It can be clearly seen that the farfield pattern widens when a higher tapered angle, $\theta = 1.5^{0}$ shown by a solid line was used; however the range of the expansion were the same.

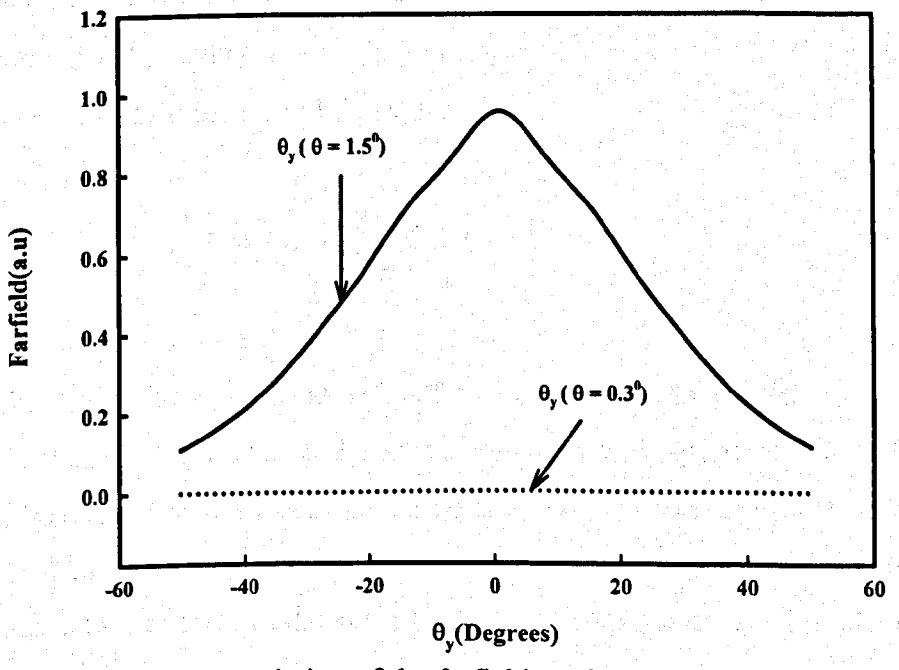

Fig. 7.4 Variation of the farfield on the vertical direction with different angles.

The pattern of the farfield for all the three different tapered angles were the same, however due to the scale of the plot when a smaller angle was used the farfield pattern appeared like a straight line shown by the dashed line.

Investigation of the effect of change of width to the spot-size area and farfield angles were examined and shown in Fig. 7.5. Firstly, the spot-size area for σ_x, σ_y with change in width is shown by the solid and dotted lines, respectively, at the left hand side of the figure. It can be observed that σ_x dropped slightly from 0.9871 μm² to 0.8831 μm² before increasing rapidly with increase in width. Therefore increase in the width on the horizontal direction contributed to the increase in the spot-size area, σ_x.
However, since the height of the waveguide was constant it was observed that spot-size area, σ_y remained stable at approximately 0.77 μm² and any change in width was insignificant. The farfield angle at the horizontal section for θ_x, and θ_x' expressed as

$$\theta_x' = \tan^{-1} \frac{\lambda}{\pi \sigma_{x/2}} \tag{7.13}$$

are shown at the right hand side of the figure. For both cases it can be clearly observed that the angles increase slightly with increase in width, however after W = 1.0 μm, it decreases slowly with increase in width. However, θ_x was experiencing a smaller farfield angle increase initially, but after W = 1.0 μm, the decrease was slower compared to θ_x', having a slight higher angle for a wider width. The farfield angle at the vertical section for θ_y, and θ_y' expressed as

$$\theta_y' = \tan^{-1} \frac{\lambda}{\pi \sigma_{y/2}} \tag{7.14}$$

are shown at the right hand side of the figure too. In this case, θ_y, and θ_y' are represented by the dotted and dashed dotted lines, respectively. Initially, for both cases increase in width increases the far field angle, however after W = 1.0 μm, they appeared to be stable, and any increase in width from henceforth was insignificant, this is due to the height of the guide being constant (formation of the structure).

Therefore, σ_x, starts from high width and when W decreases, σ_x, decreases until when it reaches σ_{min}, it approaches its cut-off, then increases. θ_x' is directly related to σ_x, by equation (7.1). For θ_x, when W reduces it reaches its maximum, further reduction causes an increase in θ_x.

Since H is fixed, as W reduces σ_y remains constant. However, as W reaches a very low value, due to cut-off σ_y increases.

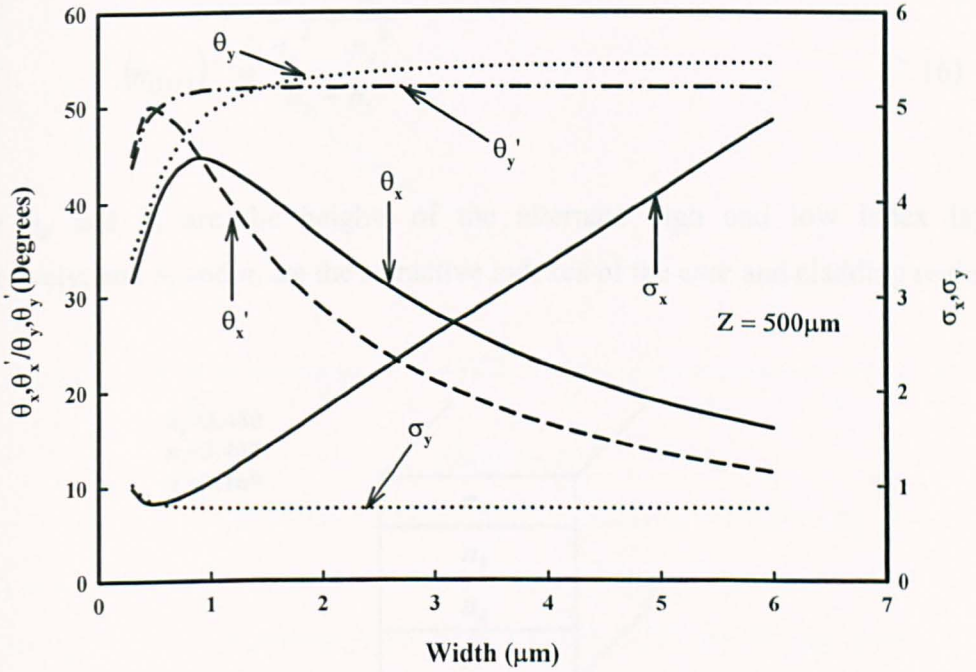

Fig. 7.5 Variation of the spot-size area and farfield angles at different widths.

7.4 Birefringence in Layered waveguides

In this section of the chapter we shall investigate the birefringence principle in layered waveguides. Some published papers have reported on polarization dependence and birefringence control/compensation [192]. It has been observed and reported that the change in the refractive index Δn_x is higher than the change in refractive index Δn_y. This implies that the effective index n_e^x of the H_x^{11} mode is lower than the effective index n_e^y of the H_y^{11} mode, having a birefringence, $\boldsymbol{B}$, expressed as $\boldsymbol{B} = n_e^y - n_e^x$.

The effective index of the TE (transverse electric polarized) mode of the layered structure can be calculated by using equation 7.15 [157], [193]

$$\left(n_{(TE)}\right)^2=\frac{n_g{}^2 h_g + n_s{}^2 h_s}{h_g + h_s} \tag{7.15}$$

and for the TM (transverse magnetic polarized modes) it can obtained by [5], [6]

$$\left(n_{(TM)}\right)^{-2}=\frac{\frac{h_g}{n_g{}^2}+\frac{h_s}{n_s{}^2}}{h_g + h_s} \tag{7.16}$$

where h_g and h_s are the heights of the alternate high and low index layers, respectively, and n_g and n_s are the refractive indexes of the core and cladding regions.

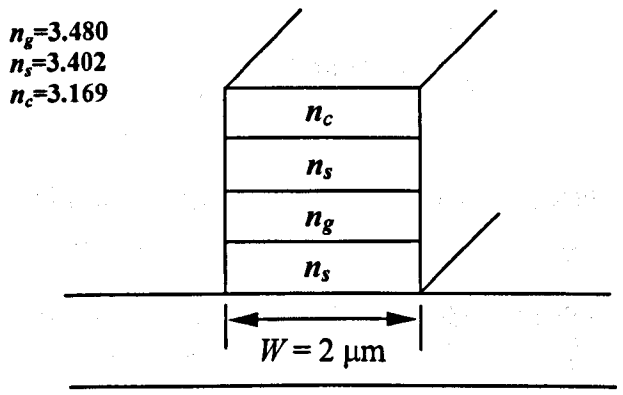

Fig. 7.6 Schematic cross section of the layered waveguide.

Initially, in this work, the width was taken as $W = 2$ μm and the refractive index of the core and cladding was taken as, n_g = *3.480* and n_s = 3.402, respectively. The modal solution of the confinement factor for the TE and TM modes were Γ_y = 0.2014 and Γ_x = 0.191, and the effective indexes, n^y_e and n^x_e were 3.299 and 3.290, respectively. In terms of both the effective indexes and the confinement factor, the TE mode was observed to have a higher value than TM mode. Hence, the layered structure $n_{eq}(TE) > n_{eq}(TM)$. This yields to a positive material birefringence, where $n_{eq}(TE)$ and $n_{eq}(TM)$

are the quasi-TE and TM modes, respectively. The material birefringence is defined as $\boldsymbol{B}_{material} = n_{eq}(TE) - n_{eq}(TM)$, and $\boldsymbol{B}_{material} = 0.009$.

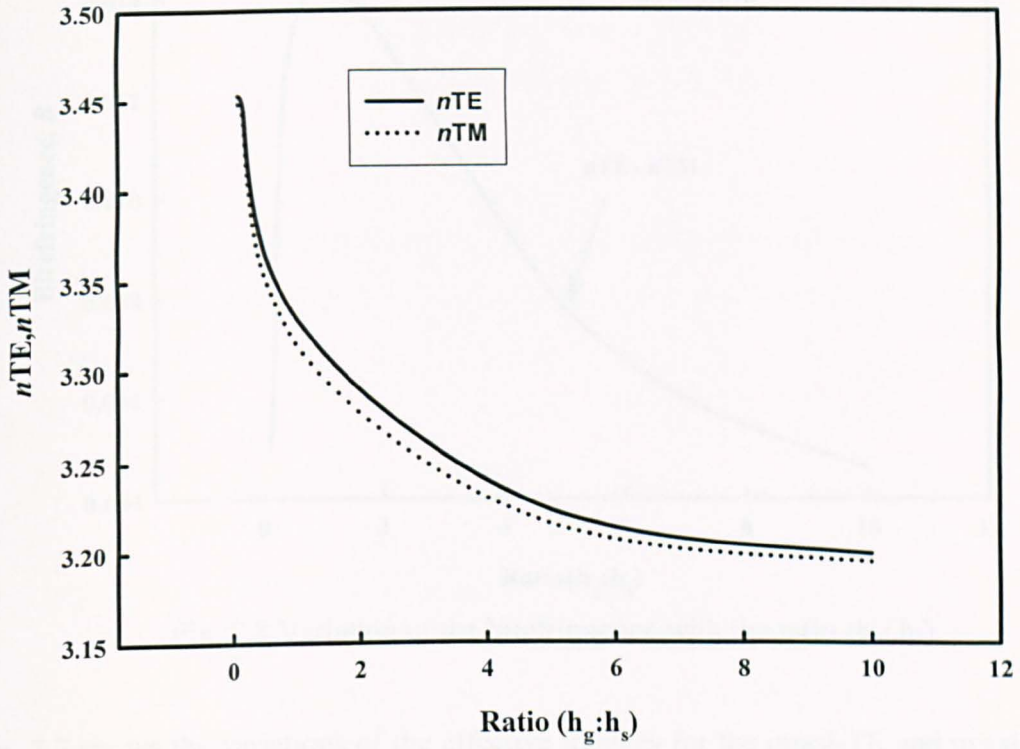

Fig. 7.7 Variations of the effective indexes against ratio (h_g: h_s).

In this work we used a layered approximation with the n_g and n_s values assumed at different layers. When Equation (7.15) was used $n_g = 3.391$ for TE and when Equation (7.16) was used $n_s = 3.402$ for TM mode. When the ratio h_g and h_s was kept to 1:2.85, the n^x_e and Γ_x was reduced to 3.284 and 0.189, respectively. This could be due to this layers assisting modal confinement.

When a layered cladding region was used to mimic homogenous n_c, and $n_c = 3.169$ for the TE mode, it yielded $n_c = 3.159$ for TM, and the TM solution was carried out the result was $\Gamma_x = 0.192$ and $n^x_e = 3.281$. Here instead of simulating a structure with a real layered region we have just assumed if the index of $n_c = 3.169$, then approximation can be done by the layered structure and there maybe a birefringence of, $\boldsymbol{B} = 0.018$. Although confinement factor, (Γ) has improved slightly it is too little to make it polarization independent by using this approach.

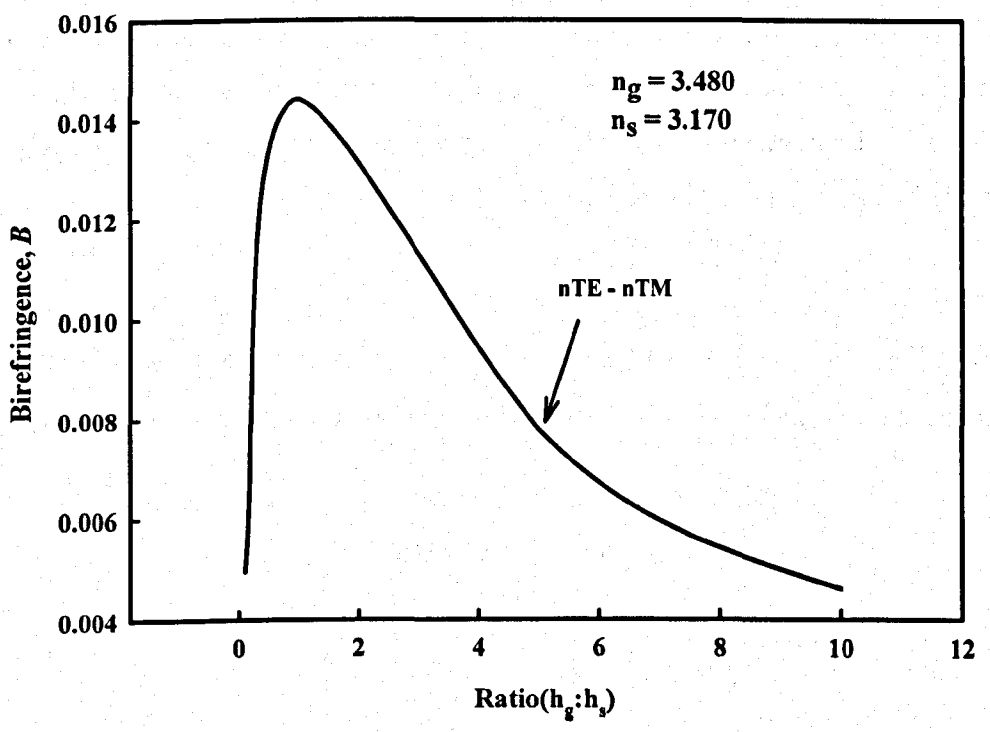

Fig. 7.8 Variation of the birefringence with the ratio (h_g: h_s).

Fig. 7.7 shows the variations of the effective indexes for the quasi-TE and quasi-TM modes against the ratio (h_g:h_s). The ratio was varied while n_g and n_s were kept constant at 3.170 and 3.480, respectively and the equivalent indexes, $n_{eq}(TE)$ and $n_{eq}(TM)$ calculated using equations (7.15) and (7.16), respectively. It was clearly observed that when the ratio (h_g:h_s) increases both the $n_{eq}(TE)$ and $n_{eq}(TM)$ decreases monotonically. Furthermore, it was also observed that the value of $n_{eq}(TE)$ is higher than $n_{eq}(TM)$, giving a result of a positive material birefringence.

The variation of the material birefringence with the ratio is shown in Fig. 7.8. As the ratio between h_g and h_s is high, the difference between $n_{eq}(TE)$ and $n_{eq}(TM)$ increases considerably, until when the ratio of h_g:h_s is 1:1, at this point the maximum material birefringence is attained, and further increase in the ratio decreases the material birefringence as shown in the figure. Therefore, it is desirable to maximize the material birefringence simulations by using a ratio of h_g:h_s = 1:1.

7.5 Summary

In this chapter, the far field profile is examined for different waveguide structures, which includes the derivation of the mode expansion and simulation results. The near field profile was usually obtained by the beam propagation method. The farfield pattern was varied when the near field was absolute, real and imaginary, all shown in this chapter.

The end section of this chapter investigates the effect of birefringence in layered structures. The mathematical equations for both the effective indexes and the material birefringence are presented.

8.0 Conclusions and Future Works

8.1 Overview of the Work

The main objective of this research work was to develop further the Finite Element based Beam Propagation Method (FEBPM) and as a result to study and analyse the evolution of the optical beam profile along semiconductor optical amplifiers. In this work various types of semiconductor waveguide structures were considered with more attention given to tapered structures. Extensive development of the powerful and robust vectorial FEBPM codes have been implemented and a range of applications analysed. The set objectives of the study at the start of this work were indeed successfully achieved, with detailed investigations and analysis of the results being undertaken during the course of the work.

It should also be stressed that in this work, the finite element-based techniques were further developed for use in the analysis and design of practical waveguides such as the rib waveguides, deeply etched waveguides and planar waveguides. Since most photonic devices are designed around optical waveguides, it is a basic and indeed indispensable approach to solve accurately for the modes of these optical waveguides. Therefore, there is a particular need for modeling techniques capable of accurately performing the modal analysis needed for a wide range of both lossless and lossy (or with gain) optical dielectric waveguides and also to provide the general complex propagation constants and the full vectorial fields of different modes of such waveguides. Thus, the analysis of light propagation in longitudinally varying optical devices has been successfully performed using one of the most common techniques, the beam propagation method (BPM), which has been incorporated with the computationally efficient finite element method.

Chapter 2 discussed the general overview of the Optical Amplifiers (OA) and their diverse applications. This include the history of the OA generation and its classification. The area of most interest, however, was Semiconductor Optical

Amplifiers (SOAs). In literature, SOAs have been reported to provide high gain, with low power consumption and their single-mode waveguide structure makes them particularly suitable for use with monomode fibers. A semiconductor laser is essentially an optical amplifier enclosed within a reflective cavity that causes it to oscillate via positive feedback. Semiconductor lasers use semiconductors as the gain medium. They are compact and can be fabricated in large volumes using advanced integrated semiconductor technology, making them the most popular light sources for optical communication systems. Semiconductor amplifiers are characterized by large optical gain, where more than 20 dB gain can be easily achieved in devices of few hundreds of microns of length. Large optical gains are always present together with low saturation power and hence, saturation mechanisms are expected to be important to set the performance of any device based on active semiconductors.

Broad-area semiconductor optical amplifiers (SOAs) were also studied in this work as they allow the output power to be boosted, although the lack of lateral structure and mode beating leads to a degradation of the beam quality in such devices and even to filamentation. SOA's with a tapered gain region have proven to be very efficient to reach high-output power in a diffraction-limited beam by the amplification of the light emitted by a master oscillator, be it integrated or not, which was detailed in the later chapters. Several aspects of these devices have been analyzed both experimentally and theoretically although comparatively little research has been performed on the correlation between the structure of the device and the beam quality and in this work some of these features was studied thoroughly. Finally, a detailed mathematical approach of the far field pattern theory was presented.

Chapter 3 presented the mathematical background for the finite element method vector **H**-field variation formulation. This technique has been proven to be a powerful and well-established numerical technique for analyzing optical waveguides. The fundamental mathematical relations derived from Maxwell's equations, for the application of this method in the solution of optical waveguide problems are considered in this chapter with a more detailed **H**-field finite element formulation. The primary concepts such as the shape functions and element matrices were also discussed in detail. With the **H**-field formulation, the appearance of spurious modes with the physical modes was a major drawback. To eliminate these spurious modes a

penalty function method was introduced and its role explained. This method was used to eliminate the spurious modes by imposing the constraint $\nabla.\mathbf{H} = 0$ in problems of microwave or optical waveguides, improving significantly the quality of the field. Furthermore, a very useful and efficient approach, which involves the extending of the domain of interest to infinity keeping the same matrix value, was considered.
The work showed that the FEM could also be used to determine the initial field distribution for simulation analysis using the vector finite element based beam propagation method.

In Chapter 4, general overviews of the various propagation algorithms were discussed, with the main features of the algorithms reviewed. More important has been the mathematical development of the vector beam propagation method approach, based on the versatile finite element method (FEBPM). The concept of the perfectly matched layer (PML) boundary conditions in absorbing the unwanted radiation waves and its incorporation with the finite element technique has also been discussed. The application of the finite elements to both the transverse cross-section and longitudinal directions produced a system of linear equations, which were solved for the modal values for a given initial field profile. The use of imaginary distance propagation with the FEBPM to generate the quasi-TE and quasi-TM modes and the calculation of the beam power has also been detailed.

In Chapter 5, the evolution of the optical beam along the tapered semiconductor laser structures, by using the rigorous full vectorial numerical approaches based on the finite element method (FEM) has been presented. Numerically simulated results obtained by using rigorous full vectorial approaches indicate that the presence of the finite discontinuity steps generates higher order modes along a tapered guided-wave structure. The existence of the odd modes for a symmetric structure has clearly been demonstrated by the correlation of its transverse field profiles, the axial variation of the beat length, and also by calculating the modal coefficients of these modes in the evolved beam. Interference between the modes allows the beam quality to deteriorate significantly both in the lateral and the axial directions. The nonlinear interaction between the forward- and the backward-propagating waves has been reported to produce a transverse spatial modulation of the phase and intensity, and similarly, the mode beating between the fundamental and higher order modes may also contribute

towards the mode filamentation. It has also been observed that the phase of the optical beam is not monotonic in the lateral direction, and this contributes further towards the deterioration of the beam filamentation and of the far-field profiles. Often, a Gaussian field is taken as the input signal to the amplifier section, which may not be launched in a way that is perfectly symmetrical with the structure, and this beam profile may also differ significantly from the fundamental mode of the input section. In that case, the modal coefficients of the excited higher order modes are higher and may even include modes with asymmetry, which would be amplified along the tapered amplifiers and are expected to deteriorate the beam quality further.

The evolution of the optical beam along deeply etched semiconductor laser structures by the use of the vectorial finite element based beam propagation method (FEBPM) is presented in Chapter 6. In this Chapter, the approach has been used to study rigorously the complex refractive index profiles to provide modal gain in such structures. The modal gain properties and field expansion has also been examined in detail. The power gain in an active photonic device, such as a laser or an amplifier is due to the presence of the imaginary part of the complex refractive index in the core. The injected current generates carrier density and when the density is above the transparent carrier density then the optical field can be amplified. In the case of a high-power tapered SOA, the width of the SOA changes continuously, which reduces the power density to improve the total gain.

The effect of gain reduction along the transverse direction, due to the transverse field profile, has been investigated and results presented. The variations of the gain along the axial direction with different parameters such as the tapered angles, power saturation, input power also was examined. For this optical structure, the stationary value of the power confinement factor in the active area is calculated by using the finite element method (FEM) and compared with the z-dependent BPM which clearly shows sharp oscillations which are due to the existence of higher order modes during propagation in the tapered section as explained in Chapter 5.

Again, it is well known that the total gain of a semiconductor amplifier also depends on the input power to the SOA. When the input power is higher, the resulting optical field reduces the carrier density and ultimately saturates the overall gain. In this work,

the saturation power and the tapered angles, along with the confinement factor have been used to find the effect of the *gain saturation*. The effect of the gain saturation on the total optical gain of the amplifier by considering both the transverse and axial variation of the local gain coefficient also has been examined.

In Chapter 2 the mathematical derivation of the farfield profile was presented: however in Chapter 7 the mode expansion and some simulations results were discussed. The waveguide field profiles assumed to be uniform along the length of the laser as long as the cross section of the guide remains uniform. At the output facet this field emerges from the laser waveguide and diffracts freely in the surrounding dielectric (usually air).

In Chapter 7 the shape of the farfield patterns contributed by the tapered section and the optical beam and near field profiles were examined. The mathematical approach of the mode expansion method for planar waveguides was discussed. The near field profile was usually obtained from the input or the output fields of the beam propagation method (BPM). The variations of the farfield patterns when the field were absolute, real and imaginary were also examined. Furthermore, the variation of the far field pattern when an input field from the BPM is launched with comparison with the output field which significantly explains the effect of the tapered section, and the appearance of ripples when a wider width was used.

Finally, the birefringence in the tapered waveguides was considered. The mathematical equations of the effective indexes of the TE and TM modes were also presented. It should be noted here that with the structure of the waveguide a positive material birefringence was attained and some useful simulations results were presented.

8.2 Future Work

In this research work it has indeed been proven, in light of several applications presented and simulation results obtained, that the versatile vector finite element based beam propagation technique is a rigorous method for characterising accurately a

wide range of guided-wave optical waveguide devices. Several design problems have been experienced and reported by many research workers in this field, some of which have been investigated in this work and various design techniques have been recommended to overcome them. Further applications of this technique (FEBPM), which are essential to better communications systems and can be investigated include, polarisation issues, analysing and investigating the effect of TE and TM modes on the modal gain of the SOA and design optimisation for their polarisation independent operation, polarisation conversion, the effect of current on both polarisation signals, the effect of facet reflectivity on the general performance of the SOA, investigating the non-linearities that arise from the carrier density dependence of the gain and the refractive index in the active regions of the amplifier.

This research work has been focussed predominantly on the optical model of the SOAs. To have a complete design package for SOAs, the electronic and thermal models also have to be incorporated. In the development of the Electronic model, the design of Multiple-Quantum Wells (MQWs) and investigating their characteristics and to develop and improve the laser performance can be considered. In a system with many quantum wells separated by spatially thick high barriers, the carriers may become non-uniformly distributed among the wells. In view of the sub-linear relationship between optical gain and carrier density, with relationship between non-radiative recombination rates and carrier density and the non-uniform carrier distribution affects the high performance laser operation. This is a drawback established by many designers and it is thus essential to study in depth the carrier distribution and the effect of the carrier on aspects such as the gain. The energy band diagram, which detects electric fields and influences current flow within the semiconductor needs to be developed and its key properties need to be investigated.

The heating effect is experienced on both the electrical and thermal models. In electrical degradation, the increase in threshold current accelerates the device through heating leading to catastrophic damage of the device, while in thermal degradation a major problem has been observed in the bonding of the device causing it to generate excessive heat. The heating effect and thermal dependence are key areas that need to be investigated. Polarisation issues such as polarisation sensitivity and polarisation variability are also very important for these devices.

Finally, a prototype design package could be developed which would incorporate the optical, electronic and thermal models. The optimised SOA can then be integrated with other devices such as the spot size converters.

Appendix 1

The Calculation of the Element Matrices

The evaluation of the elements $[\mathbf{A}]_e$ and $[\mathbf{B}]_e$ from equation (3.52) and (3.53), respectively, are shown here.

Therefore, from equation (3.52);

$$[\mathbf{A}]_e = \varepsilon^{-1} \int_{\Delta} [Q]^T [Q] d\Omega$$

$$= \varepsilon^{-1} \int_{\Delta} \begin{bmatrix} -\beta^2 [N]^T [N] + \frac{\partial [N]^T}{\partial_Y} \frac{\partial [N]}{\partial_Y} & -\frac{\partial [N]^T}{\partial_Y} \frac{\partial [N]}{\partial_X} & j\beta [N]^T \frac{\partial [N]}{\partial x} \\ -\frac{\partial [N]^T}{\partial_x} \frac{\partial [N]}{\partial_y} & -\beta^2 [N]^T [N] + \frac{\partial [N]^T}{\partial_x} \frac{\partial [N]}{\partial_x} & j\beta [N]^T \frac{\partial [N]}{\partial y} \\ j\beta \frac{\partial [N]^T}{\partial x} [N] & j\beta \frac{\partial [N]^T}{\partial y} [N] & \frac{\partial [N]^T}{\partial_Y} \frac{\partial [N]}{\partial_Y} + \frac{\partial [N]^T}{\partial_x} \frac{\partial [N]}{\partial_x} \end{bmatrix} d\Omega$$

(A1.1)

From equation (3.53);

$$[\mathbf{B}]_e = \mu \int_{\Delta} [\mathbf{N}]^T [\mathbf{N}] d\Omega$$

$$= \mu \int_{\Delta} \begin{bmatrix} [N]^T [N] & [0]^T [0] & [0]^T [0] \\ [0]^T [0] & [N]^T [N] & [0]^T [0] \\ [0]^T [0] & [0]^T [0] & [N]^T [N] \end{bmatrix} \qquad \text{(A1.2)}$$

The integration of the shape functions in the above equations (A1.1) and (A1.2) can be evaluated for a triangular element using the following relation

$$\int_{\Delta} N_1^i N_2^j N_3^k \, d\Omega = \frac{i!\, j!\, k!\, 2!}{(i+j+k+2)!} A_e \qquad \text{(A1.3)}$$

A_e is the area of the triangular element.

In this case the following integrals can be obtained,

$$\int_{\Delta} N_1^2 \, d\Omega = \int_{\Delta} N_2^2 \, d\Omega = \int_{\Delta} N_3^2 \, d\Omega = \frac{A_e}{6} \tag{A1.4}$$

$$\int_{\Delta} N_1 N_2 \, d\Omega = \int_{\Delta} N_2 N_3 \, d\Omega = \int_{\Delta} N_1 N_3 \, d\Omega = \frac{A_e}{12} \tag{A1.5}$$

$$\int_{\Delta} d\Omega = A_e \tag{A1.6}$$

From equation (A1.1) some of the elements of the 9×9 $[\mathbf{A}]_e$ matrix can be given as

$$[\mathbf{A}]_{e(1,1)} = \frac{1}{\varepsilon}\int_{\Delta} -\beta^2 N_1^2 + \left(\frac{\partial N_1}{\partial y}\right)^2 d\Omega = \frac{1}{\varepsilon}\left[\frac{-\beta^2 A_e}{6} + c_1^2 A_e\right] \tag{A1.7}$$

$$[\mathbf{A}]_{e(1,2)} = \frac{1}{\varepsilon}\int_{\Delta} -\beta^2 N_1 N_2 + \frac{\partial N_1}{\partial y}\frac{\partial N_2}{\partial y} d\Omega = \frac{1}{\varepsilon}\left[\frac{-\beta^2 A_e}{12} + c_1 c_2 A_e\right] \tag{A1.8}$$

$$[\mathbf{A}]_{e(1,4)} = \frac{1}{\varepsilon}\int_{\Delta} \frac{-\partial N_1}{\partial y}\frac{\partial N_1}{\partial x} d\Omega = -\frac{1}{\varepsilon} c_1 b_1 A_e \tag{A1.9}$$

Also, from equation (A1.2) some of the elements of the 9×9 $[\mathbf{B}]_e$ matrix can be given as

$$[\mathbf{B}]_{e(1,1)} = \mu\int_{\Delta} N_1^2 \, d\Omega = \mu\frac{A_e}{6} \tag{A1.10}$$

$$[\mathbf{B}]_{e(1,2)} = \mu\int_{\Delta} N_1 N_2 \, d\Omega = \mu\frac{A_e}{12} \tag{A1.11}$$

$$[\mathbf{B}]_{e(1,4)} = 0 \tag{A1.12}$$

Appendix 2

Power Calculation

$$E \times H = E_x \cdot H_y = \frac{\beta}{\omega\varepsilon} H_y \cdot H_y$$

$$= \frac{\eta_e \kappa_o}{\omega} \frac{1}{\varepsilon} \cdot H_y^2 \qquad \text{but} \quad \kappa_o = \omega / c$$

$$= \frac{\eta_e \cancel{\omega} / c}{\cancel{\omega}} \frac{1}{\varepsilon} \cdot H_y^2$$

$$= \frac{\eta_e}{c} \frac{1}{\varepsilon} \cdot H_y^2 \qquad \text{but} \quad c = \frac{1}{\sqrt{\mu_o \varepsilon_o}}$$

$$= \frac{\eta_e}{\varepsilon_o \varepsilon_r} \sqrt{\mu_o \varepsilon_o} \cdot H_y^2 \qquad \varepsilon = \varepsilon_o \varepsilon_r$$

$$= \frac{\eta_e}{\varepsilon_r} \eta_o \cdot H_y^2 \qquad \eta_o = \sqrt{\mu_o / \varepsilon_o}$$

$$= \eta_e \eta_o \frac{1}{\varepsilon_r} \cdot H_y^2 \qquad \varepsilon_r \approx \eta_e^2$$

$$= \frac{\eta_o}{\eta_e} \cdot H_y^2$$

$$H_y^2(x,y) = \sum_{n=1}^{ne} \int H_y^2(x,y) \partial\Omega$$

$$= \int \{H_y\}^T [N]^T [N] \{H_y\} \partial\Omega$$

$$= \begin{Bmatrix} H_{y1} \\ H_{y2} \\ H_{y3} \end{Bmatrix}^T \begin{bmatrix} \Delta/6 & \Delta/12 & \Delta/12 \\ \Delta/12 & \Delta/6 & \Delta/12 \\ \Delta/12 & \Delta/12 & \Delta/6 \end{bmatrix} \begin{Bmatrix} H_{y1} \\ H_{y2} \\ H_{y3} \end{Bmatrix}$$

$$= \begin{Bmatrix} H_{y1} & H_{y2} & H_{y3} \end{Bmatrix} \begin{bmatrix} \Delta/6 & \Delta/12 & \Delta/12 \\ \Delta/12 & \Delta/6 & \Delta/12 \\ \Delta/12 & \Delta/12 & \Delta/6 \end{bmatrix} \begin{Bmatrix} H_{y1} \\ H_{y2} \\ H_{y3} \end{Bmatrix}$$

$$= \{H_{y1} \quad H_{y2} \quad H_{y3}\} \begin{bmatrix} \Delta/6H_{y1} & \Delta/12H_{y2} & \Delta/12H_{y3} \\ \Delta/12H_{y1} & \Delta/6H_{y2} & \Delta/12H_{y3} \\ \Delta/12H_{y1} & \Delta/12H_{y2} & \Delta/6H_{y3} \end{bmatrix}$$

$$= \begin{bmatrix} \Delta/6H_{y1}^{2} & \Delta/12H_{y1}H_{y2} & \Delta/12H_{y1}H_{y3} \\ \Delta/12H_{y2}H_{y1} & \Delta/6H_{y2}^{2} & \Delta/12H_{y2}H_{y3} \\ \Delta/12H_{y1}H_{y3} & \Delta/12H_{y2}H_{y3} & \Delta/6H_{y3}^{2} \end{bmatrix}$$

Appendix 3

Publications by the Author

(1) B.M.A. Rahman, **R.Abdallah**, M.Rajarajan, S.S.A Obayya, and K.T.V. Grattan "Rigorous Numerical Analysis of Mode Beating in Tapered Semiconductor Amplifiers" *Journal of Lightwave Technology,* vol. 23, no. 6, pp. 2124-2130, June, 2005.

(2) B.M.A. Rahman, T.Woncharoen, C.Themistos, **R.Abdallah**, A.K.M.S. Kabir, E.O.Ladele, N.Somasiri, M.S.Alam, M.Rajarajan and K.T.V.Grattan "Finite element characterisation of photonic devices for optical communication" *IEE Proceedings- Circuits Devices Systems,* vol. 152, no. 5, October 2005.

(3) **R.Abdallah**, B.M.A.Rahman, M.Rajarajan and K.T.V.Grattan "Rigorous numerical analysis of gain saturation in deeply-etched tapered semiconductor optical amplifier" *Semiconductor and Integrated Optoelectronics (SIOE'05), Cardiff,* WALES, 21-23 Mar 2005.

(4) Rajarajan M, Rahman B.M.A, **Abdallah R.A**, Obayya S.S.A, Grattan K.T.V "Mode beating in tapered high-power deeply-etched semiconductor amplifiers" *SPIE, ISI Proc., pp 207-218, Conference on Smart Structures, Devices, and Systems II,* Sydney, Australia, Dec 13-15, 2004.

(5) B.M.A. Rahman, T. Wongcharoen, N. Somasiri, **R.A. Abdallah**, A.K.M.S. Kabir, M. Rajarajan and K.T.V. Grattan "Rigorous Design Optimization of Photonic Devices by using the Finite Element Method" *Asia Pacific Microwave Conference,* 15-18 Dec 2004.

(6) Rahman B.M.A, **Abdallah R**, Rajarajan M, Parameswaran A, Grattan K.T.V "Mode beating in tapered high power lasers" *SPIE, ISI Proc., International Conference on Applications of Photonic Technology (Photonics North 2004)* pp. 36-47, Ottawa, Canada, 2004.

(7) Rahman B.M.A, **Abdallah R**, Rajarajan M, Parameswaran A, Grattan K.T.V "Mode beating in tapered high power lasers" *SPIE, ISI Proc., Conference Optics and Photonic integrated Circuits,* pp. 233-242, April 27-29, Stranbourg, France, 2004.

(8) B M A Rahman, **R Abdallah**, M Rajarajan and K T V Grattan "Rigorous numerical analysis of mode beating and gain saturation in deeply-etched tapered semiconductor amplifiers" *(to be submitted to journal of Applied Optics, 2007)*

References

[1] G. P. Agrawal, "Fiber-optic communication systems," Third edition, 2002.

[2] R. Stoffer, H. J. W. M. Hoekstra, R. M. de Ridder, E. Van Groesen, and F. P. H. Van Beckum, "Numerical studies of 2D photonic crystals: waveguides, coupling between waveguides and filters," *Opt. Quantum Electron.*, vol. 32, pp. 947-961, 2000.

[3] H. Kogelnik, "Theory of optical waveguides in: Guided-wave optoelectronics," Ed. By T. Tamir, Heidelberg, Springer-Verlag, 1990.

[4] L. Qiao and J. Wang, "A modified ray-optic method for arbitrary dielectric waveguides," *IEEE J. Quantum Electron.*, vol. 28, no. 12, pp. 2721-2727, 1992.

[5] R. Srivastava, C. K. Kao, and R. V. Ramaswamy, "WKB analysis of planar surface waveguides with truncated index profiles," *J. Lightwave Technol.*, vol. 5, no. 11, pp. 1605-1609, 1987.

[6] E. A. J. Marcatili, "Dielectric rectangular waveguide and directional coupler for integrated optics," *Bell System Technical Journal*, vol. 48, pp. 2071-2102, 1969.

[7] K. S. Chiang, "Review of numerical and approximate methods for the modal analysis of general optical dielectric waveguides," *Opt. Quantum Electron.*, vol. 26, no. 3, pp. S113-S134, 1994.

[8] R. M. Knox and P. P. Toulios, "Integrated circuits for the millimetre through optical frequency range," in *Proceedings, Symposium on Submillimeter Waves.* Brooklyn: Polytechnic Press, pp. 497-516, 1970.

[9] W. B. Zhou and T. Itoh, "Analysis of trapped image guides using effective dielectric constants and surface impedances," *IEEE Trans. Microwave Theory Tech.*, vol. 30, no. 12, pp. 2163-2166, 1982.

[10] K. S. Chiang, K. M. Lo, and K. S. Kwok, "Effective-index method with built-in perturbation correction for integrated optical waveguides," *J. Lightwave Technol.*, vol. 14, no. 2, pp. 223-228, 1996.

[11] K. S. Chiang, "Dual effective index method for the analysis of rectangular dielectric waveguides," *Appl. Opt.*, vol. 25, no. 13, pp. 2169-2174, 1986.

[12] P. C. Kendall, P. W. A. McIlroy, and M. S. Stern, "Spectral index method for rib waveguide analysis," *Electron Lett.*, vol. 25, no. 2, pp. 107-108, 1989.

[13] A. Vukovic, P. Sewell, T. M. Benson, and P. C. Kendall, "Novel half space radiation mode method for buried waveguide analysis," *Opt. Quantum Electron.*, vol. 31, no. 1, pp. 43-51, 1999.

[14] J. B. Davies, "Review of methods for numerical solution of the hollow waveguide problem," *IEEE Proc.*, vol. 119, no. 1, pp. 33-37, 1972.

[15] C. Vassallo, "1993-1995 optical mode solvers," *Opt. Quantum Electron.*, vol. 29, no. 2, pp. 95-114, 1997.

[16] M. S. Saad, "Review of numerical methods for the analysis of arbitrarily-shaped microwave and optical dielectric waveguide," *IEEE Trans. Microwave Theory Tech.*, vol. 33, no. 10, pp. 894-899, 1985.

[17] U. Schulz and R. Pregla, "A new technique for the analysis of the dispersion characteristics of planar waveguides and its application to microstrips with tuning septums," *Radio Science*, vol. 16, no. 6, pp. 1173-1178, 1981.

[18] R. Pregla and W. Pascher, "The method of lines," *in Numerical Techniques for Microwave and Millimeter Wave Passive Structures, T. Itoh*, pp. 381-446, New York, Wiley, 1989.

[19] U. Rogge and R. Pregla, "Method of lines for the analysis of dielectric waveguides," *J. Lightwave Technol.*, vol. 11, no. 12, pp. 2015-2020, 1993.

[20] B. M. A. Rahman, F. A. Fernandez, and J. B. Davies, "Review of finite element methods for microwave and optical waveguides," *IEEE Proc.*, vol. 79, no. 10, pp. 1442-1448, 1991.

[21] J. E. Goell, "A circular-harmonic computer analysis of rectangular dielectric waveguides," *Bell Syst. Tech. J.*, vol. 48, pp. 2133-2160, 1969.

[22] N. Dagli and C. G. Fonstad, "Microwave equivalent circuit representation of rectangular dielectric waveguides," *Appl. Phys. Lett.*, vol. 49, no. 6, pp. 308-310, 1986.

[23] M. Koshiba and M. Suzuki, "Vectorial wave analysis of optical waveguides with rectangular cross-section using equivalent network approaches," *Electron. Lett.*, vol. 21, no. 22, pp. 1026-1028, 1985.

[24] P. C. Kendall, P. W. A. Mcilroy, and M. S. Stern, "Spectral index method for rib waveguide analysis," *Electron. Lett.*, vol. 25, no. 2, pp. 107-108, 1989.

[25] P. C. Kendall, M. S. Stern, and S. V. Burke, "Planar waveguide analysis by the spectral index method. I: Rib and uniformly buried waveguides," *Opt. Quantum Electron.*, vol. 25, no. 11, pp. 771-787, 1993.

[26] J. R. Pujol Pola, W. Biehlig, and F. Lederer, "A generalization of the spectral index method toward multiple rib waveguides," *J. Lightwave Technol.*, vol. 14, no. 3, pp. 454-461, 1996.

[27] W. C. Ng and M. S. Stern, "Analysis of multiple-rib waveguide structures by the discrete-spectral-index method," *IEE Proc. Optoelectron.*, vol. 145, no. 6, pp. 365-371, 1998.

[28] P. Sewell, T. M. Benson, and P. C. Kendall, "Rib waveguide spot-size transformers: Modal properties," *J. Lightwave Technol.*, vol. 17, no. 5, pp. 848-856, 1999.

[29] A. S. Sudbo, "Why are accurate computations of mode fields in spectral index method for vector modes of rib waveguide," *IEE Proc. Pt. J,* vol. 137, no. 1, pp. 21-26, 1990.

[30] C. Yeh, K. Ha, S. B. Dong, and W. P. Brown, "Single-mode optical waveguides," *Appl. Optics,* vol. 18, no. 10, pp. 1490-1504, 1979.

[31] M. S. Stern, "Semivectorial polarised finite difference method for optical waveguides with arbitrary index profiles," *IEE Proc., Pt. J.* vol. 135, pp. 56-63, 1988.

[32] K. Bierwirth, N. Schulz, and F. Arndt, "Finite difference analysis of rectangular dielectric waveguide structures," *IEEE Trans. Microwave Theory Tech.*, vol. 34, no. 11, pp. 1104-1114, 1986.

[33] L. W. Johnson and R. D. Riess, "Numerical Analysis," *Addison-Wesley*, Reading, Massachusetts, 1977.

[34] C. M. Kim and R. V. Ramaswamy, "Modelling of graded-index channel waveguides using nonuniform finite difference method," *J. Lightwave Technol.*, vol. 7, no. 10, pp. 1581-1589, 1989.

[35] B. M. A. Rahman and J. B. Davies, "Penalty function improvement of waveguide solution by finite elements," *IEEE Trans. Microwave Theory Tech.*, vol. 32, no. 8, pp. 922-928, 1984.

[36] B. M. A. Rahman and J. B. Davies, "Finite-element analysis of optical and microwave waveguide problems," *IEEE Trans. Microwave Theory Tech.*, vol. 32, no. 1, pp. 20-28, 1984.

[37] M. Koshiba and K. Inoue, "Simple and efficient finite-element analysis of microwave and optical waveguides," *IEEE Trans. Microwave Theory Tech.*, vol. MTT-40, no. 2, pp. 371-377,1992.

[38] M. D. Feit and J. A. Fleck, "Light propagation in graded-index optical fibres," *Appl. Opt.*, vol. 17, no. 24, pp. 3990-3998, 1978.

[39] Y. Chung and N. Dagli, "An assessment of finite difference beam propagation method," *IEEE J. Quantum Electron.*, vol. 26, no. 8, pp. 1135-1339, 1990.

[40] P. L. Liu and B. J. Li, "Semivectorial beam propagation method for analyzing polarized modes of rib waveguides," *IEEE J. Quantum Electron.*, vol. 28, no. 4, pp. 778-782, 1992.

[41] J. Shibayama, M. Yamauchi, and H. Nakano, "Efficient non-uniform schemes for paraxial and wide-angle finite-difference beam propagation method," *J. Lightwave Technol.*, vol. 17, no. 4, pp. 677-683, 1999.

[42] R. S. Flamino, A. C. Cesar, and B. H. V. Borges, "Improved wide angle difference beam propagation method for the analysis of nonlinear optical waveguides," *IEEE Trans. Magnetics.*, vol. 38, no. 2, pp. 589-592, 2002.

[43] S. S. A. Obayya, B. M. A. Rahman, and H. A. El-Mikati, "New full- vectorial numerically efficient propagation algorithm based on the finite element method," *J. Lightwave Technol.*, vol. 18, no. 3, pp. 409-415, 2000.

[44] G. P. Agrawal, "Fibre-optic communication systems," *John Wiley & Sons*, New York, 1997.

[45] S. Sudo, "Optical fibre amplifiers," *Artech House*, Boston, 1997.

[46] J. Gowar, "Optical communication systems," *Prentice Hall*, London, 1993.

[47] A. Eistein, "Zur Quantentheorie der Strahlung," *Phys. Z.*, vol. 18, pp. 121-128, 1917.

[48] T. H. Maiman, "Stimulated optical radiation in Ruby," *Phys. Rev. Lett.*, vol. 4, pp. 564-566, 1960.

[49] A. Javan, W. R. Bennett, and D. R. Herriott, "Population inversion and continuous optical maser oscillation in a gas discharge containing *He-Ne* mixture," *Phys. Rev. Lett.*, vol. 6, pp. 106-110, 1961.

[50] R. N. Hall, "Coherent light emission from GaAs junctions", *Phys. Rev. Lett.*, vol. 9, p. 366, 1962.

[51] D. Wood, "Optoelectronic semiconductor devices," *Prentice Hall*, London, 1994.

[52] C. J. Koester and E. Snitzer, "Amplification in a fibre laser," *Appl. Optics.*, vol. 3, pp. 1182-1186, 1964.

[53] E. Snitzer and R. Woodcock, "Yb^{3+} - Er^{3+} Glass laser," *Appl. Phys. Lett.*, vol. 6, pp. 45-46, 1965.

[54] S. B. Poole, D. N. Payne, R. J. Mears, M. E. Fermann, and R. I. Laming, "Fabrication and characterization of low-loss optical fibers containing rare-earth ions," *J. Lightwave Technol.*, vol. 4, no. 7, pp. 870-876, 1986,

[55] R. J. Mears, L. Reekie, I. M. Jauncey, and D. N. Payne, "Low-noise erbium-doped fibre amplifier operating at 1.54 μm," *Electron. Lett.*, vol. 23, no. 19, pp. 1026-1028, 1987.

[56] E. Snitzer, H. Po, F. Hakimi, R. Tumminelli, and B. C. Macollum, "Erbium-doped fiber laser amplifier at 1.55 μm with pump at 1.49 μm and Y_b sensitised E_r oscillator," *Proc. Optical Fiber Comm. Conf.*, New Orleans, pp. 218-221, 1998.

[57] G. P. Agrawal, "Lightwave technology" *Wiley*, July, 2005

[58] R. G. Smith, "Optical power handling capacity of low loss optical fibers as determined by stimulated Raman and Brillouin scattering," *Appl. Opt.*, vol. 11, no. 11, pp. 2489-2494, 1972.

[59] D. Cotter, "Observation of stimulated Brillouin scattering in low loss silica fiber at 1.3 μm," *Electron. Lett.*, vol. 18, pp. 495-496, 1982.

[60] E. J. Murphy, "Integrated optical circuits and components. Design and Applications," *Marcel Dekken*, New York, 1999.

[61] P. C. Becker, "Erbium-doped fiber amplifiers. Fundamental and Technology," *Academic Press*, New York, 1999.

[62] A. Evans, "Raman amplification key to solving capacity, system-reach demand," *Lightwave*, pp. 69-76, August 2000.

[63] "Fibre optics products and news June and July 2000 and Lightwave 2000 worldwide directory of fibre-optic communications products and services," *March* 2000.

[64] A. E. White, "Optical fiber components and devices," *Op. F. Telec. I. P. K. and T. L. Koch (Ed.), Academic Press,* 1997.

[65] K. Richards, "Corning and Siemens team up for 40 Gbit/sec technology demostration at ECOC," *Lightwave,* pp. 35-36, *September* 2000.

[66] G. Zeidler and D. Schicetanz, "Use of laser amplifiers in glass fibre communication systems," *Siemens Forch. u. Entwickl. Ber.*, vol. 2, pp. 227-234, 1973.

[67] S. D. Personick, "Applications for quantum amplifiers in simple digital optical communication systems," *Bell Syst. Tech. J.*, vol. 52, pp. 117-133, 1973.

[68] Y. Yamamoto, "Characteristics of AlGaAs Fabry-Perot cavity type laser amplifiers," *IEEE J. Quantum Electron.*, vol. 16, no. 10, pp. 1047-1052, 1980.

[69] J. C. Simon, "GaInAsP semiconductor laser amplifiers for single-mode fibre communications," *J. Lightwave Technol.*, vol. 5, no. 9, pp. 1286-1295, 1987.

[70] N. A. Olsson, R. F. Kazarinov, W. A. Nordland, C. H. Henry, M. G. Oberg, H. G. White, P. A. Garbinski, and A. Savage, "Polarisation independent optical amplifier with buried facets," *Electron. Lett.*, vol. 25, no. 16, pp. 1048-1049, 1989.

[71] D. J. Mestdagh, "Fundamentals of multi-access optical fibre networks," *Artech House*, 1995.

[72] R. J. Manning, A. D. Ellis, A. J. Poustie, and K. J. Blow, "Semiconductor laser amplifiers for ultrafast all-optical signal processing," *J. Opt. Soc. Amer. B.*, vol. 14, no. 11, pp. 3204-3216, 1997.

[73] S. Diez, R. Ludwig, H. J. Ehrke, U. Feiste, C. Schmidt, and H. G. Weber, "160Gbit/s all-optical demultiplexer using hybrid hybrid gain-transparent SOA Mach-Zehnder interferometer," *Electron. Lett.*, vol. 36, no. 17, pp. 425-427, 2000.

[74] S. Nakamura, Y. Ueno, K. Tajima, J. Sasaki, T. Sugimoto, T. Kato, T. Shimoda, M. Itoh, H. Hatakeyama, T. Tamanuki, and T. Sasaki, "Demultiplexing of 168-Gb/s data pulses with a hybrid-integrated symmetric Mach-Zehnder all optical switch," *IEEE Photon. Technol. Lett.*, vol. 12, no. 4, pp 425-427, 2000.

[75] M. Asghari, I. White, and R. Penty, "Wavelength conversion using semiconductor laser optical amplifiers," *J. Lightwave Technol.*, vol. 15, no. 7, pp. 1181-1190, 1997.

[76] G. Bendelli, K. Komori, S. Arai, and Y. Suematsu, "A new structure for high-power TW-SLA," *IEEE Photon. Technol. Lett.*, vol. 3, no. 1, pp. 42-44, 1991.

[77] H. Ghafouri-Shiraz, P. W. Tan, and W. M. Wong, "A novel analytical expression of saturation intensity of InGaAsP tapered travelling-wave

semiconductor laser amplifier structures," *IEEE Photon. Technol. Lett.*, vol. 10, no. 11, pp. 1545-1547, 1998.

[78] A. K. Ghatak and K. Thygarajan, "Optical Electronics," Cambridge University Press, 1989.

[79] R. W. Clough, "The finite element method in plane stress analysis," *Proceedings of 2nd ASCE Conference on Electronic Computation,* Pittsburgh, PA, September 1960.

[80] R. Courant, "Variational methods for the solutions of problems of equilibrium and vibrations," *Bull. Am. Math. Soc.*, vol. 49, pp. 1-23, 1943.

[81] M. J. Turner, R. W. Clough, H. C. Martin, and L. C. Topp, "Stiffness and deflection analysis of complex structures," *J. Aeronaut. Sci.*, vol. 23, no. 9, pp. 805-824, 1956.

[82] J. Greenstadt, "On the reduction of continuous problems to discrete Form," *IBM J. Res. Dev.*, vol. 3, pp. 355-363, 1959.

[83] R. F. Harrington, "Field computation by moment methods," *Florida, R. E., Krieger Publishing Company*, 1968.

[84] M. Koshiba, K. Hayata, and M. Suzuki, "Approximate scalar finite element analysis of anisotropic optical waveguides," *Electron. Lett.*, vol. 18, no. 10, pp. 411-413, 1982.

[85] K. Morishita and M. Kumagai, "Unified approach to the derivation of variational expression for electromagnetic fields," *IEEE Trans. on Microwave Theory and Tech.*, vol. 25, no. 1, pp. 34-40, 1977.

[86] M. Koshiba, K. Hayata, and M. Suzuki, "Finite-element formulation in terms of the electric-field vector for electromagnetic waveguide problems," *IEEE Trans. Microwave Theory Tech.*, vol. 33, no. 10, pp. 900-905,1985.

[87] N. Mabaya, P. A. Lagasse, and P. Vandenbulcke, "Finite element analysis of optical waveguides," *IEEE Trans. Microwave Theory Tech.*, vol. 29, no. 6, pp. 600-605, 1981.

[88] A. D. Berk, "Variational principles for electromagnetic resonators and waveguides," *IRE Trans. Antennas Propagat.*, vol. 4, pp. 104-111, 1956.

[89] Z. J. Csendes and P. Silvester, "Numerical solution of dielectric loaded waveguides: I finite-element analysis," *IEEE Trans. Microwave Theory Tech.*, vol. 18, no. 12, pp. 1124-1131, 1970.

[90] W. J. English and F. J. Young, "An E-Vector variational formulation of the Maxwell equations for cylindrical waveguide problems," *IEEE Trans. Microwave Theory Tech.*, vol. 19, no. 1, pp. 40-46, 1971.

[91] T. Angkaew, M. Matsuhara, and N. Kumagai, "Finite-element analysis of waveguide modes: a novel approach that eliminates spurious modes" *IEEE Trans. Microwave Theory Tech.*, vol. 35, no. 2, pp. 117-123, 1987.

[92] M. Ohtaka, M. Matsuhara, and N. Kumagai, "Analysis of the guided modes in slab-coupled waveguides using a variational method," *IEEE J. Quantum Electron.*, vol. 12, no. 7, pp. 378-382, 1976.

[93] B. M. A. Rahman and J. B. Davies, "Finite-element solution of integrated optical waveguides," *J. Lightwave Technol.*, vol. 2, no. 5, pp. 682-688, 1984.

[94] M. Ikeuchi, H. Sawami, and H. Niki, "Analysis of open-type dielectric waveguides by the finite-element method," *IEEE Trans. Microwave Theory Tech.*, vol. 29, no.3, pp. 234-239, 1981.

[95] P. Silvester, D. A. Lowther, C. J. Carpenter, and E. A. Wyatt, "Exterior finite elements for 2-dimensional field problems with open boundaries," *IEE Proc.*, vol. 124, pp. 1267-1270, 1977.

[96] M. D. Feit and J. A. Fleck, "Computation of mode properties in optical fiber waveguides by a propagating beam method," *Appl. Opt.*, vol. 19, no. 7, pp. 1154-1164, 1980.

[97] B. Hermansson, D. Yevick, and P. Danielsen, "Propagating beam analysis of multimode waveguide tapers," *IEEE J. Quantum Electron.*, vol. 19, no. 8, pp. 1246-1251, 1983.

[98] P. Danielsen, "Two-dimensional propagating beam analysis of an electrooptic waveguide modulator," *IEEE J. Quantum Electron.*, vol. 20, no. 9, pp. 1093-1097, 1984.

[99] A. Neyer, W. Mevenkamp, L. Thylen, and B. Lagerstrom, "A beam propagation analysis of active and passive waveguide crossings," *J. Lightwave Technol.*, vol. 3, no. 3, pp. 635-642, 1985.

[100] R. Baets and P. E. Lagasse, "Loss calculation and design of arbitrarily curved integrated-optic waveguide," *J. Opt. Soc. Amer. B.*, vol. 37, no. 2, pp. 177-182, 1983.

[101] D. Yevick and L. Thylen, "Analysis of gratings by the beam propagation method," *J. Opt. Soc. Amer. B.*, vol. 72, no. 8, pp. 1084-1089, 1982.

[102] P. Kaczmarski, P. E. Lagasse, and J. Vandewege, "Propagating-beam model for single-mode fiber fused coupler," *IEE Proc. Pt. J.*, vol. 134, no. 2, pp. 111-116, 1987.

[103] B. Lamouroux and B. Prade, "Three-dimensional beam-propagating treatment of a monomode optical-fiber half-coupler," *J. Opt. Soc. Amer. A.*, vol. 4, no. 12, pp. 2228-2232, 1987.

[104] L. Thylen, E. M. Wright, G. I. Stegeman, C. T. Seaton, and J. V. Moloney, "Beam-propagation method analysis of a nonlinear directional coupler," *Opt. Lett.*, vol. 11, no. 11, pp. 739-741, 1986.

[105] G. R. Hadley, "Transparent boundary conditions for the beam propagation method," *IEEE J. Quantum Electron.*, vol. 28, no. 1, pp. 363-370, 1992.

[106] S. T. Hendow and S. A. Shakir, "Recursive numerical solution for nonlinear wave propagation in fibers and cylindrically symmetric systems," *Appl. Opt.*, vol. 25, no. 11, pp. 1759-1764, 1986.

[107] P. E. Lagasse and R. Baets, "Application of propagating beam methods to electromagnetic and acoustic wave propagation problems: a review," *Radio Science*, vol. 22, no. 7, pp. 1225-1233, 1987.

[108] C. Rolland, G. Mak, K. Fox, D. Adams, A. Thorpe, D. Yevick, and B. Hermansson, "Analysis of strongly-guiding rib waveguide S-bends: theory and experiment," *Electron. Lett.*, vol. 25, no. 18, pp. 1256-1257, 1989.

[109] D. Yevick and M. Glasner, "Analysis of forward wide-angle light propagation in semiconductor rib waveguide and integrated optic structures," *Electron. Lett.*, vol. 25, no. 23, pp. 1611-1613, 1989.

[110] A. Splett, M. Majd, and K. Petermann, "A novel beam propagation method for large refractive index steps and large propagation distances," *IEEE Photon. Tech. Lett.*, vol. 3, no. 5, pp. 466-468, 1991.

[111] D. Yevick and B. Hermansson, "Split-step finite difference analysis of rib waveguides," *Electron. Lett.*, vol. 25, no. 7, pp. 461-462, 1989.

[112] D. Yevick and B. Hermansson, "Efficient beam propagation techniques," *IEEE J. Quantum Electron.*, vol. 26, no. 1, pp. 109-112, 1990.

[113] G. R. Hadley, "Multistep method for wide-angle beam propagation," *Opt. Lett.*, vol. 17, no. 24, pp. 1743-1745, 1992.

[114] M. S. Al Salamed and M. R. Owais, "Full wave analysis of dielectric optical waveguides by vectorial finite elements and absorbing boundary condition," *J. Optical Comm.*, vol. 24, pp 74-78, 1999.

[115] E. E. Kriezis, P. Pantelakis, C. S. Antonopoulos, and A. G. Papagiannakis, "Full vector beam propagation method for axially dependent 3-D structures," *IEEE Trans. Magnetics.*, vol. 33, no. 2, pp. 1520-1543, 1997.

[116] F. Wijnands, T. Rasmussen, H. J. W. M. Hoekstra, J. H. Povlsen, A. Bjaeklev, and R. M. Deridder, "Efficient interface conditions for the semi-vectorial finite-difference beam propagation method," *Opt. Quantum Electron.*, vol. 27, no. 10, pp. 961-975, 1995.

[117] H. A. El-Mikati and J. B. Davies, "Coupling to an endfaced multicald optical fibre from a misaligned Gaussian beam or a separated multicald fibre," *Opt. Quantum Electron.*, vol. 17, no. 5, pp. 297-309, 1985.

[118] B. M. A. Rahman and J. B. Davies, "Analysis of optical waveguide discontinuities," *J. Lightwave Technol.*, vol. 6, no. 1, pp. 52-57, 1988.

[119] M. Razaz and J. B. Davies, "Capacitance of the abrupt transition from coaxial-to-circular waveguide," *IEEE Trans. Microwave Theory Tech.*, vol. 27, pp. 564-569, 1979.

[120] R. Jansen, "On the performance of the least-square method for waveguide junctions and discontinuities," *IEEE Trans. Microwave Theory Tech.*, vol. 23, pp. 434-436, 1975.

[121] H. Oraizi and J. Perini, "A numerical method for the solution of the junction of cylindrical waveguides," *IEEE Trans. Microwave Theory Tech.*, vol. 21, pp. 640-642, 1973.

[122] M. Reed, P. Sewell, T. M. Benson, and P. V. Kendall, "Efficient propagation algorithm for 3D optical waveguides," *IEEE Proc. Pt. J*, vol. 145, no. 1, pp. 53-58, 1998.

[123] P. G. Suchoski and V. Ramaswamy, "Design of single mode step-tapered waveguide sections," *IEEE J. Quantum. Electron.*, vol. 23, no. 2, pp. 205-211, 1987.

[124] T. B. Koch, J. B. Davies, and D. Wickramasinghe, "Finite element/finite difference propagation algorithm for integrated optical device," *Electron. Lett.*, vol. 25, no. 8, pp. 514-516, 1989.

[125] T. B. Koch, J. B. Davies, F. A. Fernandez, and R. Maerz, "Computation of wave propagation in integrated optical devices using z-transient variational principles," *IEEE Trans. Magnetics.*, vol. 27, no. 5, pp. 3876-3879, 1991.

[126] T. Tsuji, M. Koshiba, and T. Shiraishi, "Finite element beam propagation method for three-dimensional optical waveguide structures," *J. Lightwave Technol.*, vol. 15, no. 9, pp. 1728-1734, 1997.

[127] A. Niiyama and M. Koshiba, "Three-dimensional beam propagation analysis of nonlinear optical fibers and optical logic gates," *J. Lightwave Technol.*, vol. 16, no. 1, pp. 162-168, 1998.

[128] E. Montanari, S. Selleri, L. Vincetti, and M. Zoboli, "Finite-element formulation for full-vectorial propagation analysis in three-dimensional optical waveguides," *IEEE Photon. Tech. Lett.*, vol. 9, no. 9, pp. 1244-1246, 1997.

[129] E. Montanari, S. Selleri, L. Vincetti, and M. Zoboli, "Finite-element full-vectorial propagation analysis for three-dimensional z-varying optical waveguides," *J. Lightwave Technol.*, vol. 16, no. 4, pp. 703-714, 1998.

[130] S. S. A. Obayya, B. M. A. Rahman, and H. A. El-Mikati, "Full-vectorial finite-element beam propagation method for nonlinear directional coupler devices," *IEEE J. Quantum. Electron.*, vol. 36, no. 5, pp. 556-562, 2000.

[131] D. Yevick and B. Hermansson, "New formulation of the matrix beam propagation method: Application to rib waveguides," *IEEE J. Quantum Electron.*, vol. 25, no. 2, pp. 221-229, 1989.

[132] W. H. Press, S. A. Teukolsky, W. T. Vetterling, and B. P. Flannery, "Numerical recipes in fortran 77: The art of scientific computing," *Cambridge University* Press, chapter 12, New York, 1996.

[133] G. R. Hadley, " Transparent boundary conditions for the beam propagation method," *Opt. Lett.*, vol. 16, no. 9, pp. 624-626, 1991.

[134] C. Vassallo and F. Collino, "Highly efficient absorbing boundary conditions for the beam propagation method," *J. Lightwave Technol.*, vol. 14, no. 6, pp. 1570-1577, 1996.

[135] C. Vasallo and J. M. van der Keur, "Highly efficient transparent boundary conditions for finite difference beam propagation method at order four," *J. Lightwave Technol.*, vol. 15, no. 10, pp. 1958-1965, 1997.

[136] J. P. Berenger, "A perfectly matched layer for the absorption of electromagnetic waves," *J. Comput. Phys.*, vol. 114, no. 2, pp. 185-200, 1994.

[137] W. P. Huang, C. L. Xu, W. Lui, and K. Yokoyama, "The perfectly matched layer (PML) boundary condition for the beam propagation method," *IEEE Photon. Tech. Lett.*, vol. 8, no. 5, pp. 649-651, 1996.

[138] U. Pekel and R. Mittra, "An application of the perfectly matched layer (PML) concept to the finite element method frequency domain analysis of scattering problems," *IEEE Microwave and Guided Wave Lett.*, vol. 5, no. 8, pp. 258-260, 1995.

[139] U. Pekel and R. Mittra, "A finite element method frequency domain application of the perfectly matched layer (PML) concept," *Microwave and Opt. Technolog.*, vol. 9, no. 3, pp. 117-122, 1995.

[140] M. Koshiba, Y. Tsuji, and M. Hikari, "Finite element beam propagation method with perfectly matched layer boundary conditions," *IEEE Trans. on Magnetics.*, vol. 35, pp. 1482-1485, 1999.

[141] F. Fogli, G. Bellance, and P. Bassi, "TBC and PML conditions for 2D and 3D-BPM: A comparison," *Opt. Quantum Electron.*, vol. 30, pp. 443-456, 1998.

[142] S. S. A. Obayya, "Vector finite element based beam propagation analysis of optical guided-wave devices," A thesis for Ph.D. Degree, 1999.

[143] G. R. Hadley, "Wide-angle beam propagation using Pade approximation operators," *Opt. Lett.*, vol. 17, no. 20, pp. 1426-1428, 1992.

[144] O. C. Zienkiewicz, "The finite element method," *McGraw-Hill*, UK, 1977.

[145] D. Yevick and W. Bardyszewski, "Correspondence of variational finite-difference (relaxation) and imaginary-distance propagation methods for modal analysis," *Opt. Lett.*, vol. 17, no. 5, pp. 329-330, 1992.

[146] C. L. Xu, W. P. Huang, and S. K. Chaudhuri, "Efficient and accurate vector mode calculations by beam propagation method," *J. Lightwave Technol.*, vol. 11, no. 7, pp. 1209-1215, 1993.

[147] S. Ramo, J. Whinnery, T. Van Duzer, "Fields and waves in Communication Electronics," 3rd Ed., 1994.

[148] D. R. Scifres, W. Streifer, and R. D. Burnham, "Experimental and analytical studies of coupled multiple stripe diode lasers," *IEEE J. Quantum Electron.*, vol. 15, no. 9, pp. 917–922, 1979.

[149] D. Mehuys, L. Goldberg, and D. F. Welch, "5.25 CW near-diffraction limited tapered-stripe semiconductor optical amplifier," *IEEE Photon. Technol. Lett.*, vol. 5, no. 10, pp. 1179–1182, 1993.

[150] E. S. Kintzer, J. N. Walpole, S. R. Chinn, C. A. Wang, and L. J. Missaggia, "High-power strained-layer amplifiers and lasers with tapered gain region," *IEEE Photon. Technol. Lett.*, vol. 5, no. 6, pp. 605–608, 1993.

[151] B. M. A. Rahman, W. Boonthittatinont, S. S. A. Obayya, T. Wongcharoen, E. O. Ladele, and K. T. V. Grattan, "Rigorous beam propagation analysis of tapered spot-size converters in deep-etched semiconductor waveguides," *J. Lightwave Technol.*, vol. 21, no. 12, pp. 3392–3398, 2003.

[152] G. C. Dente and M. L. Tilton, "Modeling broad-area semiconductor optical amplifiers," *IEEE J. Quantum Electron.*, vol. 29, no. 1, pp. 76–88, 1993.

[153] L. Goldberg, D. Mehuys, M. R. Surette, and D. C. Hall, "High-power, near-diffraction-limited large-area traveling-wave semiconductor amplifiers," *IEEE J. Quantum Electron.*, vol. 29, no. 6, pp. 2028–2043, 1993.

[154] S. Ramanujan and H. G. Winful, "Spontaneous emission induced filamentation in flared amplifiers," *IEEE J. Quantum Electron.*, vol. 32, no. 5, pp. 784–789, 1996.

[155] R. J. Lang, A. Hardy, R. Parke, D. Mehuys, S. O'Brien, J. Major, and D. Welch, "Numerical analysis of flared semiconductor laser amplifiers," *IEEE J. Quantum Electron.*, vol. 29, no. 6, pp. 2044–2051, 1993.

[156] J. R. Marciante and G. P. Agrawal, "Nonlinear mechanism of filamentation in broad-area semiconductor laser," *IEEE J. Quantum Electron.*, vol. 32, no. 4, pp. 590–596, 1996.

[157] B. M. A. Rahman, N. Somasiri, and K. T. V. Grattan, "Birefringence compensation of silica waveguides," *IEEE Photon. Technol. Lett.*, vol. 17, no. 6, pp. 1205-1207, 2005.

[158] H. Yanagawa, T. Shimizu, S. Nakamura, and I. Ohyama, "Index-and dimensional taper and its application to photonic devices," *J. Lightwave Technol.*, vol. 10, pp. 587–591, 1992.

[159] K. Kasaya, O. Mitomi, M. Naganuma, Y. Kondo, and Y. Noguchi, "A simple laterally tapered waveguide for low-loss coupling to single-mode fibers," *IEEE Photon. Technol. Lett.*, vol. 5, pp. 345–347, 1993.

[160] O. Mitomi, K. Kasaya, and H. Miyazawa, "Design of a single-mode tapered waveguide for low-loss chip-to-fiber coupling," *IEEE J. Quantum Electron.*, vol. 30, no. 8, pp. 1787–1793, 1994.

[161] G. Bendelli, K. Komori, and S. Arai, "Gain saturation and propagation characteristics of index-guided tapered waveguided traveling wave semiconductor laser amplifiers (TTW-SLA's)," *IEEE J. Quantum Electron.*, vol. 28, no. 2, pp. 447–458, 1992.

[162] H. Ghafouri-Shiraz and P. W. Tan, "Study of a novel laser diode amplifier structure," *Semiconduct. Sci. Technol.*, vol. 11, pp. 1443–1449, 1996.

[163] H. Ghafouri-Shiraz, P. W. Tan, and T. Aruga, "Analysis of a semi-linear tapered-waveguide laser diode amplifier," *Microwave Optical Technol. Lett.*, vol. 12, no. 2, pp. 53-56, 1996.

[164] M. Mikulla, P. Chazan, A. Schmitt, S. Morgott, A. Wetzel, M. Walther, R. Kiefer, W. Pletschen, J. Braunstein, and G. Weimann, "High- brightness tapered semiconductor laser oscillators and amplifiers with low modal gain epilayer-structures," *IEEE Photon. Technol. Lett.*, vol. 10, no. 5, pp. 654-656, 1998.

[165] D. F. Welch, R. Parke, D. Mehuys, A. Hardy, R. Lang, S. O'Brien, and S. Scifres, "1.1 W CW, diffraction-limited operation of a monolithically integrated flared-amplifier master oscillator power amplifier," *Electron. Lett.*, vol. 28, no. 21, pp. 2011–2013, 1992.

[166] P. S. Yeh, I. F. Wu, S. Jiang, and M. Dagenais, "High-power high-gain monolithically integrated preamplifier/power amplifier," *Electron. Lett.*, vol. 29, no. 22, pp. 1981–1983, 1993.

[167] D. Mehuys, L. Goldberg, R. Waarts, and D. F. Welch, "4.5 W CW, near-diffraction-limited tapered-stripe semiconductor optical amplifier," *Electron. Lett.*, vol. 29, no. 2, pp. 219–221, 1993.

[168] M. Tamburrini, L. Goldberg, and D. Mehuys, "Periodic filaments reflective broad area semiconductor optical amplifier," *Appl. Phys. Lett.*, vol. 60, pp. 1292–1294, 1992.

[169] H. Ghafouri-Shiraz, P. W. Tan, and T. Aruga, "Picosecond pulse amplification in tapered-waveguide laser diode amplifiers," *IEEE J. Select. Topics Quantum Electron.*, vol. 3, no. 2, pp. 210-217, 1997.

[170] L. Goldberg, D. Mehuys, and D. Welsh, "High power mode-locked compound laser using a tapered semiconductor laser amplifier," *IEEE Photon. Technol. Lett.*, vol. 6, no. 9, pp.1070-1072, 1994.

[171] B. Zhu, I. H. White, K. A. Williams, F. R. Laughton, and R. V. Penty, "High peak power picosecond optical pulse generation from Q-switched bow-tie laser

with a tapered travelling wave amplifier," *IEEE Photon. Technol. Lett.*, vol. 8, no. 4, pp. 503-505, 1996.

[172] J. Ange, J. Chesnoy, P. M. Gabla, and A. Weygang, "Process in optical amplification (Alcatel)," *Electrical Comm.*, 4th Quarter, 1992.

[173] M. G. Oberg and N. A. Olsson, "Crosstalk between intensity modulated wavelength division multiplexed signals in a semiconductor laser amplifier," *IEEE J. Quantum Electron.*, vol. 24, no. 1, pp. 52-59, 1988.

[174] I. M. I. Habbab and G. P. Agrawal, "Asymmetric channel gain and crosstalk in travelling wave optical waveguides," *J. Lightwave Technol.*, vol. 7, no. 9, pp. 1351-1359, 1989.

[175] H. Ghafouri-Shiraz, "Single transverse-mode condition in long wavelength SCH semiconductor laser diodes," *IEICE Trans. Electron.*, vol. 70, pp. 130-134, 1994.

[176] E. El. Yumin, K. Komori, S. Arai, and G. Bendelli, "Taper-shape dependence of tapered-waveguide wave semiconductor laser amplifier (T'IV-SLA)," *IEICE Trans. Electron.*, vol. 77, pp. 7-15, 1994.

[177] G. P. Agrawal and N. A. Olsson, "Self-phase modulation and spectral broadening of optical pulses by using semiconductor laser amplifier," *IEEE J. Quantum Electron.*, vol. 25, no. 11, pp. 2297-2306, 1989.

[178] N. Nakagawa and S. Shimada, "Optical amplifiers in future optical communication systems," *IEEE LCS magazine*, vol. 1, no. 4, pp. 57-62, 1990.

[179] T. Mukai and Y. Yamamoto, "Gain frequency bandwidth and saturation output power of AlGaAs DH laser amplifiers," *IEEE J. Quantum Electron.*, vol. 17, no. 6, pp. 1028-1034, 1981.

[180] T. Mukai and Y. Yamamoto, " Noise in an AlGaAs semiconductor laser amplifier," *IEEE J. Quantum Electron.*, vol. 18, no. 4, pp. 564-575, 1982.

[181] G. Eisenstein, "Semiconductor optical amplifiers," *IEEE Circuits and Devices Magazine*, pp. 25-30, July, 1989.

[182] M. J. O'Mahony, "Semiconductor laser optical amplifiers for use in future fibre systems," *IEEE J. Lightwave Technol.*, vol. 6, no. 4, pp. 531-544, 1988.

[183] A. Yariv, "Optical Electronics," *3rd Edition*, Holt-Saunders, 1985.

[184] J. L. Gimlett and N. K. Cheung, "Effects of phase-to-intensity noise conversion by multiple reflections in giga-bit-per-second DFB laser transmission system," *J. Lightwave Technol.*, vol. 7, no. 6, pp. 888-895, 1989.

[185] M. J. Adams, "Time dependent analysis of active and passive optical bistability in semiconductors," *IEE Proc., Part J*, vol. 132, no. 6, pp. 343-348, 1985.

[186] F. Ohman, S. Bischoff, B. Tromborg, and J. Mork, "Noise and regeneration in semiconductor waveguides with saturable gain absorption," *IEEE J. Quantum Electron.*, vol. 40, no. 3, pp. 245-255, 2004.

[187] R. C. Johnson, H. A. Ecker, and J. S. Hollis, "Determination of far-field antenna patterns from near-field measurements," *IEEE Proc.*, vol. 61, no. 12, pp. 1668-1694, 1973.

[188] D. T. Paris, W. M. Leach, Jr., and E. B. Joy, "Basic theory of probe-compensated near-field measurements," *IEEE Trans. Antennas Propagat.*, vol. 26, no. 3, pp. 373-379, 1978.

[189] E. B. Joy, W. M. Leach, Jr., and G. P. Rodrigue, and D. T. Paris, "Applications of probe compensated near-field measurements," *IEEE Trans. Antennas Propagat.*, vol. 26, no. 3, pp. 379-389, 1978.

[190] P. A. O'Brien, P. M. W. Skovgaard, and J. G. McInerney, "Improved near- and far- field distributions in broad area semiconductor lasers with enhanced current spreading," *IEEE Lasers and Electo-optics Society Annual meeting*, LEO's 98, 1998.

[191] A. Larsson, M. Mittelstein, Y. Arakawa, and A. Yanv, " High efficiency broad-area single quantum well lasers with narrow single- lobed far –field patterns prepared by molecular beam epitaxy," *Electron. Lett.*, vol. 22, pp. 79-81, 1986.

[192] K. Saitoh, M. Koshiba, and Y.Tsuji, "Stress analysis method for elastically anisotropic material based optical waveguides and its application to strain-induced optical waveguides," *J. Lightwave Technol.*, vol. 17, no. 2, pp. 255-259, 1999.

[193] B. M. A. Rahman, Y. Liu, and K. T. V. Grattan, "Finite-element modeling of one- and two- dimensional MQW semiconductor optical waveguides," *IEEE Photon. Technol. Lett.*, vol. 5, no. 8, pp. 928-931, 1993.